Engineering Materials

Vadim V. Silberschmidt
Valery P. Matveenko *Editors*

Mechanics of Advanced Materials

Analysis of Properties and Performance

Springer

Engineering Materials

More information about this series at http://www.springer.com/series/4288

Vadim V. Silberschmidt · Valery P. Matveenko
Editors

Mechanics of Advanced Materials

Analysis of Properties and Performance

Springer

Editors
Vadim V. Silberschmidt
Wolfson School of Mechanical and Manufacturing Engineering
Loughborough University
Loughborough, Leicestershire
UK

Valery P. Matveenko
Institute of Continuous Media Mechanics
Russian Academy of Sciences
Perm
Russia

ISSN 1612-1317 ISSN 1868-1212 (electronic)
Engineering Materials
ISBN 978-3-319-17117-3 ISBN 978-3-319-17118-0 (eBook)
DOI 10.1007/978-3-319-17118-0

Library of Congress Control Number: 2015935404

Springer Cham Heidelberg New York Dordrecht London

Printed on acid-free paper

Springer International Publishing AG Switzerland is part of Springer Science+Business Media (www.springer.com)

Preface

In the last two decades, Mechanics of Materials as a discipline has experienced a type of revival. The main reason for this has been a continuing introduction of new materials (or even their classes) with extraordinary microstructures, properties and performance. Carbon nanotubes, quantum dots, bulk metallic glasses and graphene are some of the examples. This revival process was additionally enhanced by an application-related drive to expose these—as well as previously known and used—materials to harsher conditions: high strains, strain rates, loads and temperatures as well as combinations of various loading and environmental factors. Recent developments in aerospace, energy, automotive and defence industries as well as in microelectronics were possible thanks to extended usability envelopes for various components and structures.

Another important factor was the introduction of technologies allowing the production of materials and even final parts with precise control of their microstructural features, and, hence, properties and performances. A typical example is additive manufacturing—more known as *3d printing*—that can reproduce detailed microstructural patterns, developed by researchers in *silico*; it currently also has a capability to use multiple materials, gradual changes in properties—and with continuously improving spatial resolution.

This progress affected significantly Mechanics of Materials that its broadly used classical formulations does not fully meet the new challenges. This volume presents some of the current developments and trends in this field covering experimental, theoretical and numerical approaches and results. The examined materials include established ones such as metals and alloys (including, *i. a.*, pure indium), or polymeric fibrous networks as well as new types of materials: bulk metallic glasses, smart materials and metamaterials with a negative Poisson's ratio. Properties and deformation behaviours of composites with various types of constituents are also discussed.

Among the theoretical matters presented are the use of a phase-field formalism and its finite-element realisation for analysis of crack initiation and propagation in brittle materials; a statistical scheme for mechanics of composites with random reinforcement employing correlation functions of the second and higher orders and a variational formulation for quasi-harmonic vibrations of an electro-viscoelastic smart material consisting of elastic, viscoelastic and piezoelectric elements. All these theoretical schemes are also accompanied by examples of their numerical implementations for various case studies. Some dedicated numerical approaches and algorithms are also offered in other parts of the volume.

A wide range of experimental methods are discussed: tests at small scale (nanoindentation and micropillar compression); creep at various temperatures; wedge indentation etc. These tests were performed on specimens of various shapes and dimensions, for different stress/strain states and microstructures.

Thus, this volume would be of interest to researchers and engineers working on links between microstructures of advanced materials and their mechanical properties and performance.

Loughborough, UK Vadim V. Silberschmidt
Perm, Russia Valery P. Matveenko

Contents

Finite Element Modelling of 2D Brittle Fracture: The Phase-Field Approach

H.A.F.A. Santos and V.V. Silberschmidt

Abstract The prevention of fracture-induced failure is a major constraint in engineering design, and numerical simulations of fracture processes often play a key role in design decisions. Although huge efforts have been made to develop novel and more accurate models of fracture and an enormous progress has been achieved in the recent years, the development of an adequate scheme for the numerical simulation of crack initiation and propagation is still a significant challenge for the scientific community. The goal of this paper is twofold: (i) to give an overview of current numerical methods available in the literature for the analysis of brittle fracture problems; (ii) to present a finite element phase-field scheme for the analysis of brittle fracture problems. This scheme relies on recently developed strategies for incorporating an additional phase-field to account for fracture. The spatial finite element discretization is formulated by means of the classical Galerkin method, whereas an implicit Euler method with adaptive time-stepping is adopted for the temporal discretization. To demonstrate the capabilities of the model, some numerical experiments are modelled.

1 Introduction

The development of an adequate scheme for the numerical simulation of crack initiation and propagation is still a significant challenge for the Computational Mechanics community. Huge efforts have already been made to develop novel and accurate models for fracture and an enormous progress has been achieved.

H.A.F.A. Santos (✉)
Instituto Superior de Engenharia de Lisboa, Instituto Politécnico de Lisboa,
Rua Conselheiro Emídio Navarro 1, 1959-007 Lisbon, Portugal
e-mail: hugofreixialsantos@gmail.com

V.V. Silberschmidt
Wolfson School of Mechanical and Manufacturing Engineering, Loughborough University,
Loughborough, Leicestershire LE11 3TU, UK

V.V. Silberschmidt and V.P. Matveenko (eds.), *Mechanics of Advanced Materials*,
Engineering Materials, DOI 10.1007/978-3-319-17118-0_1

A particularly successful approach is provided by the Linear Elastic Fracture Mechanics (LEFM) theory based on Griffith's theory for brittle fracture, which relates crack nucleation and propagation to a critical value of the energy release rate.

The efforts to model brittle fracture focus essentially on two broad approaches: (i) the discrete methods, such as the element deletion method [2], the embedded finite element method [13] or the extended finite element method [23, 27], which use the finite element method in conjunction with Griffith's-type LEFM models to incorporate discontinuities into the displacement field, and (ii) the continuum-damage (CD) methods [12], which incorporate a damage parameter into the model that describes the material's deterioration and controls its strength. Some of these methods are already available in commercial CAE software packages and can be used for various design applications. However, it has long been recognized that, while discrete methods are well suited mostly for static fracture and for a moderate number of cracks, CD methods are not effective when modelling large dominant cracks, since the damage zone tends to widen in a direction normal to the crack initiation as the simulation proceeds. Another shortcoming of the CD methods is that regularization algorithms are needed to overcome mesh dependency. Additionally, current methods for predicting crack propagation, in particular for dynamic loading conditions and 3D problems, still lack accuracy and robustness, even when applied to relatively simple benchmark tests [26]. Due to these reasons, several efforts were made in the last decade for the development of alternative schemes. Recently, a new method for the numerical simulation of fracture has emerged—*the Variational Phase-Field Method* [14, 21].

Variational methods are a relatively new development in the field of Fracture Mechanics. The underlying theory was introduced in [14] for quasi-static brittle fracture, and is based on the idea that cracks should propagate along a path of least energy. The goal of variational methods is to circumvent several weaknesses of the classical LEFM theory of Griffith. As pointed out in [14], the inverse proportionality of the critical stress to the square root of the initial crack length indicates that the classical LEFM theory is unable to predict crack initiation. Indeed, for a solid without an initial crack, the stress required for crack propagation becomes infinite. Other important weaknesses of this theory are the inadequacy for predicting the direction of crack propagation and its inability to handle crack jumps.

Later, Bourdin et al. [5, 6] carried out numerical tests based on this method, and introduced a phase-field approximation of the energy functional in order to facilitate the determination of the numerical solution of the variational method. The phase-field was included in the energy functional in addition to the primary displacement field in order to regularize the jumps of the displacement field representing the cracks. The phase-field parameter models the continuous change in stiffness between broken and undamaged parts of the material on a small lengthscale controlled by a regularization parameter. This regularization allows for the treatment of the global energy minimization as a standard variational problem, for which classical finite element methods are adequate. In the variational phase-field approach, the evolution of fracture surfaces follows from the solution of a coupled system of partial differential equations. Due to this—and contrarily to many discrete methods—its implementation does not require fracture surfaces to be tracked algorithmically.

The variational phase-field approach has been recently applied in a dynamic setting by Bourdin et al. [7] and Larsen et al. [19, 20].

Alternative phase-field models of fracture were proposed by Miehe et al. [21, 22]. An important addition to the existing theory was the modelling of anisotropic degradation, which allows the analysis of tensile fracture, thus resolving the issue of interpenetration encountered in [7] for crack branching simulations. This model has been extended by Borden et al. [4] to the dynamic case.

In the phase-field approach to fracture, a crack is a small region in which damage accumulates, as quantified by the order parameter. This description is conceptually similar to the ones employed within the framework of continuum gradient theories for damage [25], wherein the damage gradient is considered as an independent constitutive variable. The phase-field approach to fracture may be viewed as a continuum gradient theory for damage with an alternative derivation for the equation governing damage evolution.

The goal of this paper is to give an overview of current numerical methods proposed for analysis of brittle fracture problems and to present a finite element phase-field model to deal with such problems. Additionally, some numerical experiments are presented, which demonstrate that, unlike many of the current numerical methods based on the classical theory of Griffith, the presented phase-field fracture model is able to reproduce various complex phenomena, such as deflection or branching of pre-existing cracks, as well as the nucleation of new cracks in originally undamaged domains.

2 Literature Review

2.1 General Considerations

The prevention of fracture-induced failure is a major constraint in engineering designs, and the numerical simulation of fracture processes often plays a key role in design decisions. A successful model is provided by the LEFM theory based on Griffith's theory for brittle fracture. A general concept in this theory is that, upon the attainment of a critical energy release rate, a fully opened crack is nucleated or propagated. As a result, the process zone, i.e., the zone in which the material changes from an undamaged state to a damaged one, is lumped into a single point at the crack tip. In the dynamic setting, crack growth velocity is selected based on the balance between the mechanical energy that flows within the process zone per unit time and the dissipated energy within the process zone over the same period. Although LEFM predictions agree well with observations for a sufficiently slow crack growth, large discrepancies may be found at high loading speeds.

Due to the complexity of fracture processes in engineering applications, numerical methods play a crucial role in fracture analyses. Efforts to model crack propagation were focused mainly on two broad approaches: (i) discrete methods, which use the FEM in conjunction with Griffith's-type LEFM models in order to incorporate discontinuities into the displacement field, and (ii) continuum-damage methods, which incorporate a damage parameter into the model that controls the strength of the material.

Among the most commonly used methods in the first category are: the Element Deletion Method (EDM) [2], the Interelement Separation Method (ISM) [9], the Embedded Element Method (EFEM) [13], the Cohesive Zone Method (CZM) [24], and the Extended Finite Element Method (XFEM) [23, 27]. All of these approaches represent cracks as discrete discontinuities, either by inserting discontinuity lines by means of remeshing strategies, or by enriching the displacement field with discontinuities using the partition of unity method. Continuum-Damage methods were particularly adopted to model diffusive fracture processes [12].

Some of the aforementioned methods are already available in commercial CAE software packages and can be used for various applications. However, it has long been recognized that discrete methods are only well suited for static fracture, and when a moderate number of cracks occurs. The EDM, for instance, suffers from extreme mesh dependency and is not well suited for dynamics. In the case of the ISM, cracks are only allowed to develop along existing interelement edges, which also leads to strong mesh dependency. Also, the EFEM may be sensitive to the orientation of the discontinuity surface. As for the XFEM, it requires an algorithm to ensure crack path continuity, which is particularly challenging in 3D. Additionally, and unlike the EFEM, the enrichment parameters used in the XFEM cannot be condensed at the element level, yielding computationally demanding algorithms, mostly when dealing with an increasing number of cracks and crack branches. Another important shortcoming of XFEM is that numerical integration requires special attention, particularly around the crack tip when employing non-polynomial enrichment functions, where several thousand Gauss-points may be needed to reduce the integration error. These shortcomings, together with those for CD methods mentioned in Sect. 1, resulted in many efforts, in particular in the last decade, to develop novel, efficient, and accurate computational methods for brittle dynamic fracture.

2.2 *Extended Finite Element Method*

Simulating the propagation of cracks using traditional finite element methods is challenging since the topology of the domain changes continuously. XFEM has been very successfully employed to model cracks, since the finite element mesh can be created independently from the crack geometry, and, in particular, since the domain does not have to be remeshed as the crack propagates. Remeshing is particularly cumbersome in dynamic crack propagation problems. Indeed, as the crack advances over a large part of the mesh, remeshing needs to be performed many times, leading unavoidably to computationally expensive simulations.

The basic idea behind the XFEM is to decompose the displacement field into continuous and discontinuous parts. The continuous part is the standard finite element interpolation, while the discontinuous, or enrichment, part is introduced into the finite element interpolation by means of the local partition of unity method. This enrichment is carried out with additional degrees of freedom introduced into the discretization of the test and trial functions, which are multiplied by the so-called *enrichment shape functions* incorporating the near tip asymptotic solutions and allowing displacements to be discontinuous across the crack face.

Application of the XFEM to cracks began with Belytschko and Black in [1]. In [23], the XFEM was used to create a technique for simulating crack propagation in two dimensions without the need to remesh the domain. The extension to three dimensions was initiated in [27].

However, the XFEM approach carries technical challenges: assembling the stiffness matrix requires integration of singular/discontinuous functions, and implementing enrichment requires resolving material connectivity (often using a level set representation). As for the integration issue, as noted in [11], the use of Gauss quadrature or Monte Carlo integration techniques is unstable. Indeed, since the crack path through a given triangle is a priori unknown, the singularities can move very close to quadrature points. Regarding the material connectivity issue, in a region unambiguously separated into two pieces (i.e., away from the crack tip), the enrichment is provided by a Heaviside function, defined to be 1 on one side of the crack and -1 on the other side. This is easy for the case of a single straight crack, but more challenging for more complex crack geometries.

The XFEM was mainly applied to problems involving the growth of a single crack or a few cracks; there are only a few contributions dealing with fracture problems that involve the growth of numerous (several hundreds of) cracks [8, 30]. The case of complex crack patterns such as branching and merging cracks was dealt with in [11], with separate enrichments used for each crack, and an additional enrichment function used to represent the junction itself. However, the formulation becomes cumbersome with increasing number of cracks and crack branches. Moreover, those methods suffer (in practice) from the absence of a reliable crack branching criteria.

In the last few years, several implementations of the XFEM have been presented in the literature. Bordas et al. in [3] developed object-oriented libraries for the XFEM. The implementation of the XFEM within a general-purpose Fortran finite element code was discussed in [28]. Wyart et al. in [29] proposed a substructuring approach to decompose a cracked domain into a safe subdomain and a cracked subdomain analyzed separately by FEM and XFEM codes, respectively. An alternative approach was pursued in [15], where the XFEM was implemented in the commercial finite element software Abaqus. Although Abaqus is a very general and well known finite element software tool, its XFEM package can handle only static analyses. Another important limitation of the XFEM in Abaqus is that only linear continuum elements are allowed.

2.3 Variational Approach: Phase-Field Models

Macroscopic continuum models for fracture can be classified into two main groups: (i) sharp-crack models, where crack surfaces are zero-traction boundaries extending to a sharp tip, and (ii) smeared-crack approaches, where the change in stiffness between broken and undamaged parts of an elastic material is modelled continuously with a damage parameter. The classical Griffith theory, as well as the variational approach to brittle fracture, belongs to the first group. In both theories the evolution of cracks results from a competition between a release of elastic energy and an increase of the surface energy. Thus, the energy release rate plays an important role in the determination of crack propagation. A numerical treatment of sharp-crack models is always faced with the difficulty of dealing with discontinuous displacement fields across the cracks. Phase-field models avoid these difficulties by introducing a continuous scalar field—the phase-field parameter—which smoothly interpolates between undamaged and failed states.

The reasons for introduction of variational approaches as a means to overcome limitations of LEFM were presented in Sect. 1 together with some models.

Standard approaches for dynamic crack propagation represent cracks as discrete discontinuities, either by inserting discontinuity lines, by means of remeshing techniques, or by enriching the displacement field with discontinuities using the partition of unity method. Tracing the evolution of complex fracture surfaces has, however, proven to be a tedious task, particularly in 3D. Contrarily, within the framework of a variational approach, discontinuities are not introduced into the solid. Instead, the fracture surface is approximated by a phase-field, which smoothens the boundary of the crack over a small region. The evolution of fracture surfaces follows from the solution of a coupled system of partial differential equations. From an implementation point of view, it does not require the fracture surfaces to be tracked algorithmically, which is particularly advantageous when multiple branching and merging cracks are considered in 3D. The numerical solution of the strong form of the equations of motion requires both spatial and temporal discretizations. The spatial discretization was carried out by means of the Galerkin method, either using the standard C^0-continuous finite elements [21], or, more recently, Non-Uniform Rational Basis Splines (NURBS) and T-Spline basis functions used within the framework of the Isogeometric Analysis [4]. For the temporal discretization, two different schemes were adopted: the monolithic scheme, which requires to solve the coupled system of equations simultaneously, and the staggered scheme, in which the displacements and the phase-field are solved for separately [19, 20].

A challenge that emerges with the use of phase-field models for fracture is their computational cost associated with mesh size requirements. Indeed, the use of a mesh with a characteristic length that is not small enough compared to the crack regularization parameter yields erroneous results with regard to the energy.

The variational approach is a robust technique for dealing with dynamic crack propagation problems. Still, it might be anticipated that, combining the advantages of partition of discrete methods (such as XFEM) and the variational approach will not be an easy task, although it could lead to a new efficient and reliable pathway to model complex fracture patterns.

One of the simplest two-dimensional isoparametric C^0-continuous finite elements is the four-node quadrilateral element, with three degrees of freedom per node, i.e. two displacement degrees of freedom and one phase-field degree of freedom per node. The discretization of arbitrarily shaped structures also requires an approximation of the geometry. The isoparametric concept makes use of the same shape functions to represent both the element geometries and the unknown displacement fields.

The presence of the transient term in the phase-field evolution equation requires the application of a time integration scheme in addition to the spatial discretization. For the temporal discretization, two different schemes can be adopted: (i) the monolithic scheme, based on the generalized-alpha method introduced in [10], which requires to solve the coupled system of equations simultaneously using a Newton-Raphson method, and (ii) the staggered scheme, in which the displacements and the phase-field are solved for separately [19, 20]. In the staggered time integration scheme, the momentum equation is solved first, at a given time step, in order to get the updated displacements. Using these updated displacements, the phase-field equation is solved subsequently. In addition to reducing the problem of solving two (possibly linear) systems, this scheme also allows greater flexibility in terms of how the momentum equation is solved, i.e., either implicit or explicit schemes can be used. This scheme can also be generalized to a predictor/multi-corrector format where additional Newton-Raphson iterations can be performed within a time step.

To be physically consistent, phase-field fracture models have to enforce irreversibility of the fracture process. In other words, all cracks must only grow with time. Different approaches were proposed in the literature to enforce irreversibility. The approach suggested in [6] constrains a subset of the discrete phase-field control variables that meet a minimum threshold value. This approach is easy to solve numerically but it requires the selection of an additional numerical parameter. An alternative approach, based on a strain-history functional was introduced in [21]. One advantage of this approach is its computational efficiency. The only computational cost is a floating point comparison, and it only requires storing one history variable per integration point. Another advantage of this approach is that an initial strain-history functional can be used to model initial cracks. Furthermore, the initial cracks can be located anywhere in the domain without reference to the mesh, which may prove highly advantageous in specifying complex surface cracks, in particular in three-dimensional bodies.

The width of the transition zone, where the phase-field interpolates between 1 and 0, is controlled by a length scale parameter. In order to obtain reasonable results, without overestimating the influence of the fractured zone, this length parameter should be chosen sufficiently small compared to the global dimensions of the considered sample. The mesh size has to be chosen sufficiently small in order to accurately resolve steep gradients and high curvatures of the crack field in the transition zones between cracked and uncracked areas. The accurate approximation of the crack field is important to capture the surface energy and, thus, the thresholds and dynamics of crack propagation correctly. However, small values of the length parameter require a high level of mesh refinement, which is numerically demanding in terms of computation time and required memory. Several approaches were proposed in the literature in order to meet the requirements for a sufficiently fine resolution, on the one hand, and to keep the computation time within bounds, on the other hand. In an effort to accomplish this, Kuhn and Muller [17, 18] introduced specially engineered finite element shape functions of an exponential nature to discretize the phase-field. These shape functions are parametrized by the ratio between the element size and the phase-field regularization parameter. Their results showed that, with these special shape functions, an accurate prediction of the surface energy associated with the phase-field is possible with a much lower level of refinement when compared to the standard finite element shape functions. The drawback of this approach is that some information regarding crack orientation is necessary for the proper construction of the exponential shape functions. Also, the choice of a good quadrature method is crucial for the performance of this approach.

3 Griffith's Theory of Brittle Fracture

Consider an arbitrary body $\Omega \in \mathcal{R}^2$ with external boundary $\partial\Omega$ and an internal discontinuity boundary Γ. Let $\partial\Omega = \partial\Omega_N \cup \partial\Omega_D$, with $\partial\Omega_N$ and $\partial\Omega_D$ being the Neumann and Dirichlet boundaries, respectively, such that $\partial\Omega_N \cap \partial\Omega_D = \emptyset$. The displacement of a point $\boldsymbol{x} \in \Omega$ at time t is denoted by $\boldsymbol{u}(\boldsymbol{x}, t)$. $\boldsymbol{u}$ may be a result of either the applied body forces $\boldsymbol{b}$, tractions $\bar{\boldsymbol{t}}$, prescribed boundary displacements $\bar{\boldsymbol{u}}$, or a combination of these actions. The body is assumed linear elastic, homogeneous, and isotropic with Young's modulus E, Poisson's ratio v and mass density ρ.

According to the Griffith's theory of brittle fracture, the energy required to create a unit area of fracture surface is equal to the critical energy release rate $\mathcal{G}_c$.

The Lagrangian for the discrete fracture problem is

$$L(\boldsymbol{u}, \dot{\boldsymbol{u}}, \Gamma) = \Pi_k(\dot{\boldsymbol{u}}) - \Pi_p(\boldsymbol{u}, \Gamma) \tag{1}$$

where

$$\Pi_k = \int_{\Omega} \left(\frac{1}{2} \rho \dot{\boldsymbol{u}} \cdot \dot{\boldsymbol{u}} \right) d\Omega \tag{2}$$

is the kinetic energy functional, and

$$\Pi_p = \int_{\Omega} W(\boldsymbol{\varepsilon}) \, d\Omega + \int_{\Gamma} \mathcal{G}_c \, d\Gamma \tag{3}$$

is the potential energy functional, with

$$\boldsymbol{\varepsilon} = \boldsymbol{D}\boldsymbol{u} \tag{4a}$$

$$W(\boldsymbol{\varepsilon}) = \frac{1}{2}\boldsymbol{\varepsilon}^T\boldsymbol{C}\boldsymbol{\varepsilon} \tag{4b}$$

$$\boldsymbol{\sigma} = \frac{\partial W}{\partial \boldsymbol{\varepsilon}} = \boldsymbol{C}\boldsymbol{\varepsilon} \tag{4c}$$

Here, W represents the strain energy density. $\boldsymbol{\varepsilon}$ and $\boldsymbol{\sigma}$ are the infinitesimal strain vector and the Cauchy stress vector, respectively, represented in Voigt's notation as follows

$$\boldsymbol{\sigma} = \begin{bmatrix} \sigma_{xx} \\ \sigma_{yy} \\ \sigma_{xy} \end{bmatrix}, \boldsymbol{\varepsilon} = \begin{bmatrix} \varepsilon_{xx} \\ \varepsilon_{yy} \\ 2\varepsilon_{xy} \end{bmatrix} \tag{5}$$

In (4a, 4b, 4c), $\boldsymbol{D}$ is the compatibilty operator and $\boldsymbol{C}$ is the constitutive matrix, defined as

$$\boldsymbol{D} = \begin{bmatrix} \frac{\partial}{\partial x_1} & 0 \\ 0 & \frac{\partial}{\partial x_2} \\ \frac{\partial}{\partial x_2} & \frac{\partial}{\partial x_1} \end{bmatrix} \quad \text{and} \quad \boldsymbol{C} = \frac{1}{E'} \begin{bmatrix} 1 & -v' & 0 \\ -v' & 1 & 0 \\ 0 & 0 & 2(1+v') \end{bmatrix}$$

where $E' = E,\ v' = v$ for plane-stress problems, and $E' = E/(1-v^2),\ v' = v/(1-v)$ for plane-strain problems.

The Euler-Lagrange equations of this functional determine the motion of the body.

3.1 Phase-Field Approximation

In this approach, the fracture energy is approximated as

$$\int_{\Gamma} \mathcal{G}_c \, d\Gamma \approx \int_{\Omega} \mathcal{G}_c \left(\frac{(1-c)^2}{4\varepsilon} + \varepsilon \nabla c \right) d\Omega \tag{6}$$

where c is the phase-field, taking values from 0 to 1. $c = 0$ inside the crack and $c = 1$ away from the crack. ε is the regularization parameter that controls the width of the smooth approximation of the crack.

To model the loss of material stiffness in the failure zone, the strain energy density is redefined as

$$W(\boldsymbol{\varepsilon}, c) = \frac{1}{2}(c^2 + \eta)\boldsymbol{\varepsilon}^T \boldsymbol{C}\boldsymbol{\varepsilon} \tag{7}$$

where η is the small dimensionless parameter $0 < \eta \ll 1$ introduced to avoid numerical difficulties where the material is broken (i.e., where $c = 0$). The degradation of stiffness in the broken phase is modelled by the factor $(c^2 + \eta)$.

Substitution of the phase-field approximation for the fracture energy (6) and the elastic energy density (7) into the Lagrange energy functional (1) yields

$$L(\boldsymbol{u}, \dot{\boldsymbol{u}}, c) = \int\limits_{\Omega} \left(\frac{1}{2}\rho \dot{\boldsymbol{u}} \cdot \dot{\boldsymbol{u}} - \frac{1}{2}(c^2 + \eta)\boldsymbol{\varepsilon}^T \boldsymbol{C}\boldsymbol{\varepsilon} \right) d\Omega - \int\limits_{\Omega} \mathcal{G}_c \left(\frac{(1-c)^2}{4\epsilon} + \epsilon \nabla c \right) d\Omega \tag{8}$$

Note that, in order to conserve mass, the kinetic energy term is unaffected by the phase-field approximation.

The Euler-Lagrange equations of the problem can be used to arrive at the following strong form of the equations of motion in a Cartesian reference system (x_1, x_2) to be solved in Ω

$$\boldsymbol{D}^T \boldsymbol{\sigma} + \boldsymbol{b} = \rho \ddot{\boldsymbol{u}} \tag{9a}$$

$$\dot{c} = -M\left(c\boldsymbol{\varepsilon}^T \boldsymbol{C}\boldsymbol{\varepsilon} - \mathcal{G}_c \left(2\epsilon \Delta c + \frac{1-c}{2\epsilon} \right) \right) \tag{9b}$$

with

$$\boldsymbol{\sigma} = (c^2 + \eta)\boldsymbol{C}\boldsymbol{\varepsilon}$$

Here, M is the mobility parameter, taken as constant and positive (classical Ginzburg-Landau equation).

The equations of motion are coupled with the phase-field c. Since c varies continuously, the singularity at the crack tip is replaced with a smooth region where c varies rapidly from 1 to 0.

It should also be emphasized that, within the framework of this model, the irreversibility condition $\Gamma(t) \subseteq \Gamma(t + \Delta t)$ needs to be enforced.

Additionally, the following sets of boundary conditions

$$\boldsymbol{u} = \bar{\boldsymbol{u}}, \text{ on } \partial\Omega_D$$

$$\mathbf{N}\boldsymbol{\sigma} = \bar{\boldsymbol{t}}, \text{ on } \partial\Omega_N$$

with

$$\mathbf{N} = \begin{bmatrix} n_1 & 0 & n_2 \\ 0 & n_2 & n_1 \end{bmatrix}$$

where n_j are the components of the external unit normal $\boldsymbol{n}$ of $\partial\Omega_N$, and initial conditions

$$\begin{aligned} \boldsymbol{u}(\boldsymbol{x},0) &= \boldsymbol{u}_0(\boldsymbol{x}),\ \boldsymbol{x} \in \Omega \\ \dot{\boldsymbol{u}}(\boldsymbol{x},0) &= \boldsymbol{v}_0(\boldsymbol{x}),\ \boldsymbol{x} \in \Omega \end{aligned}$$

must hold, where $\boldsymbol{u}_0$ and $\boldsymbol{v}_0$ are the initial displacements and velocities, respectively.

4 Finite Element Formulation

An implementation of the initial boundary-value problem into a finite element scheme is given in this section. The numerical solution of the initial boundary-value problem requires both a spatial and temporal discretization. In this work, the spatial discretization is formulated by means of the Galerkin method, whereas an implicit Euler method is adopted for the temporal discretization. In particular, for the discretization in space, four-node quadrilateral (bilinear Lagrangian) elements with three degrees of freedom per node, i.e., two displacement and one phase-field degrees of freedom per node, and a 2 × 2 Gauss quadrature rule are adopted in this work. The nonlinear coupled system of equations is solved using a Newton-Raphson algorithm.

4.1 Weak Form of the BVP

The trial solution spaces are defined as

$$\mathcal{U}_u = \{\boldsymbol{u}(t) \in (\mathcal{H}^1(\Omega))^d | \boldsymbol{u} = \bar{\boldsymbol{u}} \text{ on } \partial\Omega_D\} \tag{10a}$$

$$\mathcal{U}_c = \{c(t) \in \mathcal{H}^1(\Omega)\} \tag{10b}$$

Similarly, the weighting function spaces are defined as

$$\mathcal{V}_u = \{\boldsymbol{w} \in (\mathcal{H}^1(\Omega))^d | \boldsymbol{w} = 0 \text{ on } \partial\Omega_D\} \tag{11a}$$

$$\mathcal{V}_c = \{q \in \mathcal{H}^1(\Omega)\} \tag{11b}$$

Multiplying Eqs. 9a, 9b by the appropriate weighting functions and applying integration by parts leads to the following weak formulation: given $\bar{\boldsymbol{u}}$, $\bar{\boldsymbol{t}}$, $\boldsymbol{b}$, $\boldsymbol{u}_0$, $\boldsymbol{v}_0$ and c_0 find $\boldsymbol{u}(t) \in \mathcal{U}_u$ and $c(t) \in \mathcal{U}_c,\ t \in [0, T]$, such that for all $\boldsymbol{w} \in \mathcal{V}_u$ and $q \in \mathcal{V}_c$, the following conditions hold

$$\int\limits_{\Omega} (\sigma^T \boldsymbol{D}\boldsymbol{w} + \rho \ddot{\boldsymbol{u}}^T \boldsymbol{w})\, d\Omega - \int\limits_{\Omega} \boldsymbol{b}^T \boldsymbol{w}\, d\Omega - \int\limits_{\partial\Omega_N} \boldsymbol{t}^{-T} \boldsymbol{w}\, d\partial\Omega = 0 \tag{12a}$$

$$\int\limits_{\Omega} \left(\left(c\boldsymbol{\varepsilon}^T \boldsymbol{C}\boldsymbol{\varepsilon} - \frac{\mathcal{G}_c}{\epsilon}(1-c) \right) q - \frac{\dot{c}}{M} q + \boldsymbol{\xi}^T \nabla q \right) d\Omega = 0 \tag{12b}$$

$$\int\limits_{\Omega} \rho(\boldsymbol{u}^T(0) - \boldsymbol{u}_0^T)\boldsymbol{w}\, d\Omega = 0 \tag{12c}$$

$$\int\limits_{\Omega} \rho(\boldsymbol{v}^T(0) - \boldsymbol{v}_0^T)\boldsymbol{w}\, d\Omega = 0 \tag{12d}$$

$$\int\limits_{\Omega} \rho(\boldsymbol{c}(0) - \boldsymbol{c}_0) q\, d\Omega = 0 \tag{12e}$$

4.2 Discrete Weak Form

Following the Galerkin method, the finite-dimensional approximations to the function spaces are assumed as $\mathcal{U}_u^h \in \mathcal{U}_u$, $\mathcal{U}_c^h \in \mathcal{U}_c$, $\mathcal{V}_u^h \in \mathcal{V}_u$ and $\mathcal{V}_c^h \in \mathcal{V}_c$, leading to the discrete form of the problem as: given $\bar{\boldsymbol{u}}$, $\bar{\boldsymbol{t}}$, $\boldsymbol{b}$, $\boldsymbol{u}_0$, $\boldsymbol{v}_0$ and c_0 find $\boldsymbol{u}^h(t) \in \mathcal{U}_u^h$ and $c^h(t) \in \mathcal{U}_c^h,\ t \in [0, T]$, such that for all $\boldsymbol{w}^h \in \mathcal{V}_u^h$ and $q^h \in \mathcal{V}_c^h$, the following conditions hold

$$\int\limits_{\Omega} (\boldsymbol{\sigma}^{h^T} \boldsymbol{D}\boldsymbol{w}^h + \rho \ddot{\boldsymbol{u}}^{h^T} \boldsymbol{w}^h)\, d\Omega - \int\limits_{\Omega} \boldsymbol{b}^T \boldsymbol{w}^h\, d\Omega - \int\limits_{\partial\Omega_N} \boldsymbol{t}^{-T} \boldsymbol{w}^h\, d\partial\Omega = 0 \tag{13a}$$

$$\int\limits_{\Omega} \left(\left(c\boldsymbol{\varepsilon}^{h^T} \boldsymbol{C}\boldsymbol{\varepsilon}^h - \frac{\mathcal{G}_c}{\epsilon}(1-c^h) \right) q^h - \frac{\dot{c}^h}{M} q^h + \boldsymbol{\xi}^{h^T} \nabla q^h \right) d\Omega = 0 \tag{13b}$$

$$\int\limits_{\Omega} \rho(\boldsymbol{u}^{h^T}(0) - \boldsymbol{u}_0^T)\boldsymbol{w}^h\, d\Omega = 0 \tag{13c}$$

$$\int_{\Omega} \rho(\boldsymbol{v}^{h^T}(0) - \boldsymbol{v}_0^T)\boldsymbol{w}^h \, d\Omega = 0 \tag{13d}$$

$$\int_{\Omega} \rho(\boldsymbol{c}^h(0) - \boldsymbol{c}_0)q^h \, d\Omega = 0 \tag{13e}$$

The explicit representations of the approximations for the displacement and phase-field variables in terms of the basis functions and nodal variables are

$$\boldsymbol{u}^h = \sum_I N_I \boldsymbol{u}_I \tag{14a}$$

$$c^h = \sum_I N_I c_I \tag{14b}$$

with $I = 1, 2, 3, 4$. Similarly, assuming that both the finite-dimensional trial solution and weighting function spaces are defined by the same set of basis functions, the approximations for the weighting functions are defined as

$$\boldsymbol{w}^h = \sum_I N_I \boldsymbol{w}_I \tag{15a}$$

$$q^h = \sum_I N_I q_I \tag{15b}$$

where the N_I are the global basis functions and $\boldsymbol{u}_I$, c_I, $\boldsymbol{w}_{\mathrm{I}}$ and q_I are the nodal degrees of freedom.

Making use of these approximations, $\boldsymbol{\varepsilon}^h$ and ∇c^h can be written as

$$\boldsymbol{\varepsilon}^h = \sum_I \boldsymbol{B}_I^u \boldsymbol{u}_I \tag{16a}$$

$$\nabla c^h = \sum_I \boldsymbol{B}_I^c c_I \tag{16b}$$

with

$$\boldsymbol{B}_I^u = \begin{bmatrix} N_{I,x} & 0 \\ 0 & N_{I,y} \\ N_{I,y} & N_{I,x} \end{bmatrix} \quad \text{and} \quad \boldsymbol{B}_I^c = \begin{bmatrix} N_{I,x} \\ N_{I,y} \end{bmatrix}$$

4.3 Element Residuals and Their Derivatives

To solve the resulting coupled nonlinear system of equations, an incremental iterative Newton-Raphson solution strategy based on a consistent linearization of the governing equations is used. The element residuals can be written as

$$\boldsymbol{R}_I^u = -\boldsymbol{F}_{int,I}^u + \boldsymbol{F}_{ext,I}^u \tag{17a}$$

$$\boldsymbol{R}_I^c = -\boldsymbol{F}_{int,I}^c \tag{17b}$$

with

$$\boldsymbol{F}_{int,I}^u = \int_\Omega \left(\rho N_I \ddot{\boldsymbol{u}}^h + \boldsymbol{B}_I^{u^T} \boldsymbol{\sigma}^h\right) d\Omega \tag{18a}$$

$$\boldsymbol{F}_{ext,I}^u = \int_\Omega N_I \boldsymbol{b}^h \, d\Omega + \int_\Gamma N_I \boldsymbol{t}^{-h} \, d\Omega \tag{18b}$$

$$\boldsymbol{F}_{int,I}^c = \int_\Omega \left(N_I \frac{\dot{c}^h}{M} + \boldsymbol{B}_I^{c^T} \boldsymbol{\xi}^h + N_I \left(c^h \boldsymbol{\varepsilon}^{h^T} \boldsymbol{C} \boldsymbol{\varepsilon}^h - \frac{\mathcal{G}_c}{2\epsilon}(1 - c^h) \right) \right) d\Omega \tag{18c}$$

where $\boldsymbol{\xi}^h = 2\mathcal{G}_c \epsilon \nabla c^h$.

The derivatives of the element residuals with respect to the nodal degrees of freedom come out as

$$\boldsymbol{K}_{IJ}^{uu} = \frac{\partial \boldsymbol{R}_I^u}{\partial \boldsymbol{u}_J} = \int_\Omega \boldsymbol{B}_I^{u^T} (c^2 + \eta) \boldsymbol{C} \boldsymbol{B}_J^u \, d\Omega \tag{19a}$$

$$\boldsymbol{K}_{IJ}^{uc} = \frac{\partial \boldsymbol{R}_I^u}{\partial c_J} = 2 \int_\Omega \boldsymbol{B}_I^{u^T} c \boldsymbol{C} \boldsymbol{\varepsilon} N_J \, d\Omega \tag{19b}$$

$$\boldsymbol{K}_{IJ}^{cc} = \frac{\partial \boldsymbol{R}_I^c}{\partial c_J} = \int_\Omega \left(2\boldsymbol{B}_I^{c^T} \mathcal{G}_c \boldsymbol{\epsilon} \boldsymbol{B}_J^c + N_I (\boldsymbol{\varepsilon}^T \boldsymbol{C} \boldsymbol{\varepsilon} + \frac{\mathcal{G}_c}{2\epsilon}) N_J \right) d\Omega \tag{19c}$$

$$D_{IJ}^{cc} = \frac{\partial \boldsymbol{R}_I^c}{\partial \dot{c}_J} = \int_\Omega N_I \frac{1}{M} N_J \, d\Omega \tag{19d}$$

$$M_{IJ}^{uu} = \frac{\partial \boldsymbol{R}_I^u}{\partial \ddot{\boldsymbol{u}}_J} = \int_\Omega N_I \rho N_J \, d\Omega \tag{19e}$$

4.4 Time Discretization: Quasi-static Regime—Implicit Euler Method

The global residual vector that results from the assembly of the element residuals is defined as

$$\boldsymbol{R}(\boldsymbol{d},\dot{\boldsymbol{d}}) = \boldsymbol{F}_{ext} - \boldsymbol{F}_{int}(\boldsymbol{d},\dot{\boldsymbol{d}}) := 0 \tag{20}$$

Let $\boldsymbol{d}_n$ and $\dot{\boldsymbol{d}}_n$ denote the global vector of degrees of freedom for time step n and its time derivative, respectively, defined as follows

$$\boldsymbol{d} = \begin{bmatrix} \boldsymbol{d}_1 \\ \boldsymbol{d}_2 \\ \vdots \end{bmatrix}, \ \dot{\boldsymbol{d}} = \begin{bmatrix} \dot{\boldsymbol{d}}_1 \\ \dot{\boldsymbol{d}}_2 \\ \vdots \end{bmatrix} \tag{21}$$

with

$$\boldsymbol{d}_I = \begin{bmatrix} \boldsymbol{u}_I \\ \boldsymbol{c}_I \end{bmatrix}, \ \dot{\boldsymbol{d}}_I = \begin{bmatrix} \dot{\boldsymbol{u}}_I \\ \dot{\boldsymbol{c}}_I \end{bmatrix} \tag{22}$$

The implicit (or backward) Euler method is stated as follows: given $(\boldsymbol{d}_n, \dot{\boldsymbol{d}}_n)$, find $(\boldsymbol{d}_{n+1}, \dot{\boldsymbol{d}}_{n+1})$ such that

$$\boldsymbol{R}(\boldsymbol{d}_{n+1}, \dot{\boldsymbol{d}}_{n+1}) = 0 \tag{23}$$

with

$$\dot{\boldsymbol{d}}_{n+1} = \frac{\boldsymbol{d}_{n+1} - \boldsymbol{d}_n}{\Delta t} \tag{24}$$

where Δt is the time step. This problem can be redefined as

$$\boldsymbol{R}(\boldsymbol{d}_n, \boldsymbol{d}_{n+1}) = 0 \tag{25}$$

At each time step, the solution to this problem is obtained using a Newton-Raphson method to solve the non-linear system of equations. Letting k be the k-th Newton iteration step, the linearized system of equations that needs to be solved is

$$\boldsymbol{R}^{(k)}_{n+1} - \boldsymbol{T}^{(k)}_{n+1} \Delta \boldsymbol{d}^{(k)}_{n+1} = 0 \tag{26}$$

with $\boldsymbol{T}$ the global tangent matrix, formed by assembly of the element matrices given by

$$\boldsymbol{T}_{IJ} = \boldsymbol{K}_{IJ} + \frac{1}{\Delta t_n}\boldsymbol{D}_{IJ} \tag{27}$$

with

$$\boldsymbol{K}_{IJ} = \begin{bmatrix} \boldsymbol{K}_{IJ}^{uu} & \boldsymbol{K}_{IJ}^{uc} \\ \boldsymbol{K}_{IJ}^{uc^T} & \boldsymbol{K}_{IJ}^{cc} \end{bmatrix} \tag{28}$$

and

$$\boldsymbol{D}_{IJ} = \begin{bmatrix} \boldsymbol{O} & \boldsymbol{O} \\ \boldsymbol{O} & D_{IJ}^{cc} \end{bmatrix} \tag{29}$$

being the element stiffness and damping matrices, respectively.

The problem is initialized with

$$\boldsymbol{d}_{n+1}^{(0)} = \boldsymbol{d}_n \tag{30}$$

and the solution is computed iteratively using the update formula given by

$$\boldsymbol{d}_{n+1}^{(k+1)} = \boldsymbol{d}_{n+1}^{(k)} + \Delta\boldsymbol{d}_{n+1}^{(k)} \tag{31}$$

where the increment $\Delta\boldsymbol{d}_{n+1}^{(k)}$ is determined from the linearized system of Eq. 26. The iteration procedure continues until convergence of the residual vector is achieved.

4.5 Irreversibility of Cracking

Perhaps the most significant drawback of variational phase-field models is that they typically allow for crack healing. To rule out such unphysical behavior, Hakim and Karma proposed constraining the time-rate of the phase field to be less than or equal to zero at all points and times [16]. In simulations of quasi-static fracture processes in anti-plane shear and plane strain, they observed that, while slightly larger loads appear to be required when their irreversibility criterion is imposed, crack paths were essentially unaffected. Alternatively, following the approach proposed in [5], the irreversibility of cracking can be guaranteed by imposing homogeneous Dirichlet boundary conditions on the phase-field once a crack as been detected. The latter formulation is adopted in this work.

5 Numerical Results

5.1 Square Plate Under Quasi-static Prescribed Displacement

The square plate under quasi-static prescribed displacement depicted in Fig. 1 was considered. A uniform 64 × 64 mesh was adopted. The material parameters (assumed to be dimensionally consistent) were set to $E = 10^6$, $\nu = 0.3$ and $\mathcal{G}_c = 0.01$, and plane stress was assumed. The regularization, viscosity and mobility parameters were chosen to be $\epsilon = 0.02$, $\eta = 10^{-5}$ and $M = 10^9$, respectively. The prescribed displacement was set to $\bar{u} = 4.5 \times 10^{-4}$. The problem was solved in an incremental-iterative fashion by resorting to the Newton-Raphson method. An adaptive time-stepping scheme was used, for which the convergence tolerance was set to 1.0×10^{-9} and the optimal number of iterations to 4. For a larger number of iterations, the adaptive scheme automatically decreases the time step size, whereas for a smaller number of iterations the adaptive scheme increases it.

The obtained distributions of stresses and phase-field are shown in Fig. 2. Two cracks initiate from the corners of the built-in edge at a displacement of $\bar{u} = 2.9 \times 10^{-4}$. At $\bar{u} = 4.1 \times 10^{-4}$ the cracks start deviating from the vertical edge. As expected, high stress gradients can be observed at the crack tips.

The undeformed and deformed configurations of the plate are plotted in Fig. 3.

5.2 Pre-notched Square Plate Under Quasi-static Prescribed Displacement

The pre-notched square plate under quasi-static prescribed displacement depicted in Fig. 4 is considered in this section. The same 64 × 64 mesh and material parameters were employed. The regularization, viscosity and mobility parameters remained at

Fig. 1 Square plate under quasi-static tensile load: problem definition

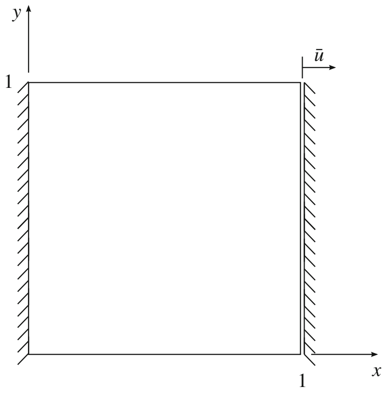

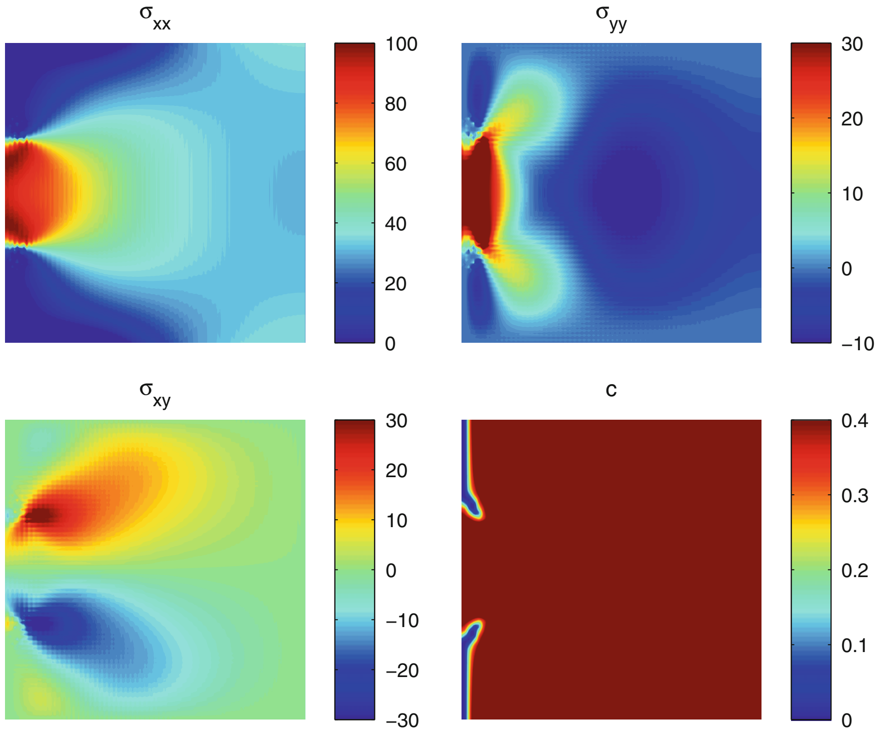

Fig. 2 Square plate under quasi-static prescribed displacement: stresses and phase-field obtained on a 64 × 64 mesh for $\bar{u} = 4.5 \times 10^{-4}$

Fig. 3 Square plate under quasi-static prescribed displacement: deformed (scaled) and undeformed configurations of the plate obtained for $\bar{u} = 4.5 \times 10^{-4}$

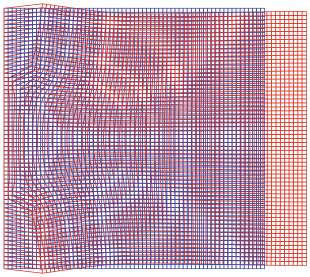

the same level. The prescribed displacement in this case was set to $\bar{u} = 1.5 \times 10^{-4}$. The problem was solved in an incremental-iterative fashion similar to the previous example.

The obtained distributions of stresses and phase-field are shown in Fig. 5.

The obtained results indicate that the proposed phase-field fracture model is capable to reproduce various complex phenomena, such as deflection or branching

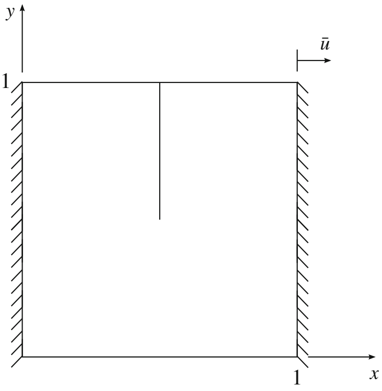

Fig. 4 Pre-notched square plate under quasi-static prescribed displacement: problem definition

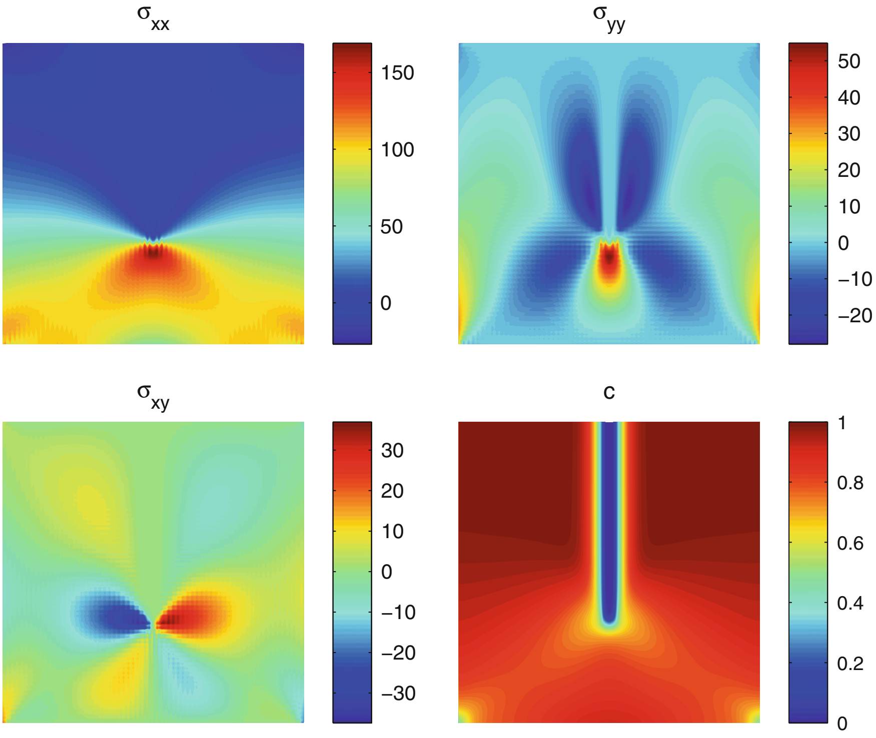

Fig. 5 Pre-notched square plate under quasi-static prescribed displacement: stresses and phase-field obtained on a 64×64 mesh for $\bar{u} = 1.5 \times 10^{-4}$

of pre-existing cracks, as well as the nucleation of new cracks in originally undamaged domains. However, a high resolution of the crack is needed, leading to computationally expensive simulations.

6 Conclusions

The numerical simulation of brittle fracture is still a significant challenge for the Computational Mechanics community. An overview of the main current numerical methods available in the literature for the analysis of brittle fracture problems was given. It can be concluded that discrete methods are well suited only for static fracture and a moderate number of cracks. On the other hand, continuum damage methods are not effective when modelling large dominant cracks. The recently introduced variational approach circumvents the implementation of complex crack-tracking algorithms and the need to describe the topology of the crack surface.

A finite element phase-field scheme relying on the variational approach to model brittle fracture problems was presented and some numerical experiments were implemented with this scheme. It was demonstrated that the presented model is capable to reproduce various complex phenomena, although it requires a high resolution of the crack, which may lead to computationally expensive simulations.

Acknowledgments The research leading to these results has received funding from the European Union Seventh Framework Programme (FP7/2007-2013) under grant agreement No. PIAPP-GA-284544-PARM-2. The authors are grateful for this financial support.

References

1. Belytschko, T., Black, T.: Elastic crack growth in finite elements with minimal remeshing. Int. J. Numer. Meth. Eng. **45**, 601–620 (1999)
2. Belytschko, T., Lin, J.I.: A three-dimensional impact penetration algorithm with erosion. Int. J. Impact Eng. **5**(1–4), 111–127 (1987)
3. Bordas, S., Nguyen, P.V., Dunant, C., Guidoum, A., Nguyen-Dang, H.: An extended finite element library. Int. J. Numer. Meth. Eng. **71**(6), 703–732 (2007)
4. Borden, M.J., Verhoosel, C.V., Scott, M.A., Hughes, T.J.R., Landis, C.M.: A phase-field description of dynamic brittle fracture. Comput. Methods Appl. Mech. Eng. **217–220**, 77–95 (2012)
5. Bourdin, B., Francfort, G.A., Marigo, J.-J.: Numerical experiments in revisited brittle fracture. J. Mech. Phys. Solids **48**(4), 797–826 (2000)
6. Bourdin, B., Francfort, G.A., Marigo, J.-J.: The variational approach to fracture. J. Elast. **91** (1–3), 5–148 (2008)
7. Bourdin, B., Larsen, C., Richardson, C.: A time-discrete model for dynamic fracture based on crack regularization. Int. J. Fract. **168**(2), 133–143 (2011)
8. Budyn, E., Zi, G., Moes, N., Belytschko, T.: A method for multiple crack growth in brittle materials without remeshing. Int. J. Numer. Meth. Eng. **61**(10), 1741–1770 (2004)
9. Camacho, G.T., Ortiz, M.: Computational modelling of impact damage in brittle materials. Int. J. Solids Struct. **33**, 2899–2938 (1996)
10. Chung, J., Hulbert, G.M.: A time integration algorithm for structural dynamics with improved numerical dissipation: the generalized-alpha method. J. Appl. Mech. **60**(2), 371–375 (1993)
11. Daux, C., Moes, N., Dolbow, J., Sukumar, N., Belytschko, T.: Arbitrary branched and intersecting cracks with the extended finite element method. Int. J. Numer. Meth. Eng. **48**, 1741–1760 (2000)

12. de Borst, R.: Encyclopedia of Computational Mechanics, vol. 2: Solids and Structures, chapter Damage, Material Instabilities, and Failure, pp. 335–373. Wiley, New York (2004)
13. Dvorkin, E.N., Cuitino, A.M., Gioia, G.: Finite elements with displacement interpolated embedded localization lines insensitive to mesh size and distortions. Int. J. Numer. Meth. Eng. **30**(3), 541–564 (1990)
14. Francfort, G.A., Marigo, J.-J.: Revisiting brittle fracture as an energy minimization problem. J. Mech. Phys. Solids **46**(8), 1319–1342 (1998)
15. Giner, E., Sukumar, N., Tarancón, J.E., Fuenmayor, F.J.: An abaqus implementation of the extended finite element method. Eng. Fract. Mech. **76**, 347–368 (2009)
16. Hakim, V., Karma, A.: Laws of crack motion and phase-field models of fracture. J. Mech. Phys. Solids **57**(2), 342–368 (2009)
17. Kuhn, C., Muller, R.: Exponential finite element shape functions for a phase field model of brittle fracture. In: Proceedings of the 11th International Conference on Computational Plasticity, pp. 478–489, 2011
18. Kuhn, C., Muller, R.: A new finite element technique for a phase field model of brittle fracture. J. Theor. Appl. Mech. **49**, 1115–1133 (2011)
19. Larsen, C.J.: Models for dynamic fracture based on Griffith's criterion. In: Hackl, K. (ed.) IUTAM Symposium on Variational Concepts with Applications to the Mechanics of Materials, vol. 21, pp. 131–140. Springer, Netherlands (2010)
20. Larsen, C.J., Ortner, C., Suli, E.: Existence of solutions to a regularized model of dynamic fracture. Math. Models Methods Appl. Sci. **20**(7), 1021–1048 (2010)
21. Miehe, C., Hofacker, M., Welschinger, F.: A phase field model for rate-independent crack propagation: robust algorithmic implementation based on operator splits. Comput. Methods Appl. Mech. Eng. **199**(45–48), 2765–2778 (2010)
22. Miehe, C., Welschinger, F., Hofacker, M.: Thermodynamically consistent phase-field models of fracture: variational principles and multi-field fe implementations. Int. J. Numer. Meth. Eng. **83**(10), 1273–1311 (2010)
23. Moes, N., Dolbow, J., Belytschko, T.: A finite element method for crack growth without remeshing. Int. J. Numer. Meth. Eng. **46**(1), 131–150 (1999)
24. Ortiz, M., Pandolfi, A.: Finite-deformation irreversible cohesive elements for three-dimensional crack-propagation analysis. Int. J. Numer. Meth. Eng. **44**, 1267–1282 (1999)
25. Peerlings, R.H.J., De Borst, R., Brekelmans, W.A.M., De Vree, J.H.P.: Gradient enhanced damage for quasi-brittle materials. Int. J. Numer. Meth. Eng. **39**, 3391–3403 (1996)
26. Song, J.-H., Wang, H., Belytschko, T.: A comparative study on finite element methods for dynamic fracture. Comput. Mech. **42**, 239–250 (2008)
27. Sukumar, N., Moes, N., Moran, B., Belytschko, T.: Extended finite element method for three-dimensional crack modelling. Int. J. Numer. Meth. Eng. **48**, 1549–1570 (2000)
28. Sukumar, N., Prévost, J.H.: Modeling quasi-static crack growth with the extended finite element method part i: Computer implementation. Int. J. Solids Struct. **40**(26), 7513–7537 (2003)
29. Wyart, E., Duflot, M., Coulon, D., Martiny, P., Pardoen, T., Remacle, J.-F.: Substructuring fe-xfe approaches applied to three-dimensional crack propagation. J. Comput. Appl. Math **215**, 626–638 (2008)
30. Zi, G., Song, J.H., Budyn, E., Lee, S.H., Belytschko, T.: A method for growing multiple cracks without remeshing and its application to fatigue crack growth. Modell. Simul. Mater. Sci. Eng. **12**(5), 901–915 (2004)

Crystalline Deformation in the Small Scale

Murat Demiral, Anish Roy and Vadim V. Silberschmidt

Abstract In the last two decades, experimental observations demonstrated—and numerical simulations confirmed—that plastic deformation in the small scale, i.e. at the micron or sub-micron scales, is different from that at the macro-scale; this phenomenon is known as *size effect*. It was observed mostly in indentation, torsion and bending experiments, being ascribed to strong gradients of strain in such deformation processes. The size effect was also reported in uniaxial micro- and nano-pillar compression experiments in spite of their inherent lack of (or limited) macroscopic strain gradients. In the present study, we first review some critical and essential experimental studies that were conducted over the years to analyse various mechanisms that govern deformation in the small scale. In the second part, different modelling approaches describing this phenomenon are briefly reviewed.

1 Introduction

Modern high-technology applications such as medical devices, thermal barrier coatings, micro- and nano-electro mechanical systems and semiconductors as well as gems industry increasingly use components with sizes down to a few micrometres and even smaller. The respective manufacturing processes can thus include

---

M. Demiral (✉)
Department of Mechanical Engineering, University of Turkish Aeronautical Association,
06790 Ankara, Turkey
e-mail: mdemiral@thk.edu.tr

A. Roy · V.V. Silberschmidt
Wolfson School of Mechanical and Manufacturing Engineering,
Loughborough University, Loughborough, Leicestershire LE11 3TU, UK
e-mail: A.Roy3@lboro.ac.uk

V.V. Silberschmidt
e-mail: V.Silberschmidt@lboro.ac.uk

V.V. Silberschmidt and V.P. Matveenko (eds.), *Mechanics of Advanced Materials*,
Engineering Materials, DOI 10.1007/978-3-319-17118-0_2

forming and shaping at a small scale. Plastic deformations in such a scale are known to differ from those at the macro-scale, resulting in a so-called ‘size effects’.

Understanding deformation mechanisms and assessing mechanical performance at small scales are necessary to realize the full potential of emerging nano- and micro-technologies and to design new products with superior characteristics. Also, knowledge of links between the microstructural and geometrical factors can provide additional ways to enhance component performance and clarify their design constraints.

The phenomena of size effect can be separated into two groups—“intrinsic” and “extrinsic”. Intrinsic size effects are related to strengthening due to microstructural constraints such as grain size and second-phase particles and have been studied by a materials science community for more than a century. Extrinsic size effects arise from dimensional constraints, e.g. due to a sample size and were discovered in the last two decades; hence, they are currently a topic of rigorous investigations [1].

An extrinsic size effect was mostly observed in indentation, torsion and bending experiments, where it was ascribed to a higher dislocation density due to the generation of geometrically necessary dislocations (GNDs), which, in turn, led to strong gradients of strain in a deformation process. To understand the underlying physics for this phenomenon, uniaxial compression experiments of surface-dominated micro-pillars, eliminating the effect of strain gradients, were performed. However, the size effect was still reported, with the ultimate tensile strength and yield strength scaling with an external sample size in a power-law fashion, sometimes attaining a significant fraction of material’s theoretical strength. Several different explanations were proposed in the literature to elucidate it.

Alongside with experimental studies, various numerical simulations were used to investigate the size effect. Though they are in many cases less cumbersome to implement than detailed test at microscale, these methods have their own limitations. For instance, quantum and atomistic simulations cannot be performed on realistic time scale and structures while classical continuum plasticity theories cannot explain the dependence of mechanical response on size as no length scale enters the constitutive description. Multi-scale continuum theories incorporating spatial gradients and/or volume integrals accounting for non-local interactions provide an alternative for this.

The purpose of the present review is to survey crystalline deformation in the small scale. Both experimental and numerical applications of size effects are briefly reviewed.

2 Experimental Observations

In this section we review some critical and essential experimental studies that were conducted over the years and paved the way for theoretical and modelling work to characterise and study various mechanisms that govern deformation in the small scale.

2.1 Indentation Size Effects

Experiments carried out in the past few decades demonstrated strong indentation size effects (ISEs) in crystalline materials. Stelmashenko et al. [2] and [3] reported that the measured hardness values were observed to increase with a decreasing indentation size, especially in the sub-micrometre depth regime. Figure 1 demonstrates a typical ISE observed in single-crystal copper and a cold worked polycrystalline copper.

This observation is not surprising as hardness measurements have been recognized to be size-dependent since early experiments by Tabor [4]. The research into the ISE gained prominence partly motivated by the development of large-scale application of thin films in electronic components and partly by the availability of novel methods of probing mechanical properties in very small volumes. Different physical and geometric mechanisms were suggested for ISE. Some of the proposed mechanisms or factors are: (1) a pile-up or a sink-in of the deformed surface during indentation; (2) a loading rate of the indenter; (3) a grain size, or the Hall-Patch effect; (4) presence of an oxidation layer or a work-hardened surface layer and (5) a geometric effect of indenter's tip (e.g. its radius) [5].

Some authors argued that the size dependence of material's mechanical properties resulted from an increase in strain gradients inherent to localized zones, which necessitated the presence of geometrically necessary dislocations resulted in additional hardening [6]. The characteristic features of deformation in metals are formation, motion and storage of dislocations. According to a Taylor's hardening rule, dislocation storage is responsible for material hardening. Stored dislocations can be divided into two groups: statistically stored dislocations (SSDs) and GNDs. SSDs are generated by trapping each other in a random way and believed to be dependent on effective plastic strain. On the other hand, GNDs are the stored dislocations that relieve plastic-deformation incompatibilities within the material caused by non-uniform dislocation slip. The density of GNDs is directly proportional to the gradients of effective plastic strain, and their presence causes additional storage of defects and,

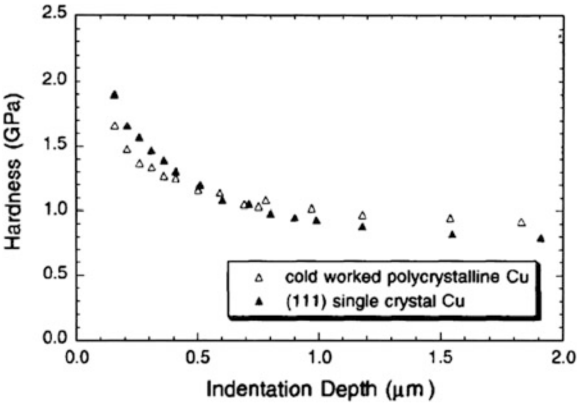

Fig. 1 Indentation size effect in crystalline materials. Reprinted with permission from [3]

hence, increases the deformation resistance by acting as obstacles to SSDs [6]. The dependency of SSDs and GNDs, respectively, on the effective plastic strain and its gradients is responsible for the size effect. The smaller the length scale, the larger the density of GNDs relative to that of SSDs and, consequently, the higher the plastic strain gradients compared to average plastic strains. An important and often misunderstood caveat is that SSDs and GNDs are essentially identical and simply labelled differently for convenience. Such an approach inevitably leads to the requirement for additional phenomenological laws with non-physical parameters to account for the interaction between GNDs and SSDs (e.g. in the form of annihilation and generation rules). A physically reasonable and accurate model of continuum dislocation mechanics should account for all dislocations consistently. Such an approach was proposed by Acharya [7] and developed to model most of the well-known benchmark problems in small-scale plasticity [8, 9].

Different indenter types were also used to study ISE. For instance, Qu et al. [10] used five different spherical indenter tips with radius ranging from 14 to 1600 μm to measure hardness. It was observed that indentation hardness *H* increased with an increase in the ratio of contact radius *a* to the indenter radius *R* (Fig. 2). Swadener and George [11] also observed that *H* increased continuously with an increase in the indentation depth using a spherical indenter, i.e., the so-called *reversed size effect*, contrary to the usual size effect observed in sharp indentation. The reverse dependence of hardness on indentation depth is explained by different dislocation densities underneath the indenters. In the case of a sharp indenter, the average density of SSDs is independent of the indentation depth, while the density of GNDs is inversely proportional to it (Fig. 3a). On the other hand, in the case of a spherical indenter, although the density of SSDs increases with an increase in the indentation depth (through a contact radius) the density of GNDs becomes essentially independent (Fig. 3b). The total dislocation density, therefore, displays a reversed depth dependence for sharp and spherical indenters; so does the magnitude of indentation

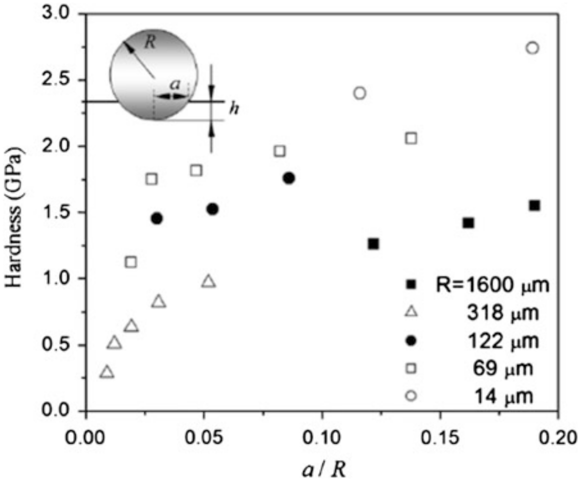

Fig. 2 Effect of ratio of contact radius (a) to spherical indenter radius (R) on indentation hardness of iridium. Reprinted with permission from [10]

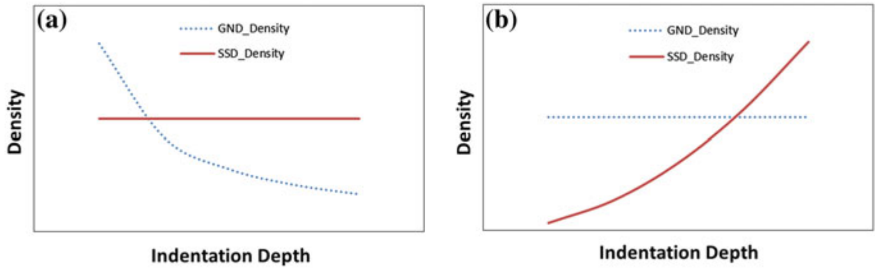

Fig. 3 Schematic plot of variations in GND and SSD densities with indentation depth using a sharp (**a**) and spherical indenter (**b**)

hardness [5]. On the other hand, the experimental study of [12] with a sharp indenter demonstrated that the total GND density below the indents decreased with decreasing indentation depth. This observation contradict the strain-gradient theories attributing size-dependent material properties to GNDs. Abu Al-Rub and Voyiadjis [13] interpreted the size effect in hardness experiments with a spherical indenter in a different way. It was explained that to get ISE in spherical indentation similar to that in sharp indentation, plastic strain should be independent of the sphere size to provide independence of plastic strain on indentation depth. In that study, the hardness values obtained with different spherical indenters were compared for the same a/R ratio representing the same plastic strain value. A decrease in hardness with an increasing spherical indenter size was reported, which can be also interpreted based on Fig. 2.

2.2 *Size Effect in Pillar Compression*

Recently, Uchic and co-workers [14] developed a testing methodology to measure the flow behaviour of miniature samples in compression. In this test micro-scale cylindrical samples fabricated using a focused-ion-beam (FIB) milling technique (for instance Fig. 4a) were uniaxially compressed in a nano indentation system equipped with a flat punch [15]. This method was specifically designed to probe mechanical properties as a function of the decreasing sample size. Later this technique was extended by [16] to perform uniaxial compression tests on Au nano-pillars.

Uchic et al. [14] tested three different materials with a pillar size from 1 to 40 μm: Ni, Ni3Al-1 %Ta and a Ni-based super alloy with a (269) orientation. These experiments showed an increase in the strength of crystals by up to 15 times compared to bulk Ni with a decrease in the sample size. However, no significant increase in the work-hardening rate of the crystals was observed. It was also reported that frequent strain bursts—avalanches of dislocations—and finite discrete

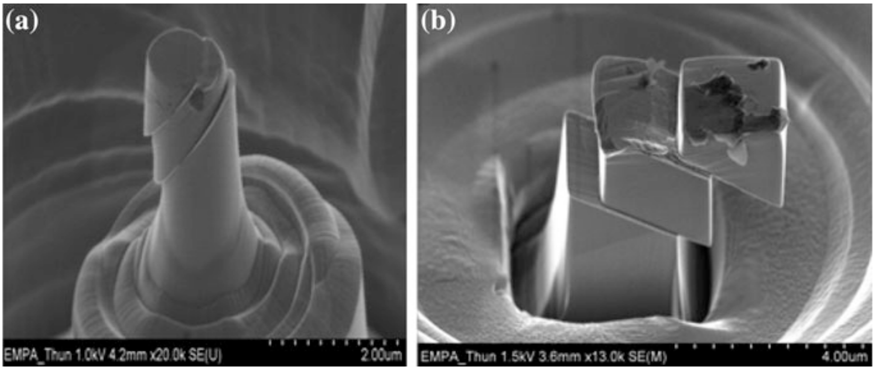

Fig. 4 SEM images of Ti-15-333 single-crystal micro-pillars with circular (**a**) and square (**b**) cross sections after compression

slip bands along the gauge length of the crystal were observed when its size diminished. In contrast to a smooth stress-strain curve obtained during compression of a bulk material, the stress-strain curves of small-size pillars contained several discrete strain bursts, with strain jumping discontinuously to an increased value while the stress value remained constant or decreased. Figure 5 demonstrates typical strain bursts, more frequent in small-size pillars, observed on a stress-strain curve of f.c.c. nano pillars. Greer and Nix [17] performed similar tests on (001)-oriented Au crystals with dimensions of less than 1 μm. The study showed a trend of an increase in the strength of the pillar with a decrease in its size. It was also revealed that the flow-stress value of ~800 MPa was observed in compression of 200 nm Au specimens, which was extraordinarily high compared to its bulk counterpart with a corresponding value around 25 MPa at 10 % strain.

Fig. 5 Typical stress-strain curves in compression of Au pillars with various diameters. Reprinted with permission from [34]

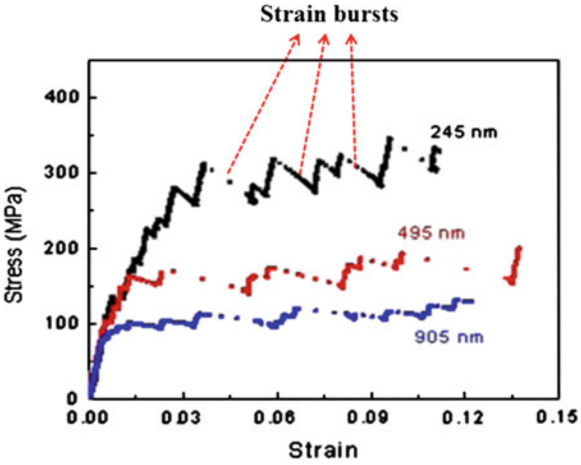

Recently, Kiener et al. [18] reported a new method to measure tensile behaviour of single-crystals at the micro- and nano-scales using the samples fabricated with FIB. The mechanical test was performed inside a scanning electron microscope (SEM) and a transmission electron microscope (TEM). In this experiment, f.c.c. Single-crystal Cu samples with diameters ranging from 500 nm to 8 μm with an aspect ratio ranging from 1 to 13.5 were tested. This study revealed the presence of a size effect, which strongly depended on the sample's aspect ratio; however, the reported size effect was less pronounced than its compression counterpart. It was reported that size-dependent hardening was linked to dislocation pile-ups due to their constrained glide in the sample. Jennings and Greer [19] performed an in situ tensile-deformation test with (111)-oriented single-crystal Cu nano-pillars with diameters ranging from 75 to 165 nm fabricated with e-beam lithography and electroplating. A power-law relationship between strength and diameter of nano-pillar was reported similar to that for fabricated with FIB machining. In that study, inhomogeneous deformation was explained by annihilation of dislocations at free surfaces of the pillar.

Most studies of size effects deal with f.c.c. Materials with only recent studies investigating b.c.c. Crystalline materials. In the following section we discuss studies in f.c.c. and b.c.c. crystals. The relevant reviews for more complex microstructures such as non-cubic single-crystals, shape memory alloys, nano-crystalline metals, nano-laminate composites and metallic glasses are available elsewhere [1] and the references therein).

2.2.1 Face-Centred Cubic Metals

Several mechanisms have been proposed for deformation of nano- and micron-size f.c.c. pillar structures. Among the suggested theories "hardening by dislocation starvation" is the mostly accepted one to explain the size effects in f.c.c. nano-pillars. The basic premise of the theory is as follows: Owing to smaller dimensions of the nano-size pillars, dislocations present at the onset of plastic deformation leave the specimen before they multiply. Having reached this "dislocation starvation" state, new dislocations are necessary to nucleate both at the sample surface and in the bulk of the crystal in the course of deformation since the movement of dislocations is required for compatible plastic deformation. As the nucleation of these new dislocations requires high stresses approaching near-theoretical strength, the strength of nano-size pillars is observed to increase with a decreasing sample size. This theory appears to be in good agreement with in situ TEM performed by [20]. Figure 6a demonstrates the FIB micro-fabricated (111) Ni pillar with 160 nm of diameter in this study. It is apparent that there is a high initial dislocation density in the pillar. However, the pre-existing dislocations progressively leave the pillar during the initial compression stage, and a completely dislocation-free pillar is finally obtained (Fig. 6b). Computational atomistic simulations performed by different research groups also justify this theory [21].

A prominent deformation mechanism for micron-sized pillars (larger than 500 nm) is described in terms of a single-arm source theory proposed and

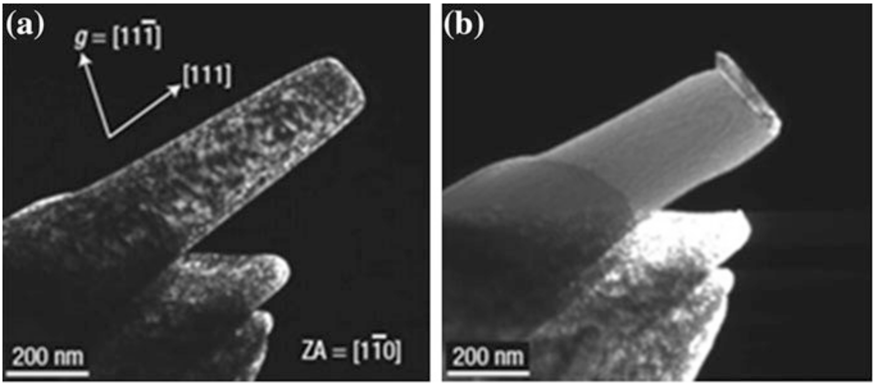

Fig. 6 Dark-field TEM image of Ni pillar before tests (**a**) and after first compression (**b**). Reprinted with permission from [20]

developed by [22]. In this theory, creation of dislocations occurred as a result of operation of partial Frank-Read sources or truncated sources also known as *single-arm sources*. This approach suggested that a random distribution of dislocation sources either existed initially in pillars or generated by interaction of initially present dislocations, and the average source strength τ_s was related with the average source length λ by the following equation:

$$\tau_s = k_s \mu \frac{\ln(\lambda/b)}{(\lambda/b)}, \tag{1}$$

where k_s is a source-hardening rate, μ is the shear modulus and b is the Burgers vector. According to this equation, with a decrease in the diameter of pillar, the source length became smaller, hence overall strength increased. Ng and Nyan [23] studied the size effect of Al micro-pillars with diameters ranging from 1.2 to 6 μm either coated or centre-filled with a tungsten-based compound. A higher strain-hardening rate and a much smoother stress-strain curve suggested suppression of dislocation avalanches and a lack of nucleation-controlled plasticity. The TEM analysis revealed higher dislocation densities in the post-deformed specimens confirming the trapping of dislocations inside the micro-pillars rather than annihilating at the free surface in contrast to nano-sized pillars [1].

Maass and co-workers studied the role of strain gradients on plastic deformation of micron-size pillars using a synchrotron micro-diffraction technique [24]. These studies demonstrated that geometrically necessary dislocations were generated during the deformation process leading to strain gradients. The assumed dislocation starvation theory, therefore, was not applicable to micron-size pillars since it was impossible to squeeze all the dislocations to the surface of the pillar. Likewise, [25] argued that although deformation in a pillar-compression test was macroscopically homogenous, it was heterogeneous microscopically, i.e. GNDs vanished macroscopically but were presented locally. Akarapu et al. [26] numerically demonstrated that deformation was heterogeneous from its onset and was confined to the discrete slip bands. On the other hand, SEM images of micron-sized pillars taken after their compression in [27] suggested that deformation evolved in an inhomogenous manner, though it was applied homogeneously since the end regions of the pillars appeared non-deformed while the sample's centre was sheared by multiple slip zones.

The FIB technique is currently the most prevalent method for producing small-size pillars to investigate the influence of sample's dimensions on mechanical properties. In this method Ga^+ ions are bombarded and implanted to fabricate the pillars. This process inevitably introduces surface dislocation loops, and precipitates also instigate surface amorphization. The presence of FIB-induced defects led several researchers to infer that the fabrication process may play a significant role in the observed size effects. On the one hand, [28] proposed that increasing strength of pillars with a decrease in their size would be a consequence of the increased volume fraction of a FIB-damaged layer with a decreasing pillar diameter. Kiener et al. [29] investigated Ga^+ ion-induced damage with TEM and Monte Carlo simulations, where a non-negligible influence of the ion damage in the order of 100 MPa (assuming Taylor hardening) was reported for submicron-sized samples. In order to understand importance of the fabrication technique on the size effects, [30] developed a FIB-less method to produce nano-pillars. In this method, arrays of vertically oriented gold and copper nano-pillars were created based on patterning polymethylmethacrylate with electron beam lithography and subsequent electroplating into the prescribed template. In this technique, pillars were produced intentionally with non-zero dislocation densities to compare and contrast them with those produced with the FIB method; otherwise, pillars without dislocations would render theoretical strengths regardless of size. That study demonstrated that nano-size pillars created without Ga^+ bombardment and containing initial dislocations with density comparable with that for pillars created with Ga^+ bombardment exhibited an identical size effect with the FIB-produced pillars. The study evidently suggested that the observed size effect in small-size pillars was a function of microstructure rather than the fabrication technique.

2.2.2 Body-Centred Cubic Structures

Experimental and computational studies of compression of single-crystal Mo nano-pillars showed that the deformation mechanism in b.c.c. nano-pillars was fundamentally different from that of f.c.c. nano-pillars. Brinckmann et al. [31] reported a comparison of uniaxial compression results for Mo and Au nano-pillars. That study revealed that size-dependent strengths, stochastic discrete bursts in stress-strain curves, fractions of attained theoretical strength as well as extents of strengthening were different. These discrepancies were attributed to profound differences in the plasticity mechanisms of f.c.c. and b.c.c. metals as also confirmed by atomistic simulations [32]. In b.c.c. metals, glide of screw components of a dislocation loop is not restricted to any particular single plane and can also cross-slip on any other favourable crystallographic plane during shearing of the crystal, whereas the edge components glide on a specific plane. In b.c.c. metals mobility of screw dislocations is estimated at around one fortieth of the motion of edge dislocations. The dislocations in b.c.c. nano-pillars, therefore, are likely to have a higher residence time inside a pillar rather than leaving it, significantly increasing the probability of interaction of individual dislocations, their multiplication and formation of junctions, which, in turn, lead to new dislocation sources. As the junction size is proportional to the size of the pillar, the junctions are shorter for small-size b.c.c. pillars. It is therefore harder to break through the gliding mobile dislocations leading to an increase in strength of the pillar. On the other hand, as the increase in temperature greatly increases mobility of screw dislocations, the number of formed junctions is reduced requiring nucleation of new dislocations. The size effect, therefore, in b.c.c. metals would be expected to become closer to that in f.c.c. metals at higher temperatures. However, the b.c.c. pillars never become dislocation starved as in the f.c.c. nano-pillars; instead, a complex networks of short dislocation segments are formed [32]. This is also consistent with molecular-dynamics (MD) and dislocations-dynamics (DD) simulations of [33].

Kim and Greer [34] reported size-dependent strengths of (001) oriented Mo nano-pillars in compression and tension. The observed higher flow stresses were explained by an increase in yield strength rather than strain-hardening. It was also reported that the amount of strain-hardening under tension was much lower compared to that under compression demonstrating a tension-compression asymmetry. This observed asymmetry was attributed to the differences in the Peierls stress, i.e. lattice resistance to dislocation motion, in twinning and anti-twinning direction. It is worth mentioning that friction stress or intrinsic lattice resistance, accounting for the flow-stress indirectly related to dislocation activities, is negligibly small in f.c.c. metals but it is significant in b.c.c. metals [35]. In [34], TEM images of Mo nano-pillars with diameter of 100 nm before and after the deformation were analysed. The results indicated formation of an entangled dislocation substructure and justified differences in the deformation behaviour of f.c.c. and b.c.c. metals. The effect of crystal orientation on the tension-compression asymmetry of Mo nano-pillars was also studied by Kim and Greer [34]. It was shown that compressive flow stresses were higher in (001) orientation and smaller in (011) orientation compared to tensile flow-stresses. This study revealed that tension-compression asymmetry was a function of size of the pillar for sizes less than 800 nm, whereas strength for larger pillars approached size-independent bulk values.

The influence of applied strain-rate on the size effect in b.c.c. single crystals was investigated by [36]. Under a constant displacement rate, the imposed strain-rate varied by around one order of magnitude between the largest and smallest Mo pillar ranging from 200 to 800 nm. In that study, differences in the yield stress of around 50 % for the smallest and around 20 % for the largest pillars were reported. The study revealed that the strain rate had an influence on the observed size effects in nano-size pillars. Kim et al. [36] also studied different b.c.c. metals in addition to Mo. (011)-oriented single-crystal nano-size pillars of Ta, W, Nb and Mo were subjected to uniaxial compression and tension. A power-law for size-dependent flow-stress of pillars was found together with size-dependency of observed tension-compression asymmetry. However, the authors did not observe any consistent correlation between the strain-hardening exponent and the material's type or size. That implied that strain-hardening was more likely to be a function of the initial microstructure rather than the pillar size, whereas the yield and flow-stress fundamentally depended on the size of nano-pillar [1].

The deformation mechanism in micron-sized b.c.c. pillars is similar to that in nano-sized pillars, unlike the different mechanism in f.c.c. nano- and micro-pillars. Therefore, the mechanisms explained above for b.c.c. single-crystal nano-pillars can be generalized to micron-size pillars.

In summary, it is justified that in b.c.c. single-crystals a single dislocation can generate multiple new dislocations. Dislocation segments will further interact and form Frank-Read sources leading to an increase in dislocation density and requiring significant levels of flow stress due to inherent characteristic of screw dislocation gliding at different slip planes. The hardening mechanism of b.c.c. single crystals via entanglement of dislocation segments is similar to the forest-hardening model in bulk crystal plasticity [31].

3 Modelling Approaches

3.1 Models Developed for ISE

A classical continuum plasticity theory cannot explain the size dependence of mechanical response as no length scale enters the constitutive description. However, strain-gradient plasticity schemes have been successful in characterizing the size effect in components subjected to inhomogeneous loading states. This success is related to the inclusion of a microstructural length-scale parameter in the governing equations for deformation. Gradient approaches typically retain terms in the constitutive equations of higher- or lower-order gradients with coefficients that characterize length-scale measures of the deformation microstructure associated with the non-local continuum [13]. Therefore, classical continuum plasticity theories including strain gradients represent a collective behaviour of dislocations and their interactions at the micro-scale. However, there exists a lower limit on the length scale, below which the continuum plasticity theories are not applicable. In other words, the continuum plasticity theories are only applicable at scales larger than spacing between individual dislocations. This is similar to the relation between the elasticity and lattice theories; where the elasticity theory is applicable to a few lattice spacing (atomic spacing), below which the lattice theory governs. Gao et al. [37] identified that the lower limit for applicability of a strain-gradient plasticity theory was around 100 nm. In other words, only when the characteristic length of deformation is larger than 100 nm, strain-gradient plasticity theories can be used.

In gradient-plasticity theories, a constitutive length-scale parameter l is used to scale the effects of strain gradients and is thought of as an internal material length, related to storage of GNDs. The strain-gradient effects become important when the characteristic length associated with deformation becomes comparable to the intrinsic material length-scale parameter l. In other words, if the representative length of non-uniform deformation is much larger than l, strain-gradient effects are negligible, and the strain-gradient theories degenerate to classical plasticity theories [37]. The study of [38] indicated that indentation experiments might be the most effective way of measuring the length-scale parameter as a typical tension test cannot be effectively used to determine the material properties of gradient theories due to uniform deformation, whereas in indentation significant work-hardening evolves due to severe and non-uniform plastic deformation and damage concentrates in the localized region directly below the indenter.

Nix and Gao [39] modelled the indentation size effect for crystalline materials. The following characteristic form explaining the depth dependence of hardness was obtained from this model:

$$\frac{H}{H_0} = \sqrt{1 + \frac{h^*}{h}}, \tag{2}$$

where H is hardness for a given indentation depth h, H_0 is hardness in the limit of infinite depth and h^* is the characteristic length depending on the indenter shape, shear modulus and H_0. They estimated the material length scale parameter l from the micro-indentation experiments of [3] to be 12 and 5.84 μm for annealed single-crystal copper and for cold-worked polycrystalline copper, respectively. Yuan and Chen [40] proposed that the unique intrinsic material length parameter l could be computationally determined by fitting the [39] model from micro-indentation experiments, and they identified $l = 6$ μm for poly-crystal copper and $l = 20$ μm for single-crystal copper using the finite element (FE) method. Begley and Hutchinson [38] estimated that the material length-scale associated with the stretch gradients ranged from $1/4$ to 1 μm, while the material lengths associated with rotation gradients were on the order of 4 μm by fitting micro-indentation hardness data.

Strain-gradient plasticity theories can be attributed to two frameworks: higher-order and lower-order continuum theories. The higher-order theories belong to the Mindlin's framework. In this framework, higher-order stresses are involved as a work conjugate of the strain gradient described with the following equation:

$$\delta w = \sigma'_{ij}\delta\varepsilon_{ij} + \tau'_{ijk}\delta\eta_{ijk}, \tag{3}$$

where δw is the work increment per unit volume of an incompressible solid due to a variation of displacement, σ'_{ij} is the deviatoric part of the Cauchy stress, $\delta\varepsilon_{ij}$ is the variation of strain, τ'_{ijk} is the deviatoric part of higher-order Cauchy stress and $\delta\eta_{ijk}$ is the variation of strain gradient. Here, the order of equilibrium equations is higher than that of the conventional continuum theories requiring additional boundary conditions. On the other hand, in the lower-order strain gradient plasticity theory, the higher-order stresses are not incorporated in the constitutive equations; hence, no additional boundary conditions are required. In this type of non-local plasticity theory, the strain gradient effects come into play through the incremental plastic modulus.

Huang et al. [41] compared the solutions obtained using higher-order and lower-order strain gradient theories for a one-dimensional hypothetical problem, where a bar was fixed at one end and subjected to a constant body force and a uniform stress at the free end along the main axis of the bar (Fig. 7). The distribution of strain gradient in the bar using lower-order and higher-order strain gradient theories is shown in Fig. 7. It is clearly visible that both theories agree very well except the area near the ends of the bar. As the higher-order stresses become significant at the boundaries, different strain-gradient distributions are obtained using different frameworks of the theories.

Various numerical simulation techniques are also used to study the underlying mechanics in indentation experiments in the small scale. For instance, deformation-induced lattice rotations below an indent have attracted attention as there exists a close connection between crystallographic shear, the main mechanism governing deformation, and the resulting lattice spin.

Some studies have attempted to characterize the observed phenomena, with the use of different experiments such as non-destructive 3D synchrotron diffraction, 3D electron backscattered diffraction (EBSD) and transmission electron microscopy (TEM). A limited number of numerical studies attempted to analyse physical deformation mechanisms leading to lattice rotations. For instance, Wang et al. [42] demonstrated lattice rotations for a single crystal of Cu with different orientations using a 3D crystal-plasticity (CP) FE method. Zaafarani et al. [43] proposed a physically based CP model based on dislocation-rate formulations to explain likely reasons for deformation-induced patterns consisting of multiple narrow zones with alternating crystalline reorientation. However, the model consistently overestimated the extent of lattice rotations observed in experiments. Recently, Demiral et al. [44, 45] developed a

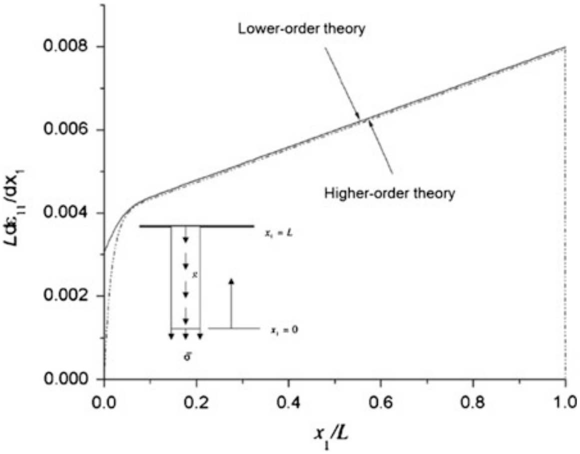

Fig. 7 Distribution of strain gradients in bar predicted by lower-order (conventional theory of mechanism-based strain gradient) and higher-order (mechanism-based strain gradient theory) theories. Reprinted with permission from [41]

3D elastic–viscoplastic enhanced modelling of strain-gradient crystal-plasticity (EMSGCP) (its details are given in Sect. 3.2) FE model for nano-indentation of Ti alloy to demonstrate the influence of strain gradients on the resulting deformation patterns. The study demonstrated that the introduction of strain gradients changed the activity of the slip systems as well as a relative contribution to the overall plastic slip. The EMSGCP theory predicted that plasticity occurred due to activity of multiple slip systems when compared to that of the CP theory.

3.2 Modelling Size Effect in Pillar Compression Experiment

Numerical modelling and simulations of pillar-compression experiments have been performed by several research teams. Among these, Zhang et al. [46] presented a parametric study of design of accurate pillar-compression experiments using 2D and 3D isotropic plasticity FE modelling. In that study, geometric factors such as the curvature at the area of pillar's connection to the substrate, the aspect ratio and taper of the pillar, misalignment between the indenter tip and the pillar, different material characteristics and plastic bucking phenomena were analysed extensively. Schuster et al. [47] followed that work and studied the effect of specimen taper on compressive strength of metallic glass. On the other hand, Chen et al. [48] focused on local stress concentration in metallic-glass pillars using an isotropic plasticity model. Raabe et al. [49] used a CP FE model to investigate the influence of stability of the initial crystal orientation, aspect ratio and contact conditions between the indenter tip and the pillar on anisotropy and changes in crystallographic orientation during the deformation. That study revealed that the evolution of orientation changes was in part due to a shape change owing to buckling rather than crystallographic orientation solely. Shade et al. [50] performed a combined experimental and CP FE study to examine lateral constraint effects on compression of single crystals. It was reported there that the degree of lateral constraint in a compression test system could influence the behaviour of the material tested.

Recently, Demiral et al. [51] proposed the EMSGCP theory, which accounts for geometric effects in addition to intrinsic properties in capturing the size effect. In the following section this theory is briefly explained.

In the EMSGCP theory, the initial strength of a slip systems ($g_T^\alpha|_{t=0}$), i.e. the *critical resolved shear stress* (CRSS), was governed by pre-existing GNDs in the workpiece together with SSDs, i.e. $g_T^\alpha|_{t=0} = g_S^\alpha|_{t=0} + g_G^\alpha|_{t=0}$. In this theory, $g_S^\alpha|_{t=0}$ and $g_G^\alpha|_{t=0}$ were linked with initial densities of SSDs ($\rho_S|_{t=0}$) and GNDs ($\rho_G|_{t=0}$) as $g_S^\alpha|_{t=0} = K\sqrt{\rho_s|_{t=0}}$, $g_G^\alpha|_{t=0} = K\sqrt{\rho|_{t=0}\left(\overline{S/V}\right)^2}$ via the constant K, similar to the Taylor relation. The GND density term was expressed as a function of the normalized surface-to-volume ratio $\overline{S/V}$ (hence, dimensionless) for the component under study. In the study, the surface-to-volume ratio of the workpiece materials was normalized with an idealised workpiece geometry corresponding to $S/V = 1\ \mu\mathrm{m}^{-1}$.

The evolution of slip resistance during loading was the result of hardening due to the SSDs (Δg_S^α) and GNDs (Δg_G^α) on the slip system, which followed:

$$g_T^\alpha = g_S^\alpha|_{t=0} + g_G^\alpha|_{t=0} + \sqrt{\left(\Delta g_S^\alpha\right)^2 + \left(\Delta g_G^\alpha\right)^2}, \tag{4a}$$

where

$${}_S^\alpha = \sum_{\beta=1}^{N} h_{\alpha\beta}\Delta\gamma^\beta, \Delta g_G^\alpha = \alpha_{\mathrm{T}}\mu\sqrt{bn_G^\alpha}. \tag{4b}$$

Here, $h_{\alpha\beta}$, α_{T}, μ, b and n_G^α correspond to the slip-hardening modulus, the Taylor coefficient, the shear modulus, the Burgers vector and the effective density of geometrically necessary dislocations, respectively.

The hardening model was used to represent $h_{\alpha\beta}$, as follows:

$$\begin{aligned} h_{\alpha\alpha} &= h_0 \mathrm{sech}^2\left|\frac{h_0\tilde{\gamma}}{g_T^\alpha|_{\mathrm{sat}} - g_T^\alpha|_{t=0}}\right|, h_{\alpha\beta} = q h_{\alpha\alpha}(\alpha \neq \beta), \\ \tilde{\gamma} &= \sum_\alpha \int_0^t |\dot{\gamma}^\alpha| dt, \end{aligned} \tag{5}$$

where h_0 is the initial hardening parameter, $g_T^\alpha|_{\mathrm{sat}}$ is the saturation stress of the slip system α, q is the latent hardening ratio, and $\tilde{\gamma}$ is the Taylor cumulative shear strain on all slip systems. The effective GND density n_G^α was given by

$$n_G^\alpha = \left|\boldsymbol{m}^\alpha \times \sum_\beta s^{\alpha\beta}\nabla\gamma^\beta \times \boldsymbol{m}^\beta\right|, \tag{6}$$

where $\boldsymbol{s}^\alpha$ is the slip direction, $\boldsymbol{m}^\alpha$ is the slip-plane normal, $s^{\alpha\beta} = \boldsymbol{s}^\alpha \cdot \boldsymbol{s}^\beta$ and $\nabla\gamma^\beta$ is the gradient of shear strain in each slip system. To calculate $\nabla\gamma^\beta$ the scheme proposed in [44] was followed. The model was implemented in the implicit FE code ABAQUS/Explicit using the user-defined material subroutine (VUMAT).

This model is consistent with the model proposed by Hurtado and Ortiz [52], where the self-energy of dislocations and the energy of dislocation steps at the boundary of the solid in the context of surface effects were accounted for in the CP theory. Horstemeyer et al. [53] performed atomistic simulations of plasticity via the embedded atom method (EAM) for single-crystal f.c.c. metals. The results of molecular-dynamics simulations indicated that plastic deformation was intrinsically inhomogeneous and the yield strength scaled inversely with the volume-to-surface area ratio, even in the absence of strain gradients. This model also complies with the EMSGCP theory. Higher-order strain-gradient models for single-crystal micro-pillars were also developed by Zhang and Aifantis [54] to describe the deformation behaviour of single-crystal micro-pillars.

Experimental data in micro-pillar deformation typically show several discrete slip bursts (Fig. 5), where the stress remains almost constant while the strain jumps discontinuously to increasing values. Zhang and Shang [55] formulated a continuum model accounting for strain bursts observed in the experiments by considering the intermittent space and time displaying in displacements of the pillar and constructing the microscopic boundary conditions in the hybrid loading mode. Zhang and Aifantis [54] used strain gradients to capture strain bursts that were experimentally observed in single-crystal Ni micro-pillars under compression. In that study, plastic deformation was realised through slip zones in a gauge region, where they were divided into elastic and plastic zones, and a strain burst occurred when two adjacent zones deformed plastically. The predicted results were in good agreement with the experimental stress-strain curves. On the other hand, Ng and Nyan [56] developed a Monte Carlo model, which could predict statistical aspects of the deformation process, including the stochastic nature of the stress-strain relation and the power-law distribution of the burst size.

FE implementations of phenomenological models such as dislocation starvation and dislocation nucleation have been employed to investigate the effect of physics on micro-pillar deformation. For instance, Greer and Nix [17] proposed a phenomenological model for sub-micron sized pillars, where initially present mobile dislocations annihilated in the vicinity of a free surface. It was given as

$$s_{starv} = 0.5\,\mu b\sqrt{\rho} + 1.4\frac{\mu b}{4\pi a(1-\vartheta)}\ln\left(\frac{\alpha a}{b}\right), \tag{7}$$

where ϑ and α are the Poisson's ratio and constant of order unity, and where the instantaneous pillar diameter $a = a_0(1-\varepsilon)^{0.5}$ and density $\rho = \rho_0 + \frac{(\delta - \frac{1}{a})}{b}\frac{\varepsilon_p}{M}$ with a_0 and ρ_0 being the pillar diameter and the initial dislocation density, ε and ε_p are the overall engineering strain and plastic strain, M is the Schmid factor and δ is the breeding coefficient, representing the inverse of the distance a dislocation travels before replicating itself. This model captured one single strain burst followed by elastic loading. Following that work, Jérusalem et al. [57] characterized starvation of pre-existing dislocations and nucleation of new ones independently by two references with $\mathrm{S}_{0,\mathrm{starv}}$ being initial starvation CRSS and $\mathrm{S}_{0,\mathrm{nucl}}$ a reference nucleation CRSSs for each slip system i as follows:

$$s_0^i = \mathrm{Min}\left(\left(1 - \frac{\varepsilon_p}{\varepsilon_p^{\mathrm{starv}}}\right)s_{0,\mathrm{starv}} + \frac{\epsilon_p}{\epsilon_p^{\mathrm{starv}}}s_{0,\mathrm{nucl}}, s_{0,\mathrm{nucl}}\right), \tag{8}$$

where

$$s_{\mathrm{starv}} = 0.5\,\mu b\sqrt{\rho_0} + 1.4\frac{\mu b}{4\pi a_0(1-\vartheta)}\ln\left(\frac{\alpha a_0}{b}\right).$$

In this equation, $\epsilon_p^{\mathrm{starv}}$ is a model parameter corresponding to plastic strain, for which nucleation dislocation was more favourable than dislocation starvation and at which the nucleation CRSS $s_{0,\mathrm{nucl}}$ was reached. Here, the CRSS equalled to $s_{0,\mathrm{starv}}$ at initial yielding and then linearly increased as a function of ϵ_p as the mobile dislocations moved towards the free surface, while nucleation processes became increasingly more prevalent. Once all mobile dislocations were annihilated, plasticity was fully nucleation-driven.

4 Concluding Remarks

In this chapter we have reviewed some of the critical experimental studies in the past decades that have helped to quantify and qualify some of the essential features of deformation in the small scale. The effects of extrinsic and intrinsic parameters on the overall deformation behaviour of micro- and meso-size components have paved the way for advanced numerical modelling frameworks, which attempt to capture the deformation behaviour across length scales for given boundary constraints. With an ever-increasing capacity in computational power, numerical simulations of physically reasonable component sizes under complex loading states can now be attempted. However, much work is yet to be done, especially with the regard to developing models, which are computationally efficient and physically sound.

References

1. Greer, J.R., De Hosson, J.T.M.: Plasticity in small-sized metallic systems: intrinsic versus extrinsic size effect. Prog. Mater Sci. **56**(6), 654–724 (2011)
2. Stelmashenko, N., Walls, M., Brown, L., Milman, Y.V.: Microindentations on W and Mo oriented single-crystals: an STM study. Acta Metall. Mater. **41**(10), 2855–2865 (1993)
3. McElhaney, K., Vlassak, J., Nix, W.: Determination of indenter tip geometry and indentation contact area for depth-sensing indentation experiments. J. Mater. Res. **13**(05), 1300–1306 (1998)
4. Tabor, D.: The Hardness of Metals. Oxford University Press, Oxford, (1951)
5. Xue, Z., Huang, Y., Hwang, K., Li, M.: The influence of indenter tip radius on the micro-indentation hardness. J. Eng. Mater. Technol. **124**, 371 (2002)
6. Fleck, N., Hutchinson, J.: Strain gradient plasticity. Adv. Appl. Mech. **33**, 295–361 (1997)
7. Acharya, A.: A model of crystal plasticity based on the theory of continuously distributed dislocations. J. Mech. Phys. Solids **49**(4), 761–784 (2001)
8. Fressengeas, C., Taupin, V., Capolungo, L.: An elasto-plastic theory of dislocation and disclination fields. Int. J. Solids Struct. **48**, 3499–3509 (2011)
9. Roy, A., Acharya, A.: Finite element approximation of field dislocation mechanics. J. Mech. Phys. Solids **53**(1), 143–170 (2005)
10. Qu, S., Huang, Y., Pharr, G., Hwang, K.: The indentation size effect in the spherical indentation of iridium: a study via the conventional theory of mechanism-based strain gradient plasticity. Int. J. Plast. **22**(7), 1265–1286 (2006)
11. Swadener, J., George, E., Pharr, G.: The correlation of the indentation size effect measured with indenters of various shapes. J. Mech. Phys. Solids **50**(4), 681–694 (2002)

12. Demir, E., Raabe, D., Zaafarani, N., Zaefferer, S.: Investigation of the indentation size effect through the measurement of the geometrically necessary dislocations beneath small indents of different depths using EBSD tomography. Acta Mater. **57**(2), 559–569 (2009)
13. Abu Al-Rub, R.K., Voyiadjis, G.Z.: Analytical and experimental determination of the material intrinsic length scale of strain gradient plasticity theory from micro- and nano-indentation experiments. Int. J. Plast. **20**(6), 1139–1182 (2004)
14. Uchic, M.D., Dimiduk, D.M., Florando, J.N., Nix, W.D.: Sample dimensions influence strength and crystal-plasticity. Science **305**(5686), 986–989 (2004)
15. Uchic, M.D., Dimiduk, D.M.: A methodology to investigate size scale effects in crystalline plasticity using uniaxial compression testing. Mater. Sci. Eng. A **400**, 268–278 (2005)
16. Greer, J.R., Oliver, W.C., Nix, W.D.: Size dependence of mechanical properties of gold at the micron scale in the absence of strain gradients. Acta Mater. **53**(6), 1821–1830 (2005)
17. Greer, J.R., Nix, W.D.: Nanoscale gold pillars strengthened through dislocation starvation. Phys. Rev. B. **73**(24), 245–410 (2006)
18. Kiener, D., Grosinger, W., Dehm, G., Pippan, R.: A further step towards an understanding of size-dependent crystal plasticity: in situ tension experiments of miniaturized single-crystal copper samples. Acta Mater. **56**(3), 580–592 (2008)
19. Jennings, A.T., Greer, J.R.: Tensile deformation of FIB-less single-crystalline copper pillars. Philos. Mag. 91 (2010)
20. Shan, Z., Mishra, R., Asif, S.A.S., Warren, O., Minor, A.: Mechanical annealing and source-limited deformation in submicrometre-diameter Ni crystals. Nat. Mater. **7**(2), 115–119 (2008)
21. Rabkin, E., Nam, H.S., Srolovitz, D.: Atomistic simulation of the deformation of gold nanopillars. Acta Mater. **55**(6), 2085–2099 (2007)
22. Rao, S.I., Dimiduk, D., Parthasarathy, T.A., Uchic, M., Tang, M., Woodward, C.: A thermal mechanisms of size-dependent crystal flow gleaned from three-dimensional discrete-dislocation simulations. Acta Mater. **56**(13), 3245–3259 (2008)
23. Ng, K., Ngan, A.: Deformation of micron-sized aluminium bi-crystal pillars. Phil. Mag. **89** (33), 3013–3026 (2009)
24. Maass, R., Van Petegem, S., Borca, C., Van Swygenhoven, H.: In situ Laue diffraction of metallic micro-pillars. Mater. Sci. Eng. A **524**(1), 40–45 (2009)
25. Guruprasad, P., Benzerga, A.: Size effects under homogeneous deformation of single-crystals: a discrete-dislocation analysis. J. Mech. Phys. Solids **56**(1), 132–156 (2008)
26. Akarapu, S., Zbib, H.M., Bahr, D.F.: Analysis of heterogeneous deformation and dislocation dynamics in single-crystal micro-pillars under compression. Int. J. Plast. **26**(2), 239–257 (2010)
27. Dimiduk, D., Uchic, M., Parthasarathy, T.: Size-affected single-slip behavior of pure nickel microcrystals. Acta Mater. **53**(15), 4065–4077 (2005)
28. Bei, H., Shim, S., Miller, M., Pharr, G., George, E.: Effects of focused ion beam milling on the nanomechanical behavior of a molybdenum-alloy single-crystal. Appl. Phys. Lett. **91**(11), 111915 (2007)
29. Kiener, D., Motz, C., Rester, M., Jenko, M., Dehm, G.: FIB damage of Cu and possible consequences for miniaturized mechanical tests. Mater. Sci. Eng. A **459**(1), 262–272 (2007)
30. Jennings, A.T., Burek, M.J., Greer, J.R.: Microstructure versus size: mechanical properties of electroplated single-crystalline Cu nanopillars. Phys. Rev. Lett. **104**(13), 135503 (2010)
31. Brinckmann, S., Kim, J.Y., Greer, J.R.: Fundamental differences in mechanical behavior between two types of crystals at the nanoscale. Phys. Rev. Lett. **100**(15), 155502 (2008)
32. Greer, J.R., Weinberger, C.R., Cai, W.: Comparing the strength of f.c.c. and b.c.c. sub-micrometer pillars: compression experiments and dislocation dynamics simulations. Mater. Sci. Eng. A **493**(1–2), 21–25 (2008)

33. Weinberger, C.R., Cai, W.: Surface-controlled dislocation multiplication in metal micropillars. Proc. Natl. Acad. Sci. **105**(38), 14304 (2008)
34. Kim, J.Y., Greer, J.R.: Tensile and compressive behavior of gold and molybdenum single-crystals at the nano scale. Acta Mater. **57**(17), 5245–5253 (2009)
35. Nix, W.D.: Mechanical properties of thin films. Metall. Mater. Trans. A **20**(11), 2217–2245 (1989)
36. Kim, J., Jang, D., Greer, J.R.: Tensile and compressive behavior of tungsten, molybdenum, tantalum and niobium at the nanoscale. Acta Mater. **58**(7), 2355–2363 (2010)
37. Gao, H., Huang, Y., Nix, W., Hutchinson, J.: Mechanism-based strain gradient plasticity–I. Theory. J. Mech. Phys. Solids **47**(6), 1239–1263 (1999)
38. Begley, M.R., Hutchinson, J.W.: The mechanics of size-dependent indentation. J. Mech. Phys. Solids **46**(10), 2049–2068 (1998)
39. Nix, W.D., Gao, H.: Indentation size effects in crystalline materials: a law for strain gradient plasticity. J. Mech. Phys. Solids **46**(3), 411–425 (1998)
40. Yuan, H., Chen, J.: Identification of the intrinsic material length in gradient plasticity theory from micro-indentation tests. Int. J. Solids Struct. **38**(46), 8171–8187 (2001)
41. Huang, Y., Qu, S., Hwang, K., Li, M., Gao, H.: A conventional theory of mechanism-based strain gradient plasticity. Int. J. Plast. **20**(4), 753–782 (2004)
42. Wang, Y., Raabe, D., Klüber, C., Roters, F.: Orientation dependence of nanoindentation pile-up patterns and of nanoindentation microtextures in copper single-crystals. Acta Mater. **52**(8), 2229–2238 (2004)
43. Zaafarani, N., Raabe, D., Roters, F., Zaefferer, S.: On the origin of deformation-induced rotation patterns below nanoindents. Acta Mater. **56**(1), 31–42 (2008)
44. Demiral, M., Roy, A., Silberschmidt, V.V.: Indentation studies in bcc crystals with enhanced model of strain-gradient crystal plasticity. Comput. Mater. Sci. **79**, 896–902 (2013)
45. Demiral, M., Roy, A., El Sayed, T., Silberschmidt, V.V.: Influence of strain gradients on lattice rotation in nano-indentation experiments: a numerical study. Mater. Sci. Eng. A **608**, 73–81 (2014)
46. Zhang, H., Schuster, B.E., Wei, Q., Ramesh, K.T.: The design of accurate micro-compression experiments. Scripta Mater. **54**(2), 181–186 (2006)
47. Schuster, B.E., Wei, Q., Hufnagel, T.C., Ramesh, K.T.: Size-independent strength and deformation mode in compression of a Pd-based metallic glass. Acta Mater. **56**(18), 5091–5100 (2008)
48. Chen, C.Q., Pei, Y.T., De Hosson, J.T.M.: Effects of size on the mechanical response of metallic glasses investigated through in situ TEM bending and compression experiments. Acta Mater. **58**(1), 189–200 (2010)
49. Raabe, D., Ma, D., Roters, F.: Effects of initial orientation, sample geometry and friction on anisotropy and crystallographic orientation changes in single-crystal microcompression deformation: a crystal-plasticity finite-element study. Acta Mater. **55**(13), 4567–4583 (2007)
50. Shade, P.A., Wheeler, R., Choi, Y.S., Uchic, M.D., Dimiduk, D.M., Fraser, H.L.: A combined experimental and simulation study to examine lateral constraint effects on microcompression of single-slip oriented single-crystals. Acta Mater. **57**(15), 4580–4587 (2009)
51. Demiral, M., 2012, Enhanced gradient crystal-plasticity study of size effects in bcc metal, Ph. D. thesis, Loughborough University, UK
52. Hurtado, D.E., Ortiz, M.: Surface effects and the size-dependent hardening and strengthening of nickel micro-pillars. J. Mech. Phys. Solids **60**(8), 1432–1446 (2012)
53. Horstemeyer, M., Baskes, M., Plimpton, S.: Length scale and time scale effects on the plastic flow of fcc metals. Acta Mater. **49**(20), 4363–4374 (2001)
54. Zhang, X., Aifantis, K.: Interpreting strain bursts and size effects in micro-pillars using gradient plasticity. Mater. Sci. Eng. A **528**, 5036–5043 (2011)

55. Zhang, X., Shang, F.: A continuum model for intermittent deformation of single crystal micropillars. Int. J. Solids Struct. **51**(10), 1859–1871 (2014)
56. Ng, K., Ngan, A.: Breakdown of Schmid's law in micro-pillars. Scripta Mater. **59**(7), 796–799 (2008)
57. Jérusalem, A., Fernández, A., Kunz, A., Greer, J.R.: Continuum modeling of dislocation starvation and subsequent nucleation in nano-pillar-compressions. Scripta Mater. **66**(2), 93–96 (2012)

Methods of Stochastic Mechanics for Characterization of Deformation in Randomly Reinforced Composite Materials

Mikhail A. Tashkinov

Abstract This chapter reveals certain aspects of theoretical statistical approach to studying mechanical behavior of randomly reinforced composite materials, particularly focusing on microstructural characterization and methods of description of stress and strain fields in components of material. Mechanical properties of microstructural components are defined with conventional phenomenological equations and criteria while the effective properties of composite and characteristics of microscopic deformation fields are computed using the solutions of stochastic boundary value problems (SBVPs). Microstructural description is based on a concept of the representative volume elements (RVE) and is implemented with the correlation functions of the second and higher orders. Statistical moments of microstructural fields are used as the characteristic of deformation and fracture processes and analytically connect the microstructural correlation functions with the SBVP solution. Using the Green's functions these solutions have been obtained in elastic and elastoplastic formulations. The numerical calculations for a case study of porous composites with different microstructural properties were obtained for various loading conditions. Some milestones of emerging and development of the described methods are also addressed.

1 Introduction

Composite materials are being increasingly used in modern technologies and industry. Their main advantage is in ability to create a material with unique physical and mechanical characteristics, most appropriate for every application. The key tasks in designing of new composites are the choice of components, definition of the parameters of internal microstructure of material as well as prediction of its

---

M.A. Tashkinov (✉)
The Laboratory of Mechanics of Perspective Structural and Functional Materials, Perm National Research Polytechnic University, 29, Komsomolskiy Ave, 614990 Perm, Russia
e-mail: m.tashkinov@pstu.ru

V.V. Silberschmidt and V.P. Matveenko (eds.), *Mechanics of Advanced Materials*, Engineering Materials, DOI 10.1007/978-3-319-17118-0_3

deformation and fracture under operational loading conditions and environmental effects. Significant costs and efforts required for the experimental investigation of the properties can be saved by development of multi-scale mathematical models taking into account the microstructural features and allowing not only to calculate the effective characteristics of the composites, but also to predict response of each phase of the material during deformation.

One of the main features of the composites is randomness of the geometrical and physical parameters of their internal microstructure. Recent research in computational and experimental mechanics have shown that such parameters as volume fraction of the phases, orientation, shape, size and spatial distribution of inclusions play an important role in behavior of multicomponent materials (the results of these studies are reviewed in the works of Torquato [1], Buryachenko [2], Kaminski [3], Kanoute [4], Silberschmidt [5] and others). Thus, an urgent question in mechanics of composites is creation of non-linear multi-scale models that can take into account the peculiarities of the non-periodic random heterogeneous microstructure and can be used for developing recommendations for the optimal design of composite structures as well as for their reliability assessing.

Multi-scale hierarchy of heterogeneous materials is typically investigated using the representative volume element (RVE) concept when parameters of larger scale models are measured or calculated on a smaller scale [6–8]. However, application of traditional methods (e.g. finite elements analysis) for determination of micro-scale stress and strain fields may be challenging when reinforcement particles are distributed randomly inside the RVE, as each time the result depends on position of the inhomogeneities. The alternative methodology for investigation of the non-periodic randomly reinforced composites is based on statistical methods and the theory of random functions. It implies that mechanical properties of microstructural components are defined with conventional phenomenological equations and criteria while the effective properties of composite and characteristics of microscopic deformation fields are computed using the solutions of stochastic boundary value problems (SBVPs) with piecewise constant coefficients equations; the multipoint statistical moments of the stochastic stress and strain fields are used as the characteristics of the deformation processes in the components of the material.

The SBVPs can be formulated in realizations of the random structure [9] and in the correlation functions [10–13], when averaging over the number of realizations is replaced by volume averaging. The solution of the BVP in the latter formulation can be reduced to the integral-differential equation containing the Green's function [13]. The equation can be solved with various methods, each of which is based on a particular simplifying assumption regarding the statistical properties of the composite's material characteristics fields, which allows to enclose an infinite chain of stochastic equations formed by consecutive statistical averaging of local constitutive relations for the phases of inhomogeneous media [14].

According to the stochastic approach, the indicator function $\lambda_C(\vec{r})$ is used in physical and phenomenological equations to define the properties of each phase of a multicomponent material on a microscopic scale [2, 10, 14]. Value of this function depends on position of the radius-vector $\vec{r}$ inside the RVE. Thus $\lambda_C(\vec{r}) = 1$ if the radius-vector indicates phase C, and $\lambda_C(\vec{r}) = 0$ if it is in any different phase.

Micro-scale fields of the structural parameters of a deformation process are presented in the form of statistically homogeneous coordinate functions, so that they take into account randomness of the relative position of elements in the structure as well as statistical dispersion of the components' properties. These functions depend on the radius-vector and can be developed as a sum of a mean and a fluctuation:

$$\sigma_{ij}(\vec{r}) = \left\langle \sigma_{ij}(\vec{r}) \right\rangle + \sigma'_{ij}(\vec{r}) \tag{1}$$

$$\varepsilon_{ij}(\vec{r}) = \left\langle \varepsilon_{ij}(\vec{r}) \right\rangle + \varepsilon'_{ij}(\vec{r}) \tag{2}$$

$$u_m(\vec{r}) = \langle u_m(\vec{r}) \rangle + u'_m(\vec{r}), \tag{3}$$

$$C_{ijkl}(\vec{r}) = \left\langle C_{ijkl}(\vec{r}) \right\rangle + C'_{ijkl}(\vec{r}), \tag{4}$$

$$\lambda_C(\vec{r}) = \langle \lambda_C(\vec{r}) \rangle + \lambda'_C(\vec{r}) \tag{5}$$

where angle brackets $\langle \rangle$ denote a volume average, Eq. (1) is a stress field, Eq. (2) is a strain field, Eq. (3) is a field of displacements, Eq. (4) is a field of structural elasticity modulus, Eq. (5) is the indicator function. Such representation of the fields allows taking into account randomness of the structural elements as well as the statistical dispersion of the components properties. It is usually supposed that random function $\lambda_C(\vec{r})$ is ergodic. It means that averaging by realizations is equal to the averaging by volume and $\langle \lambda_C(\vec{r}) \rangle = \langle \lambda_C(\vec{r}_1) \rangle$ for every $\vec{r}$ and $\vec{r}_1$.

As the characteristics of deformation processes the multipoint statistical moments of stochastic stress and strain fields in the microstructural components of composite can be introduced. The first order moments (or mean values) are usually suitable only for prediction of the effective elastic properties. The higher order moments are used in elastic and elastoplastic models for the fracture processes studying [10, 12, 13].

The major contribution to development of stochastic approach for composites was made by the representatives of the Russian and other post-Soviet countries' schools of mechanics, however, some of them were not acknowledge properly. The short review of these works is presented below.

The study of behavior of composites with random structures in the framework of the statistical methodology was established by works of Lifshitz and Rosenzweig [15, 16], which were devoted to SBVPs of elasticity theory for polycrystalline media. Subsequently, this approach was developed by Bolotin [17], Lomakin and Sheinin [18], Shermergor [13], Volkov and Stavrov [10], Stavrov et al. [19], Vanin [9], as well as Beran [14], Sokolkin and Tashkinov [12], Maslov [20] and others. Depending on the SBVP solution, the following statistical methods can be distinguished: a method based on the hypothesis of strong isotropy; method of conditional moments; method of periodic components; local approximation method;

method based on the hypothesis of limiting locality of the correlation functions; singular and generalized singular approximation; correlation and full correlation approximation.

If composite components are isotropic and distributed inside the RVE in such a way that it can be macroscopically considered an isotropic medium, the strong isotropy hypothesis can be used [18]. It assumes that for calculation of two-point moments of deformation fields, the components that depend on a choice of direction between the two considered points of can be neglected. This means that macroscopic properties of the composite do not depend on the multipoint correlation functions of the structural elastic moduli. In various interpretations this approach was implemented by Bolotin and Moskalenko [17], Savin and Khoroshun [21], Stavrov and Volkov [10].

Method of conditional moments [22] is based on an assumption that the fluctuations of random fields within a component are quite small. This allows perform the integration and reduce the problem to a system of linear algebraic equations for the one-point conditional moments. Such modified problem is solved in two-point approximation using the statistical information and a number of simplifying hypotheses concerning the nature of the distribution of inclusions in the matrix volume.

For a wide class of stochastic heterogeneous media models deterministic periodic structure can be regarded as a realization of a random structure. The method of periodic components [12] suggests the decomposition of random fields into deterministic and random parts. The deterministic components in this case correspond to the periodic structure. This decomposition allows taking into account such parameters as fractional content, connectivity and geometric shape of components that are common both to the random and periodic structures. The mutual arrangement of the elements is taken into account in the solution of the SBVP for the random media.

Local approximation method [12] is based on the features of short-range interactions of inclusions in matrix composites, according to which the problem of deformation of the composite is reduced to the simpler problem of deformation of an unbounded domain with an ensemble of a small number of inclusions. Feature of local interactions is not related to the specific nature of the mutual arrangement of the inclusions as well as to their shape, so the method has been applied for the composites with random structures [23]. The hypothesis of limiting locality of correlation functions [24] allows obtaining a single-point approximation of SBVPs and avoiding computation of the integrals over the field of statistical dependence of the correlation functions.

Many stochastic methods are based on the assumption of statistical independence of random fields of physical and mechanical properties of composites, which means that each geometric point is identified with a grain of heterogeneity, the fluctuations of properties in the neighboring grains are not correlated, and, thus only the one-point statistical characteristics of a random structure are taken into account. For the composite with deterministic properties of the structural elements all one-point structural statistical characteristics are determined by relative volume concentration of elements in the assumption of homogeneity and ergodicity of the random fields [10, 13].

In the singular approximation [13], the integral stress equilibrium equations, which contain second derivatives of the Green function for a homogeneous unbounded medium, retain only the singular component of these derivatives. In the correlation approximation the equations also contain the formal component. However, only pair interactions are considered, so the correlation functions of a higher order than binary are discarded. In general, the correlation theory can be applied when the standard deviations of the structural elastic moduli are quite small in relation to their mathematical expectation [13]. Correlation approximation was developed by Shermergor [13], Volkov [10], Sokolkin and Tashkinov [12, 24], Pankov [25] and others. Beran [14] and Kroner [26, 27] attempted to consider moments and correlation functions up to third order. Stochastic methods in correlation approximation, for example those that are described in the monographs [10] and [13], lead to good results for a small difference in the elastic modulus of the composite or for a weak anisotropy of the polycrystal grains.

The full correlation approximation assumes that all the terms, obtained in solution of the SBVP in the first approximation, are being taken into account, including those containing correlation functions of order higher than the second. The statistical characteristics in the full correlation approximation and second approximation of the solution of the SBVP were calculated by Volkova and Sokolkin [28] and Tashkinov [29–31]. Convergence of the method of successive approximations of the BVP was studied by Volkov [32].

Despite the large number of existing stochastic approaches for the composite materials study, sometimes there are significant differences can be observed in the results obtained by various methods. This is due to the statistical nonlinearity of the problem and approximate solutions which at a different extent correspond to physical models of composites and, in particular, to their microstructure. Thus, in the statistical mechanics of composites the questions of precise description and formalization of heterogeneous microstructure as well as interactions of its components are still open. Hence there is a need to obtain a more accurate approximation of the solution that can be obtained by taking into account the structural correlation functions of higher order.

This work is related to development of stochastic models of nonlinear mechanics of composites with random structure on the basis of higher-order approximations of SBVPs solutions.

2 Statistical Description of Micro-scale Stress and Strain

2.1 Conditional and Unconditional Statistical Moments

The stochastic methodology will be illustrated on the example of obtaining of the first two moments of microstructural fields for two-component matrix composites.

In case of two-component material both phases can be described by the only indicator function $\lambda(\vec{r})$:

$$\begin{aligned}&\lambda_I(\vec{r}) = \lambda(\vec{r}), \langle\lambda_I\rangle = \langle\lambda\rangle = p, \lambda'_I(\vec{r}) = \lambda'(\vec{r})\\&\lambda_{II}(\vec{r}) = 1-\lambda(\vec{r}), \langle\lambda_{II}\rangle = 1-\langle\lambda\rangle = 1-p, \lambda'_{II}(\vec{r}) = -\lambda'(\vec{r}),\end{aligned}$$

where $p = \langle\lambda(\vec{r})\rangle$ is the inclusions volume concentration.

Statistical information about the geometry of the structure is formalized by in the multipoint correlation functions, which can be obtained from experiments or from modelling [2, 22, 24, 33]. The required moments of stress and strain fields are determined from the solution of boundary value problems.

The formulas for mean values and second order moments (dispersions) in matrix *M* and inclusions *I* in general form were obtained in [10] and [24] and are expressed through the fluctuations of the stochastic fields (1)–(5):

$$\left\langle\varepsilon_{ij}\right\rangle_I = e_{ij} + \frac{1}{p}\left\langle\lambda'(\vec{r})\varepsilon'_{ij}(\vec{r})\right\rangle \tag{6}$$

$$\left\langle\varepsilon_{ij}\right\rangle_M = e_{ij} - \frac{1}{1-p}\left\langle\lambda'(\vec{r})\varepsilon'_{ij}(\vec{r})\right\rangle \tag{7}$$

$$\begin{aligned}\left\langle\varepsilon'_{ij}(\vec{r})\varepsilon'_{\alpha\beta}(\vec{r})\right\rangle_I =& \left\langle\varepsilon'_{ij}(\vec{r})\varepsilon'_{\alpha\beta}(\vec{r})\right\rangle + e_{ij}e_{\alpha\beta} - \left\langle\varepsilon_{ij}\right\rangle_I\left\langle\varepsilon_{\alpha\beta}\right\rangle_I\\&+\frac{1}{p}\left(\left\langle\lambda'(\vec{r})\varepsilon'_{ij}(\vec{r})\varepsilon'_{\alpha\beta}(\vec{r})\right\rangle + e_{ij}\left\langle\lambda'(\vec{r})\varepsilon'_{\alpha\beta}(\vec{r})\right\rangle + e_{\alpha\beta}\left\langle\lambda'(\vec{r})\varepsilon'_{ij}(\vec{r})\right\rangle\right)\end{aligned} \tag{8}$$

$$\begin{aligned}\left\langle\varepsilon'_{ij}(\vec{r})\varepsilon'_{\alpha\beta}(\vec{r})\right\rangle_M =& \left\langle\varepsilon'_{ij}(\vec{r})\varepsilon'_{\alpha\beta}(\vec{r})\right\rangle + e_{ij}e_{\alpha\beta} - \left\langle\varepsilon_{ij}\right\rangle_M\left\langle\varepsilon_{\alpha\beta}\right\rangle_M\\&-\frac{1}{1-p}\left(\left\langle\lambda'(\vec{r})\varepsilon'_{ij}(\vec{r})\varepsilon'_{\alpha\beta}(\vec{r})\right\rangle + e_{ij}\left\langle\lambda'(\vec{r})\varepsilon'_{\alpha\beta}(\vec{r})\right\rangle + e_{\alpha\beta}\left\langle\lambda'(\vec{r})\varepsilon'_{ij}(\vec{r})\right\rangle\right),\end{aligned} \tag{9}$$

$$\left\langle\sigma_{ij}\right\rangle_I = \left\langle\sigma_{ij}\right\rangle + \frac{1}{p}\left\langle\lambda'(\vec{r})\sigma'_{ij}(\vec{r})\right\rangle \tag{10}$$

$$\left\langle\sigma_{ij}\right\rangle_M = \left\langle\sigma_{ij}\right\rangle - \frac{1}{1-p}\left\langle\lambda'(\vec{r})\sigma'_{ij}(\vec{r})\right\rangle \tag{11}$$

$$\begin{aligned}\left\langle\sigma'_{ij}(\vec{r})\sigma'_{\alpha\beta}(\vec{r})\right\rangle_I =& \left\langle\sigma'_{ij}(\vec{r})\sigma'_{\alpha\beta}(\vec{r})\right\rangle + \left\langle\sigma_{ij}\right\rangle\left\langle\sigma_{\alpha\beta}\right\rangle - \left\langle\sigma_{ij}\right\rangle_I\left\langle\sigma_{\alpha\beta}\right\rangle_I\\&+\frac{1}{p}\left(\left\langle\lambda'(\vec{r})\sigma'_{ij}(\vec{r})\sigma'_{\alpha\beta}(\vec{r})\right\rangle + \left\langle\sigma_{ij}\right\rangle\left\langle\lambda'(\vec{r})\sigma'_{\alpha\beta}(\vec{r})\right\rangle + \left\langle\sigma_{\alpha\beta}\right\rangle\left\langle\lambda'(\vec{r})\sigma'_{ij}(\vec{r})\right\rangle\right)\end{aligned} \tag{12}$$

$$\left\langle \sigma'_{ij}(\vec{r})\sigma'_{\alpha\beta}(\vec{r})\right\rangle_M = \left\langle \sigma'_{ij}(\vec{r})\sigma'_{\alpha\beta}(\vec{r})\right\rangle + \langle\sigma_{ij}\rangle\langle\sigma_{\alpha\beta}\rangle - \langle\sigma_{ij}\rangle_M\langle\sigma_{\alpha\beta}\rangle_M$$
$$- \frac{1}{1-p}\left(\left\langle \lambda'(\vec{r})\sigma'_{ij}(\vec{r})\sigma'_{\alpha\beta}(\vec{r})\right\rangle + \langle\sigma_{ij}\rangle\left\langle \lambda'(\vec{r})\sigma'_{\alpha\beta}(\vec{r})\right\rangle + \langle\sigma_{\alpha\beta}\rangle\left\langle \lambda'(\vec{r})\sigma'_{ij}(\vec{r})\right\rangle\right) \tag{13}$$

where p is inclusions' volume fraction, e_{ij} is constant tensor of small deformation defining the boundary conditions on the surface of a RVE:

$$u_i(\vec{r})|_{\vec{r}\in\Gamma_V} = e_{ij}r_j. \tag{14}$$

The principal difference between conditional and unconditional moments is that unconditional moments $\left\langle \sigma'_{ij}(\vec{r})\sigma'_{\alpha\beta}(\vec{r})\right\rangle$, $\left\langle \varepsilon'_{ij}(\vec{r})\varepsilon'_{\alpha\beta}(\vec{r})\right\rangle$ characterize RVE as homogenous, while conditional moments $\langle\varepsilon_{ij}(\vec{r})\rangle_C$, $\langle\sigma_{ij}(\vec{r})\rangle_C$, $\left\langle \sigma'_{ij}(\vec{r})\sigma'_{\alpha\beta}(\vec{r})\right\rangle_C$, $\left\langle \varepsilon'_{ij}(\vec{r})\varepsilon'_{\alpha\beta}(\vec{r})\right\rangle_C$ are characteristics of fields in phases, where C denotes a specific constituent.

2.2 Method of Successive Approximations for the SBVP

The stochastic boundary volume problem statement for the RVE with boundary conditions in displacements can be defined as follows:

$$\sigma_{ij,j}(\vec{r}) = 0, \tag{15}$$

$$\varepsilon_{ij}(\vec{r}) = \frac{1}{2}\left(u_{i,j}(\vec{r}) + u_{j,i}(\vec{r})\right), \tag{16}$$

$$\sigma_{ij}(\vec{r}) = C_{ijkl}(\vec{r})\varepsilon_{kl}(\vec{r}), \tag{17}$$

$$u_i(\vec{r})|_{\vec{r}\in\Gamma_V} = e_{ij}r_j, \tag{18}$$

where Eq. (15) is stress equilibrium equation, $,j$ stands for the derivative $\partial/\partial x_j$, Eq. (16) is Cauchy relations, Eq. (17) is state equation, $C_{ijkl}(\vec{r})$ is tensor of structural elasticity modulus. The boundary conditions (18) on the RVE surface are set in displacements and provide uniformity of the macroscopic deformation, $\vec{r}$ is radius-vector with components (x_1, x_2, x_3), r_j are coordinates of points on the RVE surface Γ_V.

The ideal adhesion type of interface between two phases of the material will be considered. In mathematical terms:

$$u_i^{(M)}(\vec{r})\Big|_{\vec{r}\in\Gamma_{V_M}} = u_i^{(I)}\Big|_{\vec{r}\in\Gamma_{V_I}}(\vec{r}),$$

where Γ_{V_M} is the inner surface of the matrix, Γ_{V_I} is the outer surface of an inclusion.

The problem is solved in fluctuations of displacements field $u_i'(\vec{r})$. The equation system (15)–(18) can be transformed to the following differential equation:

$$\left(C_{ijkl}(\vec{r})\frac{1}{2}\left(u_{k,l}(\vec{r}) + u_{l,k}(\vec{r})\right)\right)_{,j} = 0.$$

From the symmetry of the tensor of elasticity modulus $C_{ijkl}(\vec{r}) = C_{ijlk}(\vec{r})$ follows:

$$\left(C_{ijkl}(\vec{r})u_{k,l}(\vec{r})\right)_{,j} = 0. \tag{19}$$

Taking into account decompositions (3) and (4), Eq. (19) is represented as:

$$\left[\left(\langle C_{ijkl}\rangle + C'_{ijkl}(\vec{r})\right)\left(\langle u_k(\vec{r})\rangle_{,l} + u'_{k,l}(\vec{r})\right)\right]_{,j} = 0, \tag{20}$$

Since the mean value of displacements $\langle u_k(\vec{r})\rangle$ is defined from the boundary conditions (18), the Eq. (20) can be solved regarding fluctuations of displacements $u_k'(\vec{r})$. Taking into account $e_{kl} = {}^1\!/_2(\langle u_k(\vec{r})\rangle_{,l} + \langle u_l(\vec{r})\rangle_{,k})$

$$\left(\langle C_{ijkl}\rangle u'_{k,l}(\vec{r})\right)_{,j} = -\left[C'_{ijkl}(\vec{r})e_{kl} + C'_{ijkl}(\vec{r})u'_{k,l}(\vec{r})\right]_{,j} \tag{21}$$

The right part of this equation can be denoted as the tensor $P_{ij,j}(\vec{r})$:

$$\langle C_{ijkl}\rangle u'_{k,lj}(\vec{r}) = -P_{ij,j}(\vec{r}). \tag{22}$$

Equation (22) can be formally considered as a boundary value problem with modulus of elasticity tensor $\langle C_{ijmn}(\vec{r})\rangle$, displacements $u_i'(\vec{r})$ and body forces $P_{ij,j}(\vec{r})$. If the RVE sizes are considerably larger than structural elements sizes, this heterogeneous differential equation can be solved with Green's function method [2, 12, 13, 15, 24]. If the tensor $\langle C_{ijkl}\rangle$ is a constant, the Green's function $G_{kn}(\vec{r},\vec{r}_1)$ and its derivatives is equal zero for the infinite arguments. The Green's function also satisfies the following differential equation:

$$\langle C_{ijkl}\rangle G_{kn,jl}(\vec{r},\vec{r}_1) = -\delta_{in}\delta(\vec{r}-\vec{r}_1), \tag{23}$$

where $\delta(\vec{r}-\vec{r}_1)$ is the delta-function, δ_{in} is the Kronecker delta.

The solution of the SBVP for the indeterminate field of displacements' fluctuations takes a form of the integral-differential equation containing the Green's function:

$$u_i'(\vec{r}) = \int\limits_{V_1} G_{ij}(\vec{r},\vec{r}_1)\frac{\partial P_{jn}(\vec{r}_1)}{\partial x_{1n}}dV_1. \tag{24}$$

Equation (24) contains the displacements $u'_i(\vec{r})$ both in its left and right parts, so the equation has the recurrent form:

$$\frac{\partial u_i'^{(\chi)}(\vec{r})}{\partial x_j} = \int\limits_{V_1} \frac{\partial G_{im}(\vec{r},\vec{r}_1)}{\partial x_j}\left[C'_{mnkl}(\vec{r}_1)e_{kl} + C'_{mnkl}(\vec{r}_1)\frac{\partial u_k'^{(\chi-1)}(\vec{r}_1)}{\partial x_l}\right]_{,1n} dV_1 \tag{25}$$

where χ is approximation order. Selection of the appropriate form of the Green's function depends on the type of the considered heterogeneous media. There is a specific Green function for an isotropic tensor $\left\langle C_{ijmn}(\vec{r})\right\rangle$. Thus, if RVE dimensions are much smaller than the solid body, the Kelvin-Somigliana tensor is used as the Green's function [9]:

$$G_{mk}(\vec{r},\vec{r}_1) = A\frac{\delta_{mk}}{|\vec{r}-\vec{r}_1|} + B\frac{(r_m - r_{1m})(r_k - r_{1k})}{|\vec{r}-\vec{r}_1|^3}, \tag{26}$$

In the first approximation fluctuations of displacements in the right part of Eq. (25) are being neglected:

$$u_{i,j}'^{(1)}(\vec{r}) = e_{kl}\int\limits_{V_1} G_{im,j}(\vec{r},\vec{r}_1)\big(C'_{mnkl}(\vec{r}_1)\big)_{,1n}\, dV_1. \tag{27}$$

The solution in this form with some assumptions is used in correlation and singular approximation methods [13, 24, 28, 29]. In the second approximation, result obtained from the first approximation is substituted into the right part of the equation.

$$\begin{aligned} u_{i,j}'^{(2)}(\vec{r}) = e_{kl}&\int\limits_{V_1} G_{im,j}(\vec{r},\vec{r}_1)\big(C'_{mnkl}(\vec{r}_1)\big)_{,1n}\, dV_1 \\ &+ e_{oq}\int\limits_{V_1}\int\limits_{V_{11}} G_{im,j}(\vec{r},\vec{r}_1)\Big[C'_{mnkl}(\vec{r}_1)G_{kf,l}(\vec{r}_1,\vec{r}_{11})\Big(C'_{fsoq}(\vec{r}_{11})\Big)_{,11s}\Big]_{,1n} dV_{11}dV_1. \end{aligned} \tag{28}$$

In further numerical examples in this work the solution in the second approximation (28) will be used. The solution of the SBVP is applied to form the equations for the moments of stress and strain fields as a superposition of multidimensional integrals.

2.3 SBVP Solution in Elastic Case

For elastic two-component materials the field of structural elasticity modulus can be expressed with the indicator function:

$$C_{ijkl}(\vec{r}) = \lambda(\vec{r})C^{I}_{ijkl} + (1 - \lambda(\vec{r}))C^{M}_{ijkl}, \tag{29}$$

where $C^{(I)}_{ijkl}$ и $C^{(M)}_{ijkl}$ are tensors of elasticity modulus of matrix and inclusions, which in isotropic case can be represented as:

$$C^{(I)}_{ijkl} = \lambda_I\delta_{ij}\delta_{kl} + \mu_I\left(\delta_{ik}\delta_{jl} + \delta_{il}\delta_{jk}\right),\ C^{(M)}_{ijkl} = \lambda_M\delta_{ij}\delta_{kl} + \mu_M\left(\delta_{ik}\delta_{jl} + \delta_{il}\delta_{jk}\right),$$

where λ_I, λ_M, μ_I, μ_M are Lame constants of inclusions and matrix which are defined as $\lambda_I = \frac{E_I v_I}{(1+v_I)(1-2v_I)}$, $\mu_I = \frac{E_I}{2(1+v_I)}$, E_I is coefficient of elasticity of inclusion, v_I is Poisson's ratio. Similarly for λ_M and μ_M.

Averaging Eq. (29) gives a constant isotropic tensor:

$$\left\langle C_{ijkl}(\vec{r})\right\rangle = \left\langle C_{ijkl}\right\rangle = pC^{I}_{ijkl} + (1-p)C^{M}_{ijkl}, \tag{30}$$

where $p = \langle\lambda(\vec{r})\rangle$ is the inclusions volume concentration.

By combining Eqs. (5), (29) and (30), the fluctuation $C'_{ijkl}(\vec{r})$ can be linked with fluctuation of the indicator function:

$$C'_{ijkl}(\vec{r}) = \lambda'(\vec{r})(C^{I}_{ijkl} - C^{M}_{ijkl}), \tag{31}$$

The SBVP solution in the second approximation (28) then can be brought to the integral over the first derivatives of the Green's function and indicator function fluctuation:

$$\begin{aligned} u'^{(2)}_{i,j}(\vec{r}) &= e_{kl}\bar{C}_{mnkl}\int\limits_{V_1} G_{im,j}(\vec{r},\vec{r}_1)(\lambda'(\vec{r}_1))_{,n}\,dV_1 \\ &+ e_{oq}\bar{C}_{mnkl}\bar{C}_{fsoq}\int\limits_{V_1}\int\limits_{V_{11}} G_{im,j}(\vec{r},\vec{r}_1)\left[\lambda'(\vec{r}_1)G_{kf,l}(\vec{r}_1,\vec{r}_{11})(\lambda'(\vec{r}_{11}))_{,11s}\right]_{,1n} dV_{11}dV_1, \end{aligned} \tag{32}$$

where $\bar{C}_{mnkl} = C^{I}_{mnkl} - C^{M}_{mnkl}$.

The coefficients A and B of the Green's function (26) are connected with Lame constants of the components:

$$A = \frac{\langle\lambda\rangle + \langle 3\mu\rangle}{8\pi\langle\mu\rangle\langle\lambda + 2\mu\rangle},\ B = \frac{\langle\lambda\rangle + \langle\mu\rangle}{8\pi\langle\mu\rangle\langle\lambda + 2\mu\rangle},$$

where $\langle\lambda\rangle = \lambda_I p + \lambda_M(1-p)$, $\langle\mu\rangle = \mu_I p + \mu_M(1-p)$.

2.4 SBVP Solution in Elastoplastic Case

In the elastoplastic case the field of structural elasticity modulus has the following representation [31]:

$$C_{ijkl}(\vec{r},\varepsilon) = 3K(\vec{r},j_\varepsilon^{(1)},j_\varepsilon^{(2)})V_{ijkl} + 2\mu(\vec{r},j_\varepsilon^{(1)},j_\varepsilon^{(2)})D_{ijkl}, \tag{33}$$

where $K\left(\vec{r},j_\varepsilon^{(1)},j_\varepsilon^{(2)}\right) = \lambda(\vec{r})K_I(j_\varepsilon^{(1)},j_\varepsilon^{(2)}) + (1-\lambda(\vec{r}))K_M(j_\varepsilon^{(1)},j_\varepsilon^{(2)})$ is the nonlinear bulk modulus, $\mu\left(\vec{r},j_\varepsilon^{(1)},j_\varepsilon^{(2)}\right) = \lambda(\vec{r})\mu_I(j_\varepsilon^{(1)},j_\varepsilon^{(2)}) + (1-\lambda(\vec{r}))\mu_M(j_\varepsilon^{(1)},j_\varepsilon^{(2)})$ is the shear modulus. Both of them are material functions of the invariants $j_\varepsilon^{(1)},j_\varepsilon^{(2)}$ of microstrain tensor. V_{ijkl} and D_{ijkl} are volumetric and deviator parts of the identity tensor $I_{ijkl} = V_{ijkl} + D_{ijkl}$.

The invariants of stress and strain tensors are functions of deviator parts of the tensors:

$$j_\sigma^{(2)} = \sqrt{\breve{\sigma}_{ij}\breve{\sigma}_{ij}},\ j_\varepsilon^{(2)} = \sqrt{\breve{\varepsilon}_{ij}\breve{\varepsilon}_{ij}},\ j_\sigma^{(1)} = \sigma_{ij}\delta_{ij},\ j_\varepsilon^{(1)} = \varepsilon_{ij}\delta_{ij}.$$

where δ_{ij} is the Kronecker delta, $\breve{\varepsilon}_{ij} = \varepsilon_{ij} - {}^1\!/_3\varepsilon_{kk}\delta_{ij}$, $\breve{\sigma}_{ij} = \sigma_{ij} - {}^1\!/_3\sigma_{kk}\delta_{ij}$.

The deviator parts can be decomposed into the mean and the fluctuation. For the strain tensor: $\breve{\varepsilon}_{ij} = \left\langle \breve{\varepsilon}_{ij} \right\rangle + \breve{\varepsilon}'_{ij}$. The mean values of the invariants of tensors will be further used:

$$\left\langle j_\varepsilon^{(2)} \right\rangle = \sqrt{\left\langle \breve{\varepsilon}_{ij}\breve{\varepsilon}_{ij} \right\rangle} = \sqrt{\left\langle \breve{\varepsilon}_{ij} \right\rangle\left\langle \breve{\varepsilon}_{ij} \right\rangle + \left\langle \breve{\varepsilon}'_{ij}\breve{\varepsilon}'_{ij} \right\rangle}, \tag{34}$$

$$\left\langle j_\varepsilon^{(1)} \right\rangle = \langle \varepsilon_{ij} \rangle \delta_{ij} = \langle \varepsilon_{ii} \rangle. \tag{35}$$

The fluctuations $\left\langle \breve{\varepsilon}'_{ij}\breve{\varepsilon}'_{ij} \right\rangle$ in Eq. (34) can be considered negligible. Then the mean values of shear and bulk modulus for the matrix and inclusions are in general expressed as follows:

$$\mu_{I,M}\left(\vec{r},j_\varepsilon^{(1)},j_\varepsilon^{(2)}\right) = \mu_{I,M}\left(\langle \varepsilon_{ii} \rangle_{I,M}, \Lambda_{I,M}\right), \tag{36}$$

$$K_{I,M}\left(\vec{r},j_\varepsilon^{(1)},j_\varepsilon^{(2)}\right) = K_{I,M}\left(\langle \varepsilon_{ii} \rangle_{I,M}, \Lambda_{I,M}\right), \tag{37}$$

where $\Lambda_{I,M} = \sqrt{\left\langle \breve{\varepsilon}_{ij} \right\rangle_{I,M}\left\langle \breve{\varepsilon}_{ij} \right\rangle_{I,M}}$.

The second approximation of the solution (25) in elastoplastic case looks as follows:

$$u'^{(2)}_{i,j}(\vec{r}) = e_{kl}\int\limits_{V_1} G_{im,j}(\vec{r},\vec{r}_1)\left(C'_{mnkl}\lambda'(\vec{r}_1)\right)_{,n} dV_1 + e_{oq}\int\limits_{V_1}\int\limits_{V_{11}} G_{im,j}(\vec{r},\vec{r}_1)\left[C'_{mnkl}\lambda'(\vec{r}_1)G_{kf,l}(\vec{r}_1,\vec{r}_{11})\left(C'_{fsoq}\lambda'(\vec{r}_{11})\right)_{,11s}\right]_{,1n} dV_{11}dV_1, \tag{38}$$

where $C'_{mnkl}(\vec{r}) = \left(C^I_{mnkl}(\langle\varepsilon_{kk}\rangle_I, \Lambda_I) - C^M_{mnkl}(\langle\varepsilon_{kk}\rangle_M, \Lambda_M)\right)\lambda'(\vec{r})$.

The coefficients A and B in of the Green's function (26) depend on nonlinear shear and bulk moduli:

$$A = \frac{\left\langle\left[3K\left(\vec{r}, j_\varepsilon^{(1)}, j_\varepsilon^{(2)}\right) - 7\mu\left(\vec{r}, j_\varepsilon^{(1)}, j_\varepsilon^{(2)}\right)\right]\right\rangle}{24\pi\left\langle\mu\left(\vec{r}, j_\varepsilon^{(1)}, j_\varepsilon^{(2)}\right)\right\rangle\left\langle\left[3K\left(\vec{r}, j_\varepsilon^{(1)}, j_\varepsilon^{(2)}\right) - 4\mu\left(\vec{r}, j_\varepsilon^{(1)}, j_\varepsilon^{(2)}\right)\right]\right\rangle},$$
$$B = \frac{\left\langle\left[3K\left(\vec{r}, j_\varepsilon^{(1)}, j_\varepsilon^{(2)}\right) - \mu\left(\vec{r}, j_\varepsilon^{(1)}, j_\varepsilon^{(2)}\right)\right]\right\rangle}{24\pi\left\langle\mu\left(\vec{r}, j_\varepsilon^{(1)}, j_\varepsilon^{(2)}\right)\right\rangle\left\langle\left[3K\left(\vec{r}, j_\varepsilon^{(1)}, j_\varepsilon^{(2)}\right) - 4\mu\left(\vec{r}, j_\varepsilon^{(1)}, j_\varepsilon^{(2)}\right)\right]\right\rangle},$$

where $\left\langle K\left(\vec{r}, j_\varepsilon^{(1)}, j_\varepsilon^{(2)}\right)\right\rangle = p\left\langle K_I(j_\varepsilon^{(1)}, j_\varepsilon^{(2)})\right\rangle + (1-p)\left\langle K_M(j_\varepsilon^{(1)}, j_\varepsilon^{(2)})\right\rangle$, $\left\langle \mu\left(\vec{r}, j_\varepsilon^{(1)}, j_\varepsilon^{(2)}\right)\right\rangle = p\left\langle \mu_I(j_\varepsilon^{(1)}, j_\varepsilon^{(2)})\right\rangle + (1-p)\left\langle \mu_M(j_\varepsilon^{(1)}, j_\varepsilon^{(2)})\right\rangle$.

2.5 Analytical Expressions for the Statistical Characteristics

For both elastic and elastoplastic cases, the solutions of the SBVP are used for defining the analytical expressions for the moments of stress and strain fields. Random fields of strain and stress fluctuations depend on fluctuation of displacements $u'_{i,j}(\vec{r})$:

$$\varepsilon'_{ij}(\vec{r}) = \frac{1}{2}\left(u'_{i,j}(\vec{r}) + u'_{j,i}(\vec{r})\right), \tag{39}$$

The moments $\left\langle\varepsilon'_{ij}(\vec{r})\varepsilon'_{\alpha\beta}(\vec{r})\right\rangle$, $\left\langle\lambda'(\vec{r})\varepsilon'_{ij}(\vec{r})\right\rangle$ and $\left\langle\lambda'(\vec{r})\varepsilon'_{ij}(\vec{r})\varepsilon'_{\alpha\beta}(\vec{r})\right\rangle$, which are part of Eq. (6)–(9), can be analytically constructed using the SBVP solution in fluctuations of displacements $u'_m(\vec{r})$ and multipoint correlation functions of indicator function fluctuation $\lambda'(\vec{r})$.

Thus, using the solution in the first approximation:

$$\begin{aligned}&\left\langle \lambda'(\vec{r})\varepsilon'_{ij}(\vec{r})\varepsilon'_{\alpha\beta}(\vec{r})\right\rangle^{(1)}\\&=\frac{1}{4}e_{kl}e_{\phi h}\bar{C}_{mnkl}\bar{C}_{\gamma\eta\phi h}\int\limits_{V_1}\int\limits_{V_2}\big(G_{im,j}(\vec{r},\vec{r}_1)+G_{jm,i}(\vec{r},\vec{r}_1)\big)\big(G_{\alpha\gamma,\beta}(\vec{r},\vec{r}_2)+G_{\beta\gamma,\alpha}(\vec{r},\vec{r}_2)\big)\\&\qquad\times\frac{\partial^3 K_\lambda^{(3)}(\vec{r},\vec{r}_1,\vec{r}_2)}{\partial x_{1n}\partial x_{2\eta}}dV_2dV_1,\end{aligned} \tag{40}$$

$$\left\langle \lambda'(\vec{r})\varepsilon'_{ij}(\vec{r})\right\rangle^{(1)}=\frac{1}{2}e_{kl}\bar{C}_{mnkl}\int\limits_{V_1}\big(G_{im,j}(\vec{r},\vec{r}_1)+G_{jm,i}(\vec{r},\vec{r}_1)\big)\frac{\partial K_\lambda^{(2)}(\vec{r},\vec{r}_1)}{\partial x_{1n}}dV_1 \tag{41}$$

$$\begin{aligned}&\left\langle \lambda'(\vec{r})\varepsilon'_{ij}(\vec{r})\varepsilon'_{\alpha\beta}(\vec{r})\right\rangle^{(1)}\\&=\frac{1}{4}e_{kl}e_{\phi h}\bar{C}_{mnkl}\bar{C}_{\gamma\eta\phi h}\int\limits_{V_1}\int\limits_{V_2}\big(G_{im,j}(\vec{r},\vec{r}_1)+G_{jm,i}(\vec{r},\vec{r}_1)\big)\big(G_{\alpha\gamma,\beta}(\vec{r},\vec{r}_2)+G_{\beta\gamma,\alpha}(\vec{r},\vec{r}_2)\big)\\&\qquad\times\frac{\partial^3 K_\lambda^{(3)}(\vec{r},\vec{r}_1,\vec{r}_2)}{\partial x_{1n}\partial x_{2\eta}}dV_2dV_1,\end{aligned} \tag{42}$$

where $K_\lambda^{(n)}(\vec{r},\vec{r}_1,\ldots,\vec{r}_n)$ are multipoint correlation functions.

With the second approximation of SBVP solution the other expressions has been obtained:

$$\begin{aligned}M_{ij\alpha\beta}^{(\varepsilon)(2)}&=\left\langle \varepsilon'_{ij}(\vec{r})\varepsilon'_{\alpha\beta}(\vec{r})\right\rangle^{(2)}\\&=\frac{1}{4}\bar{C}_{mnkl}\bar{C}_{\gamma\eta\phi h}\Bigg(e_{kl}e_{\phi h}\int\limits_{V_1}\int\limits_{V_2}\big(G_{im,j}(\vec{r},\vec{r}_1)+G_{jm,i}(\vec{r},\vec{r}_1)\big)\big(G_{\alpha\gamma,\beta}(\vec{r},\vec{r}_2)+G_{\beta\gamma,\alpha}(\vec{r},\vec{r}_2)\big)\\&\qquad\times\frac{\partial^2 K_\lambda^{(2)}(\vec{r}_1,\vec{r}_2)}{\partial x_{1n}\partial x_{2\eta}}dV_2dV_1\\&\quad+e_{kl}e_{bd}\bar{C}_{vwbd}\int\limits_{V_1}\int\limits_{V_2}\int\limits_{V_{21}}\big(G_{im,j}(\vec{r},\vec{r}_1)+G_{jm,i}(\vec{r},\vec{r}_1)\big)\big(G_{\alpha\gamma,\beta}(\vec{r},\vec{r}_2)+G_{\beta\gamma,\alpha}(\vec{r},\vec{r}_2)\big)\\&\qquad\times G_{\phi v,h}(\vec{r}_2,\vec{r}_{21})\frac{\partial^3 K_\lambda^{(3)}(\vec{r}_1,\vec{r}_2,\vec{r}_{21})}{\partial x_{1n}\partial x_{2\eta}\partial x_{21w}}dV_{21}dV_2dV_1\\&\quad+e_{\phi h}e_{oq}\bar{C}_{fsoq}\int\limits_{V_1}\int\limits_{V_2}\int\limits_{V_{11}}\big(G_{im,j}(\vec{r},\vec{r}_1)+G_{jm,i}(\vec{r},\vec{r}_1)\big)\big(G_{\alpha\gamma,\beta}(\vec{r},\vec{r}_2)+G_{\beta\gamma,\alpha}(\vec{r},\vec{r}_2)\big)\\&\qquad\times G_{kf,l}(\vec{r}_1,\vec{r}_{11})\frac{\partial^3 K_\lambda^{(3)}(\vec{r}_1,\vec{r}_2,\vec{r}_{11})}{\partial x_{1n}\partial x_{2\eta}\partial x_{11s}}dV_{11}dV_2dV_1\\&\quad+e_{oq}e_{bd}\bar{C}_{fsoq}\bar{C}_{vwbd}\int\limits_{V_1}\int\limits_{V_2}\int\limits_{V_{11}}\int\limits_{V_{21}}\big(G_{im,j}(\vec{r},\vec{r}_1)+G_{jm,i}(\vec{r},\vec{r}_1)\big)\big(G_{\alpha\gamma,\beta}(\vec{r},\vec{r}_2)+G_{\beta\gamma,\alpha}(\vec{r},\vec{r}_2)\big)\\&\qquad\times G_{kf,l}(\vec{r}_1,\vec{r}_{11})G_{\phi v,h}(\vec{r}_2,\vec{r}_{21})\frac{\partial^4 K_\lambda^{(4)}(\vec{r}_1,\vec{r}_2,\vec{r}_{11},\vec{r}_{21})}{\partial x_{1n}\partial x_{2\eta}\partial x_{11s}\partial x_{21w}}dV_{21}dV_{11}dV_2dV_1\Bigg),\end{aligned} \tag{43}$$

$$\begin{aligned}\left\langle \lambda'(\vec{r})\varepsilon'_{ij}(\vec{r})\right\rangle^{(2)} = \frac{1}{2}\Bigg(& e_{kl}\bar{C}_{mnkl}\int\limits_{V_1}\big(G_{im,j}(\vec{r},\vec{r}_1)+G_{jm,i}(\vec{r},\vec{r}_1)\big)\frac{\partial K_\lambda^{(2)}(\vec{r},\vec{r}_1)}{\partial x_{1n}}dV_1 \\ & + e_{oq}\bar{C}_{fsoq}\bar{C}_{mnkl}\int\limits_{V_1}\int\limits_{V_{11}}\big(G_{im,j}(\vec{r},\vec{r}_1)+G_{jm,i}(\vec{r},\vec{r}_1)\big)G_{kf,l}(\vec{r}_1,\vec{r}_{11}) \\ & \times\frac{\partial^2 K_\lambda^{(3)}(\vec{r},\vec{r}_1,\vec{r}_{11})}{\partial x_{1n}\partial x_{11s}}dV_{11}dV_1\Bigg),\end{aligned} \tag{44}$$

$$\begin{aligned}&\left\langle \lambda'(\vec{r})\varepsilon'_{ij}(\vec{r})\varepsilon'_{\alpha\beta}(\vec{r})\right\rangle^{(2)} \\ &= \frac{1}{4}\bar{C}_{mnkl}\bar{C}_{\gamma\eta\phi h}\Bigg(e_{kl}e_{\phi h}\int\limits_{V_1}\int\limits_{V_2}\big(G_{im,j}(\vec{r},\vec{r}_1)+G_{jm,i}(\vec{r},\vec{r}_1)\big)\big(G_{\alpha\gamma,\beta}(\vec{r},\vec{r}_2)+G_{\beta\gamma,\alpha}(\vec{r},\vec{r}_2)\big) \\ &\qquad\times\frac{\partial^2 K_\lambda^{(3)}(\vec{r},\vec{r}_1,\vec{r}_2)}{\partial x_{1n}\partial x_{2\eta}}dV_2dV_1 \\ &\quad + e_{kl}e_{bd}\bar{C}_{vwbd}\int\limits_{V_1}\int\limits_{V_2}\int\limits_{V_{21}}\big(G_{im,j}(\vec{r},\vec{r}_1)+G_{jm,i}(\vec{r},\vec{r}_1)\big)\big(G_{\alpha\gamma,\beta}(\vec{r},\vec{r}_2)+G_{\beta\gamma,\alpha}(\vec{r},\vec{r}_2)\big)G_{\phi v,h}(\vec{r}_2,\vec{r}_{21}) \\ &\qquad\times\frac{\partial^3 K_\lambda^{(4)}(\vec{r},\vec{r}_1,\vec{r}_2,\vec{r}_{21})}{\partial x_{1n}\partial x_{2\eta}\partial x_{21w}}dV_{21}dV_2dV_1 \\ &\quad + e_{\phi h}e_{oq}\bar{C}_{fsoq}\int\limits_{V_1}\int\limits_{V_2}\int\limits_{V_{11}}\big(G_{im,j}(\vec{r},\vec{r}_1)+G_{jm,i}(\vec{r},\vec{r}_1)\big)\big(G_{\alpha\gamma,\beta}(\vec{r},\vec{r}_2)+G_{\beta\gamma,\alpha}(\vec{r},\vec{r}_2)\big)G_{kf,l}(\vec{r}_1,\vec{r}_{11}) \\ &\qquad\times\frac{\partial^3 K_\lambda^{(4)}(\vec{r},\vec{r}_1,\vec{r}_2,\vec{r}_{11})}{\partial x_{1n}\partial x_{2\eta}\partial x_{11s}}dV_{11}dV_2dV_1 \\ &\quad + e_{oq}e_{bd}\bar{C}_{fsoq}\bar{C}_{vwbd}\int\limits_{V_1}\int\limits_{V_2}\int\limits_{V_{11}}\int\limits_{V_{21}}\big(G_{im,j}(\vec{r},\vec{r}_1)+G_{jm,i}(\vec{r},\vec{r}_1)\big)\big(G_{\alpha\gamma,\beta}(\vec{r},\vec{r}_2)+G_{\beta\gamma,\alpha}(\vec{r},\vec{r}_2)\big) \\ &\qquad\times G_{kf,l}(\vec{r}_1,\vec{r}_{11})G_{\phi v,h}(\vec{r}_2,\vec{r}_{21})\frac{\partial^4 K_\lambda^{(5)}(\vec{r},\vec{r}_1,\vec{r}_2,\vec{r}_{11},\vec{r}_{21})}{\partial x_{1n}\partial x_{2\eta}\partial x_{11s}\partial x_{21w}}dV_{21}dV_{11}dV_2dV_1\Bigg),\end{aligned} \tag{45}$$

where $\bar{C}_{mnkl} = C^I_{mnkl} - C^M_{mnkl}$ in elastic case, $\bar{C}_{mnkl} = \big(C^I_{mnkl}(\langle\varepsilon_{kk}\rangle_I, \Lambda_I) - C^M_{mnkl}(\langle\varepsilon_{kk}\rangle_M, \Lambda_M)\big)$ in elastoplastic case, $K_\lambda^{(n)}(\vec{r},\vec{r}_1,\vec{r}_2,\ldots) = \langle\lambda'(\vec{r})\lambda'(\vec{r}_1)\ldots\lambda'(\vec{r}_n)\rangle$ are normalized structural correlation functions of order n.

To determine the statistical moments in elastoplastic case it is necessary to establish relation between microstructural strain characteristics in the phases $\left\langle\varepsilon_{ij}\right\rangle_{I,M}$ and macroscopic strain tensor e_{ij}. The Eqs. (6) and (7) contain mean values of microstructural strain both in their left and right parts, so the iteration procedure can be organized to determine macroscopic strain:

$$\left\langle\varepsilon_{ij}\right\rangle_M^{(n)} = e_{ij} - \frac{1}{1-p}\left\langle\lambda'(\vec{r})\varepsilon'_{ij}(\vec{r})\right\rangle^{(n-1)}, \left\langle\varepsilon_{ij}\right\rangle_I^{(n)} = e_{ij} + \frac{1}{p}\left\langle\lambda'(\vec{r})\varepsilon'_{ij}(\vec{r})\right\rangle^{(n-1)},$$

where

$$
\begin{aligned}
\left\langle \lambda'(\vec{r})\varepsilon'_{ij}(\vec{r})\right\rangle = \frac{1}{2}\Bigg(& e_{kl}\bar{C}_{mnkl}\int\limits_{V_1}\big(G_{im,j}(\vec{r},\vec{r}_1)+G_{jm,i}(\vec{r},\vec{r}_1)\big)\frac{\partial K_{\lambda}^{(2)}(\vec{r},\vec{r}_1)}{\partial x_{1n}}dV_1 \\
& + e_{oq}\bar{C}_{fsoq}\bar{C}_{mnkl}\int\limits_{V_1}\int\limits_{V_{11}}\big(G_{im,j}(\vec{r},\vec{r}_1)+G_{jm,i}(\vec{r},\vec{r}_1)\big) \\
& \times G_{kf,l}(\vec{r}_1,\vec{r}_{11})\frac{\partial^2 K_{\lambda}^{(3)}(\vec{r},\vec{r}_1,\vec{r}_{11})}{\partial x_{1n}\partial x_{11s}}dV_{11}dV_1\Bigg),
\end{aligned}
$$

At the first iteration the random values for components of tensor are chosen. The procedure stops when $\left|\left\langle\varepsilon_{ij}\right\rangle_{I,M}^{(n)}-\left\langle\varepsilon_{ij}\right\rangle_{I,M}^{(n-1)}\right|<10^{-9}$. The values of $\left\langle\varepsilon_{ij}\right\rangle_{I,M}$ and e_{ij} obtained after this procedure are used for further calculations of mean values and dispersions of microstructural stress.

The mixed moments $\left\langle\lambda'(\vec{r})\sigma'_{ij}(\vec{r})\right\rangle$ and $\left\langle\lambda'(\vec{r})\sigma'_{ij}(\vec{r})\sigma'_{\alpha\beta}(\vec{r})\right\rangle$ that forms the statistical characteristics for the stress field in components (10)–(13) are expressed with the same moments of stress fields (40)–(45) using the formula:

$$
\sigma'_{ij}(\vec{r}) = \sigma_{ij}(\vec{r}) - \left\langle\sigma_{ij}\right\rangle = C'_{ijkl}(\vec{r})e_{kl} - \left\langle C'_{ijkl}(\vec{r})\varepsilon'_{kl}(\vec{r})\right\rangle + C_{ijkl}(\vec{r})\varepsilon'_{kl}(\vec{r}). \tag{46}
$$

Thus, the conditional moments of strain and stress fields are determined from the mixed moments $\left\langle\varepsilon'_{ij}(\vec{r})\varepsilon'_{\alpha\beta}(\vec{r})\right\rangle$, $\left\langle\lambda'(\vec{r})\varepsilon'_{ij}(\vec{r})\right\rangle$ and $\left\langle\lambda'(\vec{r})\varepsilon'_{ij}(\vec{r})\varepsilon'_{\alpha\beta}(\vec{r})\right\rangle$:

$$
\left\langle\lambda'(\vec{r})\sigma'_{ij}(\vec{r})\right\rangle = e_{kl}\bar{C}_{ijkl}D_{\lambda}^{(2)} - \bar{C}_{ijkl}\left\langle\lambda'(\vec{r})\lambda'(\vec{r})\varepsilon'_{kl}(\vec{r})\right\rangle + \left\langle C_{ijkl}\right\rangle\left\langle\lambda'(\vec{r})\varepsilon'_{kl}(\vec{r})\right\rangle, \tag{47}
$$

$$
\begin{aligned}
\left\langle\lambda'(\vec{r})\sigma'_{ij}(\vec{r})\sigma'_{\alpha\beta}(\vec{r})\right\rangle = {} & e_{kl}e_{\phi h}\bar{C}_{ijkl}\bar{C}_{\alpha\beta\phi h}D_{\lambda}^{3} + e_{kl}\bar{C}_{ijkl}\left\langle C_{\alpha\beta\phi h}\right\rangle\left\langle\lambda'(\vec{r})\lambda'(\vec{r})\varepsilon'_{\phi h}(\vec{r})\right\rangle \\
& + e_{\phi h}\bar{C}_{\alpha\beta\phi h}\left\langle C_{ijkl}\right\rangle\left\langle\lambda'(\vec{r})\lambda'(\vec{r})\varepsilon'_{kl}(\vec{r})\right\rangle \\
& + \left\langle C_{ijkl}\right\rangle\left\langle C_{\alpha\beta\phi h}\right\rangle\left\langle\lambda'(\vec{r})\varepsilon'_{\phi h}(\vec{r})\varepsilon'_{kl}(\vec{r})\right\rangle \\
& - e_{kl}\bar{C}_{ijkl}\bar{C}_{\alpha\beta\phi h}\left\langle\lambda'(\vec{r})\lambda'(\vec{r})\lambda'(\vec{r})\varepsilon'_{\phi h}(\vec{r})\right\rangle \\
& - e_{\phi h}\bar{C}_{ijkl}\bar{C}_{\alpha\beta\phi h}\left\langle\lambda'(\vec{r})\lambda'(\vec{r})\lambda'(\vec{r})\varepsilon'_{kl}(\vec{r})\right\rangle \\
& - \bar{C}_{\alpha\beta\phi h}\left\langle C_{ijkl}\right\rangle\left\langle\lambda'(\vec{r})\lambda'(\vec{r})\varepsilon'_{\phi h}(\vec{r})\varepsilon'_{kl}(\vec{r})\right\rangle \\
& - \bar{C}_{ijkl}\left\langle C_{\alpha\beta\phi h}\right\rangle\left\langle\lambda'(\vec{r})\lambda'(\vec{r})\varepsilon'_{\phi h}(\vec{r})\varepsilon'_{kl}(\vec{r})\right\rangle \\
& + \bar{C}_{ijkl}\bar{C}_{\alpha\beta\phi h}\left\langle\lambda'(\vec{r})\lambda'(\vec{r})\lambda'(\vec{r})\varepsilon'_{kl}(\vec{r})\varepsilon'_{\phi h}(\vec{r})\right\rangle.
\end{aligned} \tag{48}
$$

The moments $\left\langle \lambda'(\vec{r})\lambda'(\vec{r})\varepsilon'_{kl}(\vec{r})\right\rangle$ and $\left\langle \lambda'(\vec{r})\lambda'(\vec{r})\lambda'(\vec{r})\varepsilon'_{kl}(\vec{r})\right\rangle$ are connected with the moments $\left\langle \lambda'(\vec{r})\varepsilon'_{kl}(\vec{r})\right\rangle$ and $\left\langle \lambda'(\vec{r})\varepsilon'_{kl}(\vec{r})\varepsilon'_{\phi h}(\vec{r})\right\rangle$:

$$\begin{aligned}
&\left\langle \lambda'(\vec{r})\lambda'(\vec{r})\varepsilon'_{kl}(\vec{r})\right\rangle = (1-2p)\left\langle \lambda'(\vec{r})\varepsilon'_{kl}(\vec{r})\right\rangle,\\
&\left\langle \lambda'(\vec{r})\lambda'(\vec{r})\lambda'(\vec{r})\varepsilon'_{kl}(\vec{r})\right\rangle = \left(1-3D_\lambda^{(2)}\right)\left\langle \lambda'(\vec{r})\varepsilon'_{kl}(\vec{r})\right\rangle,\\
&\left\langle \lambda'(\vec{r})\lambda'(\vec{r})\varepsilon'_{kl}(\vec{r})\varepsilon'_{\phi h}(\vec{r})\right\rangle = (1-2p)\left\langle \lambda'(\vec{r})\varepsilon'_{kl}(\vec{r})\varepsilon'_{\phi h}(\vec{r})\right\rangle + D_\lambda^{(2)}\left\langle \varepsilon'_{kl}(\vec{r})\varepsilon'_{\phi h}(\vec{r})\right\rangle,\\
&\left\langle \lambda'(\vec{r})\lambda'(\vec{r})\lambda'(\vec{r})\varepsilon'_{kl}(\vec{r})\varepsilon'_{\phi h}(\vec{r})\right\rangle = (1-3D_\lambda^{(2)})\left\langle \lambda'(\vec{r})\varepsilon'_{kl}(\vec{r})\varepsilon'_{\phi h}(\vec{r})\right\rangle + D_\lambda^{(3)}\left\langle \varepsilon'_{kl}(\vec{r})\varepsilon'_{\phi h}(\vec{r})\right\rangle,
\end{aligned}$$

where $D_\lambda^n = (1-p)^n p + (-p)^n(1-p)$ is the central n-order moment.

One of the techniques which is used in different variations of the stochastic approach assumes that the integrals of the SBVP solution can be expressed via second derivatives of the Green's function using Stieltjes transformation. The Stieltjes equal transformation of two functions $f(x)$ и $g(x)$ over an interval (a,b) is defined as [34]:

$$\Psi(t) \equiv \int_a^b f(t-x)g'(x)dx \equiv \int_a^b g(t-x)f'(x)dx.$$

The elastic case solution in the second approximation will take the following form:

$$\begin{aligned}
u'^{(2)}_{i,j}(\vec{r}) = e_{kl}\bar{C}_{mnkl}\int_{V_1} G_{im,jn}(\vec{r},\vec{r}_1)\lambda'(\vec{r}_1)dV_1\\
+\ e_{oq}\bar{C}_{mnkl}\bar{C}_{fsoq}\int_{V_1}\int_{V_{11}} G_{im,jn}(\vec{r},\vec{r}_1)G_{kf,ls}(\vec{r}_1,\vec{r}_{11})\lambda'(\vec{r}_1)\lambda'(\vec{r}_{11})dV_{11}dV_1.
\end{aligned} \tag{49}$$

Such transformation was performed in [13] in order to decompose the Green's function second derivative into singular and formal parts $G_{kf,ls}(\vec{r},\vec{r}_1) = G^{(s)}_{kf,ls}(\vec{r},\vec{r}_1) + G^{(f)}_{kf,ls}(\vec{r},\vec{r}_1)$, for which exact expressions were obtained:

$$G^{(s)}_{kf,ls}(\vec{r},\vec{r}_1) = -\frac{\delta(\vec{r}-\vec{r}_1)}{3\langle\mu\rangle}\left(\delta_{kf}\delta_{ls} - \frac{1}{5}\kappa\delta_{kfls}\right) = \delta(\vec{r}-\vec{r}_1)g_{kfls}, \tag{50}$$

$$G^{(f)}_{kf,ls}(\vec{r},\vec{r}_1) = \frac{1}{8\pi\langle\mu\rangle|\vec{r}-\vec{r}_1|^3}\Big((2-\kappa)\delta_{kf}(3n_f n_s - \delta_{fs}) \\ - \kappa\big[3(n_{kf}n_{ls} + n_{kl}n_{fs} + n_{ks}n_{fl} + n_{fs}n_{kl} + n_{fl}n_{ks}) - 2I_{kfls} - 15n_k n_f n_l n_s\big]\Big), \tag{51}$$

where $\kappa = \frac{\langle\lambda+\mu\rangle}{\langle\lambda+2\mu\rangle}$, $n_i = \frac{r_i - r_{1i}}{|\vec{r}-\vec{r}_1|}$, $n_{ij} = n_i n_j$, $I_{kfls} = {}^1\!/_2\big(\delta_{kl}\delta_{fs} + \delta_{ks}\delta_{fl}\big)$.

Then the integrals with the Green's function can be represented as a sum, for example:

$$\int\limits_V G_{kf,ls}(\vec{r},\vec{r}_1)K^{(2)}_\lambda(\vec{r},\vec{r}_1)dV = \int\limits_{V_0} G^{(s)}_{kf,ls}(\vec{r},\vec{r}_1)K^{(2)}_\lambda(\vec{r},\vec{r}_1)dV \\ + \int\limits_{V-V_0} G^{(f)}_{kf,ls}(\vec{r},\vec{r}_1)K^{(2)}_\lambda(\vec{r},\vec{r}_1)dV,$$

where V_0 is singularity area.

Using the definition of the generalized Dirac function $\int \delta(\vec{r}-\vec{r}_1)f(\vec{r}_1)d\vec{r}_1 = f(\vec{r})$, the singular summand becomes a constant value:

$$\int\limits_V G_{kf,ls}(\vec{r},\vec{r}_1)K^{(2)}_\lambda(\vec{r},\vec{r}_1)dV = g_{kfls}D^{(2)}_\lambda + \int\limits_{V-V_0} G^{(f)}_{kf,ls}(\vec{r},\vec{r}_1)K^{(2)}_\lambda(\vec{r},\vec{r}_1)dV. \tag{52}$$

This technique is used in the singular approach [13], which assumes the formal part of Eq. (52) negligible, leaving only the singular part and thus avoiding multidimensional integration.

3 Description of Stochastic Microstructure

3.1 Correlation Functions

Many publications were devoted to investigation of dependence of mechanical and physical properties of composites on the parameters of their microstructure [35–42]. The statistical methods, which employ the multi-point correlation functions for description of inhomogeneities' interaction, have become widespread in the micromechanics of composites with random structure. Accuracy of the statistical characteristics depends on the order of the structural moment functions used in the equations and the SBVPs solution.

The methodology based on correlation functions is also widely used for restoration and verification of microstructure models with the results of the analysis of the real materials samples. For example, Baniassadi and Ahzi [43] proposed a mathematical relationship of the correlation functions of different orders among themselves. The results of three-dimensional composites and nanocomposites models reconstruction using correlation functions were presented in the works of Sheidaei et al. [44–46], Li et al. [47], Liu and Ghosal [48], Liu et al. [39], Torquato [49–52] and others.

The n-order correlation function for the two-phase indicator function pulsation has the following expression:

$$K_{\lambda}^{(n)}(\vec{r},\vec{r}_1,\ldots,\vec{r}_n) = \langle \lambda'(\vec{r})\lambda'(\vec{r}_1)\ldots\lambda'(\vec{r}_n)\rangle. \tag{53}$$

Indicator function $\lambda(\vec{r})$ is statistically homogeneous and isotropic; thus, the correlation functions $K_{\lambda}^{n}(\vec{r},\vec{r}_1,\ldots,\vec{r}_n)$ depend only on a distance between points $|\vec{r}-\vec{r}_n|$. Values of correlation functions can be obtained in dependence of steps $|\vec{r}-\vec{r}_n|$, $|\vec{r}_m-\vec{r}_n|$ with mesh methods: the modeled or experimentally analyzed stochastic structure fragment is patterned with a mesh, values of indicator function possess 0 or 1 depending on presence of the matrix or one of the inclusions in mesh point.

While obtaining values of correlation functions all the distances between points are accepted equal and increasing proportionally:

$$|\vec{r}-\vec{r}_1| = |\vec{r}-\vec{r}_2| = |\vec{r}_1-\vec{r}_2| = \cdots = |\vec{r}_m-\vec{r}_n| = \Delta\vec{r}$$

In order to accomplish this condition, the cubic mesh (Fig. 1a) is used for the second and fourth order correlation functions, the hexagonal mesh (Fig. 1b) is suitable for third order functions, the fifth order correlation functions (Fig. 1c) were built on the centered cubic mesh.

In further calculations it is more convenient to use normalized by the central n-order moment correlation functions:

$$f_{\lambda}^{n}(\vec{r},\vec{r}_1,\vec{r}_2,\ldots) = \frac{K_{\lambda}^{n}(\vec{r},\vec{r}_1,\vec{r}_2,\ldots)}{D_{\lambda}^{n}}, \tag{54}$$

The step $\Delta\vec{r}$ is normalized by the averaged minimal distance between inclusions h_{avg}.

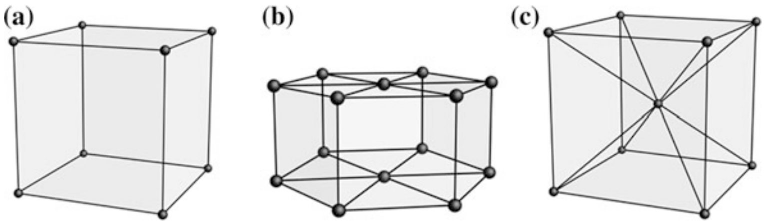

Fig. 1 Schematic representation of a mesh cell

Theoretically, the infinite number of the correlation functions completely characterizes the geometry of the random structure of composites. Besides, some of the functions have the geometrical sense. For instance, a second-order function describes relative positions of inclusions; a third-order function characterizes the form of inclusions; a fourth-order function characterizes clustering of inclusions as well as their size distribution. In other words, the correlation functions allow understanding of influence of inclusions on each other.

3.2 Modeling of Two-Component Polydisperse Microstructure with Spherical Inclusions

There are two main types of structure of the two-component composite material. First is a statistical mixture, when the components of the composite form interpenetrating frameworks, each of which has its own individual bearing capacity. Second is when the composite materials are formed by matrix reinforced with spherical, lamellar, fibrous, elliptic inclusions. Multicomponent composite may also have mixed types of structures.

The problem of modeling of heterogeneous structures is historically based on the mechanics of liquids and is tightly connected with the problem of statistical description of behavior of a system of particles [53, 54]. Structures with random arrangement of spheres had been studied actively since they can create models of simple liquids, concentrated suspensions, amorphous and powder materials.

The advances in modeling dense disordered structures were achieved with the two main groups of methods: sequential synthesis and dynamic methods. For example, [55] describes a consistent method when each new inclusion (sphere) is placed at the point closest to the first so that it comes into contact with the existing inclusions. Intersection is controlled by testing the distance between the centers. Later this method was modified by introduction of a parameter characterizing the filling of the area bounded by the tetrahedron [56]. In [57] an algorithm that allows to control the ordering of growing clusters of inclusions was proposed. Another type of sequential methods is based on a model when each new inclusion is "thrown" on a top of an arbitrary point on the surface of existing inclusions located at the "bottom" of the virtual box. This method of synthesis is used in [58–60].

The methods described above belong to a class of static method that presumes that inclusions are not being moved after having been generated. Dynamic models propose reorganization of the entire structure, depending on interaction of inclusions with each other [61]. According to the regrouping method, to each of N randomly distributed in the volume points a radius of the sphere as well as an arbitrary vector are assigned. Each sphere is moved upwards until it reaches the other. Then, the radius is increased and the process is being repeated until further increase in the radius or the movement leads to intersection of spheres. Various modifications of this method are found, for example, in [62–65].

A dense structures generation method is proposed in [55]. According to it each successive sphere "moves" in the direction of the initial one along a straight line connecting their centers, until contacting the already existing ones. In more complex models a system of differential equations is solved for specifying movements and detecting intersections [64].

There is also a group of algorithms of dynamic synthesis of polydisperse structures in which the desired density of inclusions is achieved by changing the radii of spheres. In some models, each inclusion is subject to small random movements, regardless of position of the neighbor inclusions. Thus the best position for inclusions can be found in order to achieve the denser packing [66, 67].

In addition, the models of inhomogeneous structures can be obtained by Monte Carlo methods. Some models of random structures are based on periodic lattices. Two of them are described in [68]: according to the first, inclusion centers are aligned with randomly selected lattice nodes, while in the second the physical-mechanical properties of each cell at random were assigned to the phases of the composite.

In this study geometry of the microstructure has been defined using 3D modelling. Structures with polydisperse spherical inclusions were synthesized in Wolfram Mathematica. Several algorithms of synthesis ensuring that generated spheres don't overlap were used. First is Hard-Core Model, also called random sequential adsorption model [69]. Spheres with radius r_i are placed one by one with the centre positions $X = (x_i, y_i, z_i)$. Coordinates of the centre are distributed uniformly inside the cubic region with side a, radius of the spheres are distributed uniformly inside the fixed region $[r_{\min}, r_{\max}]$. If the new sphere doesn't overlap any existing one, its position becomes fixed. Otherwise, it is rejected and another random centre position is generated. The process is finished when either assigned volume fraction is achieved or when no more particles can be added. This method generates 3D structures with volume fraction up to 38 % [70].

The Hard-Core Model can be modified for dense packing structures. The difference is that radii of new generated spheres are not being distributed randomly within the specified range but are assigned consequently from the maximum value of the range to the minimum one. When new sphere of the current radius can't be added, the radius is being reduced and the procedure continues. As in the first model, the process finishes when either assigned volume fraction is achieved or when no more particles of the smallest radius of the range can be added.

The explicit forms of normalized correlation functions are used for the formulas of the statistical characteristics. The analysis of different approximating expressions has been performed and the following expression types were chosen for second-order and higher-order correlation functions:

$$f_{\lambda}^{(n)}(\vec{r},\vec{r}_1,\vec{r}_2,\ldots,\vec{r}_n)=\exp\left(-c_1\frac{\Sigma_n}{h_{avg}}\right)\left[\cos\left(c_2\frac{\Sigma_n^{(2)}}{h_{avg}^2}\right)\right], \tag{55}$$

where $\Sigma_n=|\vec{r}-\vec{r}_1|+|\vec{r}-\vec{r}_2|+\cdots+|\vec{r}-\vec{r}_n|+|\vec{r}_1-\vec{r}_2|+\cdots+|\vec{r}_{n-1}-\vec{r}_n|$, $\Sigma_n^{(2)}=|\vec{r}-\vec{r}_1|^2+|\vec{r}-\vec{r}_2|^2+\cdots+|\vec{r}-\vec{r}_n|^2+|\vec{r}_1-\vec{r}_2|^2+\cdots+|\vec{r}_{n-1}-\vec{r}_n|^2$, c_i are approximation coefficients, which are being calculated for the correlation functions of every order for each realization of 3D composite structure, h_{avg} is averaged by a number of inclusions distance between the centre of the inclusion to the nearest inclusion.

Computational experiments have shown that the deviation between obtained values for correlation functions of third order (and higher) and the diagram of approximating expressions for them is about 1–1.5 %, while for second order correlation function it reaches 7 %. Diagrams for second order functions for some structures may have a region of negative values which indicates the periodicity of the structure. This feature is well approximated by the class of expressions [10, 24] with two periodic functions and three approximating coefficients:

$$f_{\lambda}^{(2)}(\vec{r},\vec{r}_1)=\exp(c_1,\vec{r},\vec{r}_1)[\cos(c_2,\vec{r},\vec{r}_1)+c_3\sin(c_2,\vec{r},\vec{r}_1)],$$

The following expression is offered in this work for the second order correlation functions:

$$f_{\lambda}^{(2)}(\vec{r},\vec{r}_1)=\exp\left(-c_1\frac{|\vec{r}-\vec{r}_1|}{h_{avg}}\right)\left[\cos\left(c_2\frac{|\vec{r}-\vec{r}_1|}{h_{avg}}\right)+c_3\sin\left(c_2\frac{|\vec{r}-\vec{r}_1|^2}{h_{avg}^2}\right)\right] \tag{56}$$

4 Examples of the Methodology Implementation

4.1 Numerical Integration Techniques

The mixed moments in (43)–(45) form a superposition of multidimensional integrals, which were calculated in Wolfram Mathematica using parallel computations.

Integration over the RVE in the formulas containing the Green's function can be replaced by integration over the statistical dependence of the random field of structural elastic moduli, or, in other words, the region where the values of the correlation functions are nonzero. Therefore, the upper limit of integration is equal to the radius of statistical dependence.

Integrals containing the Green's function and correlation functions in general can be denoted as follows:

$$\begin{aligned} I_{1,2,11,21}^{(\vec{r},\vec{r}_1,\vec{r}_2,\vec{r}_{11},\vec{r}_{21})} = D_\lambda^{(5)} \int\limits_{V_1} \int\limits_{V_2} \int\limits_{V_{11}} \int\limits_{V_{21}} & \left(G_{im,jn}^{(f)}(\vec{r},\vec{r}_1) + G_{jm,in}^{(f)}(\vec{r},\vec{r}_1)\right) \\ & \times \left(G_{\alpha\gamma,\beta\eta}^{(f)}(\vec{r},\vec{r}_2) + G_{\beta\gamma,\alpha\eta}^{(f)}(\vec{r},\vec{r}_2)\right) G_{kf,ls}^{(f)}(\vec{r}_x,\vec{r}_{11}) \\ & \times G_{\phi v,hw}^{(f)}(\vec{r}_x,\vec{r}_{21}) f_\lambda^{(5)}(\vec{r},\vec{r}_1,\vec{r}_2,\vec{r}_{11},\vec{r}_{21}) dV_{21} dV_{11} dV_2 dV_1, \end{aligned} \tag{57}$$

where the subscripts in parentheses indicate the presence of the corresponding factors containing the Green's function in the integral, superscripts determine the order and the argument of the correlation functions. The lower index $\vec{r}_x$ of the radius vector is uniquely determined by the integrands factors and the rules of the Dirac compression. The multiplicity of the integral is determined by the number of independent variables $\vec{r}$. The absence of variables in brackets means that there are no correlation functions under the integral.

Calculation of the statistical characteristics and their constituent integrals was performed in Wolfram Mathematica, which offers a number of different techniques for advanced numerical integration. Each method is defined with strategy and integration rules, combination of which specifies the appropriate method for the integrand.

Integration strategies determine partitioning the integration domain into subdomains. Each element can have its integrand and the corresponding integration rule defining the points in which the value of the integral is calculated. Integration rules are used for calculation of the integral value and the error estimation in subdomains using usually weighted sums. For each point x_i a weighting coefficient w_i is assigned, then the integral error estimation is performed using a weighted sum $\sum w_i f(x_i)$.

There are adaptive and non-adaptive integral strategies [71, 72]. Adaptive strategies are aimed to find the problem areas of integration and concentrate computing effort (partition into subdomains) on them. Non-adaptive strategies consequently increase the number of elements in the entire integration region. Adaptive strategies include the following components: integration rule for calculating the value of the integral and error estimation in the region; method that defines a partition of the domain into subregions; criterion for the termination of the integration.

Global adaptive strategy presumes that from all of the subdomains of the original domain of integration the subregion with the highest error estimation is selected and is divided in half. Then the value of the integral and error estimation are being calculated for each half, and the procedure is repeated for the entire set of subregions. After a bisection of a region and the subsequent integration over the new subregions, new global integral and global error estimates are computed, which are sums of the integral and error estimates of all regions. The procedure stops when the following condition is true:

$$
\begin{aligned}
&\mathit{global\,error\,estimation} \ \leq \ \mathit{global\,integral\,value} \times 10^{-pg} \\
&\vee \ \mathit{global\,error\,estimation} \leq 10^{-ag},
\end{aligned}
$$

where *pg* is given precision, *ag* is given accuracy. The procedure is also being interrupted when the number of consecutive partitions exceeds a predetermined number, or when the global error begins to fluctuate wildly. It is expected that the global error should decrease monotonically with increasing of the number of areas.

Local adaptive strategy has an initial and recursive procedure. The initial procedure computes the error in subregions, obtained from division of the region of integration on the first step. Recursive procedure computes the value of the integral and the error in each subdomain using the specified rule of integration. If the error in subregions significantly larger than the initial error, the recursive procedure continues, but only for the specific subdomain. The error for each of the primary subregions is defined as the sum of errors obtained by implementing the recursive procedure in the subregion. Recursive procedure stops when the maximum number of steps of the partition division is reached, or if an integral error in the subdomain is negligible.

To calculate the integrals in the expressions for the statistical characteristics and containing the first derivative or a formal part of the second derivative of the Green's function, the possibility of using a combination of global or local adaptive strategy in conjunction with the trapezoidal rule or multidimensional integration was investigated. Formal integration region in the calculation of integrals with the second derivative of the Green's function was set by excluding the integration points in which the integrand has a singularity.

The first derivatives of the Green's function also have the region of the singularity. For the integration of expressions with the first derivatives the Duffy coordinate transformation was implemented [73]. Its principle is that the integral over the square, cube or hypercube with the singularity in one corner, is replaced by an integral with a singularity along the line.

With global adaptive strategy the integrals convergence has been slow or oscillatory; increasing the number of partitions of an integrable region did not improve it. Local adaptive strategy achieved better convergence of the integral, but with applying trapezoidal rule the integrals converged slower than with the multi-dimensional rule, while the result within the specified accuracy was equal. Thus, for the class of integrands containing derivatives of the Green's function with singularity and the correlation functions, the method combining local adaptive strategy and multi-dimensional integration rule has been chosen.

4.2 Numerical Results in Elastic Case

As an example of the method implementation in the elastic case, the porous composites with different inclusions volume concentration (p = 0.15, 0.20, 0.25, 0.30) have been studied with the following properties of the matrix:

$E_m = 2 \times 10^{11}$ Pa, $\nu_m = 0.3$. Geometrical parameters of the model microstructures are shown in Table 1. All the widths and sizes are presented in some conditional values as the considered method and all the equations don't depend on a scale of structures. The matrix was considered to be homogenous and isotropic.

Figure 2 shows some examples of synthesized polydisperse structures of the composite with different inclusions volume concentration. Figures 3, 4, 5 and 6 contain the correlation functions for these structures.

Coefficients of correlations functions' approximating expressions for the considered structures are presented in the Table 2. Automated procedure using non-linear conjugate gradient method for calculation of the coefficients was implemented in Wolfram Mathematica.

The following states of strain of the RVE were studied: uniform extension, simple shear and uniaxial tension. Calculations were performed using the second approximation of the SBVP solution.

In the case of uniform extension, non-zero components of the tensor of macroscopic deformations e_{ij} has been defined in the following way: $e_{11} = e_{22} = e_{33} = 10^{-6}$. The numerical results for deformation fields' statistical characteristics in the matrix are presented in the Table 3. Here and further only non-zero components of the tensors are shown.

Table 1 Geometrical parameters of synthesized structures

Inclusions volume concentration, P	Number of inclusions, N	Minimal radius of inclusion	Maximal radius of inclusion	h_{avg} value
0.15	1400	4.0003	7.9927	17.2833
0.20	1047	4.0005	11.9985	18.9941
0.25	1193	4.0043	15.9450	18.2389
0.30	976	4.0029	27.3491	19.5464

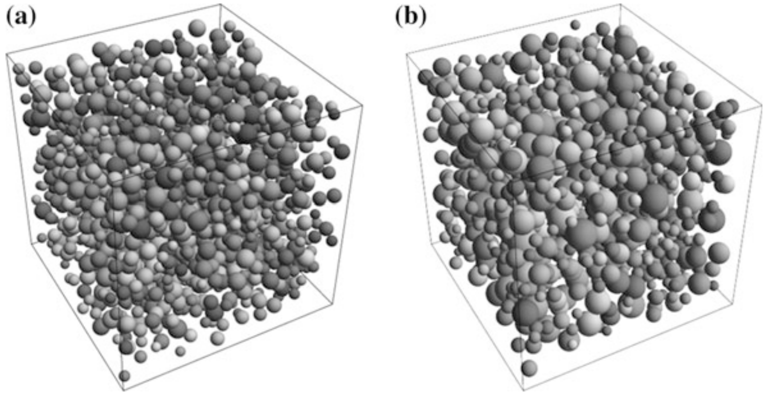

Fig. 2 Synthesized structures with various inclusions volume concentration: **a** $p = 0.15$, **b** $p = 0.25$

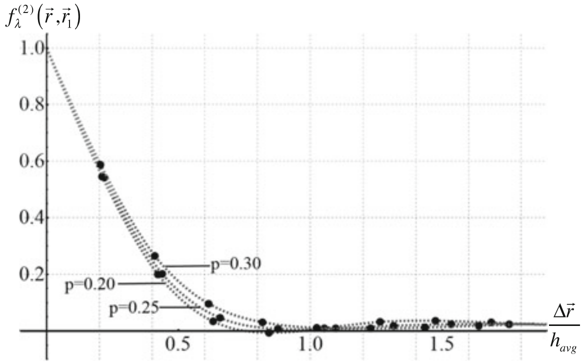

Fig. 3 Second order normalized correlation functions

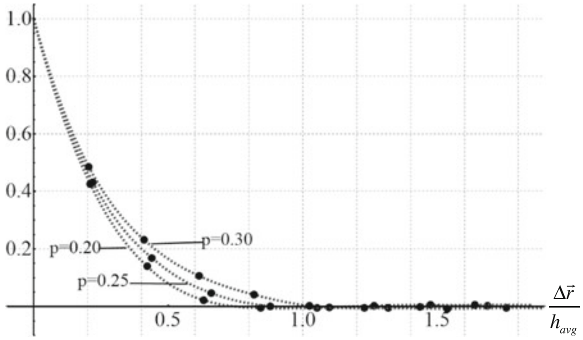

Fig. 4 Third order normalized correlation functions

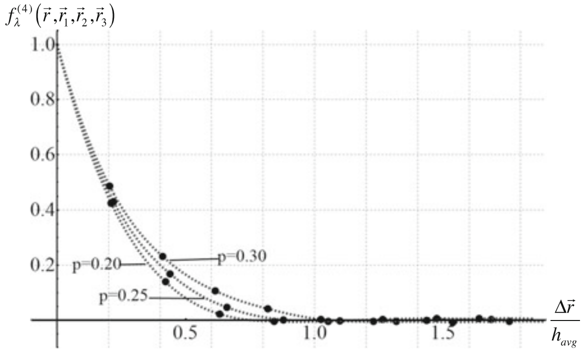

Fig. 5 Fourth order normalized correlation functions

Components of macroscopic deformation tensor in the simple shear case has been set as follows: $e_{12} = e_{21} = \alpha$, $\alpha = 10^{-6}$. The results are demonstrated in Table 4.

In the case of uniaxial tension the state of strain is defined by components of the macroscopic stresses tensor: $\sigma_{11}^{*} = 1 \times 10^{6}$ Pa. In order to set the boundary

Fig. 6 Fifth order normalized correlation functions

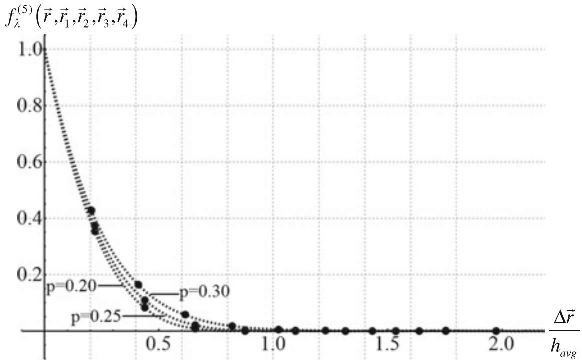

Table 2 Coefficients of approximating expressions for the correlation functions

		Second-order correlation function	Third-order correlation function	Fourth-order correlation function	Fifth-order correlation function
Structure with $p = 0.15$	c_1	51.4459	5.4650	5.5720	5.7638
	c_2	60.8700	7.6007	6.4085	6.6567
	c_3	4.8205	–	–	–
Structure with $p = 0.20$	c_1	52.5380	4.1242	4.7187	4.9281
	c_2	63.0195	3.1281	3.8203	3.9610
	c_3	6.1731	–	–	–
Structure with $p = 0.25$	c_1	52.3713	3.8509	4.2839	4.5152
	c_2	55.3549	2.0138	2.5263	2.6647
	c_3	6.5165	–	–	–
Structure with $p = 0.30$	c_1	57.4423	3.5150	4.0205	4.2141
	c_2	53.8207	1.2450	1.5240	1.5690
	c_3	8.0559	–	–	–

Table 3 Statistical characteristics of stress and strain fields in the matrix in the case of uniform extension

Statistical characteristics in matrix	$p = 0.15$	$p = 0.20$	$p = 0.25$	$p = 0.30$
Average strains, $\times 10^{-6}$				
$<\varepsilon_{11}>_M = <\varepsilon_{22}>_M = <\varepsilon_{33}>_M$	0.98664	0.98126	0.97533	0.96833
Average stresses, MPa				
$<\sigma_{11}>_M = <\sigma_{22}>_M = <\sigma_{33}>_M$	0.38843	0.49063	0.32426	0.29471
Dispersions of strains, $\times 10^{-12}$				
$<\varepsilon'_{11}\varepsilon'_{11}>_M = <\varepsilon'_{22}\varepsilon'_{22}>_M = <\varepsilon'_{33}\varepsilon'_{33}>_M$	0.03203	0.04029	0.05089	0.06907
$<\varepsilon'_{12}\varepsilon'_{12}>_M = <\varepsilon'_{13}\varepsilon'_{13}>_M = <\varepsilon'_{23}\varepsilon'_{23}>_{3M}$	0.23549	0.30662	0.38246	0.50065
Dispersions of stresses, MPa^2				
$<\sigma'_{11}\sigma'_{11}>_M = <\sigma'_{22}\sigma'_{22}>_M = <\sigma'_{33}\sigma'_{33}>_M$	0.00730	0.01426	0.02267	0.06907
$<\sigma'_{12}\sigma'_{12}>_M = <\sigma'_{13}\sigma'_{13}>_M = <\sigma'_{23}\sigma'_{23}>_M$	0.00274	0.00263	0.00229	0.00193

Table 4 Statistical characteristics of stress and strain fields in the matrix in the case of simple shear

Statistical characteristics in matrix	p = 0.15	p = 0.20	p = 0.25	p = 0.30
Average strains, $\times 10^{-6}$				
$<\varepsilon_{12}>_M$	0.98991	0.98507	0.98078	0.97561
Average stresses, MPa				
$<\sigma_{12}>_M$	0.13254	0.12535	0.11805	0.11070
Dispersions of strains, $\times 10^{-14}$				
$<\varepsilon'_{12}\varepsilon'_{12}>_M$	1.78269	2.32009	2.90176	3.79986
Dispersions of stresses, MPa^2 $\times 10^{-2}$				
$<\sigma'_{12}\sigma'_{12}>_M$	0.04742	0.09379	0.15996	0.23979

conditions in displacements it is necessary to obtain the strain tensor from the stress tensor using the tensor of effective elasticity modulus C^*:

$$\begin{aligned} e_{11} &= \frac{\sigma_{11}^*(C_{1111}^* + C_{1122}^*)}{(C_{1111}^{*2} + C_{1111}^* C_{1122}^* - 2C_{1122}^{*2})}, e_{22} = e_{33} \\ &= -\frac{\sigma_{11}^* C_{1122}^*}{(C_{1111}^{*2} + C_{1111}^* C_{1122}^* - 2C_{1122}^{*2})}, \end{aligned}$$

The results for the calculation of uniaxial tension case are shown in Table 5.

Table 5 Statistical characteristics of stress and strain fields in the matrix in the case of uniaxial tension

Statistical characteristics in matrix	p = 0.15	p = 0.20	p = 0.25	p = 0.30
Average strains, $\times 10^{-6}$				
$<\varepsilon_{11}>_M$	6.85339	7.70482	8.72686	9.96099
$<\varepsilon_{22}>_M = <\varepsilon_{33}>_M$	−1.93234	−2.12747	−2.35795	−2.63307
Average stresses, MPa				
$<\sigma_{11}>_M$	1.17675	1.2500	1.33300	1.42800
$<\sigma_{22}>_M = <\sigma_{33}>_M$	0	0	0	0
Dispersions of strains, $\times 10^{-12}$				
$<\varepsilon'_{11}\varepsilon'_{11}>_M$	0.26113	0.42816	0.70831	1.2568
$<\varepsilon'_{12}\varepsilon'_{12}>_M = <\varepsilon'_{13}\varepsilon'_{13}>_M$	0.76951	1.29773	2.14182	3.76175
$<\varepsilon'_{23}\varepsilon'_{23}>_M$	0.36306	0.62213	1.02754	1.79149
$<\varepsilon'_{22}\varepsilon'_{22}>_M = <\varepsilon'_{33}\varepsilon'_{33}>_M$	0.00057	0.00118	0.00173	0.00859
Dispersions of stresses, MPa^2				
$<\sigma'_{11}\sigma'_{11}>_M$	0.03985	0.11527	0.25570	0.56425
$<\sigma'_{12}\sigma'_{12}>_M = <\sigma'_{13}\sigma'_{13}>_M$	0.00894	0.01111	0.01275	0.01437
$<\sigma'_{23}\sigma'_{23}>_M$	0.00421	0.00531	0.00609	0.00681
$<\sigma'_{22}\sigma'_{22}>_M = <\sigma'_{33}\sigma'_{33}>_M$	0.00161	0.00215	0.00284	0.00417

4.3 Numerical Results in Elastoplastic Case

As an example of solution in elastoplastic case, the porous composites with spherical polydisperse inclusions and physically nonlinear isotropic matrix with linear hardening were considered.

Nonelastic behaviour of the matrix of such composites is modelled using the relations of the theory of small elastoplastic deformations. In the framework of the theory, the shear modulus is a function only of the second invariant of the microscopic stress tensor. Matrix has the elastic region and the region with linear hardening, the transition point corresponds to the yield stress:

$$\mu_M(j_\varepsilon^{(2)}) = \begin{cases} j_\varepsilon^{(2)} < j_{\varepsilon_\mathrm{T}}^{(2)}, & G_M \\ j_\varepsilon^{(2)} > j_{\varepsilon_\mathrm{T}}^{(2)}, & G_M \left[\frac{G'_M}{G_M} - \frac{(G'_M - G_M)}{G_M} \frac{j_{\varepsilon_T}^{(2)}}{j_\varepsilon^{(2)}} \right] \end{cases} \tag{58}$$

where G_M is shear modulus of matrix, G'_M is hardening modulus of matrix, $j_{\varepsilon_T}^{(2)}$ is the limiting value of the second invariant of strain tensor, which is corresponding to the elastic limit.

It was assumed that the matrix is incompressible, thus the bulk modulus K_M remains constant during the deformation process.

The simple shear state of strain has been chosen as the macroscopic loading conditions. The following values of non-zero components of the tensor ε_{ij}^* in the boundary conditions (18) were defined: $\varepsilon_{12}^* = \varepsilon_{21}^* = 10^{-6}$. Taking into account the formulas for deviator parts, invariants of stress and strain tensors for the simple shear case can be expressed through the mean values of stress and strain fields in matrix:

$$\Lambda_M = \sqrt{2\langle\varepsilon_{12}\rangle_M\langle\varepsilon_{12}\rangle_M}, \quad j_\sigma^{(2)}(\Lambda_M) = \sqrt{2\langle\sigma_{12}\rangle_M\langle\sigma_{12}\rangle_M},$$

The following properties of the matrix were taken:

$G_M = 44.2$ GPa, $G'_M = 14.3$ GPa,

$K_M = 132.2$ GPa, $j_{\varepsilon_T}^{(2)} = 6.37 \times 10^{-4}$.

Geometrical parameters of the considered microstructures are shown in Table 6. All the widths and sizes are presented in some conditional values as the considered method and all the equations don't depend on a real scale of structures. The structures are visualized on Fig. 7.

Coefficients of approximating expressions for the correlations functions are presented in Table 7. Automated procedure using nonlinear conjugate gradient method for calculation of the coefficients was implemented in Wolfram Mathematica.

Result of stress-strain diagram for mean stress in matrix is presented on Fig. 8 for all the studied structures.

Table 6 Geometrical parameters of the synthesized structures

Inclusions volume fraction, p	Number of inclusions, N	Minimal radius of inclusion	Maximal radius of inclusion	Average distance to centre of nearest inclusion, h_{avg}
0.20	1047	4.0	12.0	18.9941
0.30	976	4.0	27.0	19.5463
0.40	1456	5.0	9.0	18.8490
0.50	2000	4.0	14.0	16.0692
0.60	1164	4.0	39.0	17.8466
0.70	3959	5.0	99.0	22.0742

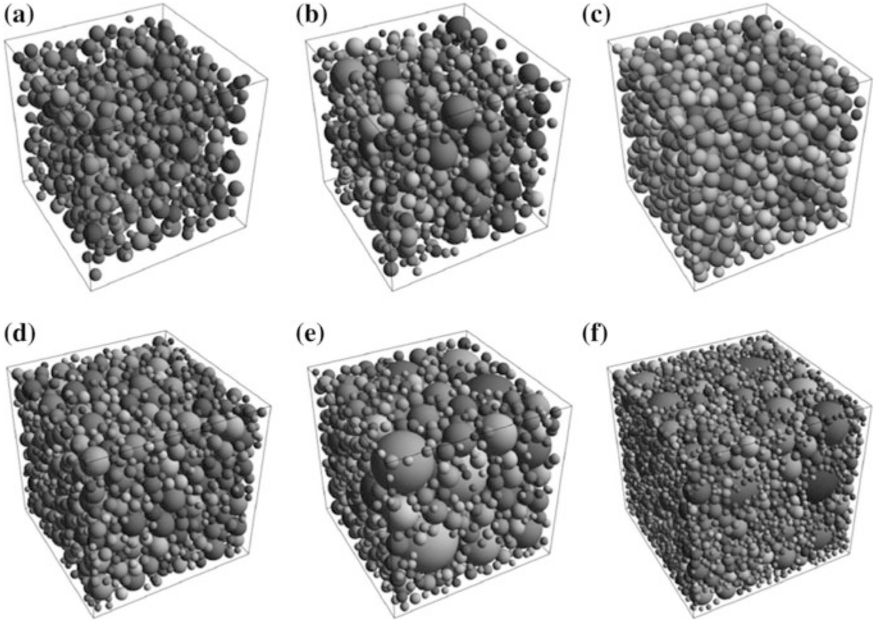

Fig. 7 Synthesized structures with various inclusions volume concentration: **a** $p = 0.20$, **b** $p = 0.30$, **c** $p = 0.40$, **d** $p = 0.50$, **e** $p = 0.60$, **f** $p = 0.70$

Figures 9 and 10 display diagrams for dispersions of stress and strain in matrix in dependence of macroscopic stress.

Figure 11 shows how the shear modulus of matrix changes during deformation process.

With the increasing of volume fraction the value of stress in matrix decreases (Fig. 8). According to Fig. 11, materials with higher porosity undergo less plastic deformations as the value of the shear modulus increases with growth of volume fraction.

Table 7 Coefficients of approximating expressions for the correlation functions

		Second-order correlation function	Third-order correlation function	Fourth-order correlation function	Fifth-order correlation function
Structure with $p = 0.20$	c_1	45.5468	89.7127	88.2568	17.7135
	c_2	−51.0195	−1692.1167	−1321.4202	−281.2605
	c_3	6.2077	–	–	–
Structure with p = 0.30	c_1	44.4819	60.3032	61.2485	12.2292
	c_2	38.9160	312.6635	32.0872	−37.3740
	c_3	11.0466	–	–	–
Structure with $p = 0.40$	c_1	52.0550	85.5348	88.2012	17.8265
	c_2	−68.1599	−2432.3143	−973.9423	−230.8578
	c_3	−7.4854	–	–	–
Structure with $p = 0.50$	c_1	38.8580	59.7961	63.8917	12.9324
	c_2	−45.6168	−859.4112	−349.0060	−97.3925
	c_3	−5.1808	–	–	–
Structure with $p = 0.60$	c_1	37.8191	114.0797	58.8228	19.2026
	c_2	41.4580	−5593.5067	−5.8723	−517.9125
	c_3	15.4891	–	–	–
Structure with $p = 0.70$	c_1	30.1759	117.2362	92.0882	22.0314
	c_2	−38.6264	−4373.0674	6.4212	−6.3527
	c_3	11.9840	–	–	–

Fig. 8 Dependence of mean stress in matrix on macroscopic strain

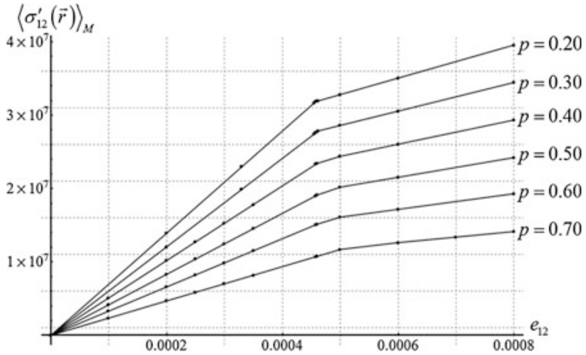

Materials with different hardening modulus G'_m have been studied for elasto-plastic matrix of composites with inclusions volume fraction p = 0.30. Figure 12 shows the different behaviour of mean values of stress in matrix for these materials. As predictable, the material with higher hardening reveals less nonlinearity.

These numerical results demonstrate the possibility of applying the methods of stochastic mechanics for analyzing the microscopic stress and strain fields in the

Fig. 9 Dependence of stress dispersion in matrix on macroscopic strain

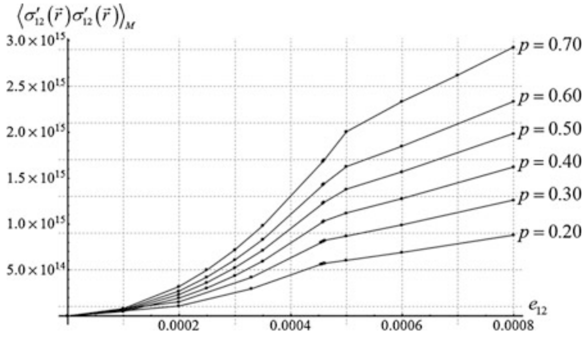

Fig. 10 Dependence of strain dispersion in matrix on macroscopic strain

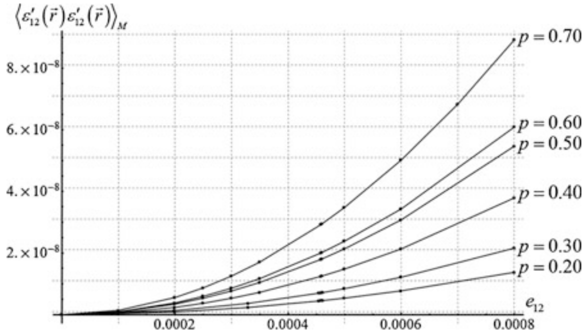

Fig. 11 Dependence of shear modulus of matrix on macroscopic strain

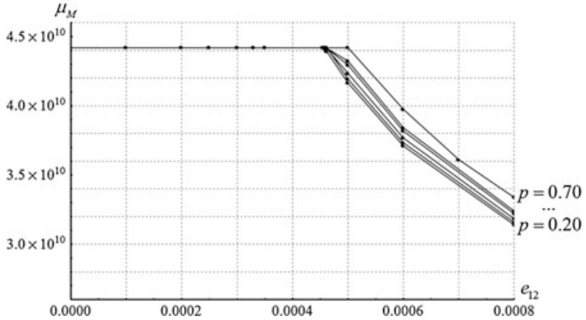

components of structurally inhomogeneous materials. The obtained statistical characteristics allow defining the characteristics of a certain class of materials without having to calculate large number of realizations of material's random microstructure, which may reduce the computational cost required to solve the problems of the composites micromechanics.

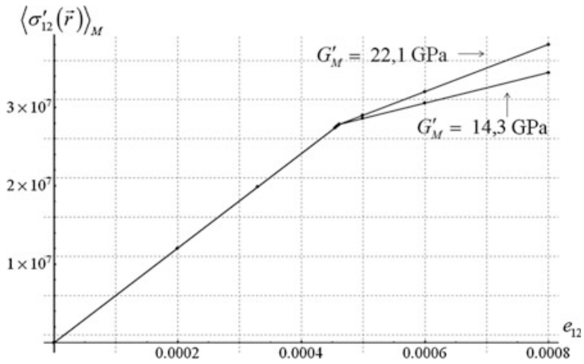

Fig. 12 Dependence of mean stress in matrix on macroscopic strain for materials with different hardening modulus

5 Conclusions

This work contains the results of development of stochastic methods based on the Green's function and statistical moments approach. The analytical expressions for microstructural stresses and strains moments in components of heterogeneous solid media were obtained using the first and second approximation of the SBVP solution in elastic and elastoplastic case. It has been shown that the integral equations depend on multipoint structural correlation functions up to fifth order. Two types of the approximating expressions were offered for the correlation functions.

The porous composites were studied to demonstrate the implementation of methodology. Their matrix was considered isotropic and physically nonlinear. In order to obtain values of the correlation functions, 3D random structures with spherical inclusions have been synthesized. The inclusions volume fraction of the considered structures ranges from 20 to 70 %. The correlation functions values as well as the coefficients of their approximating expressions were calculated for each of these structures. In the elastic case numerical results for statistical characteristics were presented in different states of strain. In the elastoplasitc case the diagrams of dependence of mean value and dispersion of stress in matrix on macroscopic stress, as well as other diagrams characterising the deformation process, have been obtained for a simple shear loading.

The developed methods of microstructure modelling and stochastic mechanics boundary value problem solution can be used for a comparative analysis of the impact of various structural parameters on the statistical characteristics of the stress field in order to create materials with predetermined set of properties and to assess their failure probability.

Acknowledgments This work was supported by the Russian Foundation for Basic Research (project 14-01-96024) and grant of the President of Russian Federation for state support of young Russian scientists (MK-5172.2015.1).

References

1. Torquato, S.: Random Heterogenous Materials, Microstructure and Macroscopic Properties. Springer, New York (2001)
2. Buryachenko, V.: Micromechanics of Heterogeneous Materials. Springer, New York (2007)
3. Kaminski, M.M.: Computational Mechanics of Composite Materials. Springer, New York (2005)
4. Kanouté, P., Boso, D.P., Chaboche, J.L., Schrefler, B.A.: Multiscale methods for composites: a review. Arch. Comput. Methods. Eng. **16**, 31–75 (2009)
5. Silberschmidt, V.V.: Account for random microstructure in multiscale models. In: Kwon, Y. W., Allen, D.H., Talreja, R. (eds.) Multiscale Modeling and Simulation of Composite Materials and Structures, pp. 1–35. Springer, New York (2008)
6. Hill, R.: Elastic properties of reinforced solids: some theoretical principles. J. Mech. Phys. Solids **11**, 357–372 (1963)
7. Drugan, W.J., Willis, J.R.: A micromechanics-based nonlocal constitutive equation and estimates of representative volume element size for elastic composites. J. Mech. Phys. Solids **44**, 497–524 (1996)
8. Kanit, T., Forest, S., Galliet, I., Mounoury, V., Jeulin, D.: Determination of the size of the representative volume element for random composites: statistical and numerical approach. Int. J. Solids Struct. **40**, 3647–3679 (2003)
9. Vanin, G.A.: Micromechanics of Composite Materials. Naukova dumka, Kiev (in Russian) (1985)
10. Volkov, S.D., Stavrov, V.P.: Statistical Mechanics of Composite Materials. Izd. Bel. Gos. Univ., Minsk (in Russian) (1978)
11. Lomakin, V.A.: Statistical Problems of the Mechanics of Solid Deformable Bodies. Nauka, Moscow (in Russian) (1970)
12. Sokolkin, Y.V., Tashkinov, A.A.: Deformation and Fracture Mechanics of Structurally Inhomogeneous Bodies. Nauka, Moscow (in Russian) (1984)
13. Shermergor, T.D.: The Theory of Elasticity of Microinhomogeneous Media. Nauka, Moscow (in Russian) (1977)
14. Beran, M.J.: Statistical Continuum Theories. Wiley Interscience Publication, New-York (1968)
15. Lifshitz, I.M., Rosenzweig, L.N.: On the theory of the elastic properties of polycrystals. J. Exp. Theor. Phys. **16**, 967–980 (1946). (in Russian)
16. Lifshitz, I.M., Rosenzweig, L.N.: Erratum to On the theory of the elastic properties of polycrystals. J. Exp. Theor. Phys. **21**, 1184 (1951) (in Russian)
17. Bolotin, V.V., Moskalenko, V.N.: Determination of the elastic constants of a microinhomogeneous medium. Zh Priklad Mekh Tekhn Fiz (J. Appl. Mech. Tech. Phys.) **1**, 66–72 (1968). (in Russian)
18. Lomakin, V.A., Sheinin, V.I.: Stress concentration at the boundary of a randomly inhomogeneous elastic body. Mekh Tverdogo Tela **9**(2), 65–70 (Engl Transl. Mech. Solids **9**(2), 58–63) (1974) (in Russian)
19. Stavrov, V.P., Dolgih, V.J., Volkov, S.D.: On the elastic constants of randomly reinforced plastics. Mech. Polym. **2**, 259–265 (1967). (in Russian)
20. Maslov, B.P.: Effective constants of the theory of geometrically nonlinear solids. Prikl Mekh. 17(5):45–50 (Engl Transl. Soviet Appl. Mech. **17**, 439–444) (1981) (in Russian)
21. Savin, G.N., Khoroshun, L.P.: Problem of elastic constants of randomly reinforced materials. Mechanics of Composite Media and Related Problems of Analysis. Nauka, Moscow, pp. 437–444 (1972) (in Russian)
22. Khoroshun, L.P.: Random functions theory in problems on the macroscopic characteristics of microinhomogeneous media. Priklad Mekh. **14**(2), 3–17 (Engl Transl. Soviet Appl. Mech. **14**, 113–124) (1978) (in Russian)

23. Anoshkin, A.N., Sokolkin, Y.V., Tashkinov, A.A.: Microstress fields and the mechanical properties of disordered fiber composites. Mech. Compos. Mater. **26**(5), 628–633 (1990)
24. Wildemann, V.E., Sokolkin, Y.V., Tashkinov, A.A.: (1997) Mechanics of inelastic deformation and fracture of composite materials. Nauka, Moscow (in Russian)
25. Pankov, A.A.: Statistical mechanics of piezocomposites. Perm Gos. Tehn. University Press, Perm (2009) (in Russian)
26. Kroner, E.: Elastic moduli of perfectly disordered composite materials. J. Mech. Phys. Solids **15**(2), 137–155 (1967)
27. Kroner, E.: Bounds for effective elastic moduli of disordered materials. J. Mech. Phys. Solids **25**(2), 137–155 (1977)
28. Sokolkin, Y.V., Volkova, T.A.: Multipoint moment functions of the stress and strain distributions in stochastic composites. Mech. Compos. Mater. **27**(4), 429–435 (1991)
29. Tashkinov, M.A., Vildeman, V.E., Mikhailova, N.V.: Method of successive approximations in a stochastic boundary-value problem in the elasticity theory of structurally heterogeneous media. Compos.: Mech. Comput. Appl. Int. J **2**(1), 21–37 (2011)
30. Tashkinov, M.A., Wildemann, V.E., Mikhailova, N.V.: Method of successive approximations in stochastic elastic boundary value problem for structurally heterogenous materials. Comput. Mater. Sci. **52**, 101–106 (2012)
31. Tashkinov, M.: Statistical characteristics of structural stochastic stress and strain fields in polydisperse heterogeneous solid media. Comput. Mater. Sci. **94**, 44–50 (2014)
32. Volkov SS (1987) The existence and uniqueness of solutions of stochastic problems of elasticity theory. Calculation and optimization of engineering products. Sverdlovsk 17–19 (in Russian)
33. Jiao, Y., Stillinger, F.H., Torquato, S.: Modeling heterogeneous materials via two-point correlation functions. II. Algorithmic details and applications. Phys. Rev. **77**(3), 031135 (2008)
34. Korn, G., Korn, T.: Mathematical Handbook for Scientists and Engineers. Nauka, Moscow (in Russian) (1968)
35. Rasool, A., Böhm, H.J.: Effects of particle shape on the macroscopic and microscopic linear behaviors of particle reinforced composites. Int. J. Eng. Sci. **58**, 21–34 (2012)
36. Liu, K.C., Ghoshal, A.: Validity of random microstructures simulation in fiber-reinforced composite materials. Compos. B **57**, 56–70 (2014)
37. Matveeva, A., Pyrlin, S.V., Ramos, M.M.D., et al.: Influence of waviness and curliness of fibres on mechanical properties of composites. Comput. Mater. Sci. **87**, 1–11 (2014)
38. Mishnaevsky Jr, L., Derrien, K., Baptiste, D.: Effect of microstructure of particle reinforced composites on the damage evolution: probabilistic and numerical analysis. Compos. Sci. Technol. **64**, 1805–1818 (2004)
39. Yu Liu, M., Greene, Steven, Chen, Wei, et al.: Computational microstructure characterization and reconstruction for stochastic multiscale material design. Comput. Aided Des. **45**, 65–76 (2013)
40. Khokhar, Z.R., Ashcroft, I.A., Silberschmidt, V.V.: Simulations of delamination in CFRP laminates: effect of microstructural randomness. Comput. Mater. Sci. **46**, 607–613 (2009)
41. Yu, M., Zhu, P., Ma, Y.: Effects of particle clustering on the tensile properties and failure mechanisms of hollow spheres filled syntactic foams: a numerical investigation by microstructure based modeling. Mater. Des. **47**, 80–89 (2013)
42. Melro, A.R., Camanho, P.P., Pinho, S.T.: Influence of geometrical parameters on the elastic response of unidirectional composite materials. Compos. Struct. **94**, 3223–3231 (2012)
43. Baniassadi, M., Mortazavi, B., Amani Hamedani, H., et al.: Three-dimensional reconstruction and homogenization of heterogeneous materials using statistical correlation functions and FEM. Comput. Mater. Sci. **51**, 372–379 (2012)
44. Sheidaei, A., Baniassadi, M., Banu, M., et al.: 3-D microstructure reconstruction of polymer nano-composite using FIB–SEM and statistical correlation function. Compos. Sci. Technol. **80**, 47–54 (2013)

45. Baniassadi, M., Ahzi, S., Garmestani, H., et al.: New approximate solution for N-point correlation functions for heterogeneous materials. J. Mech. Phys. Solids **60**, 104–119 (2012)
46. Ghazavizadeh, A., Soltani, N., Baniassadi, M., et al.: Composition of two-point correlation functions of subcomposites in heterogeneous materials. Mech. Mater. **51**, 88–96 (2012)
47. Feng, J.W., Li, C.F., Cen, S., Owen, D.R.J.: Statistical reconstruction of two-phase random media. Comput. Struct. **137**, 78–92 (2014)
48. Liu, K.C., Ghoshal, A.: Inherent symmetry and microstructure ambiguity in micromechanics. Compos. Struct. **108**, 311–318 (2014)
49. S. Torquato (1998) Morphology and effective properties of disordered heterogeneous media. Int. J. Solids Struct. 35(19): 2385–2406
50. Rintoul, M.D., Torquato, S.: Reconstruction of the structure of dispersions. J. Colloid Interface Sci. **186**, 467–476 (1997)
51. Sheehan, N., Torquato, S.: Generating microstructures with specified correlation functions. J. Appl. Phys. **89**, 53–61 (2001)
52. Jiao, Y., Stillinger, F.H., Torquato, S.: Modeling heterogeneous materials via two-point correlation functions: basic principles. Phys. Rev. **76**, 031110 (2007)
53. Binder, K., Heerman, D.W.: Monte Carlo Simulation in Statistical Physics: An Introduction. Springer, Berlin (1997)
54. Torquato, S.: Modeling of physical properties of composite materials. Int. J. Solids Struct. **37**, 411–422 (2000)
55. Bennet, C.H.: Serially deposited amorphous aggregates of hard spheres. J. Appl. Phys. **43**, 2727–2734 (1972)
56. Lu, G.Q., Ti, L.B., Ishizaki, K.: A new algorithm for simulating the random packing of monosized powder in CIP processes. Mater. Manufact. Process. **9**, 601–621 (1994)
57. Kansal, A.R., Truskett, T.M., Torquato, S.: Nonequilibrium hard-disk packing with controlled orientational order. J. Chem. Phys. **113**, 4844–4851 (2000)
58. Cesarano III, J., McEuen, M.J., Swiler, T.: Computer simulation of particle packing. Int. SAMPE Tech. Conf. **27**, 658–665 (1995)
59. Furukawa, K., Imai, K., Kurashige, M.: Simulated effect of box size and wall on porosity of random packing of spherical particles. Acta Mech. **140**, 219–231 (2000)
60. Nolan, G.T., Kavanagh, P.E.: Computer simulation of random packing of hard spheres. Powder Technol. **72**, 149–155 (1992)
61. Buryachenko, V.A., Pagano, N.J.: Multiscale analysis of multiple interacting inclusions problem: finite number of interacting inclusions. Math. Mech. Solids **10**, 25–62 (2005)
62. Clarke, A.S., Willey, J.D.: Numerical simulation of the dense random packing of a binary mixture of hard spheres: amorphous metals. Phys. Rev. B **35**, 7350–7356 (1987)
63. He, D., Ekere, N.N.: Structure simulation of concentrated suspensions of hard spherical particles. AIChE J. **47**, 53–59 (2001)
64. Knott, G.M., Jackson, T.L., Buckmaster, J.: Random packing of heterogeneous propellants. AIAA J. **39**, 678–686 (2000)
65. Ogen, L., Troadec, J.P., Gervois, A., Medvedev, N.: Computer Simulation and Tessellations of Granular Materials. Foams and Emulsions, pp. 527–545. Kluwer, Dordrecht (1998)
66. Berryman, J.G.: Random close packing of hard spheres and disks. Phys. Rev. A **27**, 1053–1061 (1983)
67. Cheng, Y.F., Guo, S.J., Lay, H.Y.: Dynamic simulation of random packing of spherical particles. Powder Technol. **107**, 123–130 (2000)
68. Kroner, E.: Statistical modeling. In: Gittus, J., Zarka, J. (eds.) Modeling Small Deformations of Polycrystals, pp. 229–291. Elsevier, London/New York (1986)
69. Hinrichsen, E.L., Feder, J., Jossang, T.: Geometry of random sequential adsorption. J. Statist. Phys. **44**, 793–827 (1986)
70. Lotwick, H.W.: Simulations on some spatial hard core models, and the complete packing problem. J. Statist. Comp. Simul. **15**, 295–314 (1982)

71. Malcolm, M.A., Simpson, R.B.: Local versus global strategies for adaptive quadrature. ACM Trans. Math. Softw. **1**(2), 129–146 (1975)
72. Krommer, A.R., Ueberhuber, C.W.: Computational Integration. SIAM Publications, Philadelphia (1998)
73. Duffy, M.G.: Quadrature over a pyramid or cube of integrands with a singularity at a vertex. J. SIAM Numer. Anal. **19**(6), 1260–1262 (1982)

Optimization of the Damping Properties of Electro-Viscoelastic Objects with External Electric Circuits

V.P. Matveenko, M.A. Yurlov and N.A. Yurlova

Abstract The paper deals with optimization of dynamic characteristics of smart structures based on piezoelectric materials with external electric circuits comprising resistance, capacitance and inductance. The dynamic parameters to be optimized are resonance frequencies and damping properties. For numerical estimation of the dynamic characteristics of the model system, a natural vibration problem of an electroviscoelastic solid with differing external electric circuits is proposed. Model examples are given to demonstrate the efficiency of the natural vibration problem in finding dynamically optimum piezoelectric smart structures with external electric circuits.

1 Introduction

In recent years, the relatively new concept of smart materials or smart structures has been much addressed in scientific research and various applications. The prospects of smart materials can be judged, for example, from the report "New Materials for Next-Generation Commercial Transport" prepared jointly by the USA Committee on New Materials for Advanced Civil Aircraft, Commission on Engineering and Technical Systems and National Research Council in 1996 [1]. These institutions came to following conclusions:

- in the nearest 15–20 years, structures containing adaptive elements will become accessible and, being feasible and rather efficient, will allow their use in cargo and passenger aircrafts;
- research in smart materials is intensive, but fast developing technologies will do allow implementation of development products in the field;

V.P. Matveenko · M.A. Yurlov (✉) · N.A. Yurlova
Institute of Continuous Media Mechanics UB RAS, Acad.Korolev str., 1,
Perm 614013, Russia
e-mail: yurlova@icmm.ru

V.V. Silberschmidt and V.P. Matveenko (eds.), *Mechanics of Advanced Materials*,
Engineering Materials, DOI 10.1007/978-3-319-17118-0_4

- capabilities of smart materials will find application primarily in monitoring the state of constructions and environment;
- first application of smart materials will be in the simplest form—passive systems.

More than 15 years has passed since this report and analysis of available data shows that the conclusions made are close to present day reality.

Smart materials or smart structures, which are also known as intelligent, sensitive, multifunctional or adaptive, can be characterized as systems capable of changing their properties in response to a change of the surroundings. A quite appropriate analogy for smart systems is with biological objects: they contain, like the nervous system, sensing elements often called detectors or sensors, actuating mechanisms or actuators similar to those of the muscular system, and real-time data processing units or processors similar to individual brain functions.

Smart systems that comprise only sensors are termed passive systems. Embedment of sensors in a smart material which, in essence, is a composite material, makes it possible to monitor the state of constructions. Successful development of passive smart structures depends on the availability of suitable sensors, principles of their operation, signal processing methods, and technologies by which they are embedded in a composite material. Now, attention of researchers is concentrated on two types of materials that are most convenient to embed in smart structures as sensors or detectors. These are optical fibers and piezoelectric materials.

Manufacturing active controlled or responsive smart structures requires actuators or actuating mechanisms capable of inducing deformation of a basic construction. At present, the materials used as actuators are shape memory alloys, piezoelectric materials, electrostrictive and magnetostrictive materials, and electrorheological liquids.

The methods of application of materials as actuators can be divided into two groups. Methods of the first group consist in making certain structural elements of these materials: for example, a truss construction section of controllable length. Methods of the second group are associated with embedding of elements made of actuator materials inside a construction: for example, a piezoelectric patch joint with a construction by either embedding in its inside or fixing on its surface can create local strains.

The most widely used materials in manufacturing smart composites are piezoelectric materials. This, in particular, owes to their direct and inverse piezoelectric effects allowing the use of piezoelectric elements both as sensors and as actuators.

Smart materials perform the following functions: object profile control, damage detections, including early detection, dynamic process control, micropositioning, geometry control, and spurious noise to useful energy conversion.

Examples of practical applications of smart materials are their use in aviation for counteraction against aeroelastic and vibrational effects [2–7] and damping of vibrations of aircraft cabins [8–10], in space technologies for control of dynamic behavior of satellite constructions [11, 12], in rail transport for detection of wear of railcar wheels [13, 14] and suppression of vibrations of railcar bodies [15], in automotive industry for elimination of vibrations [13], in fine optics [16], in high-precision devices [17, 18], and in new generation sports goods: rock skis, tennis and golf racquets, and baseball bats [4, 8, 19].

One of the main factors that determine the application of smart materials is their type. Now, a wide range of piezomaterials for various technological purposes are produced: piezoceramics [20], piezopolymers [21, 22], piezoelectric polymer films [23], multilayer piezoelements [24, 25], piezoelectric fibers of varying cross-section [26], piezocomposites based piezoelectric fibers [8, 27–34].

According the available data [27], there are about 1500 materials with piezoelectric properties known to date. The most well-known classes of piezoelectric materials in this variety are piezoceramics and piezopolymers of which the former is more efficient in piezoelectric properties but less technological due to its high brittleness and rigidity.

The objective of the work is to inquire into the most widely used function of smart structures with piezoelements—control of dynamic behavior of constructions. Piezoelectric elements connected by a shunt circuit and joined to a mechanical construction are elements at which energy is dissipated with attendant additional vibration damping. Due to the piezoelectric effect, part of the mechanical energy involved in vibration can be converted to electric energy and merely dissipated through the shunt circuit which is just the mechanism of passive damping [4].

Among shunt circuits, resonant circuits deserve special attention. These circuits, as a rule, comprise an inductor and a resistor and allow tuning to any damped frequency. Moreover, improvement of the circuit topology makes possible simultaneous damping of several vibration modes. In mechanical terms, the system as a whole (a piezoelectric element and a resonant shunt circuit) is similar to a dynamic damper. Because the piezoelectric element is a capacitor, the use of shunt circuits is the simplest way to provide energy dissipation. This fact was first demonstrated experimentally in [35], and later, in [36]. A detailed review of methods used to shunt piezoelectric elements by electric circuits for vibration damping can be found in [37].

The shunt circuits can be made either series, or parallel, or series-parallel. A series resonant shunt circuit was proposed in [36]. The same circuit was considered in [9, 37–39], etc. A parallel shunt resonant circuit was proposed for the first time in [40] in attempt to overcome troubles with realization of the series circuit.

The advantage of passive piezoelectric damping to compare with traditional damping (i.e., with viscoelastic inclusions) is in the possibility to tune a damper in a wider frequency range and in better thermal stability.

However, there is a significant difference in the mechanics of piezoelectric and classical damping. The addition of passive piezoelectric layers in a construction allows not only energy dissipation due to resistive heating (i.e., electric energy generation) but, which is no less important, a change in the main resonance of the construction due to electromechanical coupling [7].

The passive vibration damping has the following shortcomings:

- damping a certain vibration mode requires that the passive external electric circuit be tuned to an appropriate resonance frequency; simultaneous damping of several vibration modes requires elaborate hybrid circuits, and this decreases the circuit efficiency;
- damping the lowest and, as a rule, most dangerous vibration modes of frequency up to 100 Hz requires that the circuit inductance be tens and hundreds of Henry, and this necessitates the use of rather heavy and sizable coils; electronic devices like gyrators (inductance emulators), though being an alternative to inductance coils, are not deprive of specific flaws;
- leakage currents at low frequencies decrease the efficiency of electric-to-mechanical energy conversion in piezoelements.

Despite the shortcomings of passive vibration damping, it is widely used being steadily improved in response to the progress in microelectronics and analysis techniques.

The dynamic behavior of constructions can be controlled, along with the passive method, by an active method of vibration damping. The active method consists in the following: certain of piezoelements (sensors) provide information on the mechanical state of a system, while the others (actuators) are brought to an electric potential, depending on the sensor potential, with the use of special relations (feedback equations). If the actuator potential is proportional to the sensor potential, the integral stiffness characteristics of the system are changed; and if the actuator potential is proportional to the first or second derivative of the sensor potential, the changed characteristics are damping or inertial characteristics of the construction. This allows correction of dynamic properties of an object over a wide range.

One of the key problems of vibration damping by external electric circuits is in finding the simplest shunt circuit that provides efficient vibration control of a particular construction.

Assessment of the potentials of smart systems with piezoelements to control vibrations gives the following scenarios of their use. In the first scenario, piezoelements are used as sensors and actuators that realize passive or active vibration control, or their combination. In the second scenario, a piezoelement is an energy source for external electric circuits; in this case, passive and active control is possible. It is also possible to combine the first and second scenarios.

Because of the rich variety of patterns used to control dynamic characteristics of smart structures with piezoelements, the search for optimum patterns is almost impossible without mathematical simulation. In the majority of available papers, the simulation is based on the ANSYS package or algorithms realized to one or another extent in commercial program packages.

The most significant dynamic characteristics are resonance frequencies and parameters responsible for damping properties of a model system. With the ANSYS package or other well-known algorithms, the damping properties of smart systems are estimated from the vibration amplitude in resonant modes or from the rate of transient processes. In the first case, the problem of forced steady-state vibrations is solved; in the second, the dynamic problem with initial conditions. These problems provide little for optimization of dynamic characteristics for the following reasons. The problem of forced steady-state vibrations requires a multiple solution for different frequencies to obtain amplitudes in resonant modes; the optimum solutions found with the latter problem or the problem with initial conditions have to do with the loading type to be modeled for a system under study.

In the present work, a natural vibration problem is proposed for optimization of dynamic characteristics of smart systems with piezoelements and external electric circuits. Based on this problem, efficient numerical procedures for optimization are derived in which the control parameters are mechanical characteristics of the materials of a smart composite, geometry and position of piezoelements, and characteristics governing the boundary conditions. The presence of external *RLC* circuits connecting the electrodes of piezoelements increases the number of optimization parameters.

2 Mathematical Statement of the Natural Vibration Problem

The object under study is a piecewise homogeneous system of volume $V = V_1 + V_2$, where the volume V_1 consists of homogeneous elastic and viscoelastic elements, and the volume V_2, of piezoelectric elements. The piezoelectric elements can be connected via an electrodized surface (electrodes) to current or voltage generators, or to arbitrarily structured *RLC* circuits with resistances, capacitances, and inductances.

The variational equation of motion of the system consisting of elastic and piezoelectric elements is formulated using relations of the linear theory of elasticity and quasistatic Maxwell equations [41–43]:

$$\begin{aligned} &\int\limits_{V_1} \left(\sigma_{ij}\delta\varepsilon_{ij} + \rho\ddot{u}_i\delta u_i\right) dV + \int\limits_{V_2} \left(\sigma_{ij}\delta\varepsilon_{ij} - D_i\delta E_i + \rho\ddot{u}_i\delta u_i\right) dV \\ &- \int\limits_{\Omega_\sigma} \delta u_i P_i d\Omega - \int\limits_{\Omega_{el}} q_e \delta\varphi d\Omega = 0 \end{aligned} \tag{1}$$

where D, E are the inductance and electric field vectors; σ_{ij} are the symmetric Cauchy stress tensor components; u_i are the displacement vector components; P_i are the load vector components; $\varepsilon_{ij} = \frac{1}{2}\left(u_{i;j} + u_{j;i}\right)$ are the linear strain tensor components (a semicolon stands for a partial derivative with respect to an appropriate coordinate); Ω_{el} is the surface bounding a piezoelectric element; q_e and φ are the surface charge density and electric potential. Equation (1) is in rectangular Cartesian coordinates. The electric field is assigned the equipotentiality condition:

$$\varphi_{,i} = -E_i \tag{2}$$

For isothermal processes in linear electroelastic media, the following physical relations hold true:

$$\sigma_{ij} = C_{ijkl}\varepsilon_{kl} \quad \text{for } V_1 \tag{3}$$

$$\left.\begin{aligned} \sigma_{ij} &= C_{ijkl}\varepsilon_{kl} - \beta_{ijk}E_k \\ D_k &= \beta_{ijk}\varepsilon_{ij} + e_{ki}E_i \end{aligned}\right\} \quad \text{for } V_2 \tag{4}$$

where C_{ijkl} is the elastic constant tensor; β_{ijk} and e_{ki} are the piezoelectric and dielectric constant tensors.

If the element V_1 or V_2 of the system possesses viscoelastic properties, the elastic constant tensor C_{ijkl} should be replaced by an appropriate viscoelastic operator. The dissipative properties of the material are taken into account using relations of the Boltzmann-Volterra hereditary theory:

$$\sigma_{ij}(t) = C_{ijkl}\varepsilon_{kl}(t) - \int_0^t R_{ijkl}(t-\tau)\varepsilon_{kl}(\tau)d\tau \tag{5}$$

Here C_{ijkl} are the instantaneous modulus tensor components; R_{ijkl} are the relaxation kernel tensor components. Notice that the relaxation kernel tensors are of the same symmetry as the instantaneous modulus tensors. Equation (5) can be written in the tensor operator form:

$$\sigma_{ij}(t) = C^*_{ijkl}\varepsilon_{kl}(t). \tag{6}$$

Let us consider the mechanical natural vibration problem for solutions of the form:

$$u_i(x,t) = \bar{u}_i(x)e^{-i\omega t}, \tag{7}$$

where $\omega = \omega_R + i\omega_I$ is the complex natural frequency; ω_R corresponds to the natural frequency; ω_I characterizes the rate of vibration damping, $\bar{u}_i(x)$ is the eigenvibration.

If the model system has viscoelastic elements, physical relations (4) in the natural vibration problem are replaced by their approximate complex analogue [44]:

$$\sigma_{ij} \approx \left[C_{ijkl} - Q^c_{ijkl}(\omega_R) + iQ^s_{ijkl}(\omega_R)\right]\varepsilon_{kl} = \bar{C}_{ijkl}(\omega_R)\varepsilon_{kl} \tag{8}$$

where $\bar{C}_{ijkl}$ are the complex dynamic modulus tensor components; Q^c_{ijkl}, Q^s_{ijkl} are the Fourier cosine and sine transforms of relaxation kernels:

$$Q^c_{ijkl} = \int\limits_0^\infty R_{ijkl}(\tau)\cos(\omega_R\tau)\,d\tau$$

$$Q^s_{ijkl} = \int\limits_0^\infty R_{ijkl}(\tau)\sin(\omega_R\tau)\,d\tau$$

The complex dynamic modulus tensor components can be represented as follows:

$$\bar{C}_{ijkl}(\omega_R) = \left[C_{ijkl} - Q^c_{ijkl}(\omega_R) + iQ^s_{ijkl}(\omega_R)\right] = C^R_{ijkl}(\omega_R) + iC^I_{ijkl}(\omega_R), \qquad (9)$$

where $C^R_{ijkl}(\omega_R)$, $C^I_{ijkl}(\omega_R)$ are the accumulation and loss moduli, respectively.

In electroelastic problems, the boundary conditions can be divided into two groups: mechanical and electrical.

The mechanical boundary conditions in the natural vibration problem have the following form:

$$S_\sigma : \quad \sigma_{ij}n_j = 0, \; S_n : \quad u_i = 0, \qquad (10)$$

where $S = S_\sigma + S_n$ is the surface bounding the volume V of the system under study.

The physically realizable electric boundary conditions are formulated depending on the way of electric energy transfer to a piezoelectric. The energy is delivered to and removed from a deformed piezoelectric with the use of electrode coatings deposited on part of its surface. The coatings are assumed to be rather thin perfect conductors of negligibly small mass. The presence of a conducting layer on the surface Ω_{el} (electrodizing) makes the surface equipotential:

$$\int\limits_{\Omega_{el}} \delta\varphi\, q_e\, d\Omega = \delta\varphi \int\limits_{\Omega_{el}} q_e\, d\Omega = Q^{el} \qquad (11)$$

Here Q^{el} is the total electrode charge.

Of interest to us are boundary conditions for connection of external circuits to piezoelements.

Let us consider a variant of electric boundary conditions when one part of the electrodized piezoelement surface Ω^m_{el} is connected to the point of zero potential via a series *RLC* circuit and the other part Ω^k_{el} is assigned a zero potential. In this case, the potential across the ungrounded electrode is calculated by the formula:

$$\varphi_m = \frac{Q_m}{C} + RI_m + L\dot{I}_m = \frac{Q_m}{C} + R\dot{Q}_m + L\ddot{Q}_m, \qquad (12)$$

where φ_m and $Q_m = \int_{\Omega^m_{el}} q_e d\Omega$ are the electric potential and the total charge at Ω^m_{el}, $I_m = \dot{Q}_m$ is the conductor current; R is the resistance; C is the capacitance; L is the inductance. Then, the integral over the surface Ω_{el}^m in Eq. (1) determines the electric boundary conditions for piezoelectric zones:

$$\int\limits_{\Omega_{el}^m} q_e \delta\varphi \, d\Omega = -\delta\varphi_m Q_m \tag{13}$$

Equation (13) takes into account that the electrodized surface Ω_{el}^m is equipotential and the circuit is an external element for the examined system (a change of sign preceding the integral). In this statement, Eq. (1) with no external load $(P_i = 0)$ is homogeneous:

$$\begin{aligned} &\int\limits_{V_1} \left(\sigma_{ij}\delta\varepsilon_{ij} + \rho\ddot{u}_i\delta u_i\right)dV + \int\limits_{V_2} \left(\sigma_{ij}\delta\varepsilon_{ij} - D^i\delta E_i + \rho\ddot{u}_i\delta u_i\right)dV \\ &+ \delta\varphi_m Q_m = 0. \end{aligned} \tag{14}$$

Equation (12), in view of the form of the solution of natural vibration problem (7), can be solved for the total charge:

$$Q_m(t) = \frac{\bar{\varphi}_m \cdot \mathrm{e}^{i\omega t}}{C^{-1} - \omega^2 \cdot L + i \cdot \omega \cdot R} \tag{15}$$

Clearly apparent transformations give the variational equation for the natural vibration problem (the bar above the variable is omitted) [45, 46]:

$$\begin{aligned} &\int\limits_{V_2} \left(\delta\varepsilon_{ij}\left(C_{ijkl}\varepsilon_{kl} - \beta_{ijk}E_k\right) - \delta E_k\left(\beta_{ijk}\varepsilon_{ij} + e_{ki}E_i\right) - \omega^2\rho\delta u_i u_i\right) dV \\ &+ \int\limits_{V_1} \left(\delta\varepsilon_{ij}C_{ijkl}\varepsilon_{kl} - \omega^2\rho\delta u_i u_i\right) dV + \frac{\varphi_m\delta\varphi_m}{C^{-1} - L\omega^2 + i\omega R} = 0. \end{aligned} \tag{16}$$

Thus, we have derived the variational equation of quasi-harmonic vibrations with dissipative terms due to the energy loss in external electric circuits with resistance *R* for an electroviscoelastic solid. The external circuit inductance *L* and capacitance *C* are analogues of sort to mechanical mass and rigidity with which we can control the natural frequencies.

For a parallel *RLC* circuit, the current through the circuit is equal to the total current through its elements:

$$I_m = I_m^R + I_m^L + I_m^C = \frac{\varphi_m}{R} + C\dot{\varphi}_m + \frac{\int \varphi_m dt}{L} \tag{17}$$

In view of the quasi-harmonic process, we obtain

$$I_m = \bar{\varphi}_m \left(\frac{1}{R} + i\omega C - \frac{i}{L\omega} \right) \cdot \mathrm{e}^{i\omega t}$$

Time integration of the latter equation gives the total electrode charge:

$$Q_m = \bar{\varphi}_m \left(-\frac{i}{\omega R} + C - \frac{1}{L\omega^2} \right) \cdot \mathrm{e}^{i\omega t} \tag{18}$$

After transformations similar to those applied to the series *RLC* circuit, we obtain the variational equation for the natural vibration problem (the bar above the variable is omitted) with parallel external electric circuits:

$$\begin{aligned} &\int\limits_{V_2} \left(\delta\varepsilon_{ij} \left(C_{ijkl}\varepsilon_{kl} - \beta_{ijk}E_k \right) - \delta E_k \left(\beta_{ijk}\varepsilon_{ij} + e_{ki}E_i \right) - \omega^2 \rho \delta u_i u_i \right) dV \\ &+ \int\limits_{V_1} \left(\delta\varepsilon_{ij} C_{ijkl}\varepsilon_{kl} - \omega^2 \rho \delta u_i u_i \right) dV + \varphi_m \delta\varphi_m \left(-\frac{i}{\omega R} + C - \frac{1}{L\omega^2} \right) = 0. \end{aligned} \tag{19}$$

If the *RLC* circuit lacks some or other elements, appropriate terms in Eqs. (16) and (19) should be omitted. More complex circuits can be synthesized by combining Eqs. (16) and (19).

The use of smart systems with piezoelements and external electric circuits makes possible controlled nonconservative systems. To provide more efficient damping and control of constructions and a wider range of their dynamic stability, feedbacks are applied to the electric potential and/ or its time derivatives. The circuits provided with feedbacks of digital signal processing elements makes feasible efficient automatic control systems. Calculation of active systems within the framework of the continual electroviscoelastic problem requires formulation of new types of boundary conditions.

Let us rewrite Eq. (1) with a more concretely defined surface integral:

$$\begin{aligned} &\int\limits_{V_1} \left(\sigma_{ij}\delta\varepsilon_{ij} + \rho \ddot{u}_i \delta u_i \right) dV + \int\limits_{V_2} \left(\sigma_{ij}\delta\varepsilon_{ij} - D_i \delta E_i + \rho \ddot{u}_i \delta u_i \right) dV \\ &- \int\limits_{S_\sigma} P_i \delta u_i dS - \sum_{k=1}^{n} \delta\varphi_k Q_k = 0 \end{aligned} \tag{20}$$

Here φ_k and $Q_k = \int_{\Omega_{el}^k} q_e d\Omega$ are the potential and charge of the *k*-th electrode; $\Omega_{el} = \sum_{k=1}^{n} \Omega_{el}^k$ is the electrodized surface consisting of *n* zones. Without violating the generality of the approach, let us consider the case when the charge $Q_i = \alpha_{ij}\varphi_j$, where α_{ij} is the feedback factor, is transferred to the *i*-th electrode. Then, Eq. (20) takes the form:

$$\begin{aligned}&\int\limits_{V_1}\left(\sigma_{ij}\delta\varepsilon_{ij}+\rho\ddot{u}_i\delta u_i\right)dV+\int\limits_{V_2}\left(\sigma_{ij}\delta\varepsilon_{ij}-D_i\delta E_i+\rho\ddot{u}_i\delta u_i\right)dV\\&-\int\limits_{S_\sigma}P_i\delta u_i dS-\sum_{k=3}^{n}\delta\varphi_k Q_k-\delta\varphi_i\alpha_{ij}\varphi_j-\delta\varphi_j Q_j=0\end{aligned}\tag{21}$$

The modern electronic element base allows measuring the electric potential across an electrode almost with no variation in the electrode charge, i.e., $Q_j = 0$:

$$\begin{aligned}&\int\limits_{V_1}\left(\sigma_{ij}\delta\varepsilon_{ij}+\rho\ddot{u}_i\delta u_i\right)dV+\int\limits_{V_2}\left(\sigma_{ij}\delta\varepsilon_{ij}-D_i\delta E_i+\rho\ddot{u}_i\delta u_i\right)dV\\&-\int\limits_{S_\sigma}P_i\delta u_i dS-\sum_{k=3}^{n}\delta\varphi_k Q_k-\delta\varphi_i\alpha_{ij}\varphi_j=0\end{aligned}$$

If an object is free from external loads, variational Eq. (21) becomes homogeneous and can be treated as an eigenvalue problem:

$$\begin{aligned}&\int\limits_{V_1}\left(\sigma_{ij}\delta\varepsilon_{ij}+\rho\ddot{u}_i\delta u_i\right)dV+\int\limits_{V_2}\left(\sigma_{ij}\delta\varepsilon_{ij}-D_i\delta E_i+\rho\ddot{u}_i\delta u_i\right)dV\\&-\sum_{k=3}^{n}\delta\varphi_k Q_k-\delta\varphi_i\alpha_{ij}\varphi_j=0.\end{aligned}\tag{22}$$

3 Numerical Realization

The formulated problem can be solved using the finite element method. For this purpose, variational Eq. (16) can be written in the matrix form:

$$\begin{aligned}&\int\limits_{V_1}\left(\delta\{\varepsilon_1\}^T[D_1]\{\varepsilon_1\}-\omega^2\delta\{u_1\}^T[\rho_1]\{u_1\}\right)dV\\&+\int\limits_{V_2}\left(\delta\{\varepsilon_2\}^T[D_2]\{\varepsilon_2\}-\omega^2\delta\{u_2\}^T[\rho_2]\{u_2\}\right)dV\\&+\frac{\delta\varphi_m\ \varphi_m}{C^{-1}-\omega^2L+i\ \omega R}=0\end{aligned}\tag{23}$$

By analogy, for Eq. (19) we have

$$\begin{aligned}&\int\limits_{V_1}\left(\delta\{\varepsilon_1\}^T[D_1]\{\varepsilon_1\}-\omega^2\delta\{u_1\}^T[\rho_1]\{u_1\}\right)dV\\&+\int\limits_{V_2}\left(\delta\{\varepsilon_2\}^T[D_2]\{\varepsilon_2\}-\omega^2\delta\{u_2\}^T[\rho_2]\{u_2\}\right)dV\\&+\varphi_m\delta\varphi_m\left(-\frac{i}{\omega R}+C-\frac{1}{L\omega^2}\right)=0\end{aligned}\tag{24}$$

Here, the generalized displacement, strain and stress vectors and the density matrix $\{u_1\}$, $\{\varepsilon_1\}$, $\{\sigma_1\}$, $[\rho_1]$, $\{u_2\}$, $\{\varepsilon_2\}$, $\{\sigma_2\}$, $[\rho_2]$ are related to the regions V_1 and V_2, respectively.

Physical relations (4) for piezoelectric ceramics have the following matrix form:

$$\{\sigma_2\}=[D_2]\{\varepsilon_2\}=\begin{bmatrix}C & \beta\\ \beta^T & -e\end{bmatrix}\{\varepsilon_2\},\tag{25}$$

where $[C]$, $[\beta]$, $[e]$ are the matrices of elastic, piezoelectric and dielectric constants.

For the region V_2 in each point of system the vector $\{u_2\}$ contains not only components of the displacement vector but also the electric potential φ and vector of strain $\{\varepsilon_2\}$:

$$\left\{\varepsilon_x,\ \varepsilon_y,\ \varepsilon_z,\ \varepsilon_{xy},\ \varepsilon_{yz},\ \varepsilon_{zx},\ \frac{\partial\phi}{\partial x},\ \frac{\partial\phi}{\partial y},\ \frac{\partial\phi}{\partial z}\right\}.$$

With the finite element method, variational problem (23) is reduced to the algebraic eigenvalue problem:

$$\left([K]-\omega^2[M]+[G(\omega)]\right)\{X\}=0,\tag{26}$$

where $\{X\}$ is the complex vector of nodal parameters; ω is the complex natural frequency; $[K]$ is the stiffness matrix (generally complex); $[M]$ is the mass matrix; $[G]$ is the matrix of coefficients of external RLC circuits. The complex frequencies $\omega=\omega_R+i\omega_I$ obtained from the solution of eigenvalue problem (26) determines the resonance frequencies (ω_R) and the damping indices (ω_I) of the system. The complex eigenvectors determine the vibration modes and phases.

Equation (26) differs greatly from the generalized eigenvalue problem in the presence of the matrix $[G(\omega)]$. The condition for the existence of a nontrivial solution is

$$D(\omega)=\det\left([K]-\omega^2[M]+[G(\omega)]\right)=0\tag{27}$$

For solving the vibration problems for an arbitrary system with *RLC* circuits in the general form, a universal finite difference scheme is proposed. The scheme consists in the following.

As known from electrical engineering, the behavior of passive *R*, *L* and *C* elements in AC circuits is described by the dependences:

$$I = R^{-1}\left(\varphi_i - \varphi_j\right),\ I = L^{-1}\int\left(\varphi_i - \varphi_j\right)dt \text{ and } I = C\left(\dot{\varphi}_i - \dot{\varphi}_j\right)$$

Here: I is the current; R is the resistance; φ is the electric potential; L is the inductance; C is the capacitance.

In terms of the finite element method, the behavior of one-dimensional *R*, *L* and *C* elements is determined as:

$$\begin{array}{ll} \text{resistance R} & \begin{Bmatrix} I_i \\ I_j \end{Bmatrix} = R^{-1}\begin{bmatrix} 1 & -1 \\ -1 & 1 \end{bmatrix}\begin{Bmatrix} \varphi_i \\ \varphi_j \end{Bmatrix} \\ \text{inductance L} & \begin{Bmatrix} \dot{I}_i \\ \dot{I}_j \end{Bmatrix} = L^{-1}\begin{bmatrix} 1 & -1 \\ -1 & 1 \end{bmatrix}\begin{Bmatrix} \varphi_i \\ \varphi_j \end{Bmatrix} \\ \text{capacitance C} & \begin{Bmatrix} I_i \\ I_j \end{Bmatrix} = C\begin{bmatrix} 1 & -1 \\ -1 & 1 \end{bmatrix}\begin{Bmatrix} \dot{\varphi}_i \\ \dot{\varphi}_j \end{Bmatrix} \end{array} \tag{28}$$

Here $I_i,\ I_j$ and $\varphi_i,\ \varphi_j$ are the current and potential in the *i*-th and *j*-th nodes of an element. This representation form is equivalent to introduction of one-dimensional finite elements.

Relations (28) is transformed with regard for the identities $I = \dot{q}$ or $q = \int_{-\infty}^{t} Idt$:

$$\begin{aligned} \{q_R\} &= R^{-1}[G]\int\{\varphi\}dt = [K_R]\int\{\varphi\}dt \\ \{q_L\} &= L^{-1}[G]\int\int\{\varphi\}dtdt = [K_L]\int\int\{\varphi\}dtdt \\ \{q_C\} &= C[G]\{\varphi\} = [K_C]\{\varphi\} \end{aligned} \tag{29}$$

where $\{q\} = \begin{Bmatrix} q_i \\ q_j \end{Bmatrix}, \quad \{\varphi\} = \begin{Bmatrix} \varphi_i \\ \varphi_j \end{Bmatrix}, \quad [G] = \begin{bmatrix} 1 & -1 \\ -1 & 1 \end{bmatrix}.$

Here q_i, q_j is the charge in the *i*-th and *j*-th nodes of an element; $[K_R],\ [K_L],\ [K_C]$ are the stiffness matrices of circuit elements.

For convenient construction of arbitrary electric circuits (parallel, series, parallel-series, etc.), we introduce a generalized element being a parallel connection of resistance, capacitance, and inductance.

By combining the nodes of individual elements and using formula (29), we obtain

$$\{q\} = [K_C]\{\varphi\} + [K_R]\int\{\varphi\}dt + [K_L]\int\int\{\varphi\}dtdt. \tag{30}$$

This expression describes a parallel *RLC* circuit. Equating the corresponding elementary stiffness matrices to zero allows us to obtain any of the circuit elements [46].

Let us consider a finite element model for systems with active feedbacks.

Let an electrode i gain a charge proportional to the electrode potential j $Q_i = \alpha_{ij}\varphi_j$, where α_{ij} is the feedback factor, which is generally complex. The presence of electrodized and, hence, equipotential surfaces in an electroelastic solid makes it possible to relate each of them to one electrical degree of freedom (potential), irrespective of the finite element grid.

Applying the finite element procedure to variational problem (22) gives the equation

$$\delta\{X\}^T\left([K]\{X\}+[M]\left\{\ddot{X}\right\}\right)-\delta x_i\alpha_{ij}x_j=0,$$

where $[K]$ is the complex stiffness matrix; $[M]$ is the mass matrix; $\{X\}$ is the eigenvector (eigenmode). It is taken here that the potential of the i-th electrode corresponds to the variable x_i, and that of the j-th electrode, to x_j in the state vector $\{X\}$. This equation can be written in terms of the modified stiffness matrix $[K^*]$ with a changed element $K^*_{ij} = K_{ij} - \alpha_{ij}$.

The solution is sought for in the form $\{X(t)\} = \{U\}e^{\omega t}$. This gives the algebraic eigenvalue problem for complex asymmetric matrices:

$$\left([K^*]+\omega^2[M]\right)\{U\}=0.$$

4 Experimental Demonstration of the Possibility of Damping Mechanical Vibrations by Means of External Electric Circuits

In order to provide evidence for the effect of damping mechanical vibrations by means of piezoelectric elements and external electric circuits, we have performed an experiment, the scheme of which is given in Fig. 1.

In the experiment, cross-polarized rectangular piezoelectric rod 1 was mounted on rigid base units. One half of the rod length was electrodized. Piezoelement 2 was used to generate longitudinal vibrations, and this led to the occurrence of electrical potential difference on electrodes 3 located on the lateral surfaces. To damp mechanical vibrations, the electrical circuit in which the electrical energy was dissipated as heat was connected to electrodes 3.

The mechanical vibration amplitude level was determined indirectly via the electric potential U_1, which occurred on the free end of the rod.

The two electric circuits, one purely resistive (R) and one resistive-inductive (RL), were considered. By changing resistance R and inductance L, it is possible to gain maximum damping of vibrations.

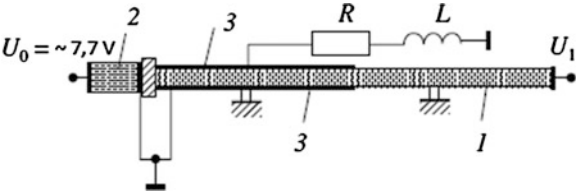

Fig. 1 Scheme of the experiment

Because the inductance coil is bulky, poorly modified, inconvenient to use and, as a rule, of large size, it is replaced, for the sake of compactness and convenience, by a gyrator. With the electric diagram of a gyrator, large inductance values can be achieved in a small-sized, light and cheap case. A gyrator is an electric circuit, which inverts impedance. The essence of the gyrator is the following: by using a capacitor voltage, it allows the voltage and current at the diagram entrance to behave like the voltage and current in the inductance coil.

The electrical diagram of the gyrator is given in Fig. 2.

The impedance of such an inductive circuit is given by

$$Z = \left(C_4 \frac{R_1 R_3}{R_2}\right) R_5,$$

there C_4 is the capacitor, R_1, R_2, R_3 are the resistances, and R_5 is the variable resistance.

Due to the variable resistance R_5, the inductance of the gyrator can vary over a broad range. For operational amplifiers, OP07CP precision amplifiers were used.

Figure 3 presents the plots of voltage at the end of the piezoceramic rod versus active resistance of the external circuit at fixed inductance values for the second vibration mode.

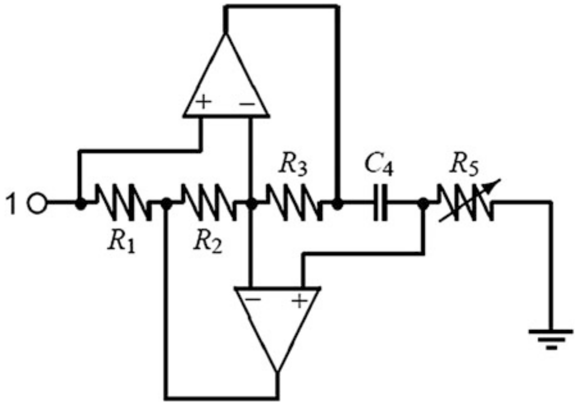

Fig. 2 Electrical diagram of the gyrator

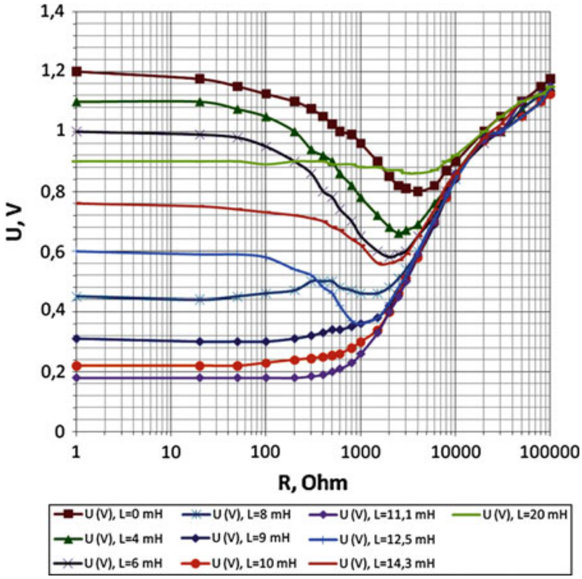

Fig. 3 Voltage at the end of the piezoceramic rod versus active resistance of the external circuit at fixed inductance values

Our experiment produced the following results:

- vibration damping by means of a resistive circuit alone is not an optimal strategy, and what is more at R = 0 or $R = \infty$ the existence of the external electric circuit has no influence on the vibrations of the system, and thus no additional vibration damping takes place;
- in the case of only resistive circuit, the maximum vibration damping at R = 4 kΩ is 30 %;
- with an increase of the inductive component in the external electric circuit up to 11 mH, the damping of the longitudinal vibrations of the rod increases as well, yet a further growth of the inductance value leads to reduction in the degree of vibration damping.

5 Examples of Numerical Analysis and Optimization of Dissipative Properties of Smart Structures

Let us consider an oblique elastic plate of volume V_1 with an adjoint piezoelectric element of volume V_2 (Fig. 4). The plate has a length b = 15 m, parallel faces $h_1 = 9$ m and $h_2 = 3$ m, and thickness t = 0.3 m and is made of aluminum alloy with the following mechanical characteristics: $E = 0.7 \times 10^{11}\ \mathrm{N/m^2}$, $\nu = 0.3,\ \rho = 2600\ \mathrm{kg/m^3}$. The piezoelectric layer of length a = 3 m and thickness

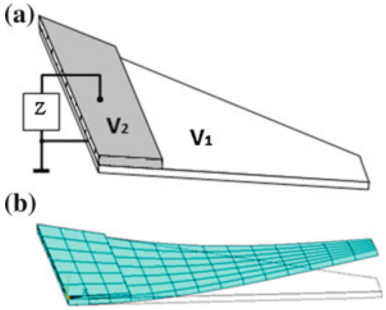

Fig. 4 Computational model of a trapezoidal plate with a piezoelement (**a**) the geometry of the computational model (**b**) the first mode of vibrations

$t_1 = 0.15$ m is made of PZT-5 piezoceramics with the following mechanical and piezoelectric characteristics:

$$\begin{aligned}
C_{11} &= 13.9 \times 10^{10}\ \mathrm{N/m^2}, \quad C_{12} = 7.78 \times 10^{10}\ \mathrm{N/m^2},\\
C_{13} &= 7.43 \times 10^{10}\ \mathrm{N/m^2}, \quad C_{33} = 11.5 \times 10^{10}\ \mathrm{N/m^2},\\
C_{44} &= 2.56 \times 10^{10}\ \mathrm{N/m^2}, \quad \beta_{13} = -52\ \mathrm{C/m^2},\\
\beta_{33} &= 151\ \mathrm{C/m^2}, \quad \beta_{15} = 127\ \mathrm{C/m^2},\\
e_{11} &= 6.45 \times 10^{-7}\ \mathrm{F/m}, \quad e_{33} = 5.62 \times 10^{-7}\ \mathrm{F/m},\\
\rho &= 7700\ \mathrm{kg/m^3}.
\end{aligned}$$

The left edge of the plate is rigidly fixed.

The model under consideration imitates an aircraft wing.

The electric circuits under consideration are individual R, L and C elements as well as series and parallel R and L elements.

Figure 5 shows diagrams of the natural frequencies $f = \omega_R/2\pi$ and damping factors $N = \omega_I$ for elementary R, L and C circuits (containing only one element) for the first vibration mode. In this case, damping takes place only for the R circuit. The maximum damping of the first eigenmode is found at $R_1 = 63{,}100\ \Omega$. For comparison, at $R_2 = 15{,}850\ \Omega$, the second mode will be damped to a maximum.

Figure 6 shows the damping factor of the first mode in relation to the resistance R at varying inductance L for series and parallel RL circuits.

With the series circuit, the maximum damping is reached at L = 6340 H, and with the parallel circuit, at L = 6500 H.

It is seem from comparison of the damping factors for the elementary R and series RL circuits that the latter provides much higher damping. This is because the piezoelement self-capacitance and inductance form a resonant LC circuit, resulting in a considerable increase in the current through the RL circuit. The natural frequency of the LC circuit thus coincides with the corresponding mechanical resonance frequency of the electroelastic system $f_i = \frac{1}{2\pi\sqrt{L_i C}}$. Diagrams for higher vibration modes are no different in character from those for the first mode.

Fig. 5 Natural frequencies and damping factors of the first mode versus the parameters of the external electric circuit for the aircraft wing model

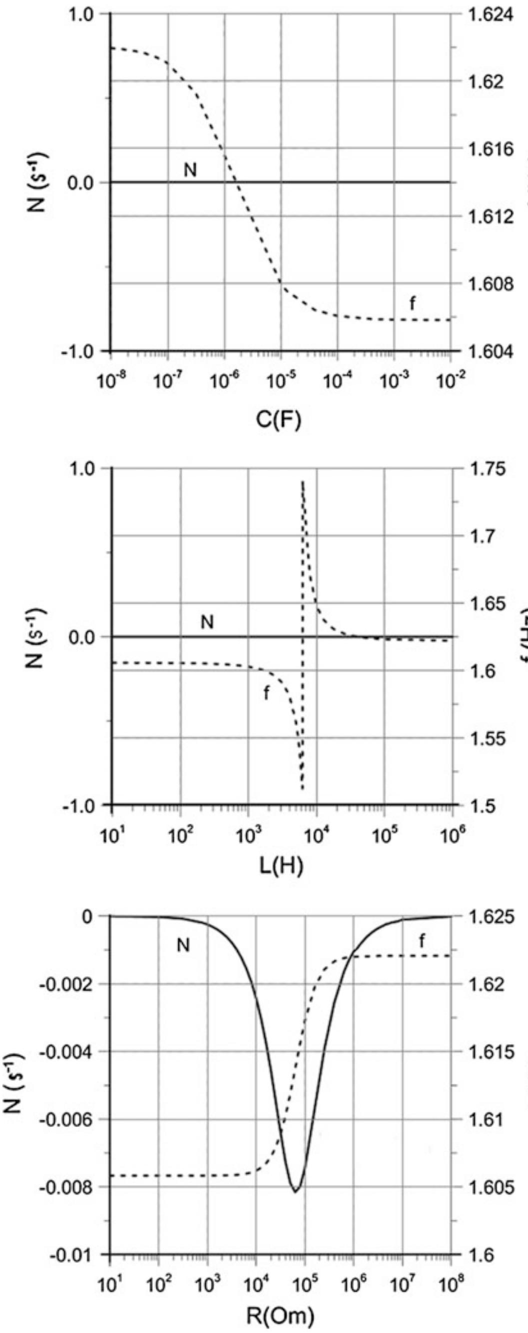

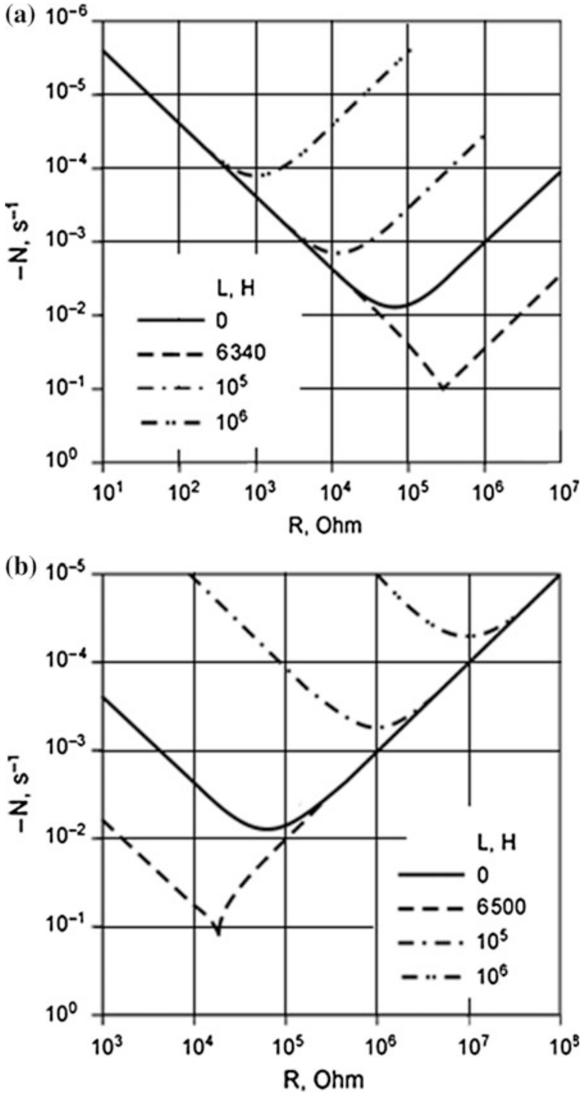

Fig. 6 Damping factor of the first mode versus the resistance *R* at varying inductance *L* for the series (**a**) and parallel (**b**) *RL* circuits

The second example is optimization of damping properties of a parabolic shell (Fig. 7a) in the form of an ellipse with semiaxes $a = 1$ m, $b = 0.75$ m and thickness of 1 mm. The shell is made of AD1M aluminum alloy and is supported by two pairs of stiffeners made of P-5-13N unidirectional composite based on carboxylic fibers. The shell material was taken to be elastic with $E = 0.7 \times 10^{11}\,\mathrm{N/m^2}$, $\nu = 0.3$, $\rho = 2600\ \mathrm{kg/m^3}$. The stiffeners were taken to be viscoelastic with a loss tangent $\chi = 10^{-5}$ and $E = 1.5 \times 10^{11}\,\mathrm{N/m^2}$, $\nu = 0.2$, $\rho = 1000\ \mathrm{kg/m^3}$. The cross-sections of the vertical and horizontal stiffeners were taken equal to 25 × 30 and 25 × 20 mm, respectively.

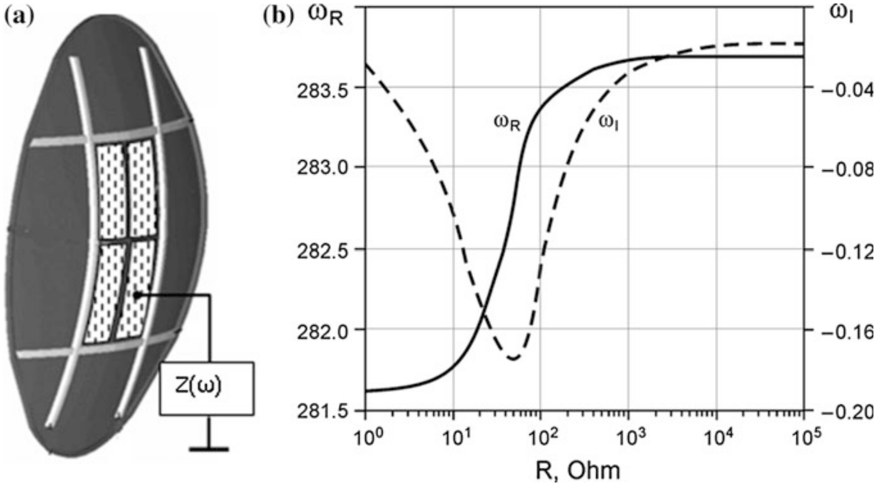

Fig. 7 Schematic of the parabolic shell (**a**), first resonance frequency ω_R and corresponding damping index ω_I versus resistance for a circuit with only one component R (**b**)

The possibility to enhance the damping effect with the use of piezoelectric materials was studied by calculating this shell with four transversely isotropic piezocomposite patches of thickness 1 mm in its central part the electrodes of which can be connected to external *RLC* circuits.

The piezocomposite with crosswise polarization has the following electromechanical characteristics:

$$\begin{aligned}
C_{11} &= 13.9\times10^{10}\ \mathrm{N/m^2}, \quad C_{12} = 7.78\times10^{10}\ \mathrm{N/m^2},\\
C_{13} &= 7.43\times10^{10}\ \mathrm{N/m^2}, \quad C_{33} = 11.5\times10^{10}\ \mathrm{N/m^2},\\
C_{44} &= 2.56\times10^{10}\ \mathrm{N/m^2}, \quad \beta_{13} = -52\,\mathrm{C/m^2},\\
\beta_{33} &= 151\,\mathrm{C/m^2}, \quad \beta_{15} = 127\ \mathrm{C/m^2},\\
e_{11} &= 6.45\times10^{-7}\ \mathrm{F/m}, \quad e_{33} = 5.62\times10^{-7}\ \mathrm{F/m},\\
\rho &= 7700\ \mathrm{kg/m^3}.
\end{aligned}$$

The problem is solved to find circuit parameters that provide the highest vibration damping of the system. By way of illustration, Fig. 7b shows the first resonance frequency ω_R and corresponding damping index ω_I versus resistance for a circuit with only one component R. In this case, the maximum damping is found at R = 36 kΩ.

6 Conclusion

Thus, we considered the problem of simulation and optimization of dynamic characteristics, namely, the resonance frequencies and the parameters responsible for damping properties of smart systems based on piezoelectric materials with external electric circuits comprising resistance, capacitance and inductance. To determine the specified dynamic characteristics, the natural vibration problem of electroviscoelastic solids with external electric circuits was proposed. The boundary conditions for passive external circuits with different connections of circuit elements and for active external circuits were formulated.

The main aspects of numerical realization of the problem by the finite element method were considered. Numerical examples were given to demonstrate efficient application of the natural vibration problem of an electroviscoelastic solid with external electric circuits to optimize damping properties of smart systems based on piezoelectric materials.

Acknowledgment The work was supported by grant of the President of the Russian Federation No. NSh-2590.2014.1 and Program of the Presidium of RAS No. 12-P-1-1018.

References

1. New Materials for Next-Generation Commercial Transports.: Report committee on new materials for advanced civil aircraft. Commission on Engineering and Technical Systems, National Research Council, USA (1996)
2. Moheimani, S.O.R., Fleming, A.J.: Piezoelectric Transducers for Vibration Control and Damping. Springer, Berlin (2006)
3. Sodano, H.A.: Macro-fiber composites for sensing, actuation and power generation. Ph.D. thesis, Blacksburg, Virginia (2003)
4. Viana, F.A.C., Steffen Jr, V.: Multimodal vibration damping through piezoelectric patches and optimal resonant shunt circuits. J. Braz. Soc. Mech. Sci. Eng **XXVIII**(3), 293–310 (2006)
5. Song, Z.-G., Li, F.-M.: Active aeroelastic flutter analysis and vibration control of supersonic beams using the piezoelectric actuator/sensor pairs. Smart Mater. Struct. **20**, 1–12 (2011)
6. Agnes, G.S., Mall, S.: Structural integrity issues during piezoelectric vibration suppression of composite structures. Compos. B **30**, 727–738 (1999)
7. Elvin, N.G., Elvin, A.A.: The flutter response of a piezoelectrically damped cantilever pipe. J. Intel. Mat. Syst. Str. **20**, 2017–2026 (2009)
8. Niederberger, D.: Smart damping materials using shunt control. Ph.D. thesis, Zurich (2005)
9. Park, C.H., Inman, D.J.: Enhanced piezoelectric shunt design. Shock Vib. **10**(2), 127–133 (2003)
10. Callahan, J., Baruh, H.: Active control of flexible structures by use of segmented piezoelectric elements. J. Guid. Control. Dynam. **19**(4), 808–815 (1996)
11. Park, G., Sausse, M., Inman, D.J., Main, J.A.: Vibration testing and finite element analysis of an inflatable structure. AIAA. J. **41**(8), 1556–1563 (2003)
12. Nye, T.W., Manning, R.A., Qassim, K.: Performance of active vibration control technology: the ACTEX flight experiments. Smart Mater. Struct. **8**, 767–780 (1999)

13. Nuffer, J., Bein, T.: Application of piezoelectric materials in transportation industry. In: Global Symposium on Innovative Solutions for the Advancement of the Transport Industry, pp. 1–11. San Sebastian, Spain, 4–6 Oct 2006 (2002)
14. Kawiecki, G., Jesse, S.: Rosette piezotransducers for damage detection. Smart Mater. Struct. **11**, 196–201 (2002)
15. Hansson, J., Takano, M., Takigami, T., Tomioka, T., Ya, Suzuki: Vibration suppression of railway car body with piezoelectric elements (a study by using a scale model). ISME Int. J. C **47**(2), 451–456 (2004)
16. Bronowicki, A.J., Abhyankar, N.S., Griffin, S.F.: Active vibration control of large optical space structures. Smart Mater. Struct. **8**, 740–752 (1999)
17. Bisegna, P., Caruso, G.: Optimization of a passive vibration control scheme acting on a bladed rotor using an homogenized model. Struct. Multidiscip. O **39**, 625–636 (2009)
18. Kajiwara, I., Uchiyama, T., Arisaka, T.: Vibration control of hard disk drive with smart structure technology for improving servo performance. In: Ulbrich, H., Ginzinger, L. (eds.) Motion and Vibration Control, pp. 165–176. Springer, Heidelberg (2009)
19. Head Intelligence Technology. http://www.ski.ru/static/127/2_11511.html (2014). Accessed 26 Sept 2014
20. Schulz, M.J., Pai, P.F., Inman, D.J.: Health monitoring and active control of composite structures using piezoceramic patches. Compos. B **30**, 713–725 (1999)
21. Sung, J.K., James, D.J.: Quasi-static control of natural frequencies of composite beams using embedded piezoelectric actuators. Smart Mater. Struct. **4**(2), 106–112 (1995)
22. Simpson, J.O., Wise, S.A., Bryant, R.G., Cano, R.J., Gates, T.S., Hinkley, J.A., Rogowski, R. S., Whitley, K.S.: Innovative materials for aircraft morphing. In: SPIE'S 5th Annual International Symposium on Smart Structures and Materials, pp. 1–10. San Diego, CA, 1–5 March 1998
23. Piezo Film Product Guide and Price List. Measurement Specialities, Inc. http://www.meas-spec.com (2014). Accessed 26 Sept 2014
24. OAO "NII Elpa". http://www.elpapiezo.ru/longitudal.shtml (2014). Accessed 26 Sept 2014
25. Kalinchuk, V.V., Belyankova, T.I.: Surface dynamics of heterogeneous media. Fizmatlit, Moscow (2008)
26. Advanced Materials Technology Company. http://www.advancedcerametrics.com, http://www.meas-spec.com (2014). Accessed 26 Sept 2014
27. Janos, B.Z., Hagood, N.W.: Overview of active fiber composite technologies, MST news. Actuator applications. Home Autom. **3**, 25–29 (1998)
28. Pizzochero, A.: Residual actuation and stiffness properties of piezoelectric composites: theory and experiment. M.Sc. dissertation (1998)
29. Nguyen, C.-H., Kornmann, X.: A comparison of dynamic piezoactuation of fiber-based actuators and conventional PZT patches. J. Intel. Mat. Syst. Str. **17**(45) (2006). doi:10.1177/1045389X06056065
30. Bennett, J., Hayward, G.: Design of 1-3 piezocomposite hydrophones using finite element analysis. IEEE T. Ultrason. Ferr. **44**, 565–574 (1997)
31. Sigmund, O., Torquato, S., Aksay, I.A.: On the design of 1-3 piezocomposite using topology optimization. J. Mater. Res. **13**, 1038–1048 (1998)
32. Smith, W.A., Auld, B.A.: Modeling 1-3 composite piezoelectrics: thickness mode oscillations. IEEE T. Ultrason. Ferr. **41**, 40–47 (1991)
33. Lloyd, J.M.: Electrical properties of macro-fiber composite actuators and sensors. Ph.D. thesis, Blacksburg, Virginia (2004)
34. Sato, H.: Study on metal core-assisted piezoelectric complex fiber. AIST Today **3**(7), 1–13 (2003)
35. Forward, R.L.: Electronic damping of vibrations in optical structures. J. Appl. Optics **18**(5), 690–697 (1979)
36. Hagood, N.W., von Flotow, A.: Damping of structural vibrations with piezoelectric materials and passive electrical networks. J. Sound Vib. **146**(2), 243–268 (1991)

37. Lesieutre, G.A.: Vibration damping and control using shunted piezoelectric materials. Shock Vib. Dig. **30**(3), 187–195 (1998)
38. Caruso, G.: A critical analysis of electric shunt circuits employed in piezoelectric passive vibration damping. Smart Mater. Struct. **10**, 1059–1068 (2001)
39. Moheimani, S.O.R., Fleming, A.J., Behrens, S.: On the feedback structure of wideband piezoelectric shunt damping systems. Smart Mater. Struct. **12**, 49–56 (2002)
40. Wu, S.Y.: piezoelectric shunts with parallel R-L circuit for structural damping and vibration control. In: Proceedings of SPIE Smart Structures and Materials, Passive Damping and Isolation. SPIE, vol. 2720, pp. 259–269 (1996)
41. Washizu, K.: Variational Methods in Elasticity and Plasticity. Pergamon Press, London (1982)
42. Parton, V.Z., Kudryavtsev, B.A.: Electromagnetoelasticity of Piezoelectric and Electroconductive Bodies. Nauka, Moscow (1988)
43. Karnaukhov, V.G., Kirichok, I.F.: Electrothermal Viscoelasticity. NaukovaDumka, Kiev (1988)
44. Kligman, E.P., Matveenko, V.P.: Natural vibration problem of viscoelastic solids as applied to optimization of dissipative properties of constructions. Int. J. Vib. Control **3**(1), 87–102 (1997)
45. Kligman, E.P., Matveenko, V.P., Yurlova, N.A.: Dynamic characteristics of thin-walled electroelastic systems. MTT **2**, 179–187 (2005)
46. Matveenko, V.P., Kligman, E.P., Yurlova, N.A., Yurlov, M.A.: Optimization of the dynamic characteristics of electroviscoelastic systems by means of electric circuits. In: Irschik H., Krommer M., Belyaev A.K. (eds.) Advanced Dynamics and Model Based Control of Structures and Machines. Springer, Wien, pp. 151–158 (2011)

Bulk Metallic Glasses: Mechanical Properties and Performance

V. Nekouie, G. Abeygunawardane-Arachchige, A. Roy and V.V. Silberschmidt

Abstract In this paper, a history of development of bulk metallic glasses (BMGs) was presented, followed by a review of fundamental mechanisms of their deformation and fracture. In this study, observations of fracture surfaces of the Zr-Cu-based BMG exposed to a 3-point test revealed features that are different from those observed in crystalline materials. Indentation techniques were extensively used to characterise elastic deformation of the studied BMG alloy, followed by a systematic analysis of initiation and evolution of shear-band localisation in the indented material. Our results, obtained with the suggested wedge-indentation technique, demonstrated initiation of shear bands in the material volume. This technique can be particularly useful for development of appropriate constitutive models to analyse plastic events in amorphous materials in the small-length scale. A current state of constitutive models of deformation and fracture behaviour of BMGs are presented together with modelling challenges. Simulation of simple tensile and compressive tests were conducted with JH-2, JHB and Drucker-Prager constitutive models by employing identical boundary conditions, type of element and specimen's geometry. Based on the obtained simulation results, the JH-2 model was considered as not suitable for quasi-static analysis due to ambiguity of the data produced with it for uniaxial tensile and compressive conditions. However, it is concluded that the extended Drucker-Prager and JHB models can be used to study deformation modes in BMGs.

V. Nekouie (✉) · G. Abeygunawardane-Arachchige · A. Roy · V.V. Silberschmidt
Wolfson School of Mechanical and Manufacturing Engineering, Loughborough University,
Loughborough, Leicestershire LE11 3TU, UK
e-mail: v.nekouie2@lboro.ac.uk

V.V. Silberschmidt and V.P. Matveenko (eds.), *Mechanics of Advanced Materials*,
Engineering Materials, DOI 10.1007/978-3-319-17118-0_5

1 Introduction

1.1 Motivation

Bulk metallic glasses (BMGs) are relatively new materials under that are increasingly for various applications due to their unique and remarkable properties. These properties make them ideal candidate for such applications as MEMS (Microelectromechanical systems), miniaturised biomedical devices and implants as well as micro-robotics devices. In the last few decades, researches have led to the discovery and development of new BMGs in a variety of multi-component alloy systems including those on rare earths based with easy verification during conventional solidification resulting in thicknesses of several centimetres and weigh up to several kilograms [20, 28]. BMGs have received much scientific and technological attention due to their prominent mechanical properties such as a high ratio of elastic limit to the Young's modulus and higher fracture toughness, when compared to their crystalline counterparts of similar composition. On average specific strength of metallic glasses is more than twice of their crystalline counterparts. Metallic glasses also absorb less energy in stress-induced deformation compared with crystalline materials. This is typically attributed to the absence of a long-range order in their atomic structure and lack of defects such as dislocations, which control ductility in traditional metallic materials. Typically, inorganic glasses are brittle at room temperature, exhibiting a smooth fracture surface as a result of mode-I brittle fracture. BMGs have nearly no plasticity in the macro-scale under tensile and compressive deformations and their mechanical behaviour is very sensitive to internal and surface flaws such as microcracks and voids. The cause of this limited macroscopic plasticity in BMGs is the absence of grain structure and an extreme localisation of plastic flow into narrow shear bands that initiate strain-softening. As shown in Fig. 1, metallic glasses fail on the plane of maximum shear stress under tension loading, which is roughly at 45 °C to the tension axis. The resulting fracture surfaces have two distinct regions smooth and veined. For BMGs, at

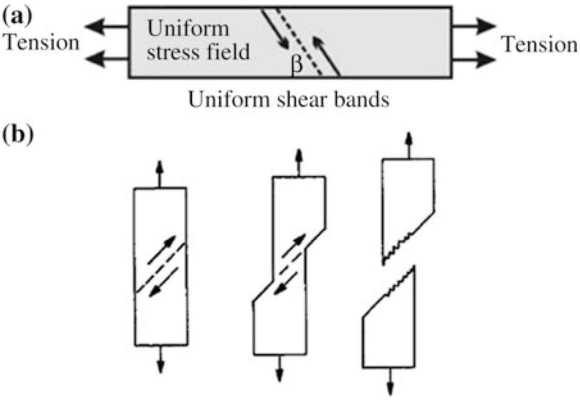

Fig. 1 **a** Shear band formation in metallic glass samples in uniaxial tension. **b** Fracture process of BMG by which specimen in tension with formation of smooth and veined regions [20]

temperatures significantly lower than the glass transition (Tg), observed plastic deformation is spatially and temporally inhomogeneous and carried by highly localised, narrow shear bands [20].

Significant efforts have been made to develop glassy metal, capable to distribute shear bands uniformly or to hinder their propagation in order to enhance their deformability. Some recent experiments on sub-micron and nano-sized metallic glass specimens showed that a process of shear localisation became more stable and less catastrophic, when compared to that in large-size samples [7]. In this chapter, we will first describe the manufacturing history of BMGs including important factors, which influence their manufacture. Subsequently, the deformation main mechanisms of metallic glasses will be analysed, highlighting the theories proposed for inhomogeneous plastic flow and explaining the effect of temperature and strain rate on the plastic flow. This will be followed by discussion about length-scale dependency of mechanical behaviour of BMGs under loading conditions. Finally, the current understanding of the constitutive models of deformation and fracture behaviour will be presented together with modelling challenges.

1.2 Historical Background

Natural glass existed from the early times of the Earth and man-made (non-metallic) glasses were fabricated in Egypt and Eastern Mesopotamia from 3500 BC. In contrast, amorphous metal or metallic glasses were first reported only around 1960s. These could be processed using solid-state amorphisation [30] via hydrogen absorption [56, 62], mechanical alloying [1], or heat treatment enabling anomalous diffusion in crystalline bi-layers [50]. In 1960, Klement et al. [32] fabricated a metallic glass (Au-Si alloy) by rapid quenching from 1300 °C to room temperature with high cooling rate of 10^6 Ks^{-1} [32]. From late 1980s, metallic glasses were manufactured in a variety of multi-component alloys with cooling rates less than 100 Ks^{-1} and thickness of several centimetres. The first commercial metallic glass, $Zr_{41.2}Cu_{12.5}Ni_{10}Ti_{13.8}Be_{22.5}$ alloy named Vitreloy 1, was produced by Johnson and Peker in 1992 with a critical cooling rate of 1 Ks^{-1}. Over the last 40 years, critical casting thickness was increased by more than three orders of magnitude, and high quantity of amorphous components was formed, as shown in Fig. 2. Inoue et al. [25] suggested three empirical rules to stabilise a supercooled metallic liquid. Firstly, the multi-component system should include three or more elements as the presence of several elements causes a significant extension of the supercooled liquid region before crystallization. Secondly, there should be a considerable difference (greater than ~ 12 %) in the atomic sizes of the main constituent elements. The atomic size differences result in a highly dense random packed structure in amorphous phases. Finally, the elements should have negative heats of mixing with each other; these increase the energy barrier at the solid-liquid interface and accelerate atomic diffusivity. Hence, the supercooled liquid temperature is extended

Fig. 2 Increase in critical casting thickness for various glass-forming alloys over 50 years [39]

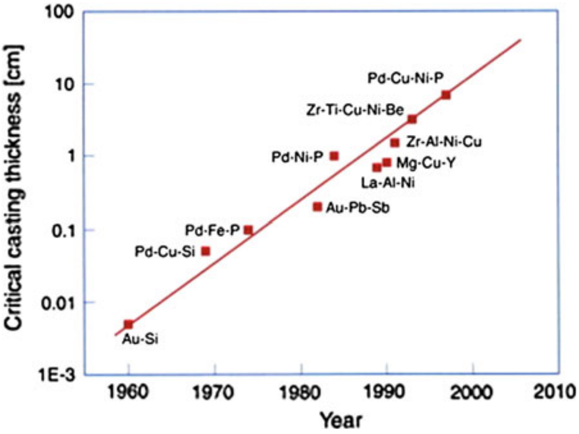

due to slowing local atomic rearrangement and crystal nucleation rate. A variety of BMGs such as Fe-based, Cu-based etc. were synthesized employing these rules.

Elastic properties of metallic glasses can be derived from the properties of constituent metallic element using a modified rule of mixture as suggested by Liu [37]; it was shown that the elastic properties of metallic glass cannot be predicted with the conventional rule of mixture in individual alloy systems. This approach originated from the motion of disordered atomic structures in metallic glasses and their intrinsic local heterogeneities. In general, metallic glasses can be considered as having short- and medium- range orders in the matrix with excess of solvent atoms. Systems with short-range orders can be modelled as solute-centred clusters while those medium-range orders are always characterized as interconnected clusters. Liu et al. [37] proposed that metallic glasses can be treated as hybrids composed of dual phases of clusters/superclusters and solvent matrix.

As shown in Fig. 3, a stiff phase (S) represents the clusters/superclusters and (M) shows a solvent matrix with lower stiffness. In Fig. 3b, BMG is considered as a homogenous material, in which the local stress is distributed uniformly among different constitute atoms. As shown in Fig. 3d, the two phases are supposed to sustain equal stress under an applied elastic loading; however, their strain responses may differ. As a result, the global elastic moduli of metallic glasses (G) can be calculated according to the modified "rule of mixture" under iso-stress conditions [37]:

$$\frac{1}{G} = \frac{V_m^M f^M}{G^M V_m} + \frac{V_m^S f^S}{G^S V_m},$$

where V_m^M and V_m^S are the molar volumes of the matrix and clustres/superclusters, respectively, G^M and G^S are their elastic moduli and f^M and f^S are the fractions of the two phases which is considered that $f^M + f^S = 1$. Unlike the conventional "rule of mixture", the hybrid model with dual phases, provides a relation to validate the

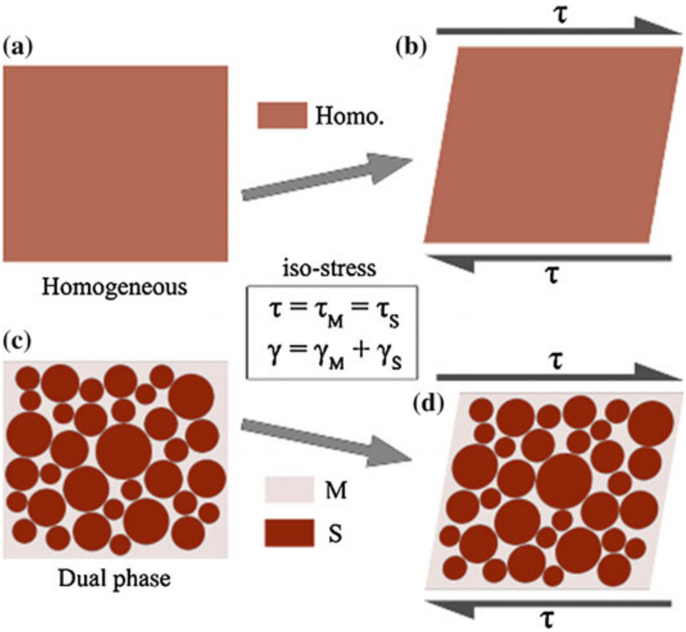

Fig. 3 Schematics ideally homogeneous BMG (**a**) and (**b**), and, dual- phases BMG (**c**) as well as their strain responses to an applied elastic shear stress τ (d). The compliant solvent matrix **M** and stiff clusters/superclusters **S** are supposed to sustain equal stress **s**, but display different strain γ, which conforms to the iso-stress condition [37]

calculated value of the elastic modulus with its experimental value. The model helps to predict and design the elasticity of metallic glasses much more precisely based on their alloy compositions. In addition, it is capable to describe softening phenomena in BMGs when the global (G) decreases due to increasing base metal contents.

Poisson's ratio (υ) of BMGs is closely related to some factors such as fragility a the liquid and its glass-forming ability. Pt-based metallic glass with a high Poison's ratio of 0.42 shows high plastic strain in compression and high fracture toughness [47]. Lewandowski et al. [35] proposed a general relation between υ of BMGs and fracture energy for a variety of as-cast metallic glasses based on Ce, Cu, Fe, Mg, Pd, Pt as well as a Zr-based glass in different annealing conditions. These metallic glass showed significant toughness only when the υ value was higher than a critical value of 0.31–0.32. The measured toughness value was considered as an intrinsic property of metallic glasses; however, they could be affected by extrinsic factors, such as the presence of brittle oxide inclusions [38]. The choice of composition can significantly influence the pattern of shear banding and, consequently, mechanical properties of the metallic glasses. It is obvious that the shear bands spacing and shear offset are important factors in shear bands pattern and they were typically decreased with higher value of v of BMGs. This prediction was verified in a limited number of experiments.

2 Deformation and Failure Mechanism

2.1 Deformation Behaviour

A number of mechanistic theories have been proposed to describe the plastic flow and deformation behaviour of metallic glasses. The plastic deformation in BMGs was described using free-volume and shear transformation zones (STZs) proposed in Argon and Spaepen's model, based on the atomic motion [2, 52]. A free volume mechanism includes the redistribution of free volumes, where a single crystal atom jumps from an area of low free volume to an area of high free volume, as illustrated in Fig. 4. As can be seen, shear transformation takes place by reorganization of a local cluster of randomly closed-packed atoms referred to as "shear transformation zones (STZs)", which are thermally activated around high free volume regions under inelastic transition.

At macro-scale, the deformation mechanism of metallic glasses based on the free volume and STZs theory can occur homogenously or inhomogeneously depending on the values of strain rate, temperature and applied stress. Thus, the deformation map for metallic glasses was developed based on that for crystalline materials proposed by Ashby and Frost [17]. Spaepen [52] suggested a deformation map showing a transition from a homogeneous behaviour to inhomogeneous one as a

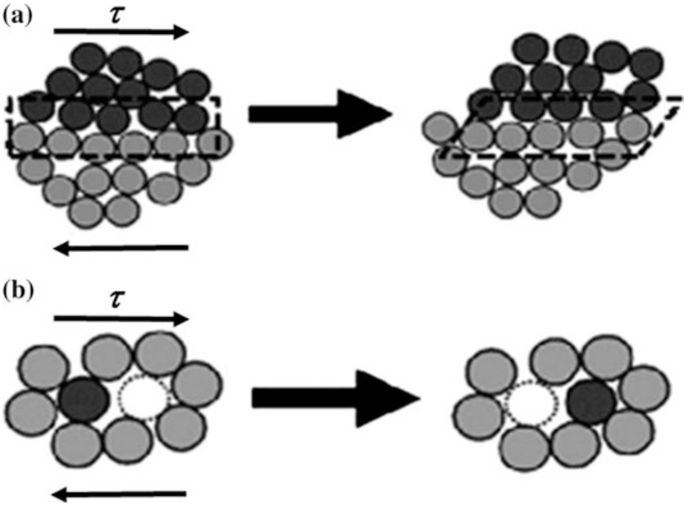

Fig. 4 Schematics of deformation mechanism: **a** STZ; **b** free volume [2]

function of temperature and strain rate. Based on this deformation map, homogeneous deformation happens at low stresses and high temperatures considering also that stress is a strong function of strain rate, as indicated by strain rate contours. Moreover, inhomogeneous deformation takes place at high stress levels and low temperature, and it is insensitive to the strain rate. The suggested deformation map can be used for melt-spun metallic glass ribbons as BMGs show wide-range supercooled- liquid regions.

Schuh et al. [48] modified the previous deformation-mechanism map to incorporate other observations. They indicated the deformation modes with two complementary deformation maps using the concept of STZ. Figure 5a represents normalised stress as a function of temperature similar to that proposed by Spaepon [52]. Figure 5b is in a coordinates of shear strain rate and temperature and follows the analysis suggested by Megusar et al. [40]. The most important aspect is that the deformation map presents a boundary, at which a transition occurs from the homogeneous mode at high temperature and low stresses and strain rates to the inhomogeneous mode of deformation at low temperature and higher levels of stress and strain rate. As shown in Fig. 5, Schuh et al. [48] modified the deformation map with inclusion of strain rate contours instead of putting a single dividing line to show this transition. In the map, the homogeneous regime is divided into “elastic”, “Newtonian”, and “non-Newtonian” sub regions. The transition Newtonian to non-Newtonian occurs at 10^{-5} s^{-1}; the non-Newtonian flow is observed at strain rate below this value. However, it is important to mention that at high enough shear rates, the non-Newtonian flow as well as shear localisation can happen at high temperatures even in the supercooled region. The pressure dependence is also shown in Fig. 5a as iso-pressure contours for a single value of shear stress. The pressure effect on inhomogeneous behaviour can be more clearly observed in Fig. 5b with iso-pressure contours for various applied shear stresses. This figure presents the effect of shear strain rate on shear banding and serrated flow patterns as the high strain rate and lower temperature result in shear bands of smaller offset that are more finely spaced. The deformation map developed by Schuh et al. [48] does not consider the evolution of glass structure during the deformation and cannot be used to explain the fracture behaviour. However, this map can be employed to compare the mechanical response of different metallic glasses at same absolute temperature (e.g. room temperature) but at different homologous temperatures.

2.2 Length Scale Effect

Modern advanced manufacturing processes often need to control component’s dimensions and material’s microstructure down to a nanometre level. In addition, recent advances such as focused ion beam (FIB), which a technique for specimen preparation or nanoindentation allowed materials characterisation at micron and sub-micron length scales. These developments help to achieve or design new material systems at micron and sub-micron scales as an alternative to traditional

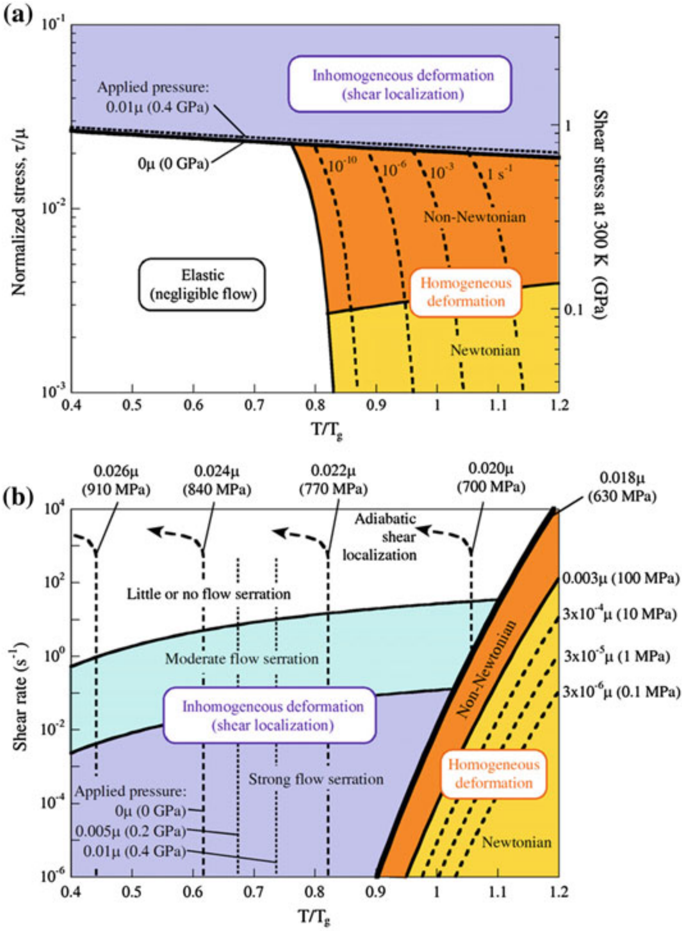

Fig. 5 Deformation maps for **a** normalised stress and **b** strain rate and various normalised temperatures [48]

strengthening techniques (Fig. 6) and it is necessary to investigate mechanical properties and deformation mechanism of MGs to understand their length-dependency and its effect on structural integrity.

Various research groups produced contradicting conclusions on the length-scale effect, based on different experiments performed on various BMG systems. The magnitude of yield stress measured for a large number of Cu-based and Zr-based micropillars are plotted in Fig. 7 as a function of the effective pillar diameter [21]. Apparently, the yield stress is independent of pillar diameter over the studied size scale due to a lack of dislocation sliding. In addition, it was claimed that MG strength is controlled by interatomic bonding, and there is a rarely linear relationship with the elastic modulus. However, it was shown that there was a considerable

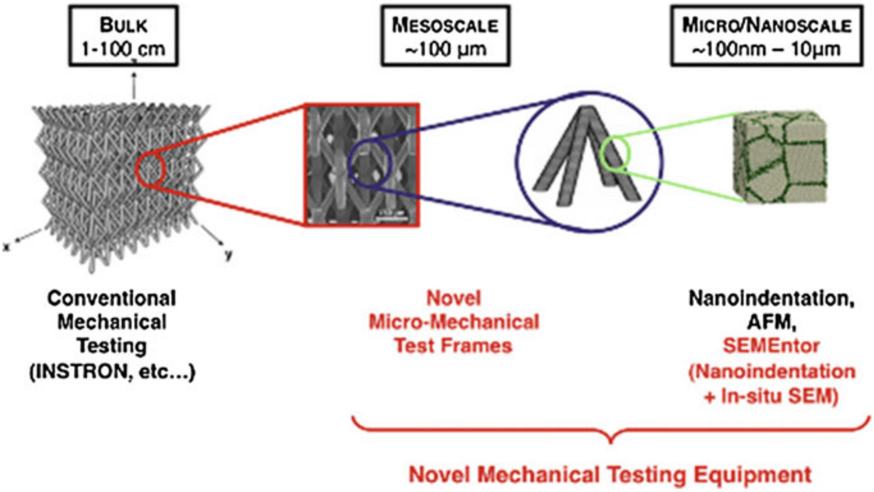

Fig. 6 Micro-truss structure at various length scales as concept of "architectured" material [21]

Fig. 7 Yield stress versus pillar diameter for Cu- and Zr-based metallic glasses with trend line indicated [21]

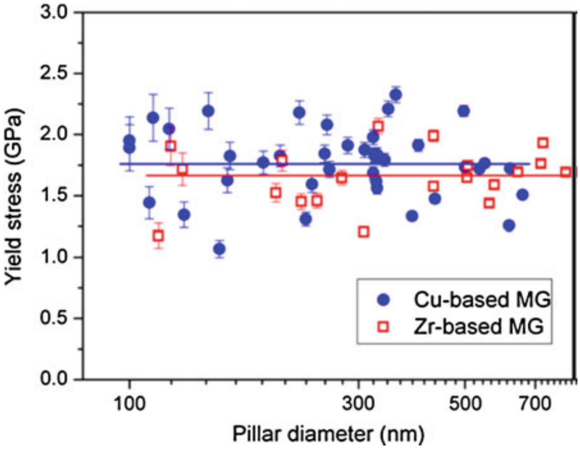

size effect leading to increase yield stress of micrometre sized specimens of Mg-based and Zr-based metallic glasses. Other groups carried out micro-compression experiments on metallic glass micropillars and reported a correlation between a reduced size and several mechanical properties including maximum plastic strain before failure, yield strength and deformation mode; however, most of them were inconsistent as can be seen in Table 1. An imperfect geometry, including tapering and top curvature of cylindrical pillars, is the main reason for the lack of agreement in micro-compression tests [20]. Moreover, when the sample size is reduced to nanometre scale, surface diffusion may contribute to plastic deformation and yielding, resulting in a decrease in strength. Schuster et al. [49] also confirmed that

Table 1 Literature on size effect of strength in metallic glasses [21]

References	BMGs	Strength size dependence
Lee et al. [34]	Mg-based metallic glass	Dramatic increase
Lai et al. [33]	Zr-based metallic glass	Dramatic increase
Volkert et al. [58]	Pd-based metallic glass	Slight reduction
Schuster et al. [49]	Pd-based metallic glass	Slight reduction
Dubach et al. [13]	Zr-based metallic glass	No change
Jang and Greer [28]	Zr-based metallic glass	Small increase
Bharathula et al. [3]	Zr-based metallic glass	Yes
De Hosson et al. [12]	Zr-Cu-based metallic glass	No change

there was no size-dependent strength and deformation mode in compression of a Pd-based metallic glass. However, this finding is in contrast to other studies showing dramatic size effects in increasing the yield stress of micrometer sized Mg-based and Zr-based metallic glasses [21].

As reported by Shimizu [21] that the critical lengths to nucleate and develop shear bands is 100 nm. If the specimen length is smaller than the critical length, shear bands are localised in the form of necking during plastic deformation of MG samples are in tension. Greer et al. [20] showed that Zr-based MG nano-pillars with 100 nm diameter could attain ceramic-like strength (2.25 GPa) and metal like ductility (25 %) simultaneously for non-tapered, free stranding nano-tension specimens for their in situ uniaxial tension [28]. Shear banding developed and distributed deformation was observed in the form of non-localised flow followed by necking. However, it was found that the yield strength of metallic glass nanopillars showed size independency up to 500 nm diameters with changing deformation modes.

As results a phenomenological model of two competing processes was proposed to explain the unique size-dependency including highly localised and homogeneous deformation mechanisms, related to the micro pillar diameter and the level of applied stress. These characteristics of plasticity impart distinct features to the mechanical behaviour of BMGs, such as flow softening, pressure sensitivity and ductile-to-brittle transition [57]. Thus, studying the influence of plasticity at microscopic length scales becomes essential for the development of robust modelling frameworks for BMGs.

2.3 *Modelling of Deformation in BMGs*

Degradation of elastic properties is related to accumulation of damage in brittle materials and primarily caused by evolution of micro cracks. Degradation of mechanical properties is a unique feature of brittle material behaviour. Both mode and stability of crack growth in brittle materials strongly depend on the sign and magnitude of applied stress. Weakening of effective elastic properties of a solid by a distribution of micro cracks and other defects was accounted in several analytical models by Nemat-Nasser and Li [43]. Various models were proposed for brittle fracture of materials [60] by Glucklich [19], Brace and Bombolaski [5], Brandtzaeg et al. [6] namely; energy model, stress model, sliding crack model and lattice model, respectively. In all these approaches the material was assumed to be linear elastic and the analyses were limited to static or quasi-static conditions. Continuum damage mechanics models have were also used to study brittle materials with some critical drawbacks (see [59]), while micromechanical damage models are often computationally inefficient and impractical.

For metallic glasses, regardless of the experimental evidences of shear band initiation, the origin of shear band remains ambiguous. Theoretical investigations were conducted for shear -band initiation and evolution by Steif et al. [53], Huang et al. [24] and Jiang and Dai [29]. Ruan et al. [47] suggested a new model incorporating atomic structural change and free-volume generation but it lacks experimental validation. In this, the material was assumed to be viscoelastic to derive high- temperature stress–strain relationships and extension to low temperature scheme is a significant challenge.

Most acclaimed modelling strategies for BMG, mentioned in previous sections, such as free- volume theory of Argon and Spaepen and the STZ-based deformation mechanism are formulated for the atomistic domain and could not be employed in the continuum approach. For instance, as mentioned by Argon et al. [2] that the theory was based on free-volume regions typically conceived to be 5 atoms diameters across and Ghosh and Cheng [10] proposed a free volume-based constitutive model that accounts for transition from inhomogeneous to homogeneous deformation and non-Newtonian to Newtonian viscosity. The simulation results exhibit hydrostatic pressure dependence but for a certain range of temperature and strain rates. However, it does not clarify the size effect exhibited by metallic glasses. Molecular dynamics (MD) based simulations also provide deeper understanding of deformation mechanisms of metallic glasses, but for the nano scale. For instance Chu et al. [11] employed the MD scheme to conduct nano-indentation simulations of $Cu_{47}Zr_{47}Al_6$ metallic glass and Wang [59] used it to simulate nano-indentation of $(Cu_{50}Zr_{50})_{100\text{-}x}Al_x$ thin film to study the effect of different Al content on material properties. Shi and Falk [51] also adopted MD to perform 2D and 3D simulations of nano-indentation of metallic glasses. However, MD analysis is limited to high deformation rates ($>10^7\ s^{-1}$) and requires a considerable computational time. So, the use of continuum based constitutive models can support a study of the size effect exhibited by metallic glasses [54].

Finite-element analysis also contributed to the analysis of mechanical behaviour of BMG by Gao [18] and Chen et al. [9] and several contributors. Based on their studies, deformation of BMG was simulated at room temperature employing the free-volume method and considered only the effect of free volume on deformation. Later, Yang et al. [61] induced the evolution temperature into the study, while some researchers considered the effect of hydrostatic stress as well. Still, these works focused only on some facts of mechanical behaviour of BMGs and under certain deformation conditions. As mentioned by Thamburaja et al. [54]; these models were limited to relatively low strain rates and neglected the material failure of more advanced scheme with contributions of free volume, temperature, and hydrostatic stress was considered by Li et al. [36] as it also incorporated a failure criterion based on a critical free-volume concentration. However, as mentioned earlier, a single simulation still struggles to represent the entire pattern of deformation and failure in BMG [36].

3 Mechanical Characterisation of Bulk Metallic Glasses

3.1 Introduction

In 1970s and 1980s, it was difficult to measure mechanical properties of metallic glasses due to the limitations linked to small specimen volumes, which made implementation of conventional test techniques quite difficult. During that period, standard microhardness measurement was a common method to measure the mechanical strength of thin ribbons or powder of metallic glass. Advances in indentation technique allowed for researchers to perform mechanical characterisation at small scale such indentation experiments play a major role in analysis of mechanisms of plastic flow in metallic glasses. As explained previously, there are different, sometimes contradicting hypotheses about the deformation mechanisms of MGs at microscale. Hence, further studies are required to understand initiation and propagation of shear bands in the volume and at surface of metallic glasses. In this section, characterisation of a Zr-Cu-based metallic glass $Zr_{48}Cu_{36}Al_8Ag_8$ (at.%) across different length scales is discussed. Three different experimental tests were employed to assess the mechanical behaviour. First, macroscopic three-point bending tests were carried out in order to determine its Young's modulus and Poisson's ratio. The simplicity of determining the elastic modulus using bending test is worth considering in comparison to tensile test, which often suffers from fixation, gripping and alignment problems. Secondly, indentation tests were conducted to characterise shear bands with a Nano Test system (Micro Materials Ltd.) employing with a spherical and Vickers indenters. Finally, wedge-indentation experiments developed in house was performed to study shear-band evolution in the volume of the material and support for simplified analytical and numerical modelling schemes. The microstructure of samples was identified using transmission electron microscopy (TEM) and X-ray diffraction (XRD), scanning electron microscopy (SEM) was used to observe evolution of shear bands on the deformed surfaces.

3.2 XRD and TEM

The amorphous nature of the supplied beam samples of MG was initially investigated using X-ray diffraction. As shown in Fig. 8, the structure exhibited a broad

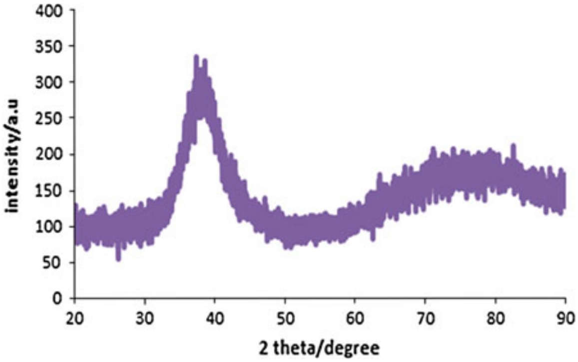

Fig. 8 XRD pattern of Zr-Cu-based metallic glass

diffuse peak without any detectable crystalline peaks on the XRD pattern showing the amorphous state. The microstructure of the as-cast BMG was further characterised with TEM. The TEM results confirmed the amorphous nature of the alloy as the first halo ring of a selected area electron diffraction (SAED) pattern did not show any presence of nanocrystals.

3.3 Bending Test

To perform the three-point bending test, beam samples with a length of 40 mm and a cross section of 10 mm × 2 mm were prepared. The bending tests were conducted using a universal testing machine Instron 3345. A biaxial strain gauge was attached to the specimen to measure the strains along the axial and transverse direction during the loading process. The load was applied by the mechanical test system operating with a displacement rate of 0.5 mm/min. The macroscale bending tests consistently led to an elastic modulus (E) of 95 GPa with a Poisson's ratio (v) of 0.35.

Figure 9 shows SEM images of fracture surface morphology for Zr-Cu-based BMG. In compression mode, the fracture surface is typically smooth with periodic bands in the direction of fracture. Formation of a vein pattern indicates that fracture occurred via shear mode II in compression mode and a river patterns are related to a fast tensile fracture mode in tension mode. The differences in fracture surfaces character are associated with the influence of normal stress and the dominance of shear stress in tension and compression modes, respectively. Shear-band zones can be found in both tension and compression sides as shown in Fig. 9. Apparently, when shear bands appeared initially, the loading curve did not show any pop-in, suggesting that the stress level at shear band initiation was smaller than flexural yield strength. Usually shear bands play the weakening role in materials and lead to lower strength and stiffness compared to that of undeformed BMG "matrix". In addition, it was also reported that shear bands often dilated and produced heat

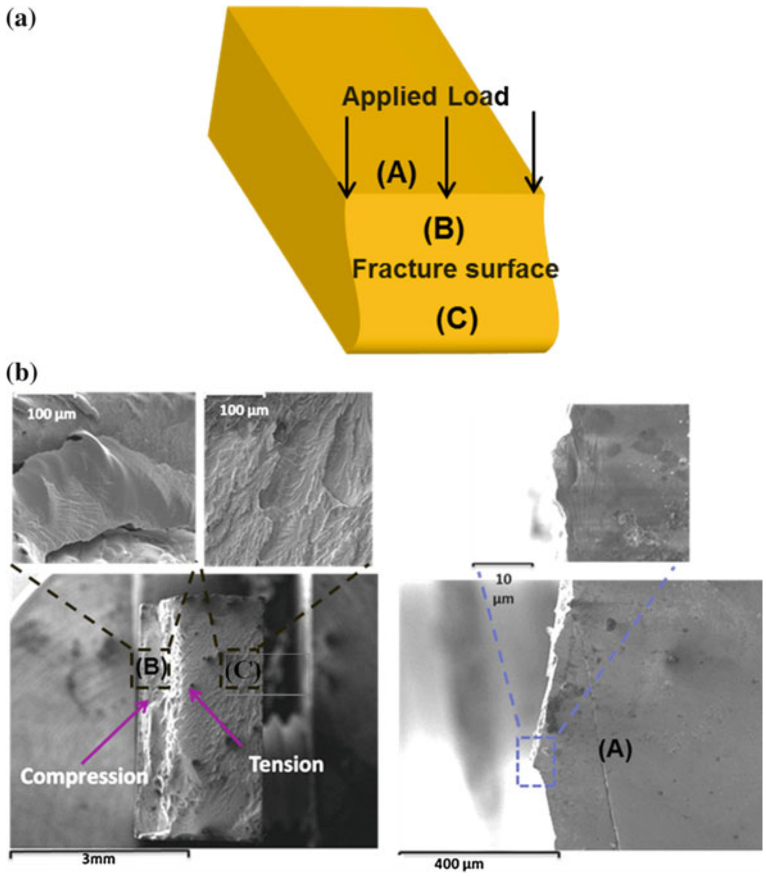

Fig. 9 SEM images of fracture surfaces of Zr-Cu-based metallic glass due to 3-point bending test. **a** Schematic of fracture surface observation. **b** High magnification images show presence of vein pattern and shear steps on fracture surface

during plastic shearing, which provided a mechanism for work-softening. The obtained shear bands were characterised using nano-indentation.

3.4 Nanoindentation Results

The NanoTest 600 system, manufactured by Micro Materials Wrexham UK, was used for the depth-sensing indentation (DSI) experiments. Specimens of BMG were cut and polished to mirror-like finish with the roughness around 5 nm. A series of nanoindentation were conducted on the polished surface under loading rate of 0.1 and 2 mN/s.

Fig. 10 Typical load-displacement responses at loading rate 0.1 mN/s for purely elastic deformation line (*AB*) and first pop-in line (*CD*)

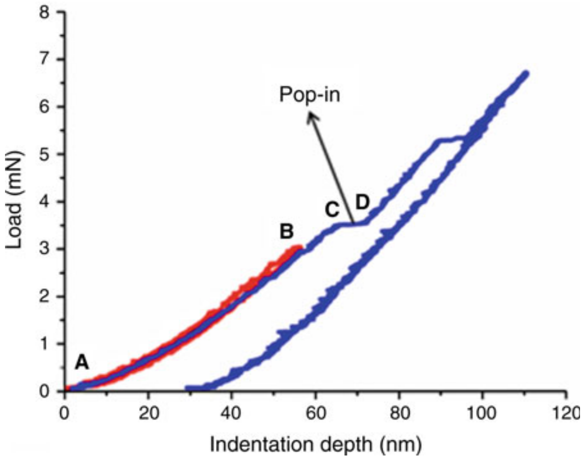

To characterise the elastic deformation, a maximum load of 7 mN was applied incrementally from 3 to 7 mN at a load rate of 0.1 mN/s (Fig. 10). The estimated yielding load was 3 mN for the typical Zr-based BMGs for a to 5 μm spherical tip following the work of Packard et al. [44]. Below 3 mN load, no evidence of plastic deformation was observed, as confirmed by the initial experiments as shown as AB in Fig. 10. With the increase in the peak load, the first 'pop-in' event occurred at ~4 mN indicating plastic deformation (represented by CD in Fig. 10), followed by an another pop-in event at around 5.5 mN. All the experiments show close correlation for the first pop-in events; the presented load-displacement plot (Fig. 10) is a typical example from several tests. One major drawbacks of this experiment is the fact that nucleation and initiation of shear band cannot be observed directly as it occurs under the indenter.

The loading-unloading cycles were also carried out at higher load magnitudes with the aim of observing shear-band steps on the material's surface and evaluating their propagation in the studied Zr-based metallic glass. The loading rate was 2 mN/s with 5 μm spherical indenter. Shear bands appeared at the surface at loads in excess of 100 mN; the features of shear bands at various loads from 130 to 275 mN are shown in Fig. 11. The shear bands exhibited some symmetry, which probably was due to indenter shape. A fractographic analysis also revealed the evolution of shear bands on the surface with increasing magnitude of load/displacement (Fig. 11). The magnitude of elastic modulus obtained from the unloading part of the load-displacement curves indicated that $E = 86$ GPa as characterised earlier via bending test was accurate.

3.5 *Micro-indentation*

Micro-indentation experiments were conducted using spherical indenter with diameter 50 μm at three different loading rates of 1, 2 and 10 mN/s. While shear

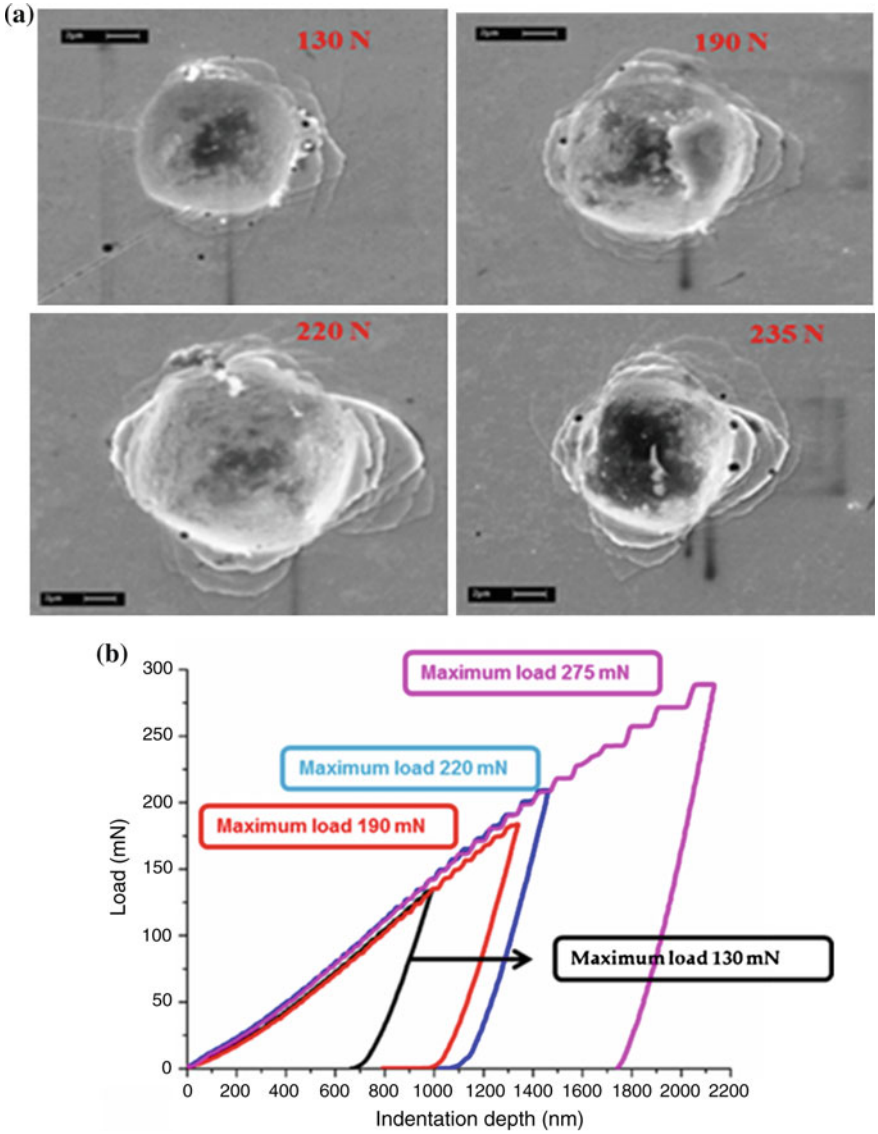

Fig. 11 Shear band evolution on surface indentation with spherical indenter with increasing load (**a**). (**b**) Indentation load-displacement curve for Zr-Cu-based BMG for incremental loading-unloading (loading rate 2 mN/s)

band slips on the surface were observed around 100 mN in nanoindentation test, the shear bands slips in spherical micro-indentation were found at loads in excess of 10 N (Fig. 12). Based on the Herztain elastic equation for a spherical indenter, the mean pressure is inversely related to the contact radius and hence, the radius affects

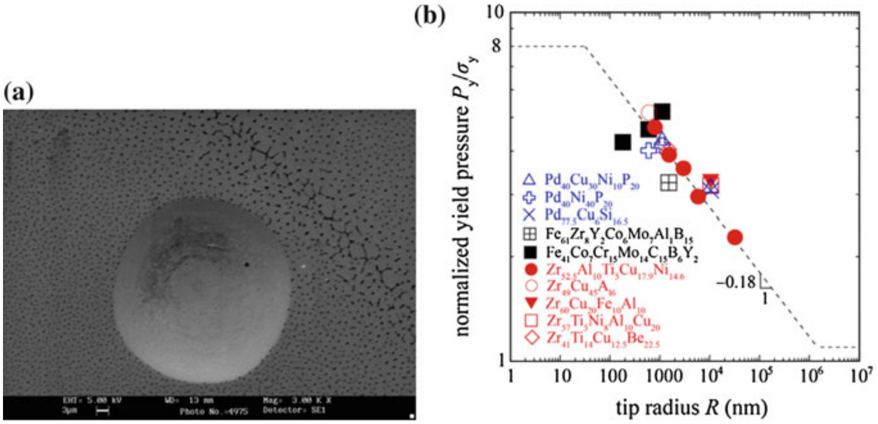

Fig. 12 **a** SEM micrograph of the micro-indents of the Zr48Cu36Al8Ag8. There are no shear bands around the indent with 10 N load **b** and normalised yield pressure versus indenter tip radius for various metallic glasses [20]

the initial yield pressure, which is revealed on the pressure-depth curve as pop-in events that occur at yield load and corresponding displacement. In addition, yielding of metallic glasses is initiated at location of maximum shear stress (τ_{max}) in the volume. As proposed by Greer et al. [20], the normalised yield pressure is increased with decreasing the indenter tip radius (Fig. 12). They found that the plastic-flow mechanism was changed by using indenter tips with various radii, with deformation controlled by heterogeneous nucleation of shear bands for small indenters changing to propagation of already nucleated shear bands at a large scale. A clear size effect can be observed (Fig. 12b) as smaller radius gives higher level of normalised yield pressure.

These subsequent cycles of loading-unloading in indentation implemented with aim of assessing the evolution of shear bands at different loading rates including are exhibited in Fig. 14 with the maximum load was 15 N. The features of shear band steps at 15 N are shown in Fig. 14. The shear bands around the indent increased with load rate without any generation of cracks. As can be seen in Fig. 13, the shear band moving from the top right corner (denoted A in Fig. 14) crossed the shear band coming from the top left corner (denoted B); however, the subsequent nucleated shear bands were arrested by the same shear bands originating from the top left to top right corner. Instability of the shear bands were observed in the form of nucleation of several secondary shear bands from the primary ones during the course of deformation. As shown in Fig. 14, the load-displacement curves became increasingly serrated as the loading rate decreases, as single shear bands are activated. At high-rate loading, the overall plastic response became homogeneous in time, since multiple shear bands operated simultaneously; this is confirmed in Fig. 13 as the density of shear bands observed at high indentation rates is increased noticeably. In order to determine the level of hardness and elastic modulus of such

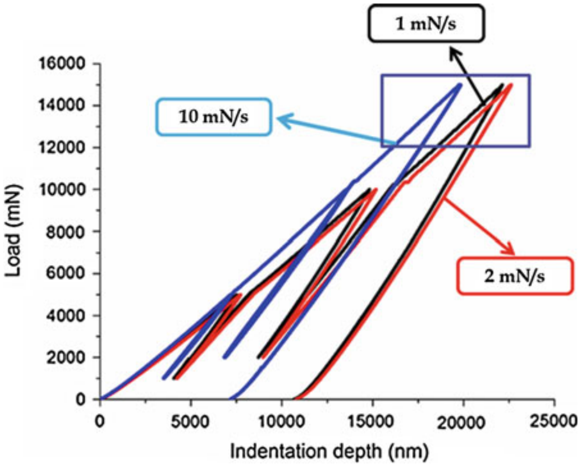

Fig. 13 Representative load-displacement curves for various loading rates (maximum load 15 N)

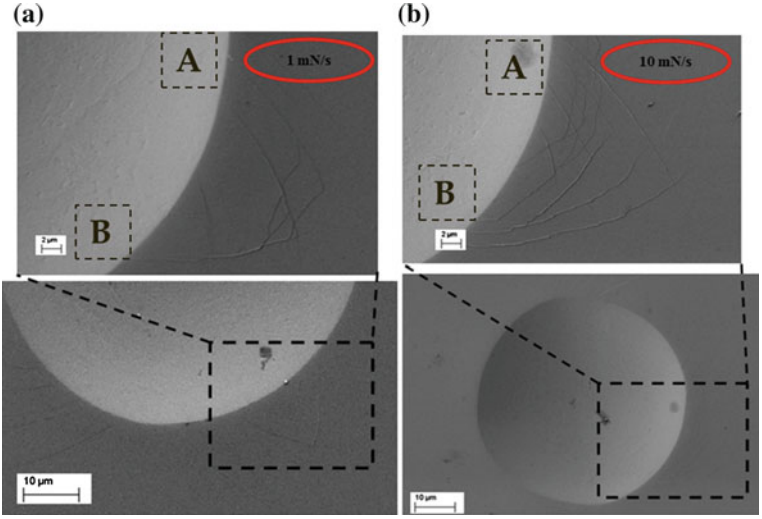

Fig. 14 SEM images of micro-indentation in $Zr_{48}Cu_{36}Al_8Ag_8$. Loading rates: **a** 1 mN/s and; **b** 10 mN/s

stiff materials as BMGs, frame compliance should also be taken into account during calculation.

The depth measured during indentation process includes the depth of penetration of the indenter into the specimens along with any displacement of the instrument due to deflection. The compliance C_f, of the system is defined as deflection of the

Fig. 15 Frame compliance as function of load for different load rates including

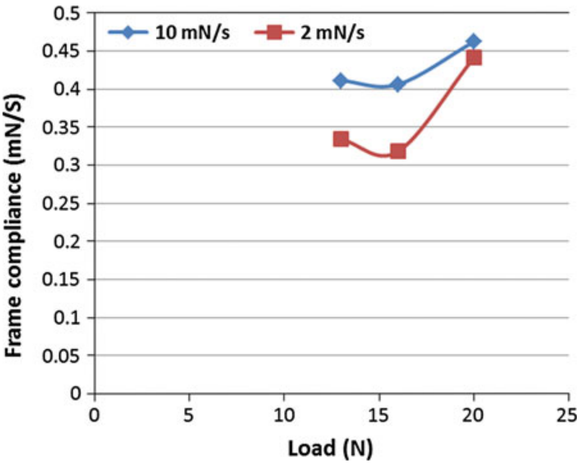

instrument divided by the load. Compliance effects become important when a relatively large radius indenter is used at high indentation loads. The compliance of the indenter material $\frac{1}{S}$ is included in the composite modulus, where the stiffness of the contact S is rearranged as:

$$\frac{\mathrm{dh}}{\mathrm{dp}} = \frac{1}{\mathrm{S}} + \mathrm{C_f} \tag{1}$$

see Fisher-Cripps [16] for full details. Equation (1) demonstrates that higher frame compliance values leads to lower stiffness. Hence, an important question was whether the loading rate in indentation studies had an effect on the measured frame compliance as this might affect significantly the measured value of material's stiffness. Tungsten was used as a standard calibration material. It was observed that the calculated frame compliance varies with loading rates for each load (Fig. 15). These results indicate that the calculated frame compliance values are relatively close to each other for loads up to 15 N and higher values were measured for higher loading rates. Based on this experiment, mechanical properties hardness and elastic modulus of the Zr-Cu-based material were determined in the micro-indentation test.

3.6 Wedge Indentation

A wedge indentation experiments was designed to overcome limitation of nano- and micro-indentation to observe the initiation and propagation of shear bands under the indenter surface. In nano- and micro- indentation experiments by the very nature of the experiment, shear bands could be observed only after they exit to the surface observation can be made.

In 1989, Donovan used serial sectioning and etching in order to investigate the plastic flow and fracture of Pd-based metallic glass loaded with spherical and Vickers indenters. In that study, it was explained that the plastic zone (shear bands) had a core region immediately beneath the contact zone, where the shear bands typically terminated before they reached the free surface. The cracks seen in the etched section were related to the regions of high tensile strain with excess of free volume [45]. Ramamurty et al. [4, 26, 27, 45] proposed a technique named 'Bonded interface' to investigate the shear-band propagation on a plane along the indentation axis in BMGs. In this technique, a pre-cut specimen is loaded along the direction in the plane of the cut with two halves of the specimen bonded along this interface by frictional forces. This technique was employed for brittle materials such as ceramics and oxide glasses in order to study the deformation mechanism underneath the indenter [8, 15]. Zhang et al. [63] employed the bonded interface technique on Vitreloy 106 in order to study the effect of increasing the load on shear bands propagation. At small indentation loads, plastic deformation was primarily accommodated by semi-circular mostly shear bands surrounding the indentation. At higher loads, secondary and tertiary shear bands were formed inside the plastic zone. The same technique was used to observe the primary shear bands (PSBs) and secondary shear bands (SSBs) caused by the indentation in Zr-based metallic glasses. As presented in Fig. 16, PSBs with a high intensity were formed near the tip of the indenter. The SSBs emanated radially from the tip. It was suggested that SSBs were formed because the tip of the indenter was not perfectly spherical and the load applied on the sample's surface was not exactly perpendicular to it. SSBs intersected with the PSBs, but rarely approached the top surface of the indent.

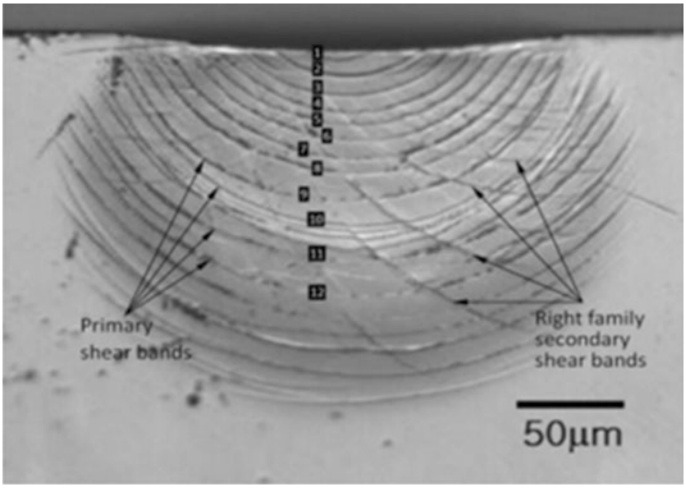

Fig. 16 Primary and secondary shear bands created during the indentation of $Zr_{52.5}Cu_{7.9}Ni_{14.6}Al_{10}Ti_5$ BMG [63]

Based on the above observation, it was reasonable to claim that hemispherical region of shear bands with different pattern was formed beneath the indentation.

The bonded interface technique was also employed at high temperatures on a Zr-based BMG to study plastic deformation characteristics in a subsurface deformation zone under a Vickers indenter and to find the reason for increased pressure sensitivity of plastic flow with the temperature [14]. Unlike the constant deformation zone, the shear-band spacing in the deformation zone increased with temperature as larger shear bands were formed due to the movement of a large number of STZs. As STZ formation is pressure sensitive, the overall plastic deformation of BMG was more sensitive to pressure with increasing temperature. The advantage of the “bonded interface” technique is its ability to image the deformation morphology, especially for metallic glasses that undergo inhomogeneous deformation. However, the “bonded interface” technique has an inherent problem with traction-free surfaces created when the specimen was split. As noted by Ramamurty et al. [4], the adhesive layer joining the sections together may relieve the elastic constraint for plastic flow, which would otherwise be present in bulk indentations. This may alter the size or shapes of the deformed zone and even the indentation mechanism itself [63]. This was noted by Mulhearn [41], who found that the relaxation could affect the size of the deformed zone and the slope of the strain gradient but would not affect the contours of equal strain significantly. It can be concluded that the shear bands observed in indentation using the “bonded interface” method represent the true behaviour of the material below the indenter, but the obtained sizes and shapes could be inaccurate. In this respect, the wedge indentation test has an advantage over the “bonded interface” technique, since it requires no adhesive and completely eliminates limitation due to the presence of interface [42]. In addition, wedge indentation can be used to apply incremental loading on any material to study evolution of the deformation mechanism under materials by increasing the load.

A wedge indenter made of high-speed steel, with nominal angle of 60° and an edge radius of 19.5 μm and height of 9.5 μm was designed and manufactured in-house. A special fixture was manufactured to attach the indenter to the testing machine (Fig. 17). Testing was carried out on the beam-shaped samples in a compression mode with a constant displacement rate of 0.05 mm/min. load was applied from 1 to 3 kN in increments of 1 kN. A Scanning Electron Microscope (SEM) 360 was used to observe shear-band propagation at the top and front surfaces as shown Fig. 17c. The indentation tests reported here were conducted at ambient temperature.

Figure 18 compares the indentation width measured on the top surface for incremental and single loading modes. As shown in Fig. 18a, b, the measured indentation imprints for single and incremental loading for 2 kN for both modes prove that the wedge indenter in the former targeted the same location that was used at the applied load of 1 kN. The difference in the indentation widths for two modes of loading was less than 5 %. A similar situation occurred for single and incremental loading of 3 kN. Contrary to micro- and nano-indentation, the described results demonstrate that wedge indentation is able to provide an incremental study of the shear- band propagation.

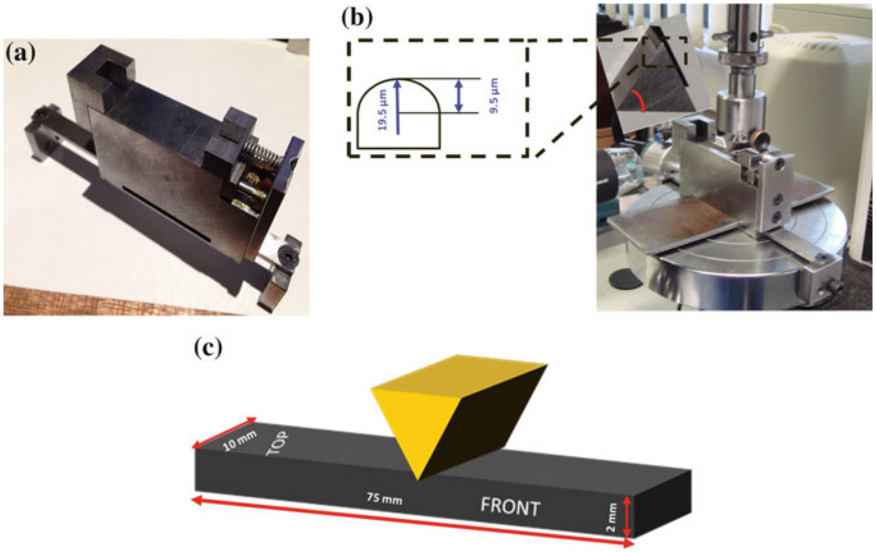

Fig. 17 Designed fixture (**a**), and experimental setup for wedge indentation (**b**). (Inset image: wedge indenter and its dimension) (**c**) Schematic of shear band observation

Evolution of deformation patterns on the front surface of the wedge indented sample are presented in Fig. 19. In all figures, several serrated semi-circular slip-steps formed by shear bands were observed. Apart the serrated slip-steps, numerous smooth semi-circular slip-steps of shear bands were seen, when the load was increased to above 2 kN. These serrated and smooth semi-circular slip-steps are named ‘primary shear bands’ in order to discriminate them from other slip-steps of the shear bands form at higher loads. The number of the slip-steps from these PSBs increased dramatically with the growing load but the spacing between them seems to remain constant. Interestingly, the slip-steps of the semi-circular PSBs seem to vanish as they approach the indentation surface. Above 1 kN, new types of shear bands, as mentioned previously, were formed inside the zone of primary shear bands, as shown in Fig. 19. These shear bands originated radially from the indenter tip. From our observations, few slip lines of the shear bands reached the top surface.

4 Modelling of Metallic Glasses: Some Challenges

A better understanding of deformation processes in BMGs and their localization in the form of shear bands, especially in bulk materials, is only possible with numerical simulation. A number of studies have demonstrated that plastic

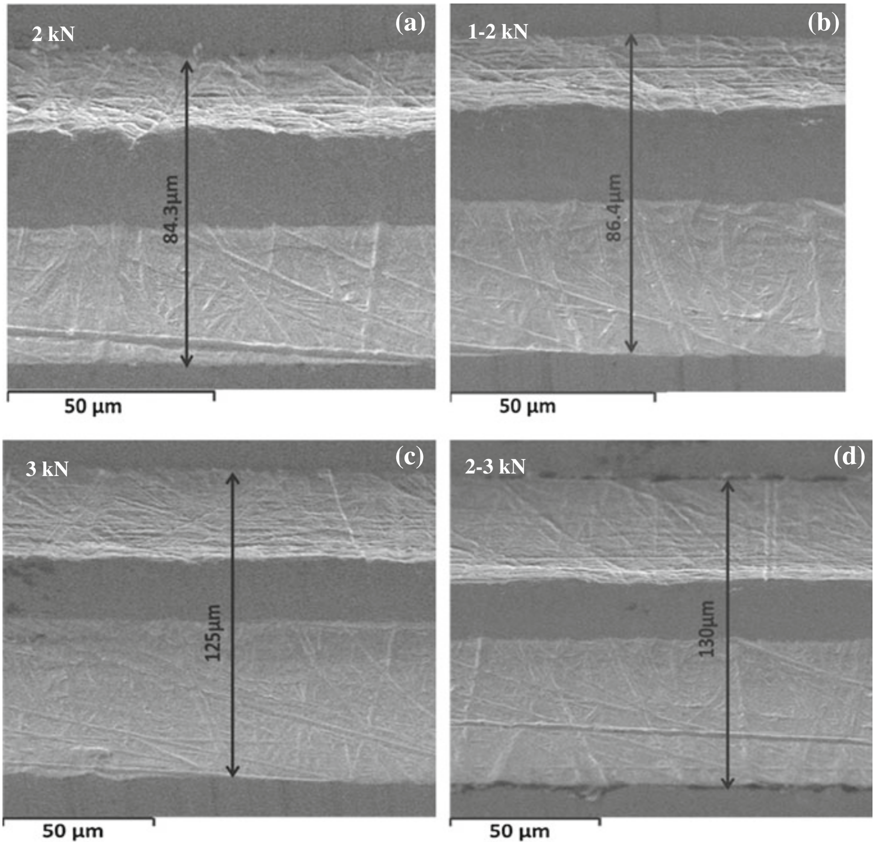

Fig. 18 SEM images of top surface (**a** and **c**) indentation width for single loading; (**b** and **d**) incremental loading. Load levels are shown in respective figures

deformation of BMGs is different to the von–Mises (J_2) type which is independent of pressure [55]. The deviation of the shear-band's inclination angle (SBIA) from classical 45° is due to the effect of shear stress and the normal stress component. Several well-established macro scale models of brittle materials already exist. Additionally, the SBIA predicted by the MC model is symmetric for both tension and compression whereas tests show large differences of it for BMGs [64].

Johnson and Holmquist proposed a constitutive relation for brittle material known as JH-2. This model requires an explicit definition of strength for both intact and fractured materials, pressure—volume relationship and a damage model. Details of this model could be found in Johnson Hulmquiest et al. [31]. Johnson-Holmquist-Beissel (JHB) model is an extension of the JH-2 model and its primary distinctive feature is the ability to include the effect of pre-stress and phase changes [23]. The JH-2 model poses for damage accumulation and progressive increase bulk pressure. In contrast, the JHB model does not include any bulking pressure until the

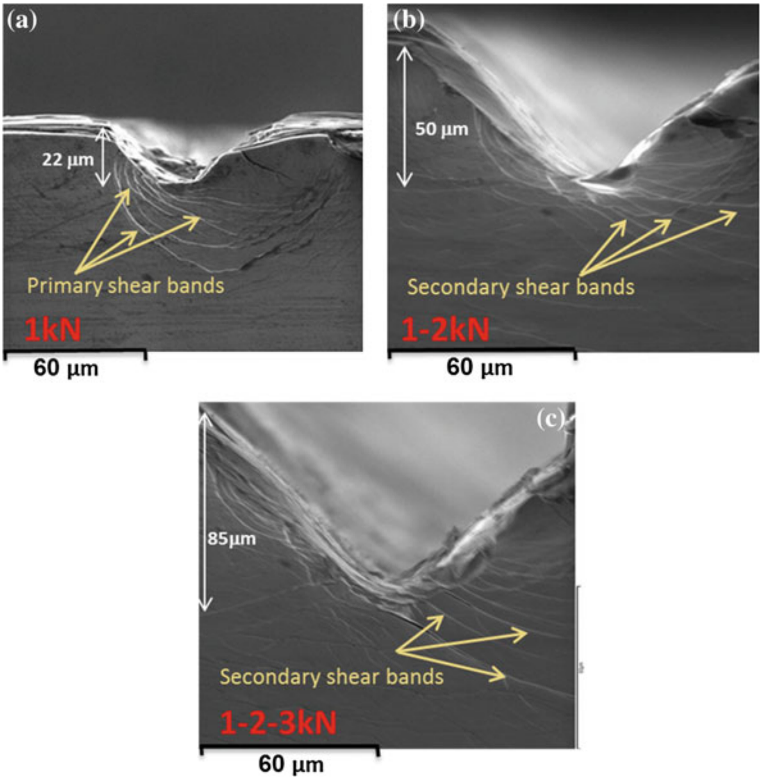

Fig. 19 Evolution of shear bands pattern with load on the front surface of the BMG sample under wedge indentation: **a** 1 kN, **b** 1–2 kN, **c** 1–2–3 kN

material is completely damaged. Another suitable model for brittle material is the Drucker—Prager one that is widely used for frictional materials that exhibit pressure–dependent yield stress and materials with higher compressive yield strength than that in tension.

Simple tensile and compressive test simulations were conducted for the above constitutive models by imposing identical boundary conditions, type of elements and specimen's geometry. The aim of the study was to analyse the relative merits and deficiencies these models with in the context of simulations of brittle materials with the ultimate goal of modelling BMGs. FE analysis based on those models was conducted in ABAQUS/Explicit Material properties for all the simulations were for silicon carbide that are readily available in the literature; this justified by the fact that both materials exhibit pressure dependency of strength and characteristics in macro scale at room temperature under compression and tension exhibit similar trends [23].

For simulation of uniaxial tests, boundary conditions were imposed as shown in Fig. 20. For displacement-control tests, amplitude of the displacement was smooth

Fig. 20 Boundary conditions for FE simulation of uniaxial tensile test

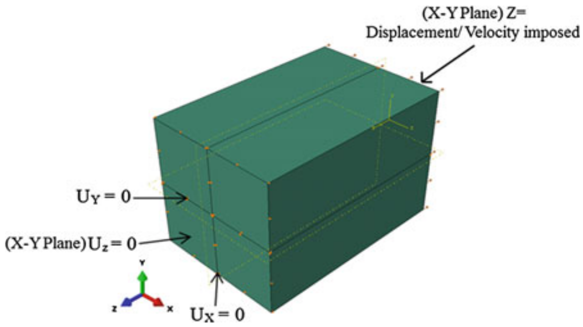

and linearly. To preserve the quasi–static conditions in explicit analysis, an average loading velocity of 0.5 mm/s was adopted [22]. Simulations of both tensile and compression tests were conducted for all the above mentioned models; initially, FE results were compared for both dog-bone-shape and cubic specimens for the JH-2 model.

4.1 FE Analysis of Tensile and Compressive Tests: JH-2 Model

Originally, displacement controlled with a linear and smooth amplitude version was considered. It was found that the dog-bone shape specimen was not suitable for further analysis as it deviate from the constraints of the JH-2 model. A specimen with constant cross section along its axis would resolve this issue and the analysis is presented in the following section. To distinguish the behaviours of the models with the smooth and linear amplitudes, velocity distributions of along the direction of applied displacement were analysed. For both models were observed distribution along the loading direction is exceptionally large velocity levels that was slightly reduced in the case of linear amplitude displacement. It can be concluded that the smooth-amplitude definition induces unrealistic velocity into the model and should be avoided in further analysis.

Field plots in Fig. 21 are for the cases with the imposed velocity boundary condition. The maximum velocity is still large for a quasi–static assumption although it is drastically reduced compared to that for the displacement boundary conditions. A peculiar shape of the deformed cubic specimen could be observed as the side with the imposed boundary condition dilated significantly; Fig. 21b demonstrates this situation. With these observations, the JH-2 model fails to represent adequately a quasi–static uniaxial tensile behaviour of the brittle material for the ranges of displacement and strain rates studied. The velocity along the loading direction was considerably large for quasi–static conditions even though the displacement was controlled at 0.5 mm/s.

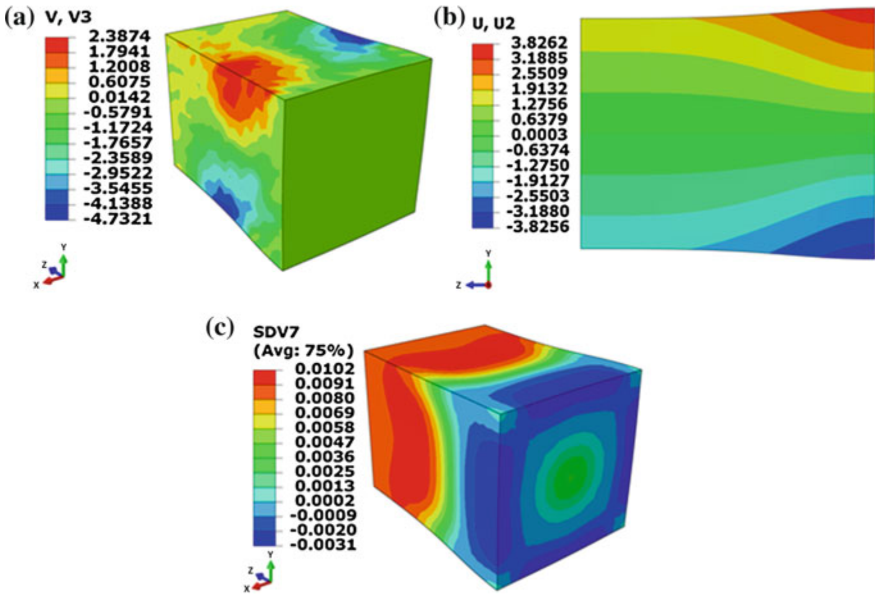

Fig. 21 **a** Velocity distribution along loading direction; **b** displacement field along lateral direction; **c** distribution of volumetric strain for tensile simulation based on velocity boundary condition

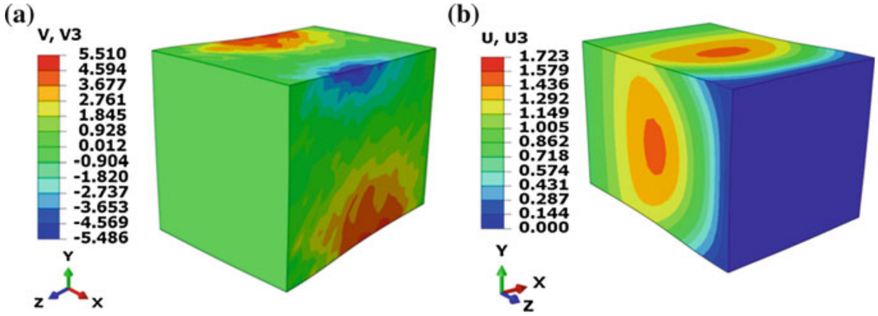

Fig. 22 **a** Maximum velocity attained in compression analysis; **b** displacement for compression simulation based on velocity boundary condition

In Fig. 22 results of compression simulations on velocity boundary conditions exemplify similar plots for fields of velocity and displacement along the loading direction with dilation as in above studies for the JH-2 model.

4.2 FE Analysis of Tensile and Compressive Tests: (JHB Model)

The JHB-based analysis was conducted in a similar manner. Our studies show that the JHB model is somewhat representative of quasi–static loading conditions. Tensile simulations with displacement boundary conditions were considered initially. Unlike simulations with JH-2 model, extensive dilatation of a portion of the specimen was not observed in this study. As apparent from Fig. 23a, volumetric strain did not change until the damage was initiated; it remained at a zero level. This value is acceptable with the pressure—volume realtion of the model as $\mu \leq 0$ for the expansion. Considering Figs. 22a and 23b, the maximum velocity in the JHB model along the loading direction drastically reduced to 0.33 mm/s; this distribution is suitable for the quasi–static conditions. As seen in Fig. 23c, the displacement field is uniform and failure occurred in a brittle mode (Fig. 23d).

The state of the deformed specimen near the onset of damage including volumetric strain, velocity and displacement along the loading direction is shown in Fig. 24. Although the maximum velocity is slightly higher compared to that in Fig. 24b; it is still acceptable to represents quasi–static conditions. The displacement field is

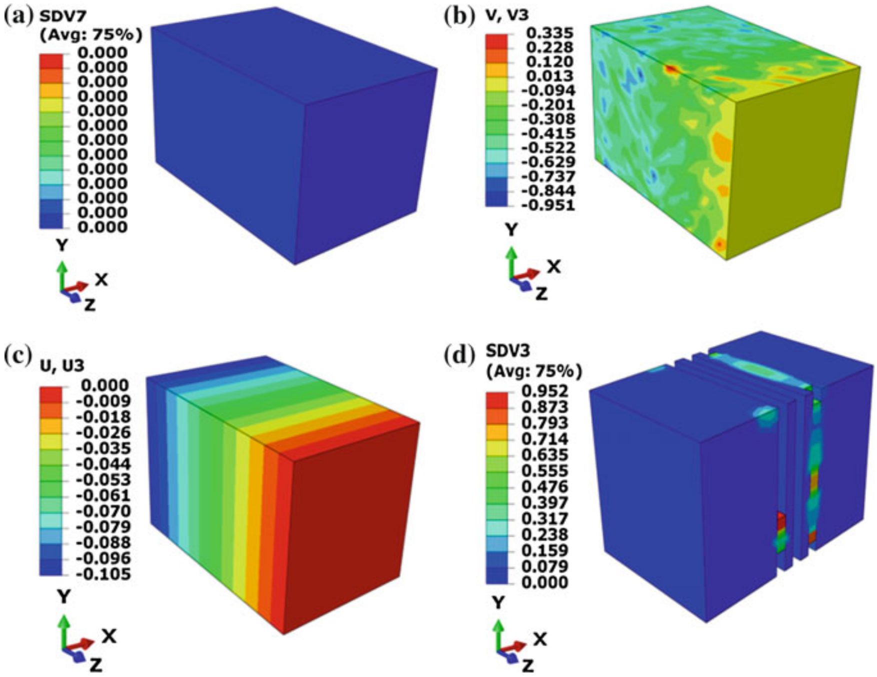

Fig. 23 Tension simulation displacement boundary condition **a** Volumetric strain; **b** maximum velocity attained; **c** displacement distributions for close failure; **d** damage initiation at failure

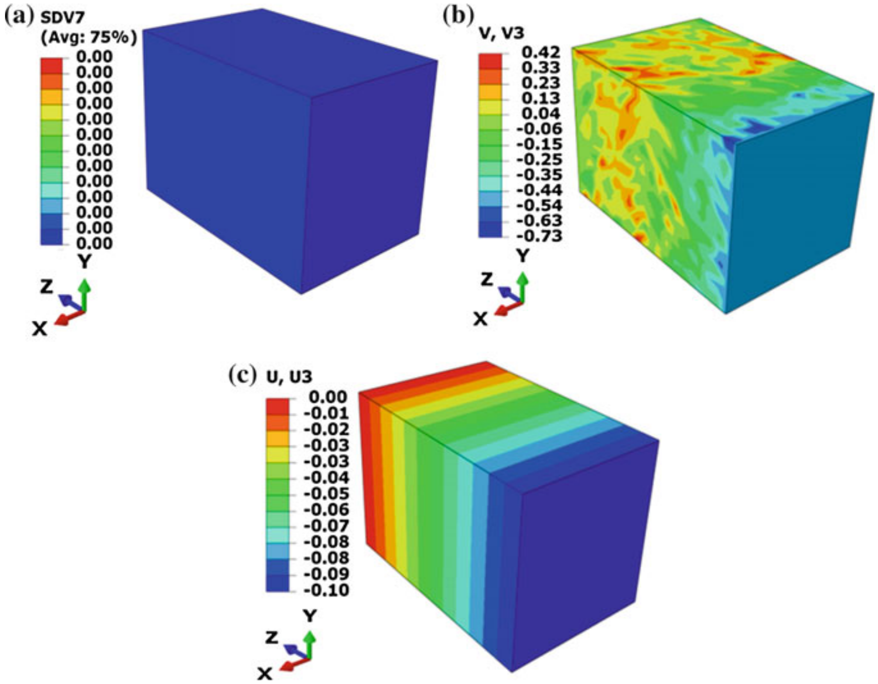

Fig. 24 Results of tension simulation with velocity boundary condition **a** Volumetric strain; **b** maximum velocity; **c** displacement distribution close to failure

uniform as it should be for displacement boundary condition, and the failure mode is identical to that tension simulation with displacement boundary condition.

Regarding Fig. 25, it could be mentioned that the JHB model does not reproduce quasi–static conditions as velocity level are still considerable. The model did not dilate, and the displacement along the loading direction is uniform, as before.

4.3 FE Analysis of Tensile and Compressive Tests: Drucker-Prager Model

In contrast to the above mentioned models, Drucker-Prager model demonstrated rather acceptable solutions. Initially, a case of displacement boundary condition with a linear was considered. All the presented field plots are for a state close to complete failure of the specimen. In the compression simulations with displacement boundary conditions, the calculated velocity components are reasonably within the

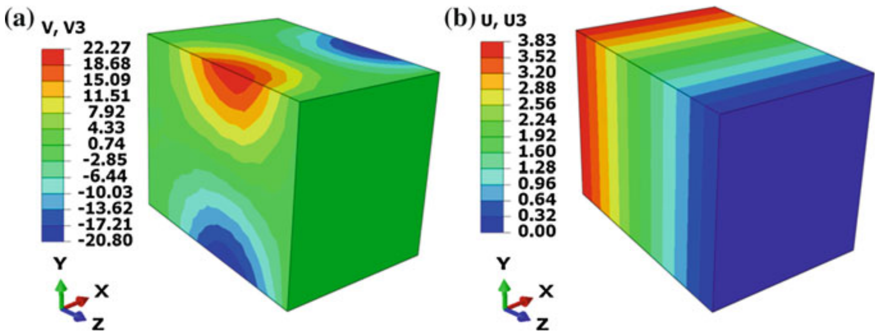

Fig. 25 **a** Maximum velocity attained during compression analysis **b** displacement distribution for compression simulation on velocity boundary condition

Fig. 26 Lateral displacement of cubic specimen close to failure under compression (displacement boundary condition)

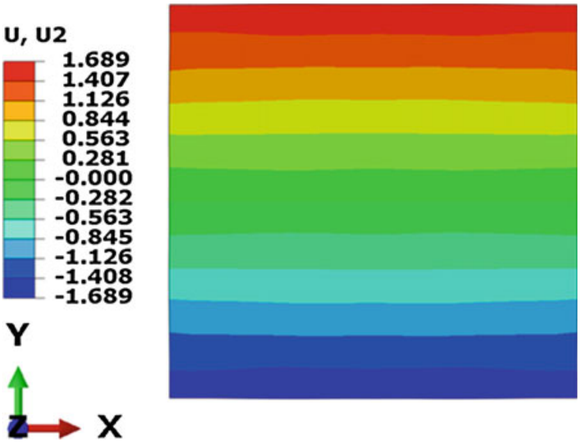

limits while the displacements are uniformly distributed. Notable features of Fig. 26 are close to failure, the lateral displacement of the specimen was slightly reduced in the middle portion of the specimen while increasing at either ends. This behaviour slightly forms a shrink domain at that portion.

For compression test with velocity boundary conditions (as shown in Fig. 27), the response to loading did not changed. The specimen seemed to expand in the middle portion. Even though the direct stress exceeded the compressive yield strength, the specimen was not damaged. Additional analysis should be carried out to find the cause of the unexpected behaviour.

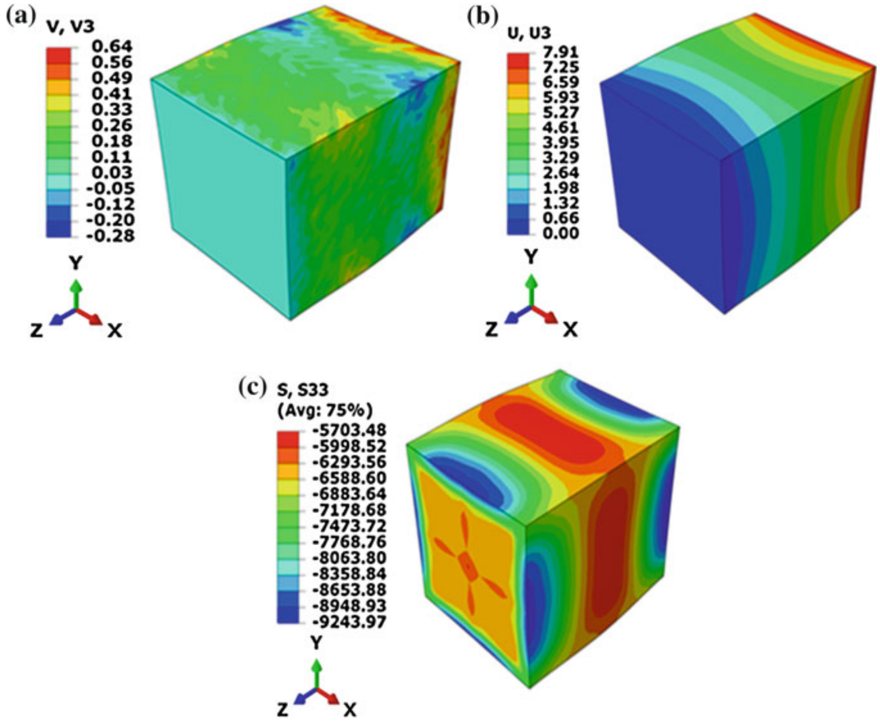

Fig. 27 Distributions of velocity, displacement and direct stress (**a**–**c**) at the time step without response to velocity boundary condition for compression test

5 Summary and Conclusion

The manufacturing development of bulk metallic glasses by the use the science and technology of supercooled metallic glasses made it possible to consider BMGs for advanced structural applications. These materials demonstrate unique mechanical properties including a combination of high hardness, specific strength, large elastic elongation and high corrosion resistance. In absence of dislocation-mediated plastic deformation of crystalline materials, metallic glasses undergo highly heterogeneous deformation by formation of localised shear bands, which can lead to catastrophic behaviours.

The fundamental mechanisms of deformation and fracture of metallic glasses were reviewed in this paper. These include the effect of low and high strain rates, temperature and pressure on the deformation mechanisms. The length-scale dependency of BMGs was studied to understand their deformation mechanism and mechanical properties at small scale.

In this study, observation of fracture surface of the Zr-Cu-based BMG under 3-point test revealed brittle failures that are different from those observed in crystalline materials. Indentation techniques were extensively used to first study the elastic deformation of the studied BMG alloy, followed by a systematic analysis of initiation and evolution of shear-band localisation in the indented material. Our results, obtained with the suggested wedge-indentation technique, demonstrated the initiation of shear bands in the material volume. This technique is particularly useful for materials scientists for development of appropriate constitutive models that characterise plastic events in amorphous materials in the small-length scale.

Continuum-based approaches to study the deformation behaviour of metallic glasses are essential for the macro scale engineering applications. Since metallic glass shows pressure- dependency, many studies were carried out to elucidate the mechanical deformation of the MG with available continuum approaches that are pressure-dependent. It was shown that most common pressure-dependent continuum models in the literature did not agree with the macro scale behaviour of the BMG and the molecular dynamics approaches with the free volume theory is not adequate for the macro scale problems. Among the available continuum models for brittle materials including JH-2, JHB and Extended Drucker Prager model were studied. Prior to the detailed study of these models with respect to metallic glass, it is important to test them. Hence, uniaxial tensile and compression simulations were conducted for the specimens with the material properties for silicon carbide. All uniaxial compression and tensile tests were conducted by utilising both velocity and displacement boundary conditions.

Based on the obtained simulation results, the JH-2 model has decided as not suitable for quasi-static analysis due to ambiguity of the data for the uniaxial tensile and compressive conditions. Compared to the JH-2, the JHB model presented main features of typical brittle-mode failure under tension whereas under compression the velocity distribution deviated from the quasi-static conditions. The use of the extended Drucker-Prager model provided results similar to those obtaining with the JHB model reasonable reproducing brittle favourable fracture in tension. Still, the level of velocity was large for quasi-static conditions. Thus, it can be conducted that the extended Drucker-Prager and JHB models can be used to study deformation modes in BMGs whereas the JH-2 model is not suitable for both quasi-static tension and compression.

References

1. Aning, A., Wang, Z., Courtney, T.: Tungsten solution kinetics and amorphization of nickel in mechanically alloyed Ni-W alloys. Acta Metall. Mater. **41**(1), 165–174 (1993)
2. Argon, A.: Plastic deformation in metallic glasses. Acta Metall. **27**(1), 47–58 (1979)
3. Bharathula, A., Lee, S.W., Wright, W.J, Flores, K.M.: Compression testing of metallic glass at small length scales: Effects on deformation mode and stability. Acta Mater. **58**, 5789–5796 (2010)
4. Bhowmick, R., Raghavan, R., Chattopadhyay, K., Ramamurty, U.: Plastic flow softening in a bulk metallic glass. Acta Mater. **54**(16), 4221–4228 (2006)
5. Brace, W.F., Bombolaski, E.G.: A note on brittle crack growth in compression. J. Geophys. Res. **68**(12), 3709–3713 (1963)

6. Brandtzaeg, A.: Failure of a Material Composed of Non-isotropic Elements, Trondnjem Bruns, Trondhjem (1927)
7. Byrne, C.J., Eldrup, M.: Materials science. Bulk metallic glasses. Science **321**(5888), 502–503 (2008). (New York)
8. Cai, H., Kalceff, S.M.A., Lawn, B.R.: Deformation and fracture of mica-containing glass-ceramics in Hertzian contacts. J. Mater. Res. **9**(03), 762–770 (1994)
9. Chen, Y., Jiang, M.Q., Dai, L.H.: How does the initial free volume distribution affect shear band formation in metallic glass? Sci China **54**(8), 1488–1494 (2011)
10. Cheng, J., Ghosh, S.: Computational modeling of plastic deformation and shear banding in bulk metallic glasses. Comput. Mater. Sci. **69**, 494–504 (2013)
11. Chu, Jinn P., Jang, J.S.C., Huang, J.C., Chouc, H.S., Yangd, Y., Yed, J.C., Wange, Y.C., Leef, J.W., Liug, F.X., Liawg, P.K., Chenh, Y.C., Leeh, C.M., Lih, C.L., Rullyania, Cut: Thin film metallic glasses: unique properties and potential applications. Thin Solid Films **520**(16), 5097–5122 (2012)
12. De Hosson, J.T.M.: Advances in transmission electron microscopy: In situ straining and in situ compression experiments on metallic glasses. Microsc. Res. Tech. **72**, (2009)
13. Dubach, A., Raghavan, R., Loffler, J.F., Michler, J., Ramamurty, U.: Micropillar compression studies on a bulk metallic glass in different structural states. Scripta Mater. **60**(7), 567–570 (2009)
14. Eswar Prasad, K., Ramamurty, U.: Effect of temperature on the plastic zone size and the shear band density in a bulk metallic glass. Mater. Sci. Eng. A **535**, 48–52 (2012)
15. Fischer-Cripps, A.: Elastic–plastic behaviour in materials loaded with a spherical indenter. J. Mater. Sci. **32**(3), 727–736 (1997)
16. Fischer-Cripps, A.: Use of combined elastic modulus in the analysis of depth-sensing indentation data. J. Mater. Res. **16**(11), 3050–3052 (2001)
17. Frost, H.J., Ashby, M.F.: Deformation Mechanism Maps: The Plasticity and Creep of Metals and Ceramics, Pergamon Press, New York (1982)
18. Gao, Y.F.: An implicit finite element method for simulating inhomogeneous deformation and shear bands of amorphous alloys based on the free-volume model. Modell. Simul. Mater. Sci. Eng. **14**(8), 1329–1345 (2006)
19. Glucklich, J.: Fracture of plain concrete. J. Eng. Mech. **89**, 127–138 (1963)
20. Greer, A.L., Cheng, Y.Q., Ma, E.: Shear bands in metallic glasses. Mater. Sci. Eng., R **74**(4), 71–132 (2013)
21. Greer, J.R., Hosson, De, Jeff, ThM: Plasticity in small-sized metallic systems: Intrinsic versus extrinsic size effect. Prog. Mater Sci. **56**(6), 654–724 (2011)
22. Gözlüklü, B., Coker, D.: Modeling of the dynamic delamination of L-shaped unidirectional laminated composites. Compos. Struct. **94**(4), 1430–1442 (2012)
23. Holmquist, T.J., Johnson, G.R.: Characterization and evaluation of silicon carbide for high-velocity impact. J. Appl. Phys. **97**(9), 093502 (2005)
24. Huang, R., Suo, Z., Prevost, J., Nix, W.: Inhomogeneous deformation in metallic glasses. J. Mech. Phys. Solids **50**(5), 1011–1027 (2002)
25. Inoue, A., Shinohara, Y., Gook, J.S.: Thermal and magnetic properties of bulk Fe-based glassy alloys prepared by copper mold casting. Mater. Trans. JIM **36**, 1427–1433 (1995)
26. Jana, S., Bhowmick, R., Kawamura, Y., Chattopadhyay, K., Ramamurty, U.: Deformation morphology underneath the Vickers indent in a Zr-based bulk metallic glass. Intermetallics **12** (10), 1097–1102 (2004)
27. Jana, S., Ramamurty, U., Chattopadhyay, K., Kawamura, Y.: Subsurface deformation during Vickers indentation of bulk metallic glasses. Mater. Sci. Eng., A **375**, 1191–1195 (2004)
28. Jang, D., Greer, J.R.: Transition from a strong-yet-brittle to a stronger-and-ductile state by size reduction of metallic glasses. Nat. Mater. **9**(3), 215–219 (2010)
29. Jiang, M.Q., Dai, L.H.: On the origin of shear banding instability in metallic glasses. J. Mech. Phys. Solids. **57** (8), 1267–1292 (2009)
30. Johnson, W.L.: Thermodynamic and kinetic aspects of the crystal to glass transformation in metallic materials. Prog. Mater. Sci. **30**(2), 81–134 (1986)

31. Johnson, G.R., Holmquist, T.J.: Response of boron carbide subjected to large strains, high strain rates, and high pressures. J. Appl. Phys. **85**(12), 8060–8073 (1999)
32. Klement, W., Willens, R. and Duwez, P.: Non-crystalline structure in solidified gold–silicon alloys. Nature. **187**(5), 867–870 (1960)
33. Lai, Y.H., Lee, C.J., Cheng, Y.T., Chou, H.S., Chen, H.M., Du, X.H., Chang, C.I., Huang, J. C., Jian, S.R., Jang, J.S.C., Nieh, T.G.: Bulk and microscale compressive behavior of a Zr-based metallic glass. **58**(10), 890–893 (2008)
34. Lee, C.J., Huang, J.C., Nieh, T.G.: Sample size effect and microcompression of $Mg_{65}Cu_{25}Gd_{10}$ metallic glass. Appl. Phys. Lett. **91**, (2007)
35. Lewandowski, J., Wang, W., Greer, A.: Intrinsic plasticity or brittleness of metallic glasses. Philos. Mag. Lett. **85**(2), 77–87 (2005)
36. Li, J.C., Wei, Q., Chen, X.W., Huang, F.L.: On the mechanism of deformation and failure in bulk metallic glasses. Mater. Sci. Eng., A **610**, 91–105 (2014)
37. Liu, Z., Wang, R., Qu, R., Zhang, Z.: Precisely predicting and designing the elasticity of metallic glasses. J. Appl. Phys. **115**(20), 203513 (2014)
38. Madge, S., Louzguine-Luzgin, D., Lewandowski, J., Greer, A.: Toughness, extrinsic effects and Poisson's ratio of bulk metallic glasses. Acta Mater. **60**(12), 4800–4809 (2012)
39. Matthews, D., Ocelik, V., Bronsveld, P., De Hosson, JThM: An electron microscopy appraisal of tensile fracture in metallic glasses. Acta Mater. **56**(8), 1762–1773 (2008)
40. Megusar, J., Argon, A., Grant, N.: Plastic flow and fracture in $Pd_{80}Si_{20}$ near T_g. Mater. Sci. Eng. **38**(1), 63–72 (1979)
41. Mulhern, J., Rogers, T., Spencer, A.: A continuum theory of a plastic-elastic fibre-reinforced material. Int. J. Eng. Sci. **7**(2), 129–152 (1969)
42. Nekouie, V., Abeygunawardane-Arachchige, G., Kühn, U., Roy, A., Silberschmidt, V.V.: Indentation-induced deformation localisation in Zr-Cu-based metallic glass. J. Alloy. Compd. **615**(5), 93–97 (2014)
43. Nemat-Nasser, S., Li, J.Y.: Electromechanical response of ionic polymer-metal composites. J. Appl. Phys. **87**(7), 3321–3331 (2000)
44. Packard, C., Schuh, C.: Initiation of shear bands near a stress concentration in metallic glass. Acta Mater. **55**(16), 5348–5358 (2007)
45. Ramamurty, U., Jana, S., Kawamura, Y., Chattopadhyay, K.: Hardness and plastic deformation in a bulk metallic glass. Acta Mater. **53**(3), 705–717 (2005)
46. Ruan, H., Zhang, L., Lu, J.: A new constitutive model for shear banding instability in metallic glass. Int. J. Solids Struct. **48**(21), 3112–3127 (2011)
47. Schroers, J., Johnson, W.L.: Ductile bulk metallic glass. Phys. Rev. Lett. **93**(25), 255506 (2004)
48. Schuh, C.A., Hufnagel, T.C., Ramamurty, U.: Mechanical behavior of amorphous alloys. Acta Mater. **55**(12), 4067–4109 (2007)
49. Schuster, B.E., Wei, Q., Hufnagel, T.C., Ramesh, K.T.: Size-independent strength and deformation mode in compression of a Pd-based metallic glass. Acta Matter. **56**, 5091–5100 (2013)
50. Schwarz, R., Johnson, W.: Formation of an amorphous alloy by solid-state reaction of the pure polycrystalline metals. Phys. Rev. Lett. **51**(5), 415 (1983)
51. Shi, Y., Falk Michael, L.: Stress-induced structural transformation and shear banding during simulated nanoindentation of a metallic glass. Acta Mater. **55**(13), 4317–4324 (2007)
52. Spaepen, F.: A microscopic mechanism for steady state inhomogeneous flow in metallic glasses. Acta Metall. **25**(4), 407–415 (1977)
53. Steif, P., Spaepen, F., Hutchinson, J.: Strain localization in amorphous metals. Acta Metall. **30** (2), 447–455 (1982)
54. Thamburaja, P.: Length scale effects on the shear localization process in metallic glasses: A theoretical and computational study. J. Mech. Phys. Solids **59**(8), 1552–1575 (2011)
55. Vaidyanathan, R., Dao, M., Ravichandran, G., Suresh, S.: Study of mechanical deformation in bulk metallic glass through instrumented indentation. Acta Mater. **49**(18), 3781–3789 (2001)

56. Van Diepen, A., Buschow, K.: Hydrogen absorption in $CeFe_2$ and $ThFe_3$. Solid State Commun. **22**(2), 113–115 (1977)
57. Vincent, S., Basu, J., Murty, B., Bhatt, J.: Micro indentation study on $Cu_{60}Zr_{20}Ti_{20}$ metallic glass. Mater. Sci. Eng., A **550**, 160–166 (2012)
58. Volkert, C.A., Donohue, A., Spaepen, F.: Effect of sample size on deformation in amorphous metals. J. Appl. Phys. **103**, 1–5 (2008)
59. Wang, W.H.: The elastic properties, elastic models and elastic perspectives of metallic glasses. Prog. Mater. Sci. **57**(3), 487–656 (2012)
60. Wang, E.Z., Shrive, N.G.: Brittle fracture in compression: Mechanisms, models and criteria. Eng. Fract. Mech. **52**(6), 1107–1126 (1995)
61. Yang, Q., Mota, A., Oriz, M.: A finite-deformation constitutive model of bulk metallic glass plasticity. Comput. Mech. **37**, 194–204 (2006)
62. Yeh, X., Samwer, K., Johnson, W.: Formation of an amorphous metallic hydride by reaction of hydrogen with crystalline intermetallic compounds—a new method of synthesizing metallic glasses. Appl. Phys. Lett. **42**(3), 242–243 (1983)
63. Zhang, H., Jing, X., Subhash, G., Kecskes, L.J., Dowding, R.J.: Investigation of shear band evolution in amorphous alloys beneath a Vickers indentation. Acta Mater. **53**(14), 3849–3859 (2005)
64. Zhao, M., Li, M.: A constitutive theory and modeling on deviation of shear band inclination angles in bulk metallic glasses. J. Mater. Res. **24**(08), 2688–2696 (2009)

Constitutive Properties of Pure Indium in Wide Temperature Range

Xiaojin Cheng, Changqing Liu and Vadim V. Silberschmidt

Abstract For microelectronic devices used in low-temperature applications, understanding of their reliability and performance has become an important research subject covering their service under severe or extreme conditions. Along with challenges due to continuing miniaturisation of such devices, various properties and relevant thermo-mechanical response of interconnection materials to temperature excursions at micro-scale became a critical factor that can affect reliable performance of microelectronics in various applications. Pure indium, as an excellent interconnection material, has been used in the pixellated detector systems, functioning at cryogenic temperatures. The properties and behaviour of indium joints determine the functionality and performance of the detector system directly since higher resolution of the sensor is achieved by bonding it with a readout assembly via ultra-fine indium bumps. In this study, deformation behaviour of indium joints was investigated by considering effects of its microstructure, including the joint size (thin and thick joints) and substrate type (In/Cu and In/Ni/Cu joints), and temperature. A constitutive relationship was thus established to describe the deformation properties of indium joints under a wide range of homologous temperatures.

1 Introduction

One serious concern in development of microelectronics for low-temperature applications is assessment of performance and reliability issues of an electronic system subjected to various temperature changes. For example, in extreme service conditions, a hybrid pixel detector [1] can undergo a temperature excursion from a low of 76 K to a high of 300 K. Another example of extreme temperatures is a

---

X. Cheng (✉) · C. Liu · V.V. Silberschmidt
Wolfson School of Mechanical and Manufacturing Engineering,
Loughborough University, Loughborough, Leicestershire LE11 3TU, UK
e-mail: nataliecheng1314@gmail.com

V.V. Silberschmidt and V.P. Matveenko (eds.), *Mechanics of Advanced Materials*,
Engineering Materials, DOI 10.1007/978-3-319-17118-0_6

space exploration rover, as recorded by Apollo 17 [2], with a range from 76 to 420 K. Apparently, thermal stresses and deformations of microelectronics arising from temperature changes are defined by constitutive properties of interconnection materials and bonding strength of under-bump-metallisation, and should be limited by threshold values related to the permissible loads for electronic components. Thus, it is essential to gain the knowledge of the deformation behaviour of interconnection materials for a wide range of temperatures as well as of characteristic features of bonding interface between solder and its under-bump-metallisation.

One typical application for low-temperature microelectronic interconnections is indium joints used in pixellated detector systems. Large facilities, for instance, the Diamond Light Source in Didcot, UK, the European Synchrotron Facility in Grenoble, France and the European X-ray Free Electron Laser in Hamburg, Germany devote considerable efforts to develop pixellated silicon and germanium detectors used in cryogenic temperatures. Also, other imaging detectors include high-resolution thermal imaging cameras and near-infrared detectors [1]. Since each indium joint represents a single pixel in detector systems by interconnecting a signal line of the sensor to a hybrid detector assembly (i.e. ASIC, see Fig. 1), the properties and behaviour of an individual joint play an important role in determining their functionality. Thus, as the pixel density determines the sensor's resolution, one of the main challenges linked with the development of finer bumps (i.e. higher pixel density) is to minimise thermal stresses in indium joints under various in-service conditions. Due to its extreme service temperature range, thermally-induced stresses in indium joints in low-temperature microelectronics are linked to a larger temperature change, for example, from room temperature (298 K) to liquid-nitrogen temperature (76 K). Hence, in this paper, the deformation behaviour of indium joints is investigated by considering the effect of such temperature change, as well as the effects of joint size and substrate material used as under-bump-metallisation (UBM).

Since deformation under external forces or temperature changes is a kinetic process, the constitutive properties related to each deformation mechanism are often determined by the levels of applied stress and homologous temperature ($T_h = T/T_m$) [3, 4]. As a result of a low melting temperature of indium (T_m = 429 K), even the room temperature (298 K) represents a homologous temperature greater than 0.6. Hence, indium joints in service can be susceptible to

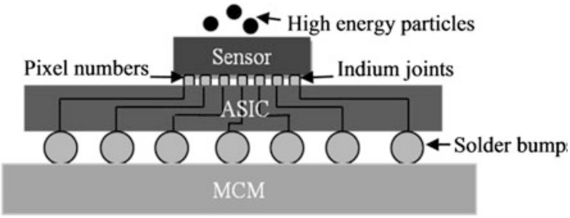

Fig. 1 Schematic of hybrid pixel detector system (after [1]): *ASIC* application-specific integrated circuit; *MCM* multichip modules

creep. For some strain-rate-sensitive metals and alloys with relatively low strain-hardening, the experimental results [5] have indicated that creep could occur at homologous temperatures of 0.1–0.3. It means that indium serving as interconnection at cryogenic temperatures, for example, is already close to 0.3 T_m at 120 K. The studies of creep for bulk indium [6] indicated that a steady-state creep strain rate predominantly increased with the increase in applied stress at 76 K. Hence, creep is an important feature of deformation properties of indium in its low-temperature applications.

In this study, the stress-strain data and creep behaviour of indium joints were obtained with consideration of joint size, substrate type and different homologous temperatures. A methodology was developed to predict deformation mechanisms with respect to a wide range of homologous temperatures, and a constitutive relationship for indium joints was proposed to cover the range of homologous temperatures between 0.18 and 0.96 based on the experimental data and the developed methodology.

2 Deformation Properties of Indium

2.1 Available Data from Literature

2.1.1 Elasticity

Kim and Ledbetter [7] investigated the elastic moduli of polycrystalline indium for a temperature range from 5 to 300 K. The elastic constants of pure indium showed a regular temperature-dependent behaviour for pure metals. However, a comparison among these constants showed that the Young's and shear moduli presented the largest change, increasing approximately 55 % when the temperature fell from 300 to 5 K. Thus, the temperature-dependent elasticity of pure indium should be an important factor to be considered in thermal stress analysis of electronic packaging if an indium joint is exposed to a wide range of temperatures.

2.1.2 Plasticity

The yield, plastic flow and fracture characteristics of metals and alloys can be distinct due to different microscopic deformation systems, which are attributed to various lattice structures. Although the crystal structure of indium is commonly known as face-centred tetragonal, it actually behaves like f.c.c. metals with respect to the strain-hardening behaviour. In the study of the tensile behaviour of indium, Reed et al. [8] compared the strain-hardening rate during deformation at 4, 10, and 76 K. It was identified that the stress-strain characteristics of pure indium at low temperatures followed a power-law form with the strain-hardening exponent (N) being 0.64 at 4 and 10 K, and 0.51 at 76 K. This corresponded very closely to the value for f.c.c. metals (e.g. copper and aluminum) at equivalent homologous temperature. Their stress-strain curves showed, under the same strain rate, the average yield stress was 0.93 MPa at 295 K, 2.8 MPa at 76 K and 3.09 MPa at 4 K. Accordingly, ultimate strength was 1.6, 15.0 and 32.0 MPa, respectively.

2.1.3 Viscoplasticity and Creep

Various researchers have carried out experimental studies to investigate the rate- and temperature-dependent stress-strain response of indium in bulk as well as in the form of solder joints [9, 10]. A wide range of strain rates and temperatures has been applied to evaluate their effects on the properties of indium, such as the Young's modulus, yield stress and ultimate strength. All of these experimental results showed similar effects: an increase in the Young's modulus, yield stress and ultimate strength with the increase in strain rate, while an increase in temperature indicates, generally, an opposite effect.

The magnitude of creep depends strongly on temperature since it is a thermally activated process. At temperatures below around 0.3 T_m, no thermal recovery process could be observed [4, 5]. From a cryogenic point of view, creep is negligible at ambient temperatures low enough for metals around 0.3 T_m and for alloys about 0.4 T_m [4, 11, 12]. Steady-state creep is not reached as it is achieved when hardening is balanced by a thermal recovery processes, in addition to the strain induced in primary creep is small. However, failures were verified in the application of pure indium as an interconnection material at low temperatures due to a combination of steady-state creep and the differential coefficient of thermal expansion [8, 13, 14].

Reed et al. [6] measured tensile creep strain of pure indium under constant loads at 4 and 76 K. A comparison of initial creep strain at 4 and 76 K showed yield stress was insensitive to temperature in the tested range since the same stress was approached at zero strain for both temperatures. The effect of applied stresses on primary creep at 76 K implied that primary strain required more time to stabilize at higher loads. In contrast, the primary strain region was completed earlier at 4 than at 76 K with less transient creep at equivalent stress. Their results also suggested that the steady-state creep could dominate the deformation process of pure indium even at low temperatures due to the observed linear relationships between the steady-state creep rate and applied stress.

The relevant and available data for indium in the literature verified that the deformation behaviour of pure metals and alloys, including indium, is strongly dependent on the following macroscopic variables: the applied stress level, strain rate, temperature and microstructure of the material. The particular equations, also known as constitutive equations, should be stated for each deformation mechanism with regard to these variables. Since deformation under external stress or temperature change is a kinetic process, the correlation of stress with homologous temperature should be implemented schematically in order to describe the possible dominance of the deformation mechanism(s) for a material [4]. Hence, the deformation properties of indium joints were investigated, especially the inelastic properties concerned with these factors. In regard to the microstructure-dependent behaviour, the effect of microstructure features (e.g. IMC) on deformation of indium joints was included by taking into account of different joint sizes and substrate types. Furthermore, a constitutive equation was proposed based on the experimental data and the developed methodology to describe the deformation behaviour of indium joints for its low-temperature applications.

2.2 This Study

2.2.1 Sample Preparation

The deformation properties of indium joints were measured at room temperature by considering various joint sizes (thin and thick joints) and substrate types (Cu and Ni/Cu). The temperature- and stress-dependent creep behaviours of the indium joints for both joint sizes were also examined. The specimen's configuration employed in experimental testing is schematically shown in Fig. 2. For the thin joints, the dimension of indium joints along the *Y* axis was 120 ± 30 µm; it was close to 1 mm on average for the thick joints. For the Ni/Cu substrate, nickel was electroplated on a Cu substrate before bonding indium on it (thus forming a In/Ni/Cu joint) in order to compare the effect of the interfacial microstructure (e.g. intermetallic compound (IMC)) on the deformation behaviour and bonding strength of the indium joints. All the joints were formed by reflow in air with a peak temperature of 500 K (227 °C) for 400 s. The cooling rate of the reflow process was about 0.2 K/s. All the specimens were stored at room temperature for 1–3 days to allow stress relaxation before testing.

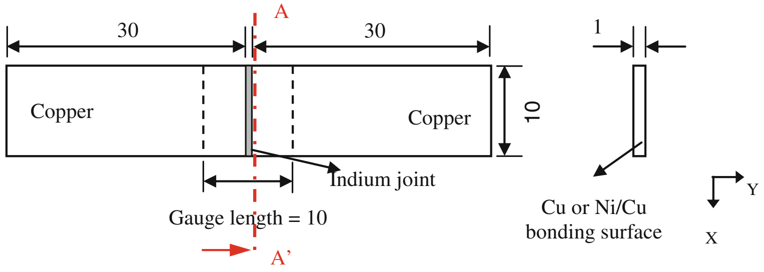

Fig. 2 Specimen configuration for testing: top view (*left*); section *A-A*' in direction of arrow (*right*). All dimensions are in mm

2.2.2 Mechanical Behaviour at Room Temperature

All the stress-strain relationships for the studied indium joints were obtained in tension at a constant displacement rate, 0.08 mm/s (the strain rate approximately 0.0075 s^{-1}), at room temperature (298 K). One set of tests with two displacement rates, 0.0013 and 0.08 mm/s, was conducted on the In/Ni/Cu joints for both joint sizes to understand the effect of strain rate on the mechanical response of indium joints. All the stress-strain characteristics of the indium joints are presented using the engineering stress-strain curve.

The typical curves of the indium joints on both the Cu substrate and Ni/Cu metallization are presented in Fig. 3 for the thin and thick joints. The stress-strain curves demonstrate the plastic deformation associated with strain hardening and necking in indium joints after a limited elastic range. Under the same displacement rate, the stress-strain response of the indium joints on Ni/Cu metallization is less sensitive to joint sizes. In contrast, for the In/Cu joints, higher strengthening was observed in the thin joints compared to the thick ones. To explain this, a reference can be made to the well-known Hall-Petch relationship [15, 16], according to which different mechanical properties of a material can be attributed to the feature of grain size, determined generally by a cooling rate during the solidification process. In the present study, the same cooling rate was adopted in the fabrication of all the samples. Due to the significant volume difference between the thin and thick joints, the cooling process is expected to be much quicker in the former than in the latter,

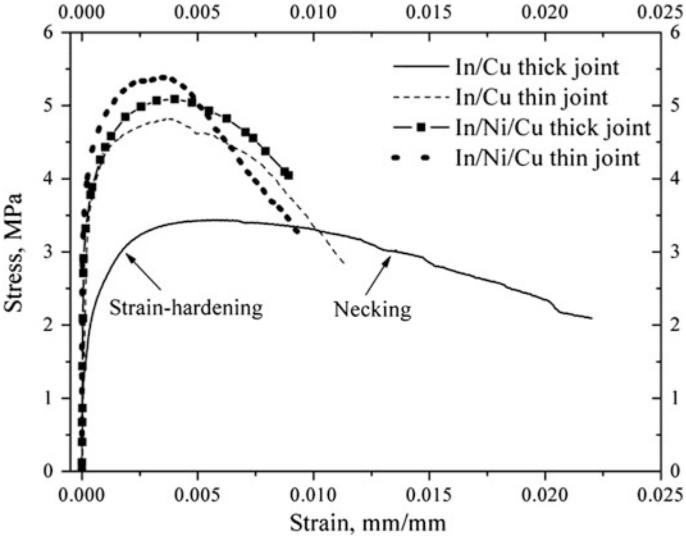

Fig. 3 Stress-strain curves of indium joints with two types of substrates: thick (*solid line*) and thin (*dashed line*) joints with Cu substrate; thick (-■-) and thin (*dotted line*) joints with Ni/Cu substrate (298 K, displacement rate 0.08 mm/s)

resulting in a finer grain structure. It subsequently led to different strengthening behaviours.

Compared to the In/Cu joints, the stress-strain characteristic of the indium joints on Ni/Cu substrate indicated less difference with regard to the joint size. As can be seen, indium joints of both sizes behaved similarly in both elastic and strain-hardening regions. The thin joints exhibited a slightly higher ultimate strength than the thick ones, which could be attributed to the grain-size effect discussed above. However, regarding the different response of indium joints between In/Cu and In/Ni/Cu to joint size, the microstructural difference is believed to be responsible for this: A number of faceted and large particles were found near the In/Ni interface, which EDX analysis revealed a composition of the $Ni_{10}In_{27}$ IMC phase; such dispersed IMC particles were only observed in the In/Ni/Cu thick joints as given in Fig. 4. Hence, the contribution of a dispersion-strengthening by IMCs as reported in many researches [17–20] is believed to be attributed to the different response between two substrate types to joint size.

For the indium joints on Ni/Cu substrate, the effect of the displacement rate was compared for joints of different sizes. The values of yield stress and ultimate strength were obtained for each rate; the stress offset method was used to estimate the yield stress. Figure 5 presents the effect of displacement rate on the yield stress (Fig. 5a) and ultimate strength (Fig. 5b). The comparison of the two parameters showed that the yield stress is less sensitive to the increase in displacement rate in comparison with the ultimate strength, especially for the thin joints.

2.2.3 Creep

The study of the effects of temperature and applied load on the creep behaviour of the indium joints was carried out on the In/Cu specimen for both joint sizes. The creep tests were performed at 298, 343 and 386 K corresponding to homologous temperature of 0.7, 0.8 and 0.9, respectively. A comparison of creep behaviour between the In/Cu and In/Ni/Cu joints is also investigated. In terms of the applied

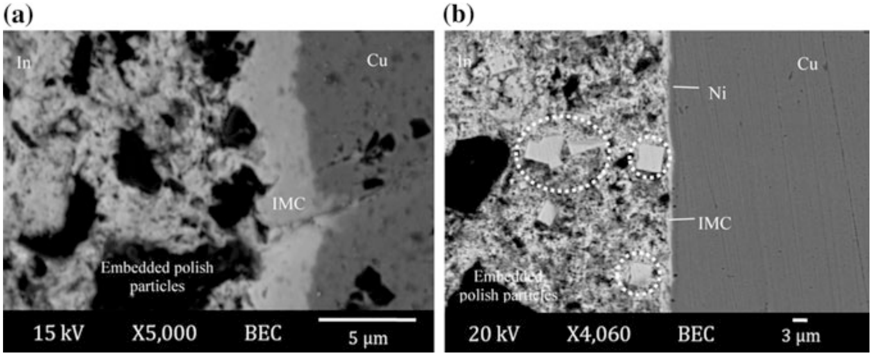

Fig. 4 SEM images of cross section of **a** In/Cu and **b** In/Ni/Cu interface of thick joints

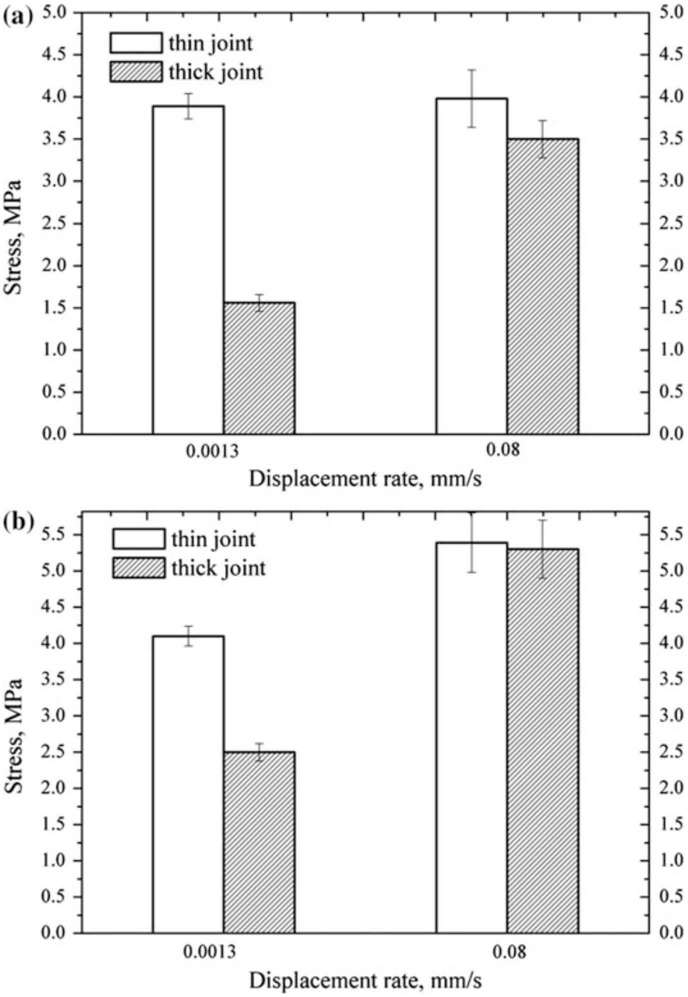

Fig. 5 Effect of displacement rate on yield stress **a** and ultimate strength **b** of thin and thick joints (Ni/Cu metallization, 298 K)

load, it is generally selected between 20 and 80 % of the yield stress. However, based on the obtained yield stress listed in Fig. 5, three loads—7.5, 10 and 15 N were chosen by considering the sensitivity of the extensometer (with a resolution of 0.2 μm) and being capable to obtain enough creep data at higher temperature (e.g. 386 K). These magnitudes correspond to 19.0, 25.1 and 37.7 % of the yield stress for the In/Ni/Cu thick joints at 0.08 mm/s displacement rate (the strain rate approximately 0.0075 s^{-1}), respectively.

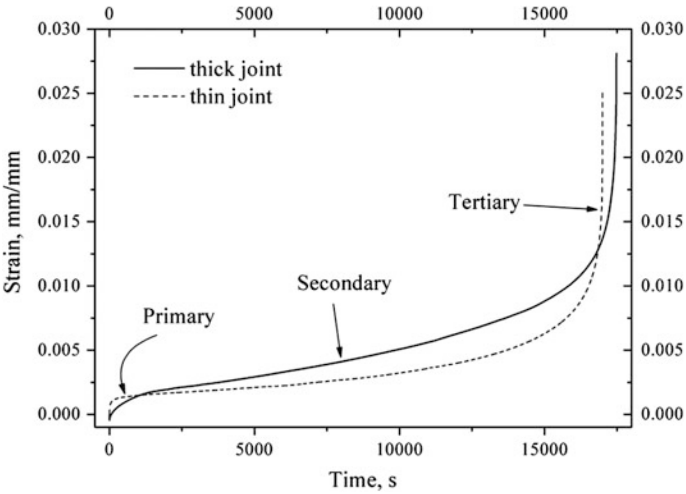

Fig. 6 Typical creep curves of indium joints on Cu substrate under load of 10 N (298 K)

Effect of Joint Size and Substrate Material

Typical creep strain—time plots of the In/Cu specimen are shown in Fig. 6 for both thin and thick joints under an applied load of 10 N at 298 K. Both curves demonstrate three stages of creep deformation as showed in Fig. 6: primary creep (transient creep), the secondary stage representing steady-state creep, and the tertiary stage resulting from necking or cracking.

The creep strain rate in the tests started at a high level and decreased to a steady-state value. It is apparent that the indium joints exhibited a normal, decelerated primary creep region, which is typical for pure metals. The onset of secondary creep in the thin joints started earlier than in the thick ones, which is believed to attribute to a higher strain-hardening rate taking place in the thin joints as observed in the stress-strain behaviour of the indium joints (see Figs. 3 and 5) since the decreasing strain rate in the primary creep is proportional to the strain-hardening rate. Overall, the creep data obtained at room temperature imply that the thin joints are more creep-resistant than the thick ones under a given loading level, which showed a consistent result with the constant-displacement-rate tests.

In order to understand the effect of microstructure on the creep behaviour of the studied indium joints, some typical strain-time plots for both types of substrate—In/Cu and In/Ni/Cu—were compared. The results are shown in Fig. 7 for the thin and thick joints. Since there was a significant difference in duration of test for both substrates, the steady-state strain rate, which is determined from the slope of the linear part of the plot, was calculated and compared as given in Fig. 7. This rate for the In/Ni/Cu joints is, on average, one order of magnitude lower than the In/Cu joints at the same loading level and temperature. These findings are in agreement with the found stress-strain behaviour of the indium joints as given in Fig. 3, demonstrating higher compliance of the In/Cu joints.

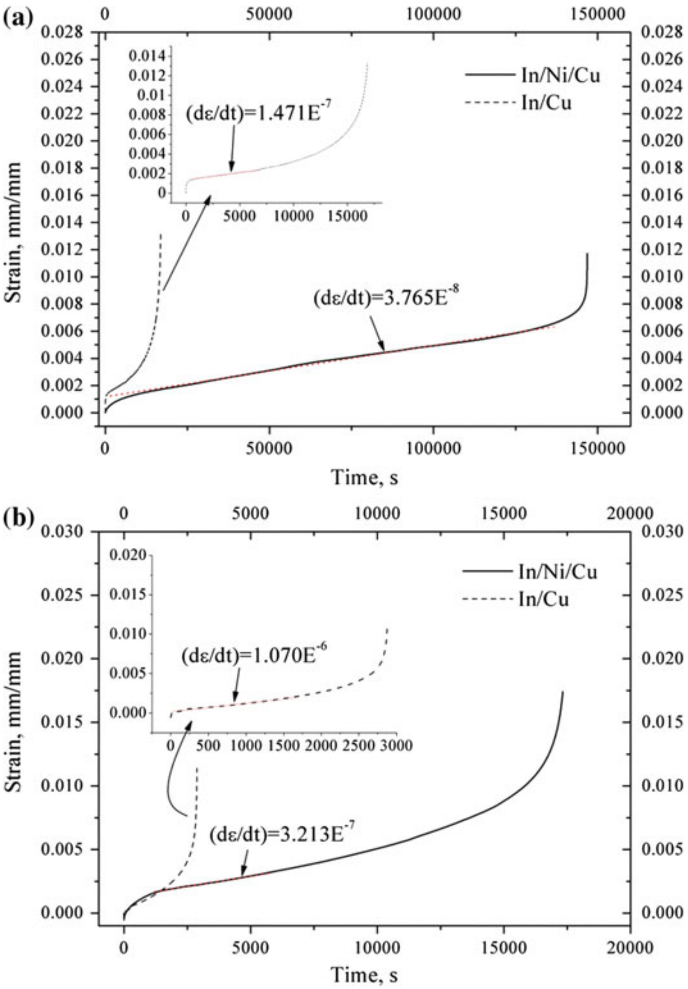

Fig. 7 Typical creep curves of indium joints on Cu and Ni/Cu substrates at 298 K: **a** thin joint, 10 N; **b** thick joint, 15 N

Effect of Temperature

In general, creep can be expressed using a power-law relationship to describe the stress-dependent behaviour and an Arrhenius relationship for the temperature-dependent behaviour [17, 21]:

$$\dot{\varepsilon}_{ss} = A_1 \sigma^n \exp\left(-\frac{Q_c}{RT}\right), \tag{1}$$

where, according to [22],

$$A_1 = \frac{AEb}{RT}\left(\frac{b}{d}\right)^p\left(\frac{1}{E}\right)^n D_0, \tag{2}$$

Q_c is the activation energy for creep, R is the Boltzmann's constant, T is the absolute temperature, A is a material constant, E is the Young's modulus, b is the magnitude of Burgers vector, d is the material's grain size, p and n are constant exponents, D_0 is a frequency factor.

Thus, creep at a given stress can be expressed as

$$\dot{\varepsilon}_{ss} = A_2 \exp\left(-\frac{Q_c}{RT}\right), \tag{3}$$

where $A_2 = A_1\sigma^n$. So, using Eq. 3, the steady-state creep rates of the In/Cu thick joints at 298, 343 and 386 K were plotted as a function of 1000/T for an applied load of 15 N, as given in Fig. 8. From the slope of the fitting curve, the activation energy for creep Q_c was obtained as 68.35 kJ/mol for the temperature range of 298–386 K. The activation energy for lattice self-diffusion of pure indium is 74.9 kJ/mol [23], so the obtained activation energy for creep is close to that for the lattice self-diffusion mechanism in the analysed temperature range with the tested stress level.

All the creep data obtained at different temperatures and stress levels were plotted as the steady-state strain rate versus the applied stress for both thin and thick joints in Fig. 9. The stress exponent, n, was calculated by using a linear fit of the creep data obtained under different stress levels at a given temperature for both

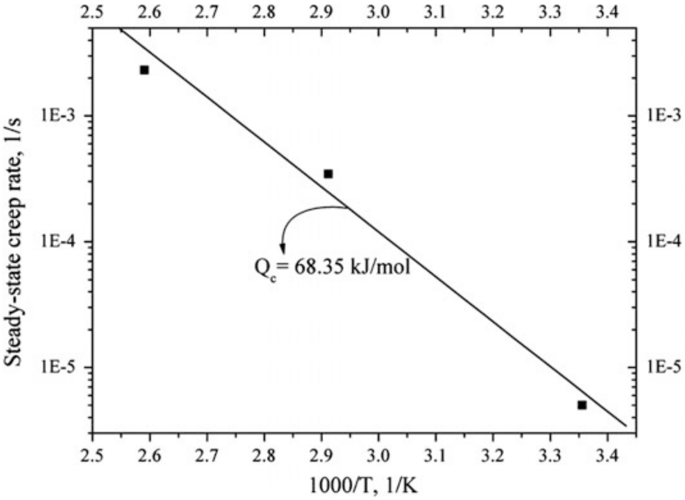

Fig. 8 Determination of activation energy using creep data at 298, 343 and 386 K (In/Cu thick joints, 15 N)

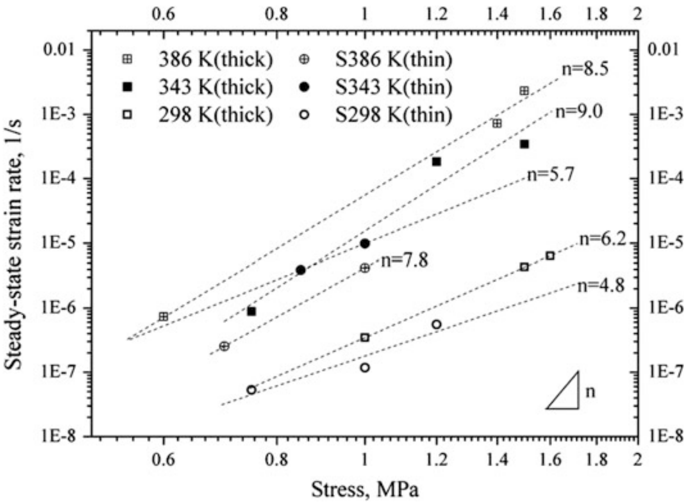

Fig. 9 Steady-state creep rate versus applied stress for various In/Cu joints at different temperatures

types of joints. Apparently, this exponent varies between 5 and 9 for all the test conditions.

When the steady-state creep is the dominant process, the map of deformation mechanisms for most metals and alloys can be schematically presented with four distinct straight-line segments on a plot of steady-state strain rate versus applied stress as regions I, II, III and IV (see Fig. 10) [24, 25]. Regions I to III occur at low and intermediate stresses: The creep usually occurs in this regime through a diffusion-controlled dislocation movement. It is also called *power-law creep* since a power-law form can generally describe plasticity of materials under this regime. At high stresses, the steady-state creep rate increases more rapidly, and the power-law

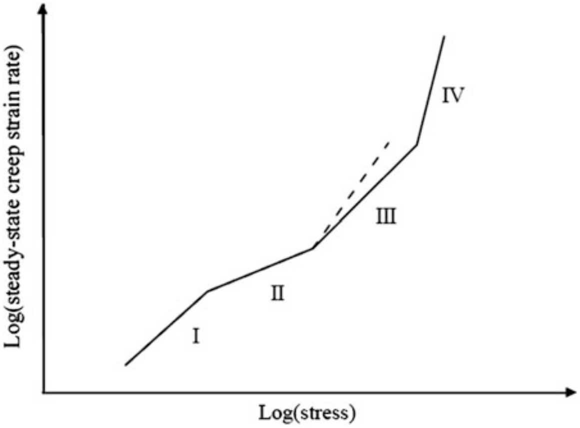

Fig. 10 Schematic of steady-state creep strain rate versus applied stress diagram (gap between *solid* and *dashed lines* in stage III presents the range of stress exponent for this stage) [25]

behaviour breaks down as presented by region IV. The first three regions have stress exponents of approximately 3, 2, 3–7, respectively, while region IV has an exponent close to 10 or above [17, 25, 26]. Therefore, the creep deformation mechanisms of the indium joints in the present study are in the power-law creep regime including breakdown, which is normally described with a hyperbolic sine law [5, 17, 25]; the stress exponents higher than 7 ($n > 7$) were found mainly for homologous temperatures in excess of 0.8 (i.e. 343 K), at which the power-law breakdown is expected.

3 Constitutive Properties for Homologous-Temperature Range 0.18–0.96

Creep deformation of the indium joints was studied under constant loads at temperatures of 0.7, 0.8 and 0.9 T_m of indium formed on Cu substrate. The activation energy obtained for creep and the stress exponent for all testing conditions suggest that dislocation climb controls the deformation mechanism followed by the power-law breakdown at higher temperatures. In addition, steady-state creep is emphasized more than primary or tertiary creep due to a relatively large fraction of creep life within this regime. Taking all these factors into account, a hyperbolic sine function, widely used in analysis of steady-state creep of solders, was employed to describe both the power-law and power-law-breakdown (PLB) stages as

$$\dot{\varepsilon}_{ss} = A_3 \exp\left[-\frac{Q_c}{RT}\right][\sinh(\alpha\sigma)]^n, \tag{4}$$

where $\dot{\varepsilon}_{ss}$ is the steady-state creep strain-rate, A_3 and α are constants, and σ is the steady-state stress. The value of n is related to the dominant creep mechanism. For example, for pure metals and alloys, the value of n generally varies from 3 to 7 over wide ranges of stresses and temperatures when the deformation is dominated by power-law creep [27–30]. It has been well established that Q_c seems to be essentially equal to the activation energy for lattice self-diffusion Q_{sd} or 0.6 Q_{sd} for a large class of materials over certain temperatures (>0.6 T_m) [17, 24, 25, 29, 30]. This is related to the deformation mechanisms which are temperature-dependent, and the lattice-diffusion climbing is dominant in the materials when the temperature is above 0.6 T_m. However, below this, many investigations [31–33] observed that the activation energy for creep is not always constant (for instance, near to the value of Q_{sd}). The study on silver [34] and aluminium [35] demonstrated a potential trend for the activation energy for creep with a possible transition for atomic diffusion mechanisms: with one regime where $Q_c \cong Q_{sd}$ between around 0.6 and 1.0 T_m. Additionally, Q_c decreased continuously when the temperature is in the range of 0.3 and 0.6 T_m, where PLB may occur. Hence, Q_c showed a stress- and temperature-dependent character, which could be another parameter to link with the dominant deformation mechanism, apart from the stress exponent n. So, the activation energy for creep in indium was analysed and calculated based on the obtained creep data, then a methodology with regard to Q_c was proposed as a basis for establishment of a constitutive equation for indium joints used in a larger temperature range.

3.1 Activation Energy for Creep

As well known, parameters of the flow behaviour of metals and alloys, for example, their yield stress and ultimate strength can change with temperature. Hence, the applied stress for creep tests needs to have an equivalent magnitude at different temperatures to account for the change of strength with temperature. By introducing the modulus-compensated stress, σ/E, as the equivalent stress at different temperatures [5], the data in Fig. 9 were re-plotted by considering the equivalent stress for the corresponding temperature, as given in Fig. 11. The activation energy for creep was calculated by using the following procedure: (i) with reference to Eq. 1, creep at a given temperature can be simplified to a linear relationship between the steady-state creep rate and modulus-compensated stress. As given in Fig. 11, for example, two relationships (dashed lines) were obtained by curve-fitting for creep data of the thick joints under different stresses at 386 and 298 K, respectively; (ii) the steady-state creep strain rate at a given value of σ/E was calculated via the relationships obtained at the respective temperature, 386 and 298 K; (iii) the activation energy for creep Q_c of the thick joints between 386 and 298 K was obtained

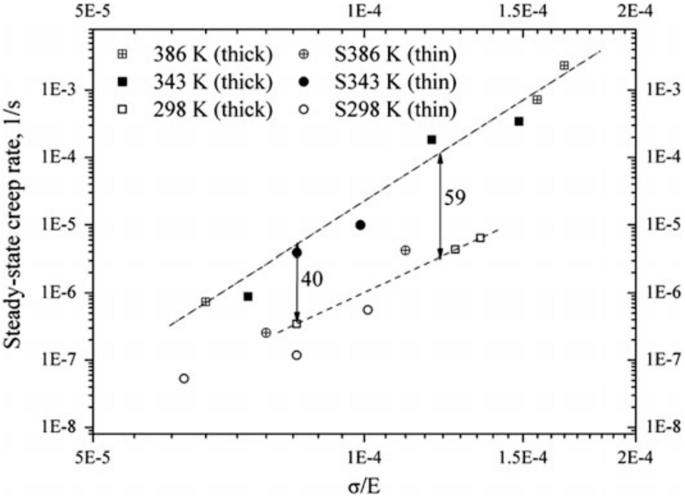

Fig. 11 Dependence of steady-state strain-rate on modulus-compensated stress of indium joints for three temperatures: *square marks* – thick indium joints; *round marks* – thin indium joints. *Dashed lines* are obtained by curve-fitting for creep data of thick joints at 386 and 298 K

by substituting the calculated steady-state creep strain rate and the corresponding temperature into the following equation (for the details of the original equation see [36]):

$$Q_c = R\left[-\frac{\left(\ln \dot{\varepsilon}_{ss}^{298K}\right) - \left(\ln \dot{\varepsilon}_{ss}^{386K}\right)}{(1/298) - (1/386)}\right]. \tag{5}$$

Thus, the magnitude of Q_c can be obtained using this method at a given stress level and for a given temperature range. Taking the creep data for the thick joints as an example, the magnitude of the activation energy varies from 40 to 59 kJ/mol for the range of modulus-compensated stress σ/E from 8.5×10^{-5} to 1.2×10^{-4} within 298–386 K (see Fig. 11).

Referring to the creep data for pure indium [6, 23], the steady-state creep rate versus the modulus-compensated stress for seven temperatures that cover the range of homologous temperature between 0.01 and 0.96 is given in Fig. 12. For a specified modulus-compensated stress, the activation energy Q_c can be calculated according to Eq. 5 based on the procedures stated above. Regarding the level of von Mises stress in indium joints obtained from simulations of a cooling-heating process with different ramp rates, the activation energies at different temperature ranges were calculated for the corresponding modulus-compensated stress range of 4.0×10^{-5} and 4.6×10^{-4} (see a hatched area in Fig. 12).

Within the targeted stress range, the activation energies for creep of indium joints were obtained between the two specified temperatures. For pure indium, the

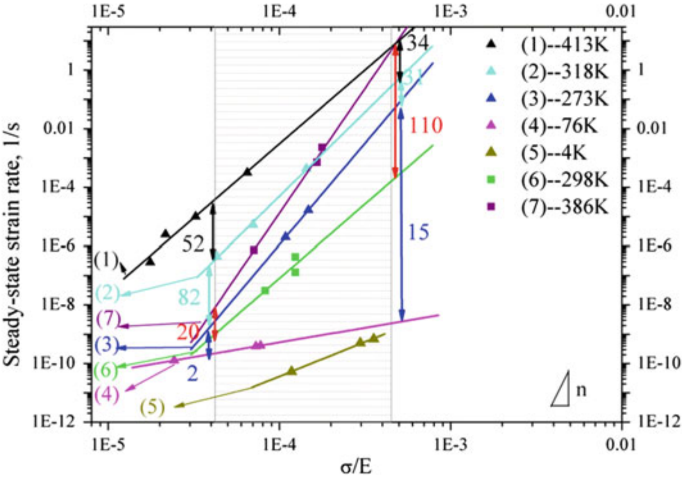

Fig. 12 Dependence of steady-state strain rate on modulus-compensated stress of indium for seven temperatures: *triangle markers* – pure indium [6, 23]; *square markers* – thick indium joints from this study. The activation energies for creep were calculated and denoted between any two fitted lines (in kJ/mol)

magnitude varies from 52 to 34 kJ/mol between 413 (curve 1) and 318 K (curve 2) with the increase in the level of applied stress, while it is in the range of 82–31 kJ/mol between 318 and 273 K (curve 3). For the indium joints, the activation energy of creep is between 20 and 110 kJ/mol in the temperature range 386–298 K (curves 6, 7). In contrast, the magnitude at temperatures below 273 K is extremely small within the targeted stress range (i.e. 2–15 kJ/mol), as given between 273 (curve 3) and 76 K (curve 4). Taking the averaged value for each temperature range as a reference, it is evident that the activation energy of creep is generally either equal to the energy for the lattice self-diffusion (Q_{sd} = 74.8 kJ/mol) or close to 0.6 Q_{sd} when the temperature is above 0.6 T_m. As the slope of the fitting graph represents the stress exponent n, all the data fall within the range of n = 5–11 for temperatures between 413 and 273 K; the exceptions are for 76 and 4 K. This explains why Eq. 5 is not suitable for cryogenic temperatures. Hence, the suggested method was applied to calculate the activation energy for temperatures above 0.6 T_m. The values obtained from the data for the indium joints (curves 7 and 6) were chosen and averaged; as a result, the activation energy at high temperatures (denoted as Q_c-HT) was found to be 65.5 kJ/mol.

For the data obtained at temperatures below 273 K (Fig. 12), the activation energy of creep was established as a function of homologous temperature using the following procedures:

(i) the value of Q_c = 24.36 kJ/mol, at 76 K ($\sim$0.18 T_m) was obtained by means of a non-linear regression of creep data at 76 K from Reed et al. [6] with Eq. 4; it is denoted as Q_c-LT;
(ii) the levels of activation energy for creep at 173 K ($\sim$0.4 T_m) and 223 K ($\sim$0.5 T_m) were determined by regression of the creep data from Rui and McCluskey [37];
(iii) a relationship was obtained by means of interpolation and curve-fitting these data points obtained between the homologous temperatures of 0.18 and 0.6 T_m associated with Q_c-HT and Q_c-LT.

Below 0.2 T_m, the activation energy for creep was assumed to be equal to Q_c-LT. Thus, a function of the activation energy for creep in indium $Q_c(T)$ was developed for a wide range of temperature as shown in Fig. 13. The activation energy for Q_c-HT—65.5 kJ/mol—in this study with this method agrees well with the value (69 kJ/mol) reported by Frenkel et al. [38].

3.2 Constitutive Equation

By employing the developed function of activation energy for creep, a master plot of the creep data was fitted to the hyperbolic-sine relationship (Eq. 4 using software DataFit [39] and manual calculations), as given in Fig. 14. These creep data are for the temperature range 76–413 K corresponding to 0.18–0.96 T_m. The modified hyperbolic-sine relationship is in good agreement with the experimental data for a

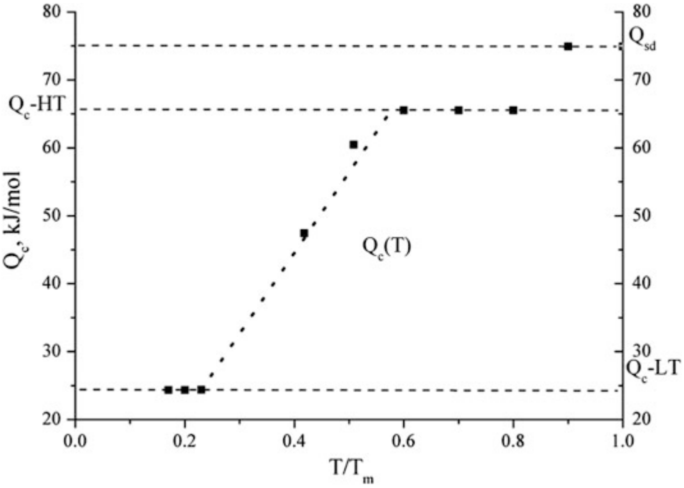

Fig. 13 Activation energy of creep versus temperature $Q_c(T)$ *(dotted line)* presents the fitted relationship between 0.18 and 0.6 T_m; Q_{sd} is activation energy of lattice self-diffusion [23]

large temperature range. However, there are a few significant deviations of some data points (marked in Fig. 14), which were obtained from the deformation of indium under compression whilst all the rest of the data were obtained under tension.

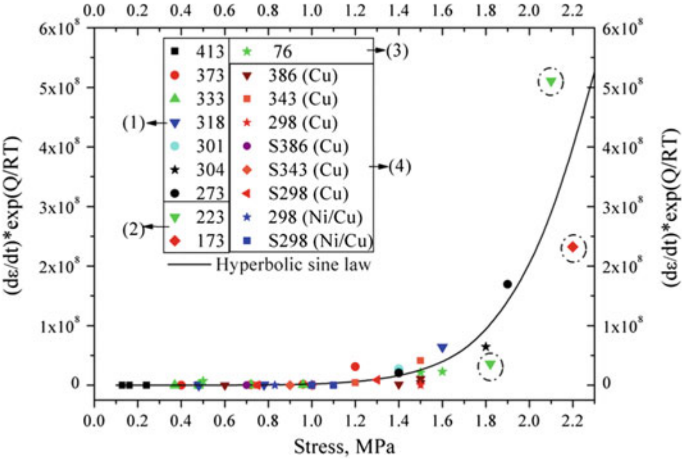

Fig. 14 Master plot of all creep data: *1* data for pure indium by Weertman [23]; *2* data for pure indium by Rui (compression) [37]; *3* data for pure indium by Reed [6]; *4* data for indium joint from this study

Overall, the proposed constitutive relationship shown in Fig. 14 produces a reasonable agreement with the experimental data, covering a wide range of homologous temperatures at certain stress levels. This provides confidence in the model's capability to predict the deformation behaviour of indium joints for large temperature changes, including cryogenic temperatures. This methodology, with respect to the activation energy, offers an approach to establish a constitutive relationship that is not only stress-dependent but also temperature-dependent, with the enhanced capability to describe a wide range of homologous temperatures.

4 Conclusions

Numerous tests of constant displacement-rate tension and creep were conducted to characterise the deformation behaviour of indium joints. According to the results obtained from these tests, the main conclusions can be drawn as follows:

1. With regard to the effect of the joint size, strain hardening during loading was more pronounced in the thin joints in comparison with that in the thick ones. The test results for the specimens formed with two different types of the substrates (i.e. Cu and Ni/Cu) demonstrated that the indium joints on Ni/Cu substrate exhibit a higher strain hardening and creep resistance than the joints on the Cu substrate.
2. Comparing the mechanical parameters, the yield stress was found to be less sensitive to the increase in the displacement rate than the ultimate strength, especially for the thin joints. The results showed that the stress-strain characteristics of the indium joints were not only size-dependent but also microstructure-dependent.
3. The stress exponent and the activation energy for creep obtained from all the creep data in this study allowed identification of the deformation mechanism of the indium joints as the power-law creep regime, which can be described by a hyperbolic sine law.
4. Employing the obtained experimental results alongside with the creep data available in the literature, a methodology for the assessment of activation energy for creep was developed to characterise the behaviour of the indium joints in a broad thermal range—from 0.18 to 0.96 of homologous temperature.
5. Finally, a constitutive relationship using varying activation energies for creep was proposed that can be used in numerical simulations of the deformation behaviour of the indium joints under thermal changes, involving low temperatures.

Acknowledgments The authors would like to acknowledge the 7th European Community Framework Programme for financial support through a Marie Curie International Research Staff Exchange Scheme (IRSES) Project entitled "Micro-Multi-Material Manufacture to Enable Multifunctional Miniaturised Devices (M6)" (Grant No. PIRSES-GA-2010-269113).

References

1. Stevens, B.: Internal report. Science and Technology Facilities Council (STFC), Rutherford Appleton Laboratory, UK (2007)
2. Chang, R.W., McCluskey, F.P.: Reliability assessment of indium solder for low temperature electronic packaging. Cryogenics **49**(11), 630–634 (2009)
3. Lau, J.H.: Thermomechanics for electronics packaging. In: Lau, J.H., Reinhold, V.N. (eds.) Thermal Stress and Strain in Microelectronics Packaging, pp. 1–72. Springer, New York (1993)
4. Frost, H.J.: Deformation-Mechanism Maps: The Plasticity and Creep of Metals and Ceramics. Pergamon Press, Oxford (1982)
5. Kassner, M.E.: Introduction. In: Fundamentals of Creep in Metals and Alloys, pp. 1–8. Elsevier, Amsterdam; London (2009)
6. Reed, R.P., Walsh, R.P.: Creep of indium at low temperature. Adv. Cryogen. Engin. (Mater) **38**, 117–126 (1992)
7. Kim, S., Ledbetter, H.: Low-temperature elastic coefficients of polycrystalline indium. Mater. Sci. Eng. A **252**(1), 139–143 (1998)
8. Reed, R.P., McCowan, C.N., Walsh, R.P., Delgado, L.A., McColskey, J.D.: Tensile strength and ductility of indium. Mater. Sci. Eng. A **102**, 227–236 (1988)
9. Darveaux, R., Turlik, I.: Shear deformation of indium solder joints. IEEE Trans. Compon. Hybrids Manuf. Technol. **13**(4), 929–939 (1990)
10. Darveaux, R., Hwang, L.-T., Reisman, A., Turlik, I.: Thermal analysis of a multichip package design. J. Electron. Mater. **18**(2), 267–274 (1989)
11. Weertman, J.: Steady-state creep of crystals. J. Appl. Phys. **28**(10), 1185–1189 (1957)
12. Weertman, J.: Dislocation model of low-temperature creep. J. Appl. Phys. **29**(12), 1685–1689 (1958)
13. Wigley, D.A.: Deformation processes in pure metals. In: Mechanical Properties of Materials at Low Temperatures, pp. 1–42. Plenum Press, New York (1971)
14. Hands, B.A.: Cryogenic Engineering, 1st edn. Academic Press, Harcourt Brace Jovanovich, London (1986)
15. Hall, E.O.: The deformation and ageing of mild steel 3: discussion of results. Proc. Phys. Soc. London Sect. B **64**(381), 747–753 (1951)
16. Petch, N.J.: The cleavage strength of polycrystals. J. Iron Steel Inst. **174**, 25–28 (1953)
17. Darveaux, R.: Mechanical evaluation of indium for die attachment in a multichip package. Ph. D. thesis, North Carolina State University, USA, (1993)
18. Jang, J.W., Silva, A.P.D., Lee, T.Y., Lin, J.K., Frear, D.R.: Direct correlation between microstructure and mechanical tensile properties in Pb-free solders and eutectic SnPb solder for flip chip technology. Appl. Phys. Lett. **79**(4), 482–484 (2001)
19. Lin, J.K., Jang, J.W.: Interfacial reactions and performance of lead-free solder joints. In: Pecht, M., Ganesan, S. (eds.) Lead-Free Electronics, pp. 406–410. Wiley, Hoboken (2006)
20. Mccormack, M., Jin, S., Kammlott, G.W., Chen, H.S.: New Pb-free solder alloy with superior mechanical properties. Appl. Phys. Lett. **63**(1), 15–17 (1993)
21. Frost, H.J., Ashby, M.F.: Rate-equations. In: Frost, H.J., Ashby, M.F. (eds.) Deformation-Mechanism Maps: The Plasticity and Creep of Metals and Ceramics, pp. 6–16. Pergamon Press, Oxford (1982)
22. Stocker, R.L., Ashby, M.F.: On the empirical constants in the Dorn equation. Scr. Metall. **7**(1), 115–120 (1973)
23. Weertman, J.: Creep of indium, lead, and some of their alloys with various metals. Trans. Am. Inst. Min. Metall. Eng. **218**(2), 207–218 (1960)
24. Schubert, A., Walter, H., Dudek, R., Michel, B., Lefranc, G., Otto, J., Mitic, G.: Thermo-mechanical properties and creep deformation of lead-containing and lead-free solders. In: International Symposium on Advanced Packaging Materials: Processes, Properties and Interfaces, Braselton, 11–14 March 2001

25. Zhang, Q., Dasgupta, A.: Constitutive properties and durability of selected lead-free solders. In: Pecht, M., Ganesan, S. (eds.) Lead-Free Electronics, pp. 237–373. Wiley, Hoboken (2006)
26. Hacke, P.L., Sprecher, A.F., Conrad, H.: Thermomechanical fatigue of 63Sn-37Pb solder joints. In: Lau, J.H., Reinhold, V.N. (eds.) Thermal Stress and Strain in Microelectronics Packaging, pp. 467–489. Springer, New York (1993)
27. Garofalo, F.: Fundamentals of Creep and Creep-Rupture in Metals. The University of California, Macmillan (1965)
28. Hertzberg, R.W., Vinci, R.P., Hertzberg, J.L.: Deformation and Fracture Mechanics of Engineering Materials, 5th edn. Wiley, Hoboken (2012)
29. Weertman, J.: Steady-state creep through dislocation climb. J. Appl. Phys. **28**(3), 362–364 (1957)
30. Weertman, J.: Theory of steady-state creep based on dislocation climb. J. Appl. Phys. **26**(10), 1213–1217 (1955)
31. Raj, S.V., Langdon, T.G.: Creep behaviour of copper at intermediate temperatures—I. Mechanical characteristics. Acta Metallurgica **37**(3), 843–852 (1989)
32. Ruano, O.A., Wadsworth, J., Sherby, O.D.: Harper-Dorn creep in pure metals. Acta Metall. **36** (4), 1117–1128 (1988)
33. Spingarn, J.R., Barnett, D.M., Nix, W.D.: Theoretical descriptions of climb controlled steady state creep at high and intermediate temperatures. Acta Metall. **27**(9), 1549–1561 (1979)
34. Kassner, M.: The rate dependence and microstructure of high-purity silver deformed to large strains between 0.16 and 0.30 T_m. Metall. Mater. Trans. A **20**(10), 2001–2010 (1989)
35. Luthy, H., Miller, A.K., Sherby, O.D.: The stress and temperature dependence of steady-state flow at intermediate temperatures for pure polycrystalline aluminium. Acta Metall. **28**(2), 169–178 (1980)
36. Cheng, X., Liu, C., Silberschmidt, V.V.: Numerical analysis of thermo-mechanical behaviour of indium micro-joint at cryogenic temperatures. Comput. Mater. Sci. **52**(1), 274–281 (2011)
37. Rui, W., McCluskey, F.P.: Constitutive relations of indium solder joint in cold temperature electronic packaging based on Anand model. J. Electron. Mater. **38**(9), 1855–1859 (2008)
38. Frenkel, R.E., Sherby, O.D., Dorn, J.E.: Activation energies for creep of cadmium, indium, and tin. Acta Metall. **3**(5), 470–472 (1955)
39. Datafit: http://www.oakdaleengr.com/ (2014). Accessed 20 Nov 2014

Metamaterials with Negative Poisson's Ratio: A Review of Mechanical Properties and Deformation Mechanisms

Xiaonan Hou and Vadim V. Silberschmidt

Abstract Compared to conventional materials, materials with a negative Poisson's ratio are endowed with many specific mechanical features; consequently, there are many potential applications for them. For the last two decades, many efforts have been made on this sort of metamaterial both experimentally and theoretically. This paper provides a brief review of those studies with a focus on mechanical properties and deformation mechanisms of the metamaterials. The latter are explained using a structure of a multi-phase metamaterial system for a more comprehensive understanding and as an inspiration for future works. Additionally, respective manufacturing methods and applications are also summarised.

1 Introduction

With the progress in modern engineering, requirements for engineering materials are becoming more specific and stringent. For centuries, many efforts have been made to improve mechanical properties of engineering materials. For example, ancient blacksmiths are known to have used different steels in the core region and sharp edge of a sword to achieve a harmonious balance of hardness and ductility. Different lamination methods of the cross section of the blades were also known to have led to different degrees of overall mechanical performance [1]. This example indicates two most important factors affecting mechanical properties of an engineering material: constituents and microstructure. In modern engineering, mechanical behaviour of composite, or multi-phase, materials is well understood. Designers employ different materials, fine-tuning their work together to achieve

---

X. Hou (✉)
Warwick Manufacturing Group, University of Warwick, Coventry CV4 7AL, UK
e-mail: Xiaonan.Hou@warwick.ac.uk

V.V. Silberschmidt
Wolfson School of Mechanical and Manufacturing Engineering,
Loughborough University, Loughborough, Leicestershire LE11 3TU, UK

V.V. Silberschmidt and V.P. Matveenko (eds.), *Mechanics of Advanced Materials*,
Engineering Materials, DOI 10.1007/978-3-319-17118-0_7

specific properties of composites. Recently, the concept of mechanical metamaterials has been introduced, which places more emphasis on the effects of a material's deliberate microstructure on its overall (effective) properties [2]. These recent developments demonstrate that a study of mechanical properties of materials underpins control and understanding of a "bottom-up" material development process. It means that engineering materials with novel mechanical properties could be designed from a concept by manipulating their constituents and microstructures. The developed concept could be applied at various—and multiple—scales according to potential applications and manufacturing techniques. Such a trend may gradually form a new research direction based on a combination of mechanics of materials, materials science and manufacturing technologies. One of the seminal directions for such studies is to develop new metamaterials with a negative Poisson's ratio (NPR).

Within the last 20 years, a variety of NPR materials and structures have been discovered, fabricated, or synthesized, ranging from macroscopic down to molecular levels, and spanning nearly all major classes of materials, such as polymers, metals, ceramics, composites, laminates and fibres, etc. [3, 4]. The present paper attempts to review the development of NPR materials using their intrinsic principles, rather than to provide a list of them, for a better understanding of this type of material. Then, special mechanical properties of such materials are summarised on basis of their specific structures. Finally, a discussion and a perspective are provided to inspire their future development.

2 Poisson's Ratio

2.1 Definition

A Poisson's ratio is named after Siméon Denis Poisson, who defined the ratio v between transverse strain ε_t and longitudinal strain ε_l in elastic loading as shown in the following equation [5, 6]:

$$v = -\frac{\varepsilon_t}{\varepsilon_l}. \tag{1}$$

Tensile deformation is considered positive while compressive is negative. The minus sign in the definition confirms that most of traditional materials have a positive Poisson's ratio [7]. From the continuum point of view, it can be explained as most materials resist a change in their volume more than they resist a change in shape [8]. From a microstructural point of view, the reason is that inter-atomic bonds tend to realign with increasing external deformation [9].

In the early development of the theory of elasticity, the Poisson's ratio was believed to be an elastic constant with the same magnitude −0.25—for all isotropic materials, according to a so called *uniconstant theory* [10–12]. Then, development of the classical elasticity theory unveiled the fact that the elastic behaviour of isotropic materials is characterized by two independent parameters: elastic modulus and Poisson's ratio, and the value of the Poisson's ratio can differ from one materials to another [6, 11]. Now, the classical elasticity theory places limits on the Poisson's ratio for isotropic materials of $-1 \leq \nu \leq 0.5$ [13]. The bounds are defined by the fact that, for an unconstrained block of an isotropic material to be stable, its elastic moduli must be positive. Using the standard interrelations depending on assumptions of isotropy, linearity and elasticity, a positive bulk modulus B

$$B = \frac{E}{3(1 - 2\nu)} \tag{2}$$

implies the Poisson's ratio less than 0.5; a positive shear modulus G

$$G = \frac{E}{2(1 + \nu)} \tag{3}$$

determines that the Poisson's ratio is greater than −1 [14, 15].

Therefore, these two magnitudes are usually used to present the Poisson's ratio as Fig. 1 that illustrates the window of Poisson's ratio for various materials [6, 16]. For most of common solid materials, such as metals, polymers and isotropic composites, $0.25 < \nu < 0.35$. When $G \leq B$, ν is approaching to 0.5. Such materials readily undergo shear deformations but resist volumetric deformation. One well known example is rubber. The plot also reminds that the theory of elasticity allows materials with negative Poisson's ratios, and the limit is −1. According to the definitions of G and B, it implies that such materials are extremely compressible,

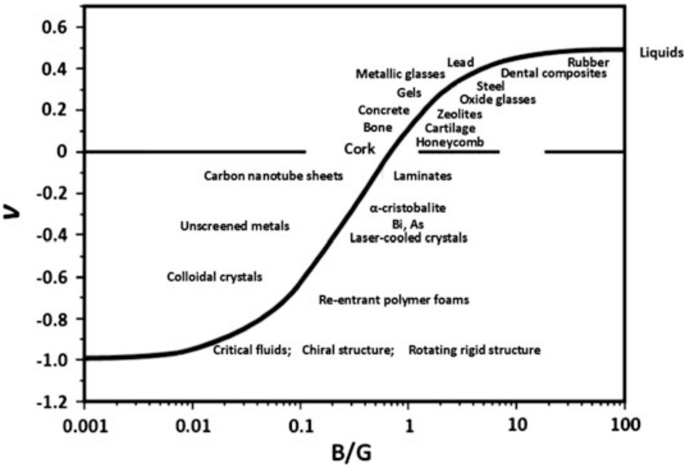

Fig. 1 Window of Poisson's ratio as function of ratio of bulk and shear moduli *B/G* for wide range of materials. Figure adapted from Ref. [6]

when the Poisson’s ratio is negative, i.e. they tend to deform volumetrically rather than shear ($G \geq B$). Such a novel and counterintuitive mechanical behaviour have attracted significant attention for the last two decades.

2.2 Negative Poisson’s Ratio

Actually, a material with a negative Poisson’s ratio (NPR) was first reported in the 1870s. According to the experimental work of W. Voigt (1887) the Poisson’s ratio of pyrites was calculated as $v \approx -\frac{1}{7}$ [17]. Nearly 90 years later, Gibson (1982) demonstrated that the negative Poisson’s effect could be found in two-dimensional cellular structures that deform by flexure of their beam elements [18, 19]. The first intentional designed material with a negative Poisson’s ratio was developed by Lakes [20, 21]. In the pioneering work, the developed re-entrant polymer foam materials exhibited a negative Poisson’s ratio $v \approx -0.7$. Later, another research was published by Evans [22, 23]; it focused on fabrication of microphagous polyethylene with the NPR and started the use of a term “auxetics” [24]. The latter is derived from the Greek word *auxetikos* ($\alpha\upsilon\chi\eta\tau\iota\kappa o\varsigma$), which is a noun form of “increase”. Although the term is well received by many researchers, it seems to describe a tensile behaviour of the NPR materials only. In fact, more and more researches focus on special compressive behaviours of these materials. Therefore, in this paper, the material is called straightforwardly as *negative Poisson’s ratio material*. However, the mentioned landmark studies actually laid a foundation of the fast development of NPR materials.

Although the Poisson’s ratio is scale-independent, it generally describes a “global” effect, i.e. the ratio is determined for the overall strains of a material in its principal directions. When the Poisson’s ratio is negative, the material exhibits a counterintuitive behaviour in contrast to that of conventional materials. For instance, when a tensile loading is applied in one direction, the NPR material expands laterally (Fig. 2b), instead of contracting as conventional materials (Fig. 2a).

The special behaviour of this sort of material is usually explained by a specific deformation mechanism related to its internal structure (microstructure). Figure 3 shows one of a typical negative Poisson’s ratio structures, which is called re-entrant honeycomb [20, 25–27]. Under a global tensile loading in x-direction,

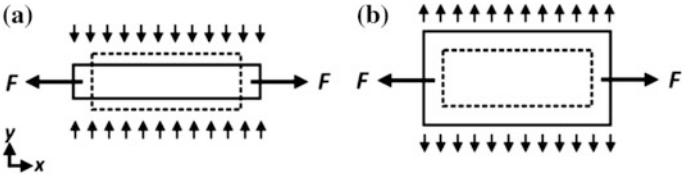

Fig. 2 Typical deformation mechanism of conventional (**a**) and NPR (**b**) materials [3]. Figures adapted from Ref. [3]

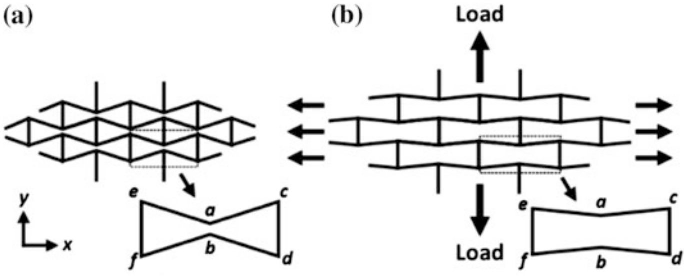

Fig. 3 Re-entrant NPR structure: **a** non deformed; **b** deformed. Figures adapted from Ref. [3]

points *a* and *b* of this rib-hinging structure move apart, while *c* and *d* maintain their separation. Consequently, the overall structure expands in *y*-direction, and the overall Poisson's ratio of this structure is negative. It is the reason for the NPR materials to be usually classified by their deformations and microstructures [7, 11, 28].

Besides the description from a structural view, the deformation mechanism could also be explained using a change of area in the 2D plane. The basic unit of this 2D structure is a re-entrant hexagon, its area apparently expands while the structure is stretched (Fig. 3). The "expansion effect" actually compensates lateral contraction occurring in conventional materials. In other words, extension or increase in the area indicates a very low bulk modulus *B* that results in a negative Poisson's ratio, as discussed using Fig. 1.

3 Effective Structures and Deformation Mechanisms

Although many NPR materials were developed during the last ten years, there are three well-established basic structures, which could explain deformation mechanisms of most of the existing NPR materials: re-entrant structures [18, 20, 22, 24, 25, 27], chiral structures [11, 29–34] and rotating rigid (semi-rigid) structures [31, 35–39].

3.1 Re-entrant Structures

The deformation mechanism of a typical re-entrant structure is presented in Fig. 3, as the first geometry model for this type of structure. The mechanism is dominated by re-alignment of ribs, based on the assumption of rigid ribs with free pivots. In reality, the mechanism is more complicated, including also deflection and axial deformation of ribs [40, 41]. This deformation mechanism is valid for nearly all re-entrant structures (Fig. 4). The double-arrowhead structure exhibits a significant

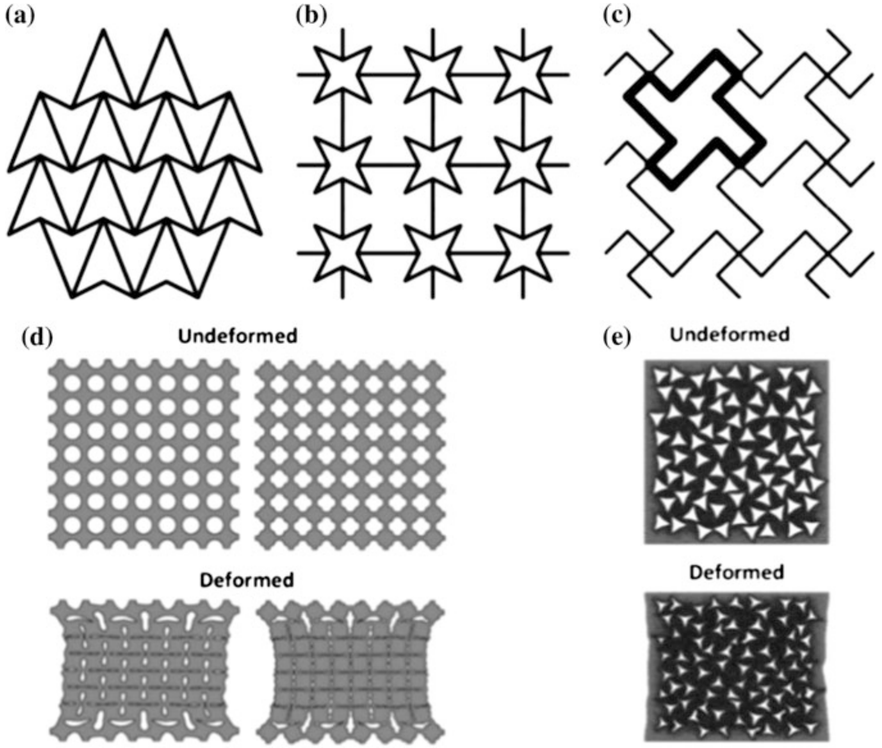

Fig. 4 Schemetic of typical re-entrant NPR structures: **a** arrowhead [7, 42]; **b** star shape [7, 43]; **c** missing rib structure [7, 29]; **d** 2D porous soft material [49, 50]; **e** 2D composite with re-entrant hollow inclusions [46]. Figures **a**–**c** adapted from Ref. [7]

NPR effect in one principal direction at both tensile and compressive loadings [42]. A star-shape re-entrant structure shows a NPR effect in both of its principal directions, and an in-plane isotropic structure could be configured on its basis [43, 44]. The structure in Fig. 4c is called *missing rib structure*, which can be used to describe auxetic foams [29, 45]. The extension of ribs of its representative unit (shown with bold lines) leads to an overall NPR effect in both in-plane orthotropic directions. Another in-plane orthotropic NPR structure is presented in Fig. 4d. Its study is important due to introduction of an elastic instability (buckling) effect into the research of NPR materials, which is an extension of the concept of re-entrant structures. Under compressive loading, the nature of the re-entrant structure leads actually to implementation of a geometry imperfection, which can cause an instability effect. Further to obtaining structures with the NPR in certain directions, researches have also been performed to gain an isotropic NPR effect [46–48]. For instance, by introducing hollow re-entrant shell inclusions randomly in a composite system, the overall Poisson's ratio is statistically isotropic (Fig. 4e).

Besides 2D structures, the principle of re-entrant structure can be also utilized in a 3D space. A 3D re-entrant structure was firstly fabricated in a form of foam

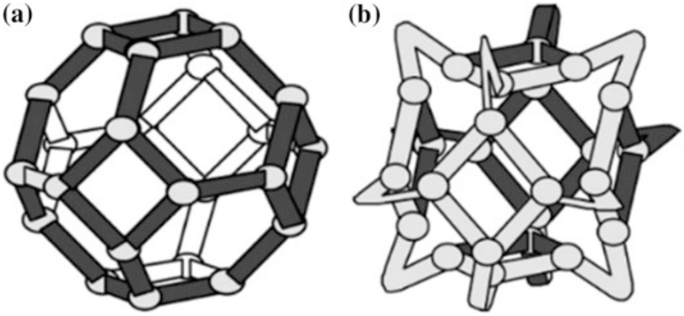

Fig. 5 Tetrakaidecahedron: **a** conventional cell model; **b** re-entrant cell model [53, 54]

[20, 51, 52]. Its deformation mechanism was then explained using the idealized tetrakaidecahedra model as shown in Fig. 5. Under tensile loading, the stretching of folding ribs causes expansion in three orthotropic directions, and the overall structure shows the NPR effect. It is easy to deduce that the structure could contract under compressive loading due to flexure of folding ribs.

A comprehensive study of 3D NPR structure is called "Bucklicrystals" (Fig. 6) [55]. A symmetry order is used as an analytical parameter to study its effect on deformation mechanism of polyhedrons, although it was explained by a number of holes in a crystal. Instead of re-entrant (folding) structures, a geometrical imperfection is introduced as struts with uneven thickness. Under compressive loading, buckling of struts leads to an overall contraction (Fig. 6b). Additionally, the importance of this study is also related to analysis of rotation as one of the dominant deformation mechanisms for this type of structures [55, 56].

Alongside the structures based on ribs and struts, the concept of re-entrant structure can also be utilised in shell structures. One of the studies deals with a 3D hollow re-entrant shell tetrahedron as shown in Fig. 7b. The structure was treated as an inclusion of a composite structure. When the overall composite structure is

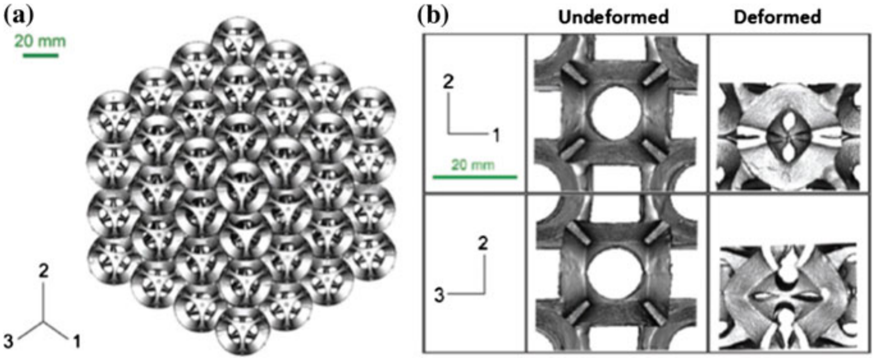

Fig. 6 NPR structure (**a**) based on 6-hole Bucklicrystal (**b**) [55]

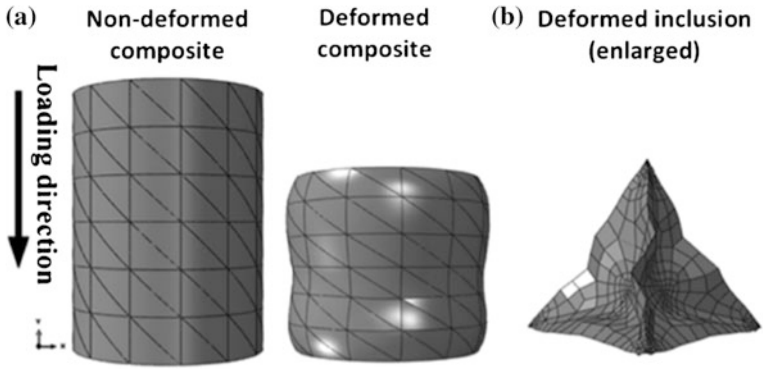

Fig. 7 Deformation mechanism of a 3D NPR composite (**a**) and its inclusion (**b**) [57]

compressed, the embedded inclusion shrinks due to buckling of its surfaces. It is so a called *closure effect* [57] (Fig. 7). Based on this deformation mechanism, the matrix materials is dragged by the inclusion into its internal void, closing it. Consequently, the Poisson’s ratio of the overall composite is reduced. Moreover, the density of inclusion can be treated as a controlling parameter for the global Poisson’s ratio. For a composite with a higher density of this sort of inclusions, the overall Poisson’s ratio could become negative.

3.2 Chiral Structures

Figure 4c shows a missing-rib NPR structure. Interestingly, its deformation mechanism can be explained not only by flexure of re-entrant ribs but also by rotation of its representative unit. Such structures with deformation dominated by rotational reflection that exhibit the NPR effect are called *chiral structures*. The earliest study on this sort of structure was a lattice model of hexagonal molecules [34, 58, 59]. Later, the concept was implemented as a two-dimensional periodic structure (Fig. 8a), which is the well-established baseline of all chiral NPR structures [11, 30]. Its basic chiral unit (highlighted in Fig. 8a) is composed of a central disc (or node) with six tangentially attached ligaments. The ligaments are arranged in such a way that this basic unit exhibits rational symmetry of order six (mechanical in-plane isotropy), which is also the number of its ligaments [30]. The basic rotation unit could be “left-handed” or “right-handed”, and the structure is globally chiral, once it is formed by basic units with the same chirality [31]. When a uniaxial load is applied in the axial direction, the central disc rotates accompanied by flexure of the ligaments. The rotational mechanism results in folding or unfolding behaviours of the ligaments around the disc under tensile and compressive loadings, respectively. Consequently, the global Poisson’s ratio is reduced. When proper geometry features are introduced into the structure, the Poisson’s ratio

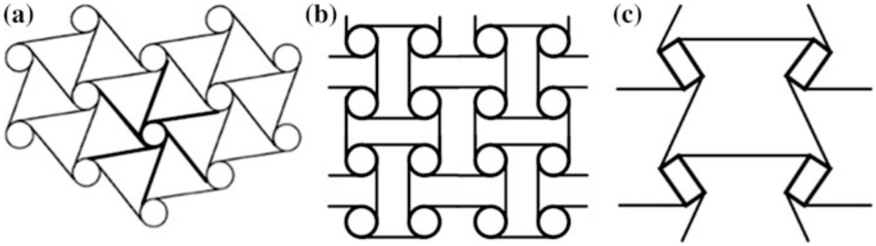

Fig. 8 Typical chiral structures with: **a** mono chirality and constrained rotational symmetry; **b** non-chirality and constrained rotational symmetry; **c** non-chirality block and relaxed rotational symmetry [31]

could be close to −1, and the NPR effect could be maintained over a relatively large range of strain [30]. Different from the structures with the same chirality, NPR structures containing both "left-handed" and "right-handed" chiral units were also developed [60]. Thus, the overall structures exhibit reflective symmetry, and are known as *non-chiral structures* [31, 61] (Fig. 8b). Besides their in-plane behaviour, the flatwise compressive behaviours of the chiral structures were also analysed by both elastic and anelastic buckling modes [33, 61–63].

However, there is one major limitation of development of chiral structures based on chiral units: the constraint of rotational symmetry. For each basic chiral unit, the rotational symmetry of order n is constrained to be equal to the number of ligaments attached to each node [64, 65]. In fact, unless the symmetry constraint is relaxed, only chiral units with $n = 3$, 4 and 6 could be used to construct space-filling periodic structures, and only five such structures can exist [31]. Once the constraint of rotational symmetry is relaxed, *meta-chiral* structures could be developed [31]. As shown in Fig. 8c, the node of basic chiral unit is rectangular with four attached ligaments, which is not equal to the rotational symmetry of the unit. According to this concept, it became possible to construct various other NPR structures based on chiral units.

3.3 Rotating Rigid (Semi-rigid) Structures

A rotating structure was first studied to explain the NPR effect in various zeolites [35, 66] (Fig. 9a). The idealized structure is assumed to contain rigid squares (grey in the figure) connected through simple hinges at their vertices (Fig. 9b) [67]. When a loading is applied to the structure, the squares rotate at the vertices, and exhibits global expansion or contraction with respect to tensile or compressive loadings. The ideal system is isotropic, irrespective of the direction of loading and dimensions of the squares, and with a constant Poisson's ratio of −1 [67]. On the basis of this concept, intensive researches have been implemented by using congruent rectangles [37, 68–70], equilateral triangles [35, 37, 71, 72], rhombi [31, 73, 74] and

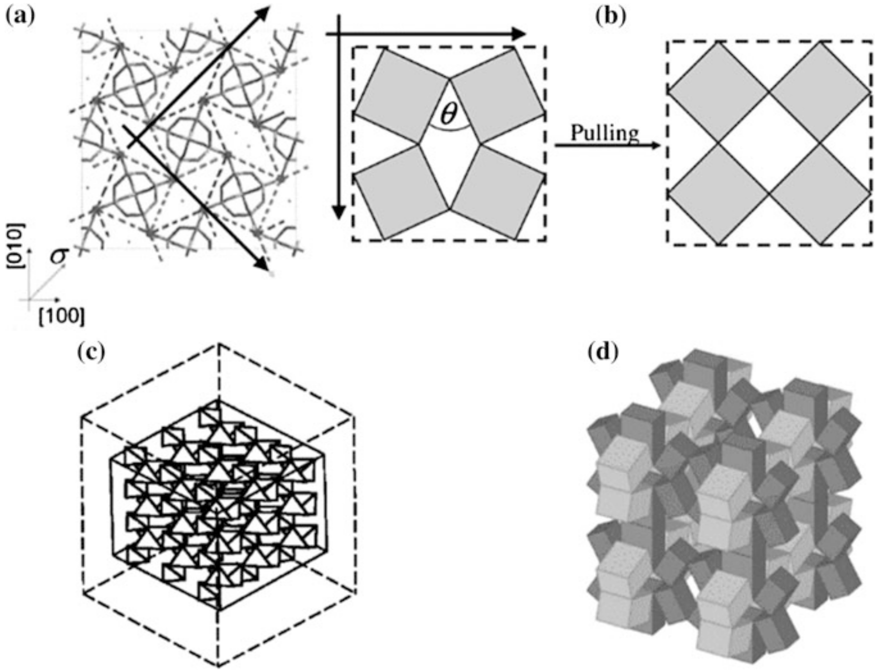

Fig. 9 Schemetic of typical NPR structures based on rotatioal units: **a** zeolite structure and **b** its idealized model [35]; **c** 3D tetrahedral [78] and **d** hexahedron structures [77]

parallelograms [68, 74–76]. The effects of shape, size, connectivity and arrangement of rotation units on the overall mechanical behaviour have been widely studied. Moreover, the concept was also validated in a 3D space (Fig. 9c and d) [39, 77–79].

In fact, there are two main assumptions of the rotation structures—the rigid unit and the hinge connection. Some of the mentioned studies also considered deformation of some rotation units [72, 80, 81], so called *semi-rigid units*. However, the constraints of connections in the units are rarely analysed. Since the deformation of this sort of structure is highly dependent on high rotational freedom of the connections, a very large strain could be generated at connections during such rotation [72]. Thus, it is cumbersome to produce NPR materials with rotation structures.

4 Deformation Mechanisms

4.1 Expansion and Closure

The NPR effect is generally determined by deformation mechanisms of specific structures, and they are usually classified accordingly. However, with the fast development of this sort of materials, there are some structures that cannot be

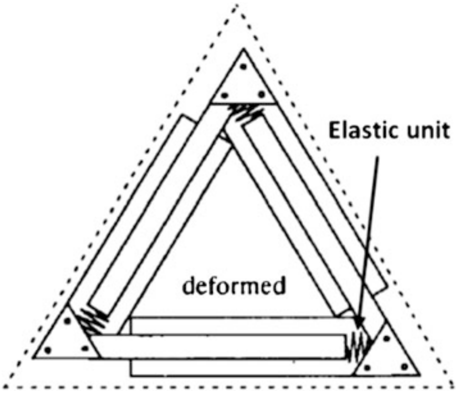

Fig. 10 Deformation of triangular elastic unit [82]

categorised using the notions of re-entrant, chiral and rotation structures. Consider an example of a triangular cell unit shown in Fig. 10, which consists of a truss and an elastic unit [82]. A network composed of such units could exhibit a global isotopic NPR effect. Although it is an idealised structure and very complicated, it reveals another view on the nature of all the NPR structures. In 2D, the trusses of this structure form a triangular area that changes with axial deformation of the trusses. When the trusses are compressed, the area starts to shrink (close), when the trusses are stretched, it expands. The *closure* and *expansion* mechanisms determine the global NPR effect of the material.

This principle can actually explain all the existing 2D NPR structures. Typical 2D re-entrant, chiral and rotation structures are shown in Fig. 11 The common feature of those structures is that their Poisson's ratio is determined by a change of internal areas (patterned in Fig 11), regardless of the cause of this change. When the overall structure is in tension, the expansion effect results in the overall negative Poisson's ratio. Under compressive loading, the closure of the microstructure predominates the NPR effect. Accordingly, a similar explanation can also be used for disordered 2D NPR structures [83–85].

In a 3D space, the principle could be described in terms of the change of volume. For example, a classical 3D re-entrant structure can be treated as a polyhedral cell

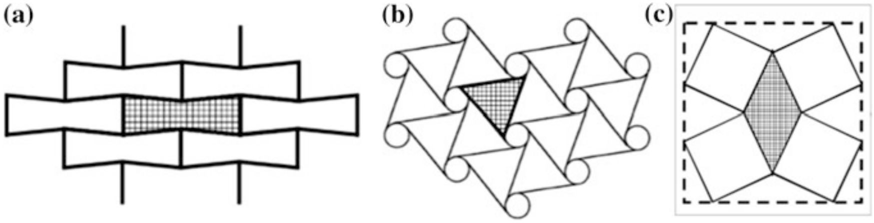

Fig. 11 Schematic of deformation mechanisms for re-entrant (**a**), chiral (**b**) and rotating (**c**) units of NPR stuctures. Figures adapted from: **a** Ref. [3]; **b** Ref. [31]; **c** Ref. [35]

with re-entrant surface (Fig. 5) [20]. Under an external loading, the deformation of the re-entrant surface could expand or close the internal volume of the cell, thus causing a global negative Poisson's ratio. A more direct example is the composite with shell inclusions (Fig. 7) [57], where the closure of the embedded inclusion in compression results in a decrease in the global volume. Such a volume change affects the global Poisson's ratio, which agrees with the classic theory. A volume of a conventional material with a positive Poisson's ratio of less than 0.5 changes under an external loading. It is indicated by bulk modulus B. For a material with a *closure* and *expansion* element, its deformation causes an additional change in its volume. As shown in the example (Fig. 7), the increased volume change of the inclusion can be treated as an additional change in the overall volume beside the change contributed by the matrix material, which is indicated by the lower B. When the material deforms volumetrically rather than in shear ($G \geq B$), its Poisson's ratio decreases and can change from positive values to negative ones [6, 14]. Apparently, the change in the Poisson's ratio is related to the extent of the volume change: a higher extent means a larger change in the Poisson's ratio. In addition, linearity of the change in the Poisson's ratio with strain was observed to be indicated by the linearity of the extent of volume changes [57].

4.2 Multi-phase Systems

If the negative Poisson's ratio effect can be related to the change in area (2D) or volume (3D), it is possible to treat the material with the NPR as a multi-phase structure. As shown for the typical idealized NPR structures (re-entrant, chiral and rotation), they generally consist of ribs (ligaments), rigid (semi-rigid) units and voids [11, 30, 35] (Fig. 11). Compared to the voids, two other types of constituents are much stiffer, with voids having vanishing levels of stiffness. Due to this contrast in stiffness, the stiffer phase(s) of the structure could deform freely and change the area of low stiff phase significantly, causing the NPR effect. This mechanism may be insignificant in the cases of skeleton structures; however, it is important for developing composite material with the NPR. When a NPR structure is embedded into a matrix, a composite material is formed [16, 43, 86, 87]. Figure 12 shows two examples of such materials) the shaded areas are the matrix, assumed to be a compressible material with low stiffness. The remaining parts are inclusions, which are assumed to be rigid (or with high stiffness). In this case, the soft matrix will not hinder deformation of the inclusions, resulting in the global NPR effect [16, 86]. Besides the two-phase systems, this principle can also be used in higher order multi-phase systems. For instance, the in-plane isotropic NPR material shown in Fig. 4e can be considered as a three-phase composite system with the following constituents: (i) inclusions with high stiffness, (ii) matrix with low stiffness and (iii) voids with zero stiffness [46]. The three-phase composite structure allows a random and discontinuous distribution of inclusions. The inclusions, with closure and expansion behaviours under external loadings are the effective component in NPR

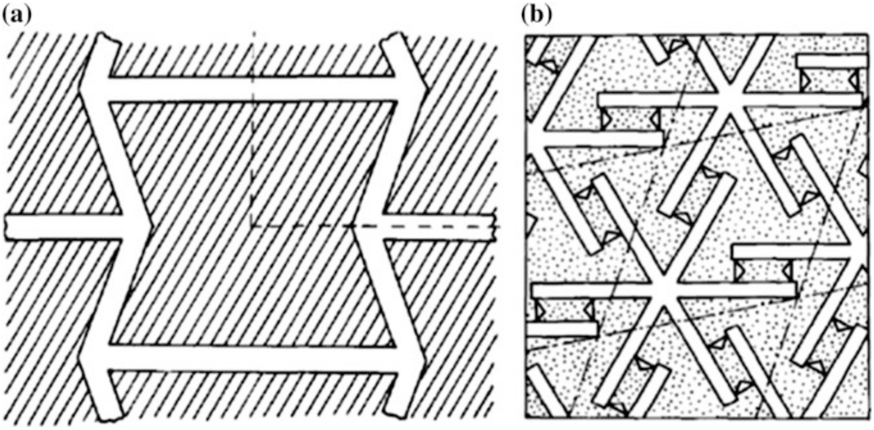

Fig. 12 2D NPR composite with **a** re-entrant honycomb [86], **b** hexanonal inclusion [16]

composites [46]. On basis of this research, the effect of the stiffness contrast of the components was also studied. A larger contrast generally causes an increased NPR effect [47, 48, 88]. For 3D composite structures, this principle is also valid [57], as shown in Fig. 7. When the stiffer shell inclusion deforms under an external compressive loading, it drags less stiff matrix material into the void space. This deformation mechanism consequently causes a significant reduction in the global Poisson's ratio.

5 Some Specific Properties

The studies on exotic NPR materials is not meant for amusement of researchers; their peculiar deformation behaviours actually can provide materials with specific, rare, useful and tuneable mechanical properties [8, 89]. The properties usually contradict to those of conventional materials, demonstrating great potential for many engineering applications.

5.1 Elastic Moduli

As a consequence of the negative Poisson's ratio, there are significant changes in the Young's modulus E and shear modulus G of NPR materials. As shown in Eq. 3, the shear resistance can be immediately enhanced, when the Poisson's ratio changes from positive to negative values. It is caused by twisting or tearing forces [90]. Theoretically, the shear resistance can become infinitely high, when the Poisson's ratio approaches -1.

For conventional isotropic materials, the Young's modulus E is at least twice the shear modulus, according to

$$E = 2G(1 + \upsilon) \tag{4}$$

When the Poisson's ratio is negative, the magnitudes of two moduli become closer. When the Poisson's ratio is −0.5, they become equal. When the Poisson's ratio is approaching to −1, the shear modulus exceeds the elastic modulus. Consequently, the material would become highly compressible, but difficult to shear. However, it must be noticed that the Young's modulus of NPR materials is not always constant. It is affected by the density ratio or volumetric change ratio [52, 91, 92]. Generally, the Young's modulus decreases with the increase in the volumetric compression ratio, when the material is under tension. Under compression, the Young's modulus increases with the increase in the volumetric compression ratio. This could be explained in a simpler way: materials with higher density usually show higher stiffness. Hence, correlation of the bulk modulus, shear modulus and Poisson's ratio can be formulated [93, 94].

5.2 Indentation Hardness

According to the theory of elasticity, the material's hardness (H) can be describes using the following equation [20, 51, 95]:

$$\mathrm{H} \propto \left[\frac{\mathrm{E}}{(1 - \mathrm{v}^2)}\right]^{\gamma}, \tag{5}$$

where γ is a constant that depends on the load applied. For uniform pressure $\gamma = 1$, and $\gamma = 2/3$ for Hertzian indentation. On the basis of this equation, the indentation resistance of a material increases with increase in the magnitude of the (negative) Poisson's ratio. Since the classic elasticity theory places limits on v for isotropic materials $-1 \leq v \leq 0.5$, $(1 - v^2)$ approaches 0 as v approaches −1. For a given value of E, the indentation resistance increases towards infinity with an increasing magnitude of the negative Poisson's ratio. A schematic explanation is shown in Fig. 13b. When a NPR material is under an impact loading, the material flows into the vicinity of the impact as a result of lateral contraction due to its negative Poisson's ratio. Hence, the material densifies under the impact in both longitudinal and transverse directions, leading to increased indentation resistance. The phenomenon is certainly different from that in conventional materials (Fig. 13a): when an impact loading is applied to them, the material generally moves away from the direction of loading, and the hardness is consequently lower than that of NPR materials. Supporting such theoretical considerations, the phenomenon has been validated by using many synthetic NPR materials: polymeric and metallic foams [96–99], fibre-reinforced composite laminates [100–102] and polymers [103–106].

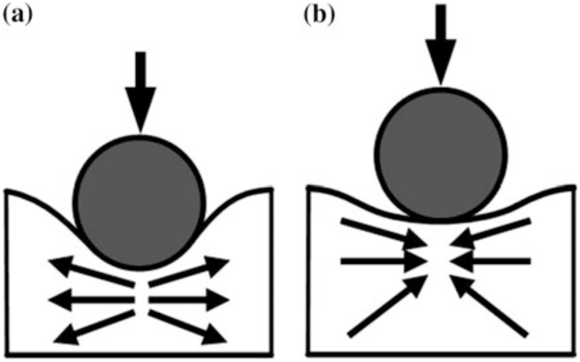

Fig. 13 Indentation resistance of conventional (**a**) and NPR (**b**) materials. Figures reproduced from [3]

5.3 Toughness

At the early stage of the research of NPR materials, their toughness was described using the following equation [20, 107]:

$$\sigma = \frac{\pi E T}{2r(1 - \upsilon^2)}, \tag{6}$$

where σ is the critical tensile stress, T is the surface tension and r is the circular crack radius. According to this equation, the material is expected to become extremely tough, when its Poisson's ratio approaches −1. Consequently, many efforts have been made to analyse toughness of various artificial NPR materials, such as re-entrant foams and composite laminates [91, 92, 102, 108, 109], since they can be fabricated using different methods.

For foams, the behaviour was studied by subjecting them to volumetric compression ratios under both compressive and tensile loadings [91, 92]. With the increase in the volumetric compression ratio, toughness of the studied materials increased. Since the microstructure of NPR foams is very sensitive to the fabrication method and post-processing, such as annealing, the results from different researches are sometimes inconsistent. However, generally, the NPR foams show higher toughness, energy absorption and lower rigidity loss than conventional foams.

For composite materials, the research focus is usually on the effects of the type and orientation of their reinforcement, fibres in most cases. However, the correlations are complicated, since the deformation mechanisms are also affected by delamination and inter-laminate shearing [109]. Besides simple quasi-static loading, behaviours of NPR materials under cyclic loading and varying strain-rate loadings were also investigated using both numerical and experimental methods [100, 101, 109–118]. Generally, the obtained results indicate higher toughness of NPR composite materials than that of conventional ones.

Moreover, NPR materials also have higher resistance to fracture than their conventional counterparts [109]. Alongside with low propensity to crack propagation, more energy is required to expand them than conventional materials [117]. Both theoretical and experimental methods were used to evaluate the mechanisms of such special properties [91, 92, 100, 116, 117, 119, 120]. However, due to the irregular and complex microstructure of NPR materials, especially foams, slight differences in fabrication methods and conditions may cause fluctuating mechanical performances [4]. Thus, it is not easy to describe their behaviours using idealized models. Fortunately, the phenomena are easy to explain employing the concept of NPR. When a NPR material is under tension, its volume expands globally and locally. Hence, when a crack is formed, the expansion of the surrounding materials tends to close it.

5.4 Other Specific Properties

Due to their specific microstructures, NPR materials also show other interesting properties. For example, beside the good energy absorption capability when subjected to mechanical loads, NPR structures also show excellent ultrasonic and acoustic damping [121–125]. When a NPR material is under an out-of-plane bending, it could form a synclastic, or double-curvature, shape instead of anticlastic curvature, or saddle shape, of conventional materials [126–128]. It provides a way to fabricate dome-like complicated structures without the necessity of using complex techniques or additional machining. Moreover, NPR materials also exhibit variable permeability [129–131], shape memory [112, 132–134], abrasive wear resistance [135], etc.

6 Remarks

For the last two decades, NPR materials have been intensively studied. The researches cover the areas of continuum mechanics, engineering mechanics, materials science and manufacturing. Certainly, this paper cannot present results of all the efforts. However, after a brief introduction of the development of this research direction, some remarks could be added for a comprehensive understanding.

6.1 Development of NPR Structures

To date, a large number of NPR materials or structures have been developed. However, some limitations also start to unveil. So far, there are three well received

NPR structures as foundational concepts: re-entrant, chiral and rotating units—and many successful researches have been performed accordingly. However, it seems that research is also constrained by those three concepts. Therefore, two generalized concepts are proposed in this paper: 3D volume (area in 2D) change and stiffness contrast.

To develop new NPR materials, a change in material's volume could be treated as a basic mechanism of the NPR effect, which is discussed in Sect. 3. Such a mechanism could be implemented not only by designing a specific microstructure for the proposed material, but also by defining proper envelopes for material properties of the components. For instance, it is easy to obtain the NPR effect using skeletal structures based on perfectly rigid components with free pivots at mutual points of the components [136]. Since the skeleton is surrounded by zero-stiffness voids, which do not apply any constraints on deformation of the structure, the desired type of deformation could be achieved easily. When a material with non-zero stiffness is introduced to replace the void phase, the structure then transfers from a skeleton to a two-phase composite material with a continuous skeleton component. Moreover, when a higher-order (≥3) multi-phase system is implemented, materials with disordered and discontinuous microstructures could be obtained. In those multi-phase materials, the interactions between different components (phases) become important. They are generally determined by the contrast of stiffness of different phases of the multi-phase material. The stiffness contrasts have to be designed to provide stability of the overall material and allow the necessary deformation behaviour for components.

On the basis of the proposed principles, more novel NPR materials could be suggested. In such a multi-phase material system, the overall mechanical properties can be tailored by controlling the shape, structure, distribution (density and orientation), fraction and stiffness contrasts of its components. This is important to modern engineering, which often requires materials with desired and non-conventional properties. Moreover, when the concept of multi-phase system is further extended, the research can be applied to other types of materials [6, 14, 137–140].

6.2 Fabrication Methods

The theory of elasticity is scale-independent, so research of the NPR effect was performed at macroscopic, mesoscopic and microscopic levels and even at molecular levels. As a result, numerous conceptual structures were developed [3, 4, 7, 28, 41, 141]. However, only a few types of NPR materials were successfully fabricated: skeletal materials [136], foam-like materials [4], composite laminates [100] and a particular helical yarn [142–144]. Since they were developed on the basis of existing materials and generally can be fabricated with conventional component materials and processing technologies. In the meantime, there are many proposed NPR materials, which are still at a theoretical stage because they are hard to fabricate due to their complicated microstructures, especially, in the case of 3D disordered structures. However, with the development of modern manufacturing methods, additive manufacturing techniques can provide a promising possibility to fabricate complex NPR structures. In fact, some efforts have already been made at both macroscale [48–50, 55, 145, 146] and microscale [147–150], but the works are still limited to periodic skeleton structures, which are generally two-phase composite systems. In fact, the latest additive manufacturing techniques could fabricate a component with different materials, which implies that fabrication of 3D disordered graded multi-phase metamaterials becomes possible.

6.3 Perspectives

Due to specific properties of NPR materials, there are multiple potential applications for automotive, defence, sports and aerospace industries [9, 41, 65, 151, 152]. Accompanied by the development of manufacturing techniques, it is not hard to foresee development and production of more novel NPR materials with tailored properties. Besides the impact on engineering, the research of NPR materials also attracts more attention to careful reviews of the classical mechanics. Firstly, as discussed in this paper, novel concepts can still be generated based on the well-known principles of classic elasticity, for instance, a negative Poisson's ratio, negative stiffness, and a negative bulk modulus. Secondly, NPR materials usually have complex microstructures. Under external loading, they generally deform with very large strains and change significantly in volume, which may contradict to some assumptions of classical continuum mechanics. This can potentially require new theories to explain such types of mechanical behaviour beyond current homogenization concepts. This is also enhanced by increased fuzziness of the boundary between materials and structures becomes as in the case of metamaterials.

References

1. Yaso M, Minagi, Y., Kanaizumi, T., Kubota, K., Hayashi, T., Morito, S., Ohba, T.: Study of Japanese sword from a viewpoint of steel strength. J. Alloys Compd. **577** (1), 690–694 (2013)
2. Lee, J., Singer, J.P., Thomas, E.L.: Micro-/nanostructured mechanical metamaterials. Adv. Mater. **24**(36), 4782–4810 (2012)
3. Evans, K.E., Alderson, A.: Auxetic materials: functional materials and structures from lateral thinking! Adv. Mater. **12**(9), 617–628 (2000)
4. Critchley, R., Corni, I., Wharton, J.A., Walsh, F.C., Wood, R.J.K., Stokes, K.R.: A review of the manufacture, mechanical properties and potential applications of auxetic foams. Phys. Status Solidi (b) **250**(10), 1963–1982 (2013)
5. Poisson, S.D.: Note sur L'extension des fils et des plaques. Annales de Chimie et de Physique **36**, 384–385 (1827)
6. Greaves, G.N., Greer, A.L., Lakes, R.S., Rouxel, T.: Poisson's ratio and modern materials. Nat. Mater. **10**, 823–837 (2011)

7. Prawoto, Y.: Seeing auxetic materials from the mechanics point of view: a structural review on the negative Poisson's ratio. Comput. Mater. Sci. **58**, 140–153 (2012)
8. Lakes, R.: No contractile obligations. Nature **358**, 713–714 (1992)
9. Liu, Q.: Literature Review: Materials with Negative Poisson's Ratio and Potential Applications to Aerospace and Defence. DSTO Defence Science and Technology Organisation, Victoria, Australia (2006)
10. Weiner, J.H.: Statistical Mechanics of Elasticity, 1st edn. Wiley, New York (1983)
11. Lakes, R.: Deformation mechanisms in negative Poisson's ratio materials: structural aspects. J. Mater. Sci. **26**, 2287–2292 (1991)
12. Timoshenko, S.: History of Strength of Materials. Courier Dover Publications, Dover (1983)
13. Sokolnikoff, I.S.: Mathematical Theory of Elasticity, 2nd edn. Krieger Publishing Company, Malabar (1983)
14. Lakes, R.S., Lee, T., Bersie, A., Wang, Y.C.: Extreme damping in composite materials with negative-stiffness inclusions. Nature **410**, 565–567 (2001)
15. Lakes, R.: Advances in negative Poisson's ratio materials. Adv. Mater. **5**(4), 293–296 (1993)
16. Milton, G.W.: Composite materials with Poisson's ratios close to—1. J. Mech. Phys. Solids **40**(5), 1105–1137 (1992)
17. Love, A.E.H.: A Treatise on the Mathematical Theory of Elasticity, 1st edn. Cambridge University Press, Cambridge (1892)
18. Gibson, L.J., Ashby, M.F., Schajer, G.S., Robertson, C.I.: The mechanics of two-dimensional cellular materials. Proc. R. Soc. Lond. A **382**(1782), 25–42 (1982)
19. Gibson, L.J., Ashby, M.F.: Cellular solids: structure and properties, 1st edn. Pergamon Press, Oxford (1988)
20. Lakes, R.: Foam structures with a negative Poisson's ratio. Science **235**(4792), 1038–1040 (1987)
21. Lakes, R.: Negative Poisson's ratio materials. Science **238**, 551 (1987)
22. Evans, K.E., Caddock, B.D: Microporous materials with negative Poisson's ratios. II. Mechanisms and interpretation. J. Phys. D Appl. Phys. **22** (12), 1883 (1989)
23. Evans, K.E.: Tensile network microstructures exhibiting negative Poisson's ratios. J. Phys. D Appl. Phys. **22** (12), 1870 (1989)
24. Evans, K.E., Nkansah, M.A., Hutchinson, I.J., Rogers, S.C.: Molecular network design. Nature **353**, 124 (1991)
25. Almgren, R.F.: An isotropic three-dimensional structure with Poisson's ratio = − 1. J. Elast. **15**(4), 427–430 (1985)
26. Masters, I.G., Evans, K.E.: Models for the elastic deformation of honeycombs. Compos. Struct. **35**(4), 403–422 (1996)
27. Kolpakov, A.G.: Determination of the average characteristics of elastic frameworks. J. Appl. Math. Mech. **49**(6), 739–745 (1985)
28. Carneiro, V.H., Meireles, J., Puga, H.: Auxetic materials—a review. Mater. Sci. Pol. **31**(4), 561–571 (2013)
29. Gaspar, N., Ren, X.J., Smith, C.W., Grima, J.N., Evans, K.E.: Novel honeycombs with auxetic behaviour. Acta Mater. **53**(8), 2439–2445 (2005)
30. Prall, D., Lakes, R.S.: Properties of a chiral honeycomb with a Poisson's ratio of −1. Int. J. Mech. Sci. **39**(3), 305–314 (1997)
31. Grima, J.N., Gatt, R., Farrugia, P.-S.: On the properties of auxetic meta-tetrachiral structures. Phys. Status Solidi (b) **245**(3), 511–520 (2008)
32. Wojciechowski, K.W.: Non-chiral, molecular model of negative Poisson ratio in two dimensions. J. Phys. A Math. Gen. **36**(47), 11765 (2003)
33. Spadoni, A., Ruzzene, M.: Elasto-static micropolar behavior of a chiral auxetic lattice. J. Mech. Phys. Solids **60**(1), 156–171 (2012)
34. Wojciechowski, K.W.: Two-dimensional isotropic system with a negative Poisson's ratio. Phys. Lett. A **137**(1–2), 60–64 (1989)

35. Grima, J.N., Jackson, R., Alderson, A., Evans, K.E.: Do zeolites have negative Poisson's ratios? Adv. Mater. **12**(24), 1912–1918 (2000)
36. He, C., Liu, P., Griffin, A.C.: Toward negative Poisson's ratio polymers through molecular design. Macromolecules **31**(9), 3145–3147 (1998)
37. Grima, J.N., Alderson, A., Evans, K.E.: Auxetic behaviour from rotating rigid units. Phys. Status Solidi (b) **242**(3), 561–575 (2005)
38. Grima, J.N., Zammit, V., Gatt, R., Alderson, A., Evans, K.E.: Auxetic behaviour from rotating semi-rigid units. Phys. Status Solidi (b) **244**(3), 866–882 (2007)
39. Alderson, A., Evans, K.E.: Molecular origin of auxetic behavior in tetrahedral framework silicates. Phys. Rev. Lett. **89**(22), 22503 (2002)
40. Evans, K.E., Alderson, A., Christian, F.R.: Auxetic two-dimensional polymer networks. An example of tailoring geometry for specific mechanical properties. J. Chem. Soc. Faraday Trans. **91**(16), 2671–2680 (1995)
41. Alderson, A., Alderson, K.L.: Auxetic materials. J. Aerosp. Eng. **221**(4), 565–575 (2007)
42. Larsen, U.D., Signund, O., Bouwsta, S.: Design and fabrication of compliant micromechanisms and structures with negative Poisson's ratio. J. Microelectromech. Syst. **6**(2), 99–106 (1997)
43. Theocaris, P.S., Stavroulakis, G.E., Panagiotopoulos, P.D.: Negative Poisson's ratios in composites with star-shaped inclusions: a numerical homogenization approach. Arch. Appl. Mech. **67**(4), 274–286 (1997)
44. Grima, J.N., Gatt, R., Alderson, A., Evans, K.E.: On the potential of connected stars as auxetic systems. Mol. Simul. **31**(13), 925–935 (2005)
45. Smith, C.W., Grima, J.N., Evans, K.E.: A novel mechanism for generating auxetic behaviour in reticulated foams: missing rib foam model. Acta Mater. **48**(17), 4349–4356 (2000)
46. Hou, X., Hu, H., Silberschmidt, V.: A novel concept to develop composite structures with isotropic negative Poisson's ratio: effects of random inclusions. Compos. Sci. Technol. **72** (15), 1848–1854 (2012)
47. Hou, X., Hu, H., Silberschmidt, V.: Numerical analysis of composite structure with in-plane isotropic negative Poisson's ratio: effects of materials properties and geometry features of inclusions. Compos. B Eng. **58**, 152–159 (2014)
48. Hu, H., Silberschmidt, V.: A composite material with Poisson's ratio tunable from positive to negative values: an experimental and numerical study. J. Mater. Sci. **48**(24), 8493–8500 (2013)
49. Bertoldi, K., Reis, P.M., Willshaw, S., Mullin, T.: Negative Poisson's ratio behavior induced by an elastic instability. Adv. Mater. **22**(3), 361–366 (2010)
50. Overvelde, J.T.B., Shan, S., Bertoldi, K.: Compaction through buckling in 2D periodic, soft and porous structures: effect of pore shape. Adv. Mater. **24**(17), 2337–2342 (2012)
51. Friis, E.A., Lakes, R.S., Park, J.B.: Negative Poisson's ratio polymeric and metallic foams. J. Mater. Sci. **23**, 4406–4414 (1988)
52. Choi, J.B., Lakes, R.S.: Nonlinear analysis of the Poisson's ratio of negative Poisson's ratio foams. J. Compos. Mater. **29**(1), 113–128 (1995)
53. Lakes, R., Rosakis, P., Ruina, A.: Microbuckling instability in elastomeric cellular solids. J. Mater. Sci. **28**(17), 4667–4672 (1993)
54. Lakes, R.S., Witt, R.: Making and characterizing negative Poisson's ratio materials. Int. J. Mech. Eng. Educ. **30**(1), 50–58 (2002)
55. Babaee, S., Shim, J., Weaver, J.C., Chen, E.R., Patel, N., Bertoldi, K.: 3D soft metamaterials with negative Poisson's ratio. Adv. Mater. **25**(36), 5044–5049 (2013)
56. Shim, J., Perdigou, C., Chen, E.R., Bertoldi, K., Reis, P.M.: Buckling-induced encapsulation of structured elastic shells under pressure. Proc. Natl. Acad. Sci. **109**(16), 5978–5983 (2012)
57. Hou, X., Hu, H., Silberschmidt, V.: Tailoring structure of inclusion with strain-induced closure to reduce Poisson's ratio of composite materials. J. Appl. Phys. **115**, 4903–4925 (2014)

58. Wojciechowski, K.W.: Constant thermodynamic tension Monte Carlo studies of elastic properties of a two-dimensional system of hard cyclic hexamers. Mol. Phys. **61**(5), 1247–1258 (1987)
59. Wojciechowski, K.W., Brańka, A.C.: Negative Poisson ratio in a two-dimensional "isotropic" solid. Phys. Rev. A **40**(12), 7222–7225 (1989)
60. Sigmund, O., Torquato, S., Aksay, I.A.: On the design of 1–3 piezocomposites using topology optimization. J. Mater. Res. **13**(04), 1038–1048 (1998)
61. Miller, W., Smith, C.W., Scarpa, F., Evans, K.E.: Flatwise buckling optimization of hexachiral and tetrachiral honeycombs. Compos. Sci. Technol. **70**(7), 1049–1056 (2010)
62. Spadoni, A., Ruzzene, M., Scarpa, F.: Global and local linear buckling behavior of a chiral cellular structure. Phys. Status Solidi (b) **242**(3), 695–709 (2005)
63. Scarpa, F., Blain, S., Lew, T., Perrott, D., Ruzzene, M., Yates, J.R.: Elastic buckling of hexagonal chiral cell honeycombs. Compos. A **38**(2), 280–289 (2007)
64. Grima, J.N.: New Auxetic Materials. University of Exeter, Exeter (2000)
65. Bornengo, D., Scarpa, F., Remillat, C.: Evaluation of hexagonal chiral structure for morphine airfoil concept. Proc. Institut. Mech. Eng. Part G J. Aerosp. Eng. **219**(3), 185–192 (2005)
66. Grima, J.N., Gatt, R., Zammit, V., Williams, J.J., Evans, K.E., Alderson, A., Walton, R.I.: Natrolite: a zeolite with negative Poisson's ratios. J. Appl. Phys. **101**(8), 086102 (2007)
67. Grima, J.N., Evans, K.E.: Auxetic behavior from rotating squares. J. Mater. Sci. Lett. **19**(17), 1563–1565 (2000)
68. Grima, J.N., Jackson, R., Alderson, A., Evans, K.E.: On the auxetic properties of 'rotating rectangles' with different connectivity. J. Phys. Soc. Jpn. **74** (10), 2866–2867 (2005)
69. Attard, D., Manicaro, E., Gatt, R., Grima, J.N.: On the properties of auxetic rotating stretching squares. Phys. Status Solidi (b) **246**(9), 2045–2054 (2009)
70. Grima, J.N., Manicaro, E., Attard, D.: Auxetic behaviour from connected different-sized squares and rectangles. Proc. R. Soc. A Math. Phys. Eng. Sci. **467**(2126), 439–458 (2011)
71. Grima, J., Evans, K.: Auxetic behavior from rotating triangles. J. Mater. Sci. **41**(10), 3193–3196 (2006)
72. Grima, J.N., Gatt, R., Ellul, B., Chetcuti, E.: Auxetic behaviour in non-crystalline materials having star or triangular shaped perforations. J. Non-Cryst. Solids **356**(37–40), 1980–1987 (2010)
73. Attard, D., Grima, J.N.: Auxetic behaviour from rotating rhombi. Phys. Status Solidi (b) **245** (11), 2395–2404 (2008)
74. Grima, J.N., Farrugia, P.-S., Gatt, R., Attard, D.: On the auxetic properties of rotating rhombi and parallelograms: a preliminary investigation. Phys. Status Solidi (b) **245**(3), 521–529 (2008)
75. Williams, J.J., Smith, C.W., Evans, K.E., Lethbridge, Z.A.D., Walton, R.I.: An analytical model for producing negative Poisson's ratios and its application in explaining off-axis elastic properties of the NAT-type zeolites. Acta Mater. **55**(17), 5697–5707 (2007)
76. Attard, D., Manicaro, E., Grima, J.N.: On rotating rigid parallelograms and their potential for exhibiting auxetic behaviour. Phys. Status Solidi (b) **246**(9), 2033–2044 (2009)
77. Attard, D., Grima, J.N.: A three-dimensional rotating rigid units network exhibiting negative Poisson's ratios. Phys. Status Solidi (b) **249**(7), 1330–1338 (2012)
78. Alderson, A., Evans, K.E.: Rotation and dilation deformation mechanisms for auxetic behaviour in the α-cristobalite tetrahedral framework structure. Phys. Chem. Miner. **28**(10), 711–718 (2001)
79. Grima, J.N., Gatt, R., Alderson, A., Evans, K.E.: An alternative explanation for the negative Poisson's ratios in α-cristobalite. Mater. Sci. Eng., A **423**(1–2), 219 (2006)
80. Grima, J., Farrugia, P., Caruana, C., Gatt, R., Attard, D.: Auxetic behaviour from stretching connected squares. J. Mater. Sci. **43**(17), 5962–5971 (2008)
81. Chetcuti, E., Ellul, B., Manicaro, E., Brincat, J.-P., Attard, D., Gatt, R., Grima, J.N.: Modeling auxetic foams through semi-rigid rotating triangles. Phys. Status Solidi (b) **251**(2), 297–306 (2014)

82. Rothenburg, L., Berlin, A.A., Bathurst, R.J.: Microstructure of isotropic materials with negative Poisson's ratio. Nature **354** (6353), 470 (1991)
83. Pozniak, A.A., Smardzewski, J., Wojciechowski, K.W.: Computer simulations of auxetic foams in two dimensions. Smart Mater. Struct. **22**(8), 084009 (2013)
84. Horrigan, E.J., Smith, C.W., Scarpa, F.L., Gaspar, N., Javadi, A.A., Berger, M.A., Evans, K. E.: Simulated optimisation of disordered structures with negative Poisson's ratios. Mech. Mater. **41**(8), 919–927 (2009)
85. Blumenfeld, R., Edwards, S.: Theory of strains in auxetic materials. J. Supercond. Novel Magn. **25**(3), 565–571 (2012)
86. Evans, K.E., Nkansah, M.A., Hutchinson, I.J.: Modelling negative Poisson ratio effects in network-embedded composites. Acta Metall. Mater. **40**(9), 2463–2469 (1992)
87. Grima, J.N., Cauchi, R., Gatt, R., Attard, D.: Honeycomb composites with auxetic out-of-plane characteristics. Compos. Struct. **106**, 150–159 (2013)
88. Hou, X., Hu, H., Silberschmidt, V.: Erratum to: a composite material with Poisson's ratio tunable from positive to negative values: an experimental and numerical study. J. Mater. Sci. **49** (1), 461 (2014)
89. Hall, L.J., Coluci, V.R., Galvão, D.S., Kozlov, M.E., Zhang, M., Dantas, S.O., Baughman, R. H.: Sign change of Poisson's ratio for carbon nanotube sheets. Science **320**(5875), 504–507 (2008)
90. Fung, Y.C.: Foundations of Solid Mechanics International Series in Dynamics. Prentice Hall, Englewood Cliffs (1965)
91. Choi, J.B., Lakes, R.S.: Non-linear properties of polymer cellular materials with a negative Poisson's ratio. J. Mater. Sci. **27**(17), 4678–4684 (1992)
92. Choi, J.B., Lakes, R.S.: Non-linear properties of metallic cellular materials with a negative Poisson's ratio. J. Mater. Sci. **27**(19), 5375–5381 (1992)
93. Xinchun, S., Lakes, R.S.: Stability of elastic material with negative stiffness and negative Poisson's ratio. Phys. Status Solidi (b) **244** (3), 807 (2007)
94. Wang, Y.C., Lakes, R.S.: Composites with inclusions of negative bulk modulus: extreme damping and negative Poisson's ratio. J. Compos. Mater. **39**(18), 1645–1657 (2005)
95. Burns, S.: Negative Poisson's ratio materials. Science **238**(4826), 551 (1987)
96. Chan, N., Evans, K.E.: Indentation resilience of convertional and auxetic foams. J. Cell. Plast. **34**(3), 231–260 (1998)
97. Lakes, R.S., Elms, K.: Indentability of conventional and negative Poisson's ratio foams. J. Compos. Mater. **27**(12), 1193–1202 (1993)
98. Lim, T.C., Alderson, A., Alderson, K.L.: Experimental studies on the impact properties of auxetic materials. Phys. Status Solidi (b) **251**(2), 307–313 (2014)
99. Bezazi, A., Scarpa, F.: Mechanical behaviour of conventional and negative Poisson's ratio thermoplastic polyurethane foams under compressive cyclic loading. Int. J. Fatigue **29**(5), 922–930 (2007)
100. Alderson, K.L., Simkins, V.R., Coenen, V.L., Davies, P.J., Alderson, A.: How to make auxetic fibre reinforced composites. Phys. Status Solidi (b) **242**(3), 509–518 (2005)
101. Alderson, K.L., Coenen, V.L.: The low velocity impact response of auxetic carbon fibre laminates. Phys. Status Solidi (b) **245**(3), 489–496 (2008)
102. Coenen, V.L., Alderson, K.L.: Mechanisms of failure in the static indentation resistance of auxetic carbon fibre laminates. Phys. Status Solidi (b) **248**(1), 66–72 (2011)
103. Alderson, K.L., Webber, R.S., Evans, K.E.: Novel variations in the microstructure of auxetic ultra-high molecular weight polyethylene. Part 2: mechanical properties. Polym. Eng. Sci. **40** (8), 1906–1914 (2000)
104. Alderson, K.L., Webber, R.S., Kettle, A.P., Evans, K.E.: Novel fabrication route for auxetic polyethylene. Part 1. Processing and microstructure. Polym. Eng. Sci. **45**(4), 568–578 (2005)
105. Alderson, K.L., Pickles, A.P., Neale, P.J., Evans, K.E.: Auxetic polyethylene: the effect of a negative poisson's ratio on hardness. Acta Metall. Mater. **42**(7), 2261–2266 (1994)

106. Alderson, K.L., Fitzgerald, A., Evans, K.E.: The strain dependent indentation resilience of auxetic microporous polyethylene. J. Mater. Sci. **35**(16), 4039–4047 (2000)
107. Lakes, R.S.: Design considerations for materials with negative Poisson's ratios. J. Mech. Des. **115**(4), 696–700 (1993)
108. Brincat, J.-P., Azzopardi, K.M., Buttigieg, A., Scarpa, F., Grima, J.N., Gatt, R.: Foams as 3D perforated systems: an analysis of their Poisson's ratios under compression. Phys. Status Solidi (b) **251**(11), 2233–2238 (2014)
109. Bezazi, A., Boukharouba, W., Scarpa, F.: Mechanical properties of auxetic carbon/epoxy composites: static and cyclic fatigue behaviour. Phys. Status Solidi (b) **246**(9), 2102–2110 (2009)
110. Bianchi, M., Scarpa, F., Smith, C.: Stiffness and energy dissipation in polyurethane auxetic foams. J. Mater. Sci. **43**(17), 5851–5860 (2008)
111. Bezazi, A., Scarpa, F.: Tensile fatigue of conventional and negative Poisson's ratio open cell PU foams. Int. J. Fatigue **31**(3), 488–494 (2009)
112. Bianchi, M., Scarpa, F., Smith, C.W.: Shape memory behaviour in auxetic foams: mechanical properties. Acta Mater. **58**(3), 858–865 (2010)
113. Scarpa, F., Pastorino, P., Garelli, A., Patsias, S., Ruzzene, M.: Auxetic compliant flexible PU foams: static and dynamic properties. Phys. Status Solidi (b) **242**(3), 681–694 (2005)
114. Scarpa, F., Ciffo, L.G., Yates, J.R.: Dynamic properties of high structural integrity auxetic open cell foam. Smart Mater. Struct. **13**(1), 49 (2004)
115. Herakovich, C.T.: Composite laminates with negative through-the-thickness Poisson's ratios. J. Compos. Mater. **18**(5), 447–455 (1984)
116. Bezazi, A.R., El Mahi, A., Berthelot, J.M., Bezzazi, B.: Flexural fatigue behavior of cross-ply laminates: an experimental approach. Strength Mater. **35**(2), 149–161 (2003)
117. Donoghue, J.P., Alderson, K.L., Evans, K.E.: The fracture toughness of composite laminates with a negative Poisson's ratio. Phys. Status Solidi (b) **246**(9), 2011–2017 (2009)
118. Scarpa, F., Yates, J.R., Ciffo, L.G., Patsias, S.: Dynamic crushing of auxetic open-cell polyurethane foam. J. Mech. Eng. Sci. **216**(12), 1153–1156 (2002)
119. Choi, J.B., Lakes, R.S.: Fracture toughness of re-entrant foam materials with a negative Poisson's ratio: experiment and analysis. Int. J. Fract. **80**(1), 73–83 (1996)
120. Hou, Y., Tai, Y.H., Lira, C., Scarpa, F., Yates, J.R., Gu, B.: The bending and failure of sandwich structures with auxetic gradient cellular cores. Compos. A Appl. Sci. Manuf. **49**, 119–131 (2013)
121. Scarpa, F., Bullough, W.A., Lumley, P.: Trends in acoustic properties of iron particle seeded auxetic polyurethane foam. Proc. Institut. Mech. Eng. Part C J. Mech. Eng. Sci. **218**(2), 241–244 (2004)
122. Haberman, M.R., Hook, D.T., Klatt, T.D., Hewage, T.A.M., Alderson, A., Alderson, K.L., Scarpa, F.L.: Ultrasonic characterization of polymeric composites containing auxetic inclusions. J. Acoust. Soc. Am. **132** (3), 1961 (2012)
123. Ruzzene, M., Scarpa, F.: Directional and band-gap behavior of periodic auxetic lattices. Phys. Status Solidi (b) **242**(3), 665–680 (2005)
124. Alderson, K.L., Webber, R.S., Mohammed, U.F., Murphy, E., Evans, K.E.: An experimental study of ultrasonic attenuation in microporous polyethylene. Appl. Acoust. **50**(1), 23–33 (1997)
125. Krödel, S., Delpero, T., Bergamini, A., Ermanni, P., Kochmann, D.M.: 3D auxetic microlattices with independently controllable acoustic band gaps and quasi-static elastic moduli. Adv. Eng. Mater. **16**(4), 357–363 (2014)
126. Chen, Y.J., Scarpa, F., Farrow, I.R., Liu, Y.J., Leng, J.S.: Composite flexible skin with large negative Poisson's ratio range: numerical and experimental analysis. Smart Mater. Struct. **22** (4), 045005 (2013)
127. Alderson, A., Alderson, K.L., Chirima, G., Ravirala, N., Zied, K.M.: The in-plane linear elastic constants and out-of-plane bending of 3-coordinated ligament and cylinder-ligament honeycombs. Compos. Sci. Technol. **70**(7), 1034–1041 (2010)

128. Lorato, A., Innocenti, P., Scarpa, F., Alderson, A., Alderson, K.L., Zied, K.M., Ravirala, N., Miller, W., Smith, C.W., Evans, K.E.: The transverse elastic properties of chiral honeycombs. Compos. Sci. Technol. **70**(7), 1057–1063 (2010)
129. Alderson, A., Rasburn, J., Evans, K.E.: Mass transport properties of auxetic (negative Poisson's ratio) foams. Phys. Status Solidi (b) **244**(3), 817–827 (2007)
130. Alderson, A., Rasburn, J., Evans, K.E., Grima, J.N.: Auxetic polymeric filters display enhanced de-fouling and pressure compensation properties. Membr. Technol. **137**, 6–8 (2001)
131. Rasburn, J., Mullarkey, P.G., Evans, K.E., Alderson, A., Ameer-Beg, S., Perrie, W.: Auxetic structures for variable permeability systems. AIChE J. **47**(11), 2623–2626 (2001)
132. Xu, T., Li, G.: A shape memory polymer based syntactic foam with negative Poisson's ratio. Mater. Sci. Eng. A **528**(22–23), 6804–6811 (2011)
133. Bianchi, M., Scarpa, F., Smith, C.W., Whittell, G.: Physical and thermal effects on the shape memory behaviour of auxetic open cell foams. J. Mater. Sci. **45**(2), 341–347 (2010)
134. Alderson, A., Alderson, K.L., McDonald, S.A., Mottershead, B., Nazare, S., Withers, P.J., Yao, Y.T.: Piezomorphic materials. Macromol. Mater. Eng. **298**(3), 318–327 (2013)
135. Uzun, M., Patel, I.: Tribological properties of auxetic and conventional polypropylene weft knitted fabrics. Arch. Mater. Sci. Eng. **44**(2), 120–125 (2010)
136. Mitschke, H., Schwerdtfeger, J., Schury, F., Stingl, M., Körner, C., Singer, R.F., Robins, V., Mecke, K., Schröder-Turk, G.E.: Finding auxetic frameworks in periodic tessellations. Adv. Mater. **23**(22–23), 2669–2674 (2011)
137. Jaglinski, T., Kochmann, D., Stone, D., Lakes, R.S.: Composite materials with viscoelastic stiffness greater than diamond. Science **315**(5812), 620–622 (2007)
138. Dong, L., Stone, D.S., Lakes, R.S.: Anelastic anomalies and negative Poisson's ratio in tetragonal. BaTiO3 ceramics. Appl. Phys. Lett. **96** (14), 141904–141903 (2010)
139. Li, D., Jaglinski, T., Stone, D.S., Lakes, R.S.: Temperature insensitive negative Poisson's ratios in isotropic alloys near a morphotropic phase boundary. Appl. Phys. Lett. **101**(25), 251903–251907 (2012)
140. Tretiakov, K.V., Wojciechowski, K.W.: Partially auxetic behavior in fcc crystals of hard-core repulsive Yukawa particles. Phys. Status Solidi (b) **251**(2), 383–387 (2014)
141. Evans, K.E.: Auxetic polymers. Membr. Technol. **2001**(137), 9 (2001)
142. Miller, W., Ren, Z., Evans, K.E.: A negative Poisson's ratio carbon fibre composite using a negative Poisson's ratio yarn reinforcement. Compos. Sci. Technol. **72**(7), 761–766 (2012)
143. Wright, J.R., Sloan, M.R., Evans, K.E.: Tensile properties of helical auxetic structure: a numerical study. J. Appl. Phys. **108**(4), 044905–044913 (2010)
144. Wright, J.R., Burns, M.K., James, E., Sloan, M.R., Evans, K.E.: One the design and characterisation of low-stiffness auxetic yarns and fabrics. Text. Res. J. **82**(7), 645–652 (2012)
145. Willshaw, S., Mullin, T.: Pattern switching in two and three-dimensional soft solids. Soft Matter **8**(6), 1747–1750 (2012)
146. Kang, S.H., Shan, S., Košmrlj, A., Noorduin, W.L., Shian, S., Weaver, J.C., Clarke, D.R., Bertoldi, K.: Complex ordered patterns in mechanical instability induced geometrically frustrated triangular cellular structures. Phys. Rev. Lett. **112**(9), 098701 (2014)
147. Xu, B., Arias, F., Brittain, S.T., Zhao, X., Grzybowski, B., Torquato, S., Whitesides, G.M.: Making negative Poisson's ratio microstructures by soft lithography. Adv. Mater. **11**(14), 1186–1189 (1999)
148. Fozdar, D.Y., Soman, P.P., Lee, J.W., Han, L.H., Chen, S.: Three-dimensional polymer constructs exhibiting a tunable negative Poisson's ratio. Adv. Funct. Mater. **21** (14), 2712–2720 (2011)
149. Buckmann, T., Stenger, N., Kadic, M., Kaschke, J., Frolich, A., Kennerknecht, T., Eberl, C., Thiel, M., Wegener, M.: Tailored 3D mechanical metamaterials made by dip-in direct-laser-writing optical lithography. Adv. Mater. **24**(20), 2710–2714 (2012)

150. Kang, S.H., Shan, S., Noorduin, W.L., Khan, M., Aizenberg, J., Bertoldi, K.: Buckling-induced reversible symmetry breaking and amplification of chirality using supported cellular structures. Adv. Mater. **25**(24), 3380–3385 (2013)
151. Sanami, M., Ravirala, N., Alderson, K., Alderson, A.: Auxetic materials for sports applications. Procedia Eng. **72**, 453–458 (2014)
152. Ma, Z., Bian, H., Sun, C., Hulbert, G.M., Bishnoi, K., Rostam-Abadi, F.: Functionally-graded NPR material for a blast-protective deflector. In: Proceedings of the 2009 Ground Vehicle System Engineering and Technology Symposium, Dearborn, 1–12 Aug 2010

Deformation and Damage of Thermally Bonded Nonwoven Networks

Farukh Farukh, Emrah Demirci, Memiş Acar, Behnam Pourdeyhimi and Vadim V. Silberschmidt

Abstract Nonwovens, composed of randomly-oriented polymer-based fibres, possess unique properties, with features common to paper, plastic and textile materials. From various types of bonding technologies used in the nonwovens industry. This chapter focuses on thermal bonding and respective fabrics as it is one of the most widely used techniques. Understanding a mechanical behaviour of polymer-based nonwoven materials that includes large-strain deformation and damage can help to evaluate a response of nonwoven fibrous networks to various loading conditions. The main deformation and damage mechanisms are analysed by means of experimental assessment of fabrics in tension alongside damage evolution based on progressive failure of fibres. Finite-element simulation strategies to gain insight into their behaviour and to achieve quantitative exploration of a design space for these materials are also discussed in this chapter.

1 Introduction

Nonwoven networks of engineered fabrics can be designed to provide particular characteristics according to their specific purpose. These characteristics are defined by a combination of various properties of nonwoven (e.g. strength, absorbency, flame retardancy) while maintaining a balance between the cost and expected product life, related e.g. to single-use (disposable) products or durable products.

F. Farukh (✉) · E. Demirci · M. Acar · V.V. Silberschmidt
Wolfson School of Mechanical and Manufacturing Engineering,
Loughborough University, Loughborough, Leicestershire LE11 3TU, UK
e-mail: F.Farukh@lboro.ac.uk

V.V. Silberschmidt
e-mail: V.Silberschmidt@lboro.ac.uk

B. Pourdeyhimi
Nonwovens Cooperative Research Center, North Carolina State University,
Raleigh, NC, USA

V.V. Silberschmidt and V.P. Matveenko (eds.), *Mechanics of Advanced Materials*,
Engineering Materials, DOI 10.1007/978-3-319-17118-0_8

The term *nonwoven* may not be very old, but such materials are oldest known textile to the man; they existed long before the weaving and knitting processes were developed. Nonwovens were used in times of great antiquity both in Asia and Europe in form of felts.[1] The invention and perfection of felt-making process can be attributed to Asiatic nomads who exploited the possibilities of its use to their maximum. The earliest felt remnant was found during excavations conducted by James Mellaart in 1965 at Catal Hüyük in Turkey. The painting on the interior wall of a shrine with its pattern and edging technique was a strong reminiscent of felt applique suggesting that this material was known to Neolithic people around 6000 B.C. This suggestion was supported by the finds of actual felt among the textiles from graves in Level VI by Harold Burnham [9]. For centuries, felt manufacturing remained manual in various parts of the world. In the 19th century, the invention of steam machinery brought the industrial revolution which led to manufacturing of various products including felt on industrial scale.

Returning to the issue of modern-day nonwovens, with the advent of new technologies, such fabrics are manufactured with different techniques depending on the type of constituent fibres, their applications and required characteristics. Various kinds of nonwovens are available in the market these days; their classification is given in the next section.

2 Classification of Nonwovens

Nonwovens can be divided into many sub-groups depending on their fibres, planar density, web forming and web bonding conditions as well as fibre geometric characteristics, as shown in Fig. 1.

A mechanical behaviour of nonwovens depends on many factors such as manufacturing parameters, material of constituent fibres etc. Changes in any of these factors can bring enormous variation in the behaviour of the fabric [2, 4, 6, 14, 32, 40, 49]. As a result, different types of nonwovens possess different characteristics and exhibit distinct behaviours. Hence, in order to define a nonwoven a complete set of information including web-forming and web-bonding technique, geometric and material properties of fibres, a type of their distribution and planar density is required. This chapter is focused mostly on low-density calendered bonded nonwovens manufactured with staple monocomponent polypropylene based fibres. A brief introduction of thermal bonding and its parameters affecting mechanical properties of the end product is given in the following sections.

---

[1] Information in this section on history of nonwovens is taken from Burkett [9] and Laufer [38]. The reader is referred to these works for more details.

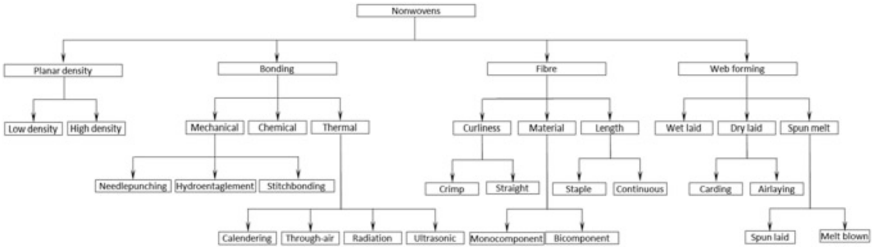

Fig. 1 Classification of nonwovens

3 Thermally Bonded Nonwovens

Thermal bonding is a process exploiting thermoplastic properties of synthetic fibres to form bonds under controlled heating. Thus, a thermoplastic component must be present in the constituent fibre or in the form of powder, film or as a sheath part of bicomponent fibres. In practice, heat is applied during thermal bonding until the thermoplastic component becomes viscous and melts. As a result, the polymer flows by surface tension and capillary action to form fibre-to fibre crossover points at localized areas of heating. These localized regions are fixed with subsequent cooling forming the bond points [5, 41, 42, 53]. Thus, the thermal bonding process converts a web of fibres with weak bonds between them into a tenacious fabric. Nowadays, thermal bonding is one of the most widely used technologies to manufacture nonwovens [6, 42, 43]. The viability of thermal bonding lies in its several advantages compared to other manufacturing processes of nonwovens. The most important of them are:

- less capital investment [47];
- lower manufacturing cost [6];
- higher production rate [1, 6];
- better control of nonwoven properties [1];
- lower environmental impact (material can be 100 % recyclable) [53];

There are several types of thermal bonding processes, such as hot calendering, through-air bonding, ultrasonic bonding, and radiant bonding [24]. Since thermally calendered nonwovens are used as a representative material for fibrous networks in this study, a further discussion is focused on this type of thermal bonding process.

During calender bonding, fibres are joined together by applying certain conditions, i.e. temperature and pressure; these external conditions are provided by two hot rolls pressed against each other. The surface design of these rolls can be smooth or have an embossed pattern. When the fibres are passed through these rolls, the temperature and pressure involved cause the fibres to melts and diffuse with other fibres resulting in bonding of a fabric. The process of transferring a fibre web into the nonwoven fabric is shown in Fig. 2.

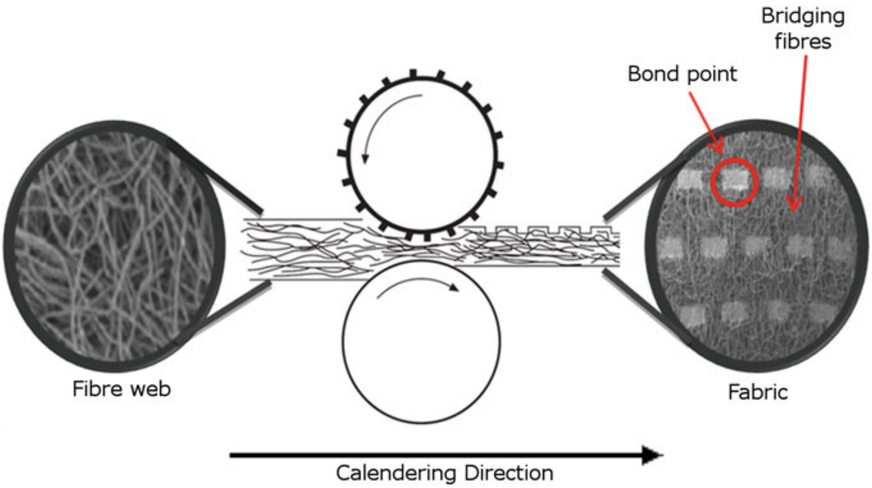

Fig. 2 Typical hot calendering process

Smooth rollers are designed to heat the entire surface of the web. Therefore, binder fibres produce bonding at all crossover points resulting in thin and stiff fabric. In contrast, engraved rollers result in localised melting and diffusion of the fibres only at their raised areas resulting in bonded spots on subsequent cooling (see Fig. 2) [7, 27]. Therefore, nonwovens manufactured with thermal bonding consist of two distinct regions: a fibrous web and bond points (Fig. 2). Bond points formed by partial melting of fibres in regions with a raised pattern on the calender surface are connected by fibrous matrix in calendered bonded nonwovens.

4 Mechanical Anisotropy

Due to the nature of web-formation and bonding processes, fibres in a nonwoven are not completely randomly distributed but predominantly oriented along the direction, in which the fabric was produced. This preferential orientation of fibres in nonwoven materials causes their anisotropic mechanical properties [32, 42] and it is the most prominent feature of their mechanical behaviour. Mechanical anisotropy of nonwovens due to a preferential orientation distribution of their fibres affect a relation between neighbouring bond points connected by fibrous matrix and, thus, the overall behaviour of the fabric [46]. Therefore, accurate determination and implementation of fibre orientation and a bond pattern into a computational model have vital importance for successful prediction of deformational behaviour as well as damage initiation and evolution processes of nonwovens.

The level of anisotropy in nonwovens is much higher than those of their woven counterparts, which have different mechanical properties in two principal directions, namely, warp and weft [48]. In the case of nonwovens, two principle directions—machine direction (MD) and cross direction (CD)—are used to characterise the anisotropy. MD is a longitudinal direction of a fabric corresponding to the manufacturing direction of the nonwoven. CD is perpendicular to MD in the plane of web.

The orientation distribution of fibres is one of the main factors defining specific features of mechanical behaviour of nonwoven materials. A "fibres' distribution function" was introduced for the first time to represent the fibre orientation in the fibrous media by Cox [13]. After this, the orientation distribution function (ODF) became a common way to deal with the character of distribution of fibres. The ODF quantifies the level of anisotropy of fibre matrix within the nonwoven material. Since, the randomness in a fabric's microstructure characterises its anisotropic behaviour, determination of its ODF is essential for predicting a direction-dependent mechanical behaviour of the fabric [62, 64].

Many studies were done to determine the ODF of fibrous networks. Initially, the phenomenon of dichroism and birefringence was suggested to determine the ODF. Then, the development of computers and imaging devices made it possible to determine ODF directly from the images of the fibrous network. The development of different techniques is presented in Table 1 in a chronological order.

Currently, two main methods are used to determine ODF of textiles: Fast Fourier Transform (FFT) and Hough Transform (HT). A Fast Fourier Transform is one of the most useful techniques in the field of image processing [64]. It is an indirect method, which decomposes the image from its spatial domain of intensities into a frequency domain. There are some drawbacks associated with this technique, e.g. lighting conditions can affect the results or binarized image may give a false ODF. Using the HT method, fibres in a fabric could be detected via straight-line segments [65]. The main advantage of HT over FFT is that the results are relatively less affected by the image noise [25].

Table 1 Techniques used for computing ODF

Technique	**Author(s)**	**Year**
Visual method based on directional phenomena of dichroism and birefringence, directly from the fibrous media	Hearle and Stevenson	[28]
Zero-span tensile testing method	Kallmes	[31]
Optical method based on illumination of fibres in a known direction with light microscopy	Chudleigh	[10]
Computer system based on a light-diffraction phenomenon	Stenemur	[58]
Random sampling algorithm and software to pick random fibres and trace them	Huang and Bresee	[26]
Skeletonization algorithm to extract the ODF from the images taken with a CCD camera	Xu and Ting	[64]
Software based on Fast Fourier Transform (FFT)	Kim and Pourdeyhimi	[34]
Hough Transform of images	Demirci et al.	[16]

In addition to randomness of the microstructure and a type of bond-point geometry, crimp of fibres also contributes to mechanical behaviour of nonwovens. Crimp is defined as a successive waviness of fibres induced mechanically or chemically [8]. Unlike natural fibres, synthetic fibres such as polymer-based ones are straight when they are extruded. These fibres do not have sufficient cohesion between them to form a web. Hence, crimp is introduced in these fibres to provide appropriate fibre-to-fibre cohesion and make it possible to process these fibres with the machinery originally developed for natural fibres. Fibre crimp is beneficial not only for manufacture of fabrics but also improves their desirable properties such as wrinkle resistance, moisture absorption, wear comfort due to porosity, warmness etc. [3].

Due to crimp and a random spatial distribution, not all the fibres are under the same loading even under externally uniform load. Crimped fibres cause considerable variations in mechanical behaviour compared to their uncrimped (straight) counterparts [56]. Therefore, crimp is an important factor in determining the mechanical behaviour of nonwovens, especially during their initial deformation.

The effect of fibre crimp on the properties of fibrous network was first studied by Hearle and Stevenson [28]. A micromechanical model to predict the behaviour of nonwoven was developed by Rawal [49] based on the earlier work by Adanur and Liao [2]. In this model, a fibre curl factor was introduced to develop the understanding of the effect of loading on a single curled fibre.

5 Deformation and Damage Behaviour

Nonwoven fabrics have unique and complex deformation and damage behaviours. Many researchers have endeavoured to investigate deformation of nonwovens, which combines features of other engineering materials, e.g. anisotropy similar to that of woven materials and viscoelasticity as in polymers. Two distinct regions of a calendar-bonded nonwoven material—bond points and fibrous matrix—have different microstructures and both regions play their role in overall deformation of, as well as damage initiation and propagation in, the fabric.

Under loading, fibres in the fabric start to re-orient and straighten themselves along the loading direction immediately after application of tensile deformation. As strain increases, they become aligned along the loading direction resulting in gradual transverse contraction from the grips on both sides of the fabric to the area of maximum contraction in the middle of the specimen. Once the fibres are uncurled and aligned along the loading direction, they undergo large elastic-plastic deformation and the maximum load was attained under this condition without any evidence of fibre fracture. As soon as fibres reach their stress or strain threshold, they fail resulting in localization of damage and development of fracture zones. These fracture zones are formed by surviving straight fibres aligned along the loading direction. Further fibre failures cause a growth of such fracture zones followed by the ultimate failure of the fabric. In tensile tests, rotation of bond-points was observed without significant deformation of them. Still, it should be noted that they play an important role in damage behaviour of thermally bonded nonwovens since fibres mostly break at the bond-point periphery. The phenomena of deformation and damage initiation as well as progression were found to be the same in both MD and CD, with the only difference that rotation of fibres before participating in load bearing was very large in CD as compared to that in MD. The sequence of these phenomena is presented in Fig. 3, demonstrating images of nonwovens at increasing levels of the overall strain.

Deformation characteristics of nonwoven materials vary with the direction of loading, due to their anisotropic behaviour. Usually, the MD and CD directions are used to explain these characteristics of nonwovens [32, 33, 36].

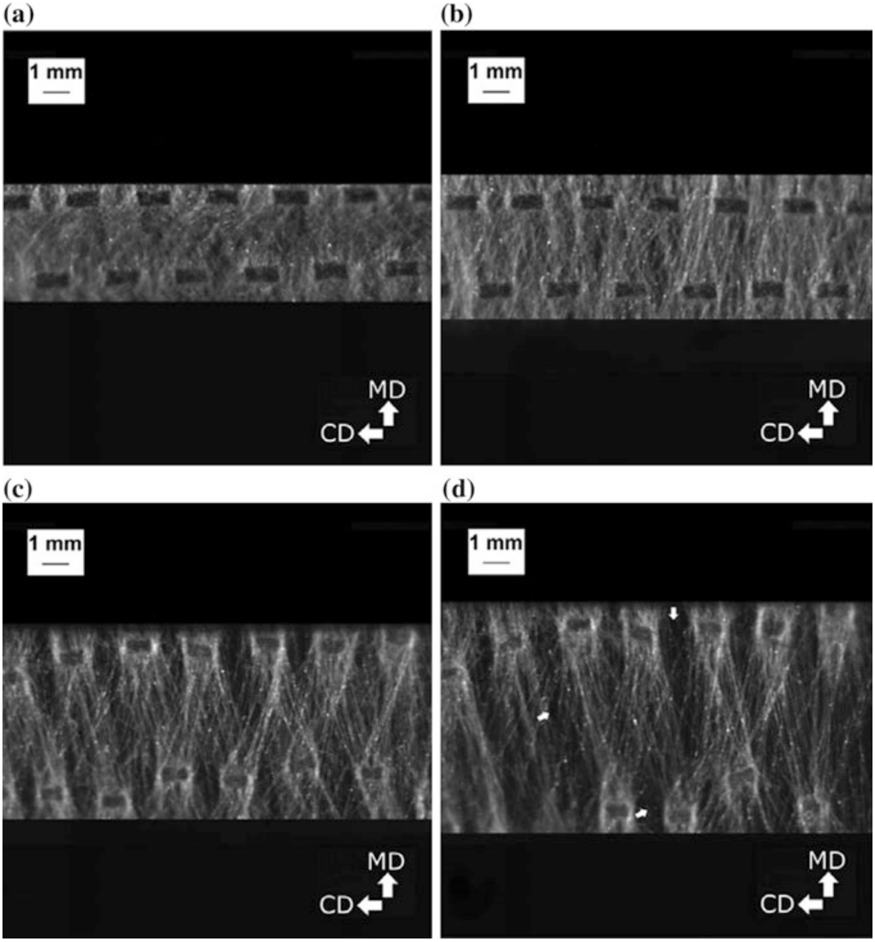

Fig. 3 Deformation and damage mechanisms in low-density thermally bonded nonwoven in tensile tests at various levels of macroscopic strain **a** 0 %; **b** 25 %; **c** 50 %; **d** 80 %. Loading direction was vertical (*Arrows* in **d** indicate fracture zones) (Faruhk et al. [19])

Deformation and damage processes of nonwovens involve many mechanisms that affect the overall behaviour of nonwovens, e.g. reorientation of fibres along the loading direction, straightening of crimped fibres, fibre sliding and stretching etc. [33, 50]. The complexity of deformation and damage behaviours of nonwoven materials until their failure can be referred to the fact that these mechanisms act simultaneously [51]. The deformation behaviour of a nonwoven is governed mostly by the loading direction with respect to the preferred orientation of constituent fibres. The type of the load acting on individual fibres during the deformation and damage processes of the fabric depends on their orientation with regard to the direction of loading [32]. Thus, a random microstructure of a nonwoven results in direction dependency of its deformation and damage behaviours. The extent of mechanical anisotropy of deformation behaviour of thermally bonded nonwovens is depicted in Fig. 4.

According to Fig. 3, the extent of deformation of the nonwoven materials in MD is less than that in CD at any load value. Thus, nonwoven materials have higher strength along MD than CD. This is a typical behaviour of spunlaid nonwovens that are manufactured by direct conversion of polymers into endless filaments and laid directly on a conveyor belt. This tend to have the filaments oriented along the conveyor belt resulting in a fabric with fibres preferentially orientation along MD. Thus, a relatively small reorientation of fibres occurs when such nonwoven materials are deformed along MD, while the loading of material in CD results in significant rotations of a large number of fibres towards the loading direction and subsequent repositioning of bond points.

As a result, a very gradual growth of damage was observed until failure of fabric along MD after small-scale reorientation of fibres. In contrast, large reorientation of fibres without damage initiation defined a large part of deformation along CD, followed by a rapid growth of damage and failure of the fabric. The preferential orientation of fibres in fabrics results in different shapes of failure loci as shown in

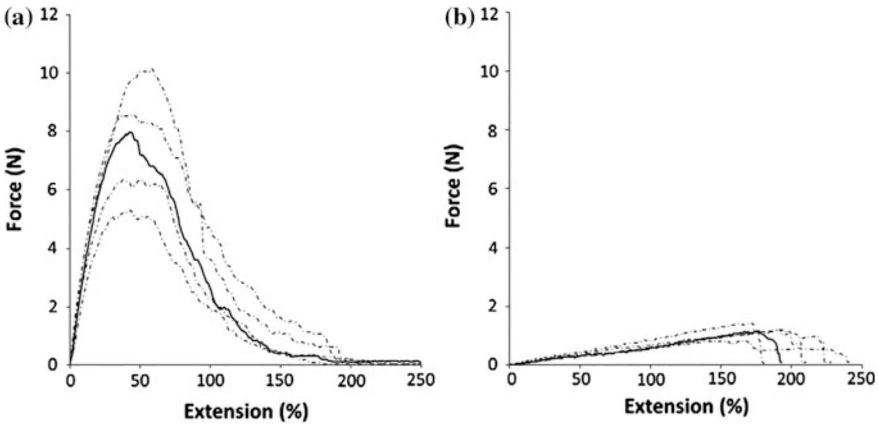

Fig. 4 Force—extension curves for rectangular specimen in tension at strain rate of 0.1 s^{-1} along MD (**a**) and CD (**b**) (20 g/m^2) [22]

Fig. 5 Failure of nonwovens in various loading directions [32]

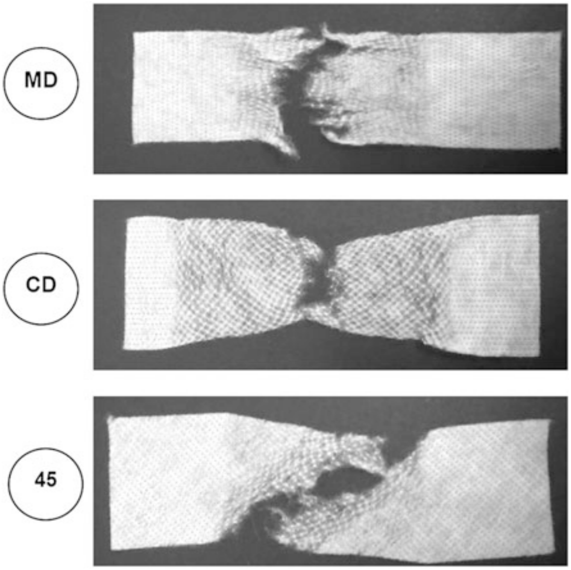

Fig. 4. The fabric's mechanical response along MD presents a stiffer behaviour, usually with smaller elongation at break as compared to CD as shown in Fig. 3. For loading in MD, the maximum load is attained at lower fabric's extension as compared to that in CD followed by a gradual process of fibre failure resulting in a bell-shaped force-extension curve. In contrast, a rapid fibre-failure process following large fabric's extension observed in CD results in a sudden drop on the force-extension curve. Failure loci in the specimen stretched along MD and CD are practically similar; however, loading along directions between these two principal ones results in different failure loci. Thus, due to anisotropic behaviour, not only deformation and damage initiation but damage evolution and ultimate failure of nonwovens have directional dependency. Heterogeneity in the microstructure of nonwoven fabrics causes anisotropic failure behaviour as shown in Fig. 5. The fabric failure occurs by tearing of fibres in MD and CD, while for the test at angles between MD and CD, it fails by shearing at preferred fibre direction [32, 42].

6 Factors Affecting Properties of Nonwovens

As discussed, a point bonded nonwoven consists of bond points and a fibrous web linking these bond points; both regions important roles in the overall mechanical behaviour of nonwovens [11]. The properties of both regions are affected by a number of manufacturing parameters, which ultimately define the deformation and damage behaviours of nonwovens. Besides, the material properties and composition of constituent fibres are prominent in determining the mechanical behaviour of nonwovens. Some important parameters that affect the mechanical behaviour of nonwoven are briefly described in this section.

The mechanical behaviour of thermally bonded nonwovens is affected by the following parameters [1]:

- bonding temperature;
- fibre composition and material properties;
- calendering pressure;
- web speed;
- morphology and form of fibres;
- orientation distribution of fibres;
- crimp in fibres;

Details on the effect of this parameters on the behaviour of nonwovens is given below.

6.1 Bonding Temperature

During thermal bonding, fibres are heated up to a certain temperature under pressure resulting in melting of fibres locally and produce a rigid bond on solidification. The ultimate tensile strength of a fabric structure increases with increase in bonding temperature until the temperature reaches its certain threshold value after that the fabric is load-bearing capacity decreases with a further increase in temperature [18, 23, 42, 53]. Thus, bond points of nonwovens bonded at temperatures below a certain level are immature, and fabric failure starts with disintegration of bond points because of insufficient fusion of fibres; this is known as *under-bonding*. Conversely, if nonwovens are bonded at temperature higher than the mentioned threshold, fabric failure starts with breaking of fibres at bond periphery leaving the bonds intact called *over-bonding*. The difference between these temperature values are referred as an optimum temperature window of a fabric. The optimal temperature range varies for fabrics composed of different materials [1]. The optimal temperature window for polypropylene-based nonwovens is 150–160 °C. The fabric bonded at optimal temperature is called *well-bonded fabric*.

6.2 Fibre Structure and Properties

Thermoplastic materials and blends containing fibres can be used to manufacture thermally bonded fabrics. According to the composition of fibres, two of their main types are used for the thermal bonding: monocomponent and bicomponent.

Table 2 Types of bicomponent fibres

Fibre type	Schematic diagram
Side by side	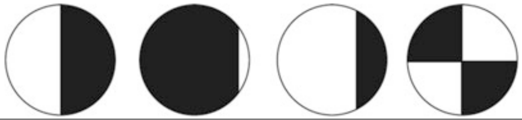
Sheath core	
Islands in the sea	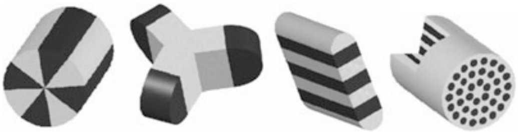

In monocomponent fibres, the entire fabric structure is produced from a single type of material. In other words, this single material determines the properties of both parts of the fabric: the fibrous network and bond points. The major disadvantage of the use of monocomponent fibres is a narrow bonding-temperature window, which is difficult to realize in the manufacturing process. Furthermore, the fibrous structure is discontinuous as formation of bond points is succeeded with the melting of fibres [14]. These problems can be rectified by using bicomponent fibres. Such fibres are composed of two different polymer components, one of which with a lower melting point that serves for bonding, while the other has a higher melting point and improves for tensile strength. When these fibres are exposed to the manufacture temperature between the melting points of two polymers, the one with the lower melting point melts and joins the neighbouring polymer under pressure and solidifies with cooling resulting in bond points. The material with the higher melting point does not melt and maintains its structure during the manufacturing process. Thus, bicomponent fibres retain their continuity in bond points, and the fabric can withstand higher stresses due to its increased strength [60]. Various types of cross-sections of bicomponent fibres are given in Table 2.

6.3 Calendering Pressure

During thermal bonding, a fibrous web is passed between two hot calenders; as a result fibres melt locally under high temperature and pressure to form the bonds on subsequent cooling. Such compression is related to the melting point of fibres forming nonwovens. The pressure applied in the bonding process performs the following tasks [1]:

- to augment heat transfer from rollers to the fibres through conduction;
- to increase the contact area of fibres by assisting in plastic flow of fibre material at bonding temperature;
- to restrict the flow of material at a bond spot.

Therefore, appropriate compression pressure is one of the pre-requisites for optimal bonding. Michielsen et al. [42] found that beyond a certain minimum value of pressure, fabric's performance was affected slightly or not at all. The minimum appropriate pressure value adequate for rigid bonding depends on the contact geometry, thermodynamic conditions and web speed in the bonding process.

6.4 Web Speed

The web speed is the speed at which a nonwoven is produced. In order to reduce the manufacturing cost of nonwovens, a high web speed is desired. As the web speed is increased, the time available to melt the material sufficiently to form rigid bond points on subsequent cooling is decreased. This issue can be resolved by increasing the bonding temperature. This approach is applicable only up to a certain point, after which an increase in speed does not provide satisfactory bonding regardless of the level of calendering temperature. Thus, the web-processing speed is defined by the optimal temperature window of nonwovens. At higher processing speeds, the calendering temperature window gets narrower and ultimately vanishes. That is the point after which no further processing of nonwovens with adequate bonding is possible [42].

6.5 Morphology and Form of Fibres

A form and morphology of fibres have a significant effect on the overall properties of nonwovens. There are many parameters defining the form and morphology of a fibre, e.g. molecular weight, linearity and orientation of the molecules, length of fibres, and presence of crystalline and amorphous zones. A length of fibres is also considered as parameters related to the form of fibres. A length of polymer molecules affects the attraction forces between the molecules during bonding, which is responsible for mechanical characteristics of nonwovens. Longer molecules can associate closer together during bonding and produce stronger bonds [59].

Ultimate tensile strength of fibres can be associated with molecular orientation and is determined by their birefringence [23]. Mechanical properties of polymer-based fibres also depend on a temperature history, which they were exposed to during their manufacturing process. Thus, any change in temperature during manufacturing stages can affect deformation and damage behaviours of nonwovens.

Hence, in order to accurately predict their mechanical behaviour up to the onset of fracture, temperature variations which the fibres were exposed to during formation of web must be known.

6.6 Orientation Distribution of Fibres

Orientation distribution of fibres plays a vital role in determining the most prominent feature of nonwovens—their mechanical anisotropy. Due to the nature of web formation and bonding processes, fibres in a nonwoven are not oriented fully randomly but predominantly aligned along the direction, in which the fabric is being produced. This preferential orientation of fibres in nonwoven materials causes their anisotropic mechanical properties [32, 42] and it is the most prominent feature of their mechanical behaviour. Mechanical anisotropy of nonwovens due to the preferential orientation distribution of their fibres affect the relation between neighbouring bond points connected by fibrous matrix and, thus, the overall behaviour of the fabric [46]. Fibres are predominantly orientated along MD in thermally bonded nonwovens offering higher resistance to deformation as compared to CD. Due to this orientation of fibres, the maximum extension at failure along CD is higher than MD.

6.7 Crimp in Fibres

When dealing with anisotropy and determination of the orientation distribution function, an important factor is the crimp in fibres. It has effects on both: it can define the ODF feature, especially for small window sizes, and an initial deformation behaviour of the fabric. Defined as successive waviness of fibres induced mechanically or chemically [8], crimp can be a dominant factor at small levels of stretching as shown in Fig. 6.

Crimp in fibres result in geometrical non-linearity of nonwovens and makes it more difficult to simulate their actual mechanical behaviour. Still, it is important for processing of fibres responsible e.g. for appropriate fibre-to-fibre cohesion for carding, drawing and can enhance some desirable properties in fabrics such as fabric bulk [12]. A mechanical behaviour of a crimped fibre is different from that of a straight fibre as shown in Fig. 6. A load-elongation curve of the crimped fibre consists of a crimp-removal part (A–B in Fig. 6) and tensile part (B–C in Fig. 6). Crimp-removal part defines a less stiff initial behaviour of fibres. In order to predict the behaviour of nonwovens accurately, the crimp should be considered.

Fig. 6 Initial portion of load-elongation curve of straight and crimped fibre [8]

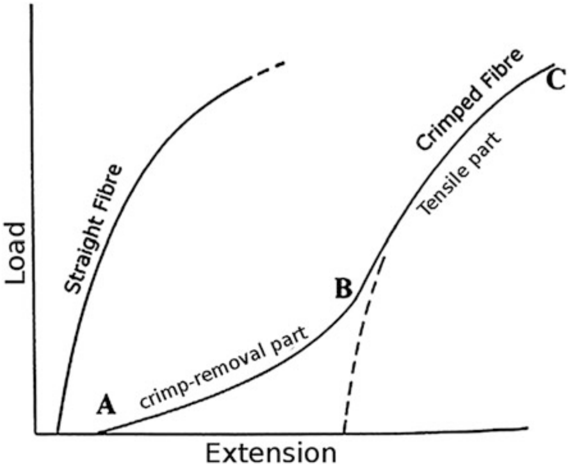

6.8 *Geometry of Bond Points*

In thermally calendered bonded nonwovens, shape, size and pattern of bond points affect the overall properties of fibres such as tensile breaking strength, drapability and softness [23, 26]. Due to the cost and lead time associated with engraved calender rolls, it is very difficult to establish a relation between bond-point geometry and fabric properties. Almost $1.5 M dollar and minimum 4 months' time is required to test the effect of each new bond-point geometry [63]. Therefore, most of thermally bonded fabrics available commercially are not optimally designed. Very few studies were performed to use computer simulations to predict the mechanical behaviour of nonwovens as a function of bond point geometry [26, 29, 55]. However, all of these models predicted the effect of bond point geometry only on the initial deformation behaviour of the fabric, without considering damage initiation and propagation. Thus, there is a need for parametric computational models that could incorporate elastic-plastic and viscous properties of the constituent fibres and their randomness alongside with shape and pattern of bond points to simulate the realistic deformation and damage behaviours of nonwovens.

7 Finite-Element Modelling of Nonwovens

Several attempts were made to simulate the behaviour of nonwoven materials using a finite-element method. These models were developed using different approaches for idealization of fabric's network geometry. A brief overview of various approaches in the literature to simulate the behaviour of nonwovens using finite-element modelling is given in this section.

A first type of models presented nonwovens as continuum to analyse their macroscopic mechanical response. Demirci et al. [15–17] idealized the geometry of nonwoven fabrics with a continuum model based on orthotropic symmetric planes. Randomness of the fabric's microstructure in terms of the orientation distribution function was introduced as orthotropic parameters calculated by using specially developed software. This scheme was very useful for predicting a stress-strain behaviour of high-density nonwovens accurately but damage was not introduced into the model. Since the model was based on the continuum approach, it was incapable to account for mechanisms involved in deformation and damage of nonwovens. Ridruejo et al. [52] introduced a continuum model to predict the meso-level response of the fabric but fibres were not explicitly introduced into that model; rather, a constitutive relation concerning with fibre orientation distribution was developed. Such a continuum model was unable to mimic the actual microstructure; and hence mechanisms of fabric's deformation. Besides, damage was implemented into the model in a phenomenological way.

The second approach, based on a composite laminate model, incorporating the effect of non-uniform fibre orientation distribution, was used in [4, 39]. A nonwoven, assumed as continuum, was made of several layers of fibres. Within each layer fibres were parallel oriented to each other. The layers of different fibre orientation were stacked and bonded along the entire contacting interface. All the fibres in one layer were oriented in the same direction. These fibres were bound together at nodal points of finite-elements mesh. The model deals with deformation of fabric and breaking of individual fibres incrementally. Such models were found to produce satisfactory results in agreement with experimental data including aspects of fibre anisotropy arising from a non-uniform orientation distribution of fibres, particularly in a small-strain regime. However, their representation of real deformation mechanisms such as non-uniform deformation and reorientation of fibres was inadequate since fibres were fixed within the layers, which could not slide on top of each other.

In an effort to incorporate the realistic effect of non-uniform microstructure of nonwovens into the model, the third approach based on homogenization of the model using a representative volume element (RVE) was used in literature. Petterson [45] introduced a model to predict the macroscopic response of the fabric by homogenizing the behaviour of a unit-cell incorporating a random distribution of fibres' orientation. This model was later modified by Hearle and Stevenson [28] and again by Kothari and Patel [37] to include the effects of fibre and a creep response of individual fibres, respectively. Still, in these models, some inelastic deformation mechanisms such as irrecoverable textural evolution were missing. More recently, Silberstein et al. [57] introduced a model based on a similar RVE-based technique to predict a macroscopic behaviour of the fabric. The model consists of a multilayer triangular network and uses a homogenization technique to predict a response to monotonic and cyclic loading. Such models based on the homogenization technique do not predict localization of damage and changes in material's microstructure caused by this damage.

The fourth approach incorporates the randomness of a nonwoven material into the model by direct introduction of fibres to simulate realistic deformation and damage behaviours of nonwovens. In this context, Mueller and Kochmann [44] proposed a FE model to simulate the behaviour of thermally bonded nonwovens. In that model, bond points were modelled as an element consisting of two regions: a bond core and a boundary zone. The boundary zone represents the deformed fibres and partly bonded fibres at the periphery of the bond points. The fibres were modelled as truss elements; each truss element represented a fibre bundle as the behaviour of several fibres was combined and mapped onto these elements. These truss elements combined the bond points in a unit cell. With this model, the effects of geometry of bond points on the behaviour of nonwovens were also investigated. However, it was almost impossible to incorporate the randomness in the microstructure of the nonwoven into the model as the model was composed of symmetric unit cells, and there was limited number of nodes on the bond point. Moreover, it failed to mimic the microstructure of nonwoven fabrics. Advancement of this approach was used by Hou et al. [30]; Sabuncuoglu et al. [54]; Farukh et al. [19–21]. A finite-element model based on direct introduction of fibres according to a realistic orientation distribution function was developed. This model is computationally expensive but can provide insight of deformation and damage behaviour of thermally bonded nonwoven network.

8 Conclusions

This paper summarises information on deformation behaviour of, as well as damage initiation and propagation in, thermally bonded fibrous networks. Nonwovens demonstrate complex deformation patterns and damage scenarios due to the presence of two regions with different structure—bond points and fibrous networks. The dominant deformation and damage phenomena under tensile loading involve rotation of fibres along the loading direction and progressive failure of fibres upon reaching their failure threshold. This process of fibre failure results in localized fracture zones, which ultimately lead to rupture of the fabric. The deformation and damage mechanisms are affected by a specific character of oriented microstructure responsible for the anisotropic nature of this type of networks. The relation between mechanical anisotropy of these nonwovens and random orientation of their fibres can be described using the fibres' orientation distribution function. Random orientation of individual fibres is quantified in terms of this ODF in order to determine the material's anisotropy. Several techniques are available in literature to determine ODF; however, the most recent technique is based on Hough Transform. Along with preferential orientation of fibres, there are several other factors that affect mechanical behaviour of thermally bonded fibrous networks and are described in this paper.

In order to predict the complex deformation behaviour, many modelling schemes have been suggested in the literature. These models are based on different simulation strategies and suitable for different conditions. The continuous modelling technique is best suited for macro-scale modelling of dense nonwovens, whereas the RVE-based schemes and complex fibre-network techniques are appropriate for meso- and micro-scale modelling.

References

1. Albrecht, W., Fuchs, H., Kittelmann, W.: Nonwoven Fabrics: Raw Materials, Manufacture, Applications, Characteristics, Testing Processes. Wiley-VCH, Weinheim (2003)
2. Adanur, S., Liao, T.: Fiber arrangement characteristics and their effects on nonwoven tensile behavior. Text. Res. J. **69**(11), 816–824 (1999)
3. Barach, J.L., Rainard, L.W.: Effect of crimp on fiber behavior. Part II: Addition of crimp to wool fibers and its effect on fiber properties. Text. Res. J. **20**, 308–316 (1950)
4. Batra, S.K.: Basics of Nonwoven Fabrics and Technology, NCRC. NC State University, Raleigh (1998)
5. Batra, S.K., Pourdeyhimi, B.: Introduction to Nonwovens Technology. DEStech Publications, Lancaster (2012)
6. Bhat, G.S., Jangala, P.K., Spruiell, J.E.: Thermal bonding of polypropylene nonwovens: effect of bonding variables on the structure and properties of the fabrics. J. Appl. Polym. Sci. **92**(6), 3593–3600 (2004)
7. Bhat, G.S., Malkan, S.R.: Extruded continuous filament nonwovens: advances in scientific aspects. J. Appl. Polym. Sci. **83**(3), 572–585 (2002)
8. Brown, A.: Measurement of crimp in single fibers. Text. Res. J. **25**(12), 969–976 (1955)
9. Burkett, M.E.: The Art of Felt Maker. Abbot Hall Art Gallery, Kendal (1979)
10. Chudleigh, P.W.: Image formation of fibers and fibers assemblies. Text. Res. J. **54**, 813 (1984)
11. Chidambaram, A., Davis, H., Batra, S.K. (ed.): Strength loss in thermally bonded polypropylene fibers. In: INTC 2000 Conference, Dallas (2000)
12. Cook, R.D., Malkus, D. S., Plesha, M.E.: Concepts and Applications of Finite Element Analysis. Wiley, New York (1984)
13. Cox, H.L.: The elasticity and strength of paper and other fibrous materials. Br. J. Appl. Phys. **3**, 72–79 (1952)
14. Datla, V.M.: The influence of fiber properties and processing conditions on the characteristics of needled fabrics. Master's thesis, North Carolina State University USA, (2002)
15. Demirci, E.: Mechanical behaviour of thermally bonded bicomponent fibre nonwovens experimental analysis and numerical modelling. Ph.D. thesis, Loughborough University (2010)
16. Demirci, E., Acar, M., Pourdeyhimi, B., Silberschmidt, V.V.: Computation of mechanical anisotropy in thermally bonded bicomponent fibre nonwovens. Comput. Mater. Sci. **52**(1), 157–163 (2011)
17. Demirci, E., Acar, M., Pourdeyhimi, B., Silberschmidt, V.V.: Finite element modelling of thermally bonded bicomponent fibre nonwovens: tensile behaviour. Comput. Mater. Sci. **50** (4), 1286–1291 (2011)
18. Dharmadhikary, R.K., Gilmore, T.F., Davis, H.A., Batra, S.K.: Thermal bonding of nonwoven fabrics. Text. Prog. **26**(2), 1–37 (1999)
19. Farukh, F., Demirci, E., Acar, M., Pourdeyhimi, B., Silberschmidt, V.V.: Meso-scale deformation and damage in thermally bonded nonwovens. J. Mater. Sci. **48**(6), 2334–2345 (2013)
20. Farukh, F., Demirci, E., Sabuncuoğlu, B., Acar, M., Pourdeyhimi, B., Silberschmidt, V.V.: Characterisation and numerical modelling of complex deformation behaviour in thermally bonded nonwovens. Comput. Mater. Sci. **71**, 165–171 (2013)

21. Farukh, F., Demirci, E., Sabuncuoğlu, B., Acar, M., Pourdeyhimi, B., Silberschmidt, V.V.: Numerical modelling of damage initiation in low-density thermally bonded nonwovens. Comput. Mater. Sci. **64**, 112–115 (2012)
22. Farukh, F., Demirci, E., Sabuncuoğlu, B., Acar, M., Pourdeyhimi, B., Silberschmidt, V.V.: Numerical analysis of progressive damage in nonwoven fibrous networks under tension. Int. J. Solids Struct. **51**, 1670–1685 (2014)
23. Fedorova, N., Verenich, S., Pourdeyhimi, B.: Strength optimization of thermally bonded spunbond nonwovens. J. Eng. Fibers Fabr. **2**(1), 38–48 (2007)
24. Gao, X., Huang, H.Y.:, Thermal bonding of nonwoven fabrics. http://www.engr.utk.edu/mse/pages/Textiles/Thermal Bonding.htm (2004). Accessed 29 Aug 2011
25. Ghassemieh, E., Acar, M., Versteeg, H.: Microstructural analysis of non-woven fabrics using scanning electron microscopy and image processing. part 1: development and verification of the methods. Proc. Instit. Mech. Eng. Part L: J. Mater. Des. Appl. **216**(3), 199–207 (2002)
26. Gilmore, T.F., Mi, Z.X., Batra, S.K.: Effect of bond point design and bond strength on the load-deformation of point bonded nonwovens: a computer-based study.In: nonwovens conference proceedings. NCRC, North Carolina (1993)
27. Hegde, R.R., Bhat, G.S., Campbell, R.A.: Thermal bonding of polypropylene films and fibers. J. Appl. Polym. Sci. **110**(5), 3047–3058 (2008)
28. Hearle, J.W.S., Stevenson, P.J.: Studies in nonwoven fabrics. Part IV: Prediction of tensile properties. Text. Res. J. **34**(3), 181–191 (1964)
29. Hou, X.: Experimental and Numerical Analysis of Deformation Of Low-Density Thermally Bonded Nonwovens, PhD Thesis, Loughborough University. (2010)
30. Hou, X., Acar, M., Silberschmidt, V.V.: 2D finite element analysis of thermally bonded nonwoven materials: continuous and discontinuous models. Comput. Mater. Sci. **46**(3), 700–707 (2009)
31. Kallmes, O.J.: Technique for determining the fibre orientation distribution function throughout the thickness of sheet. Tappi J. **52**(4), 482–485 (1969)
32. Kim, H.S.: Orthotropic theory for the prediction of mechanical performance in thermally point-bonded nonwovens. Fibers Ploym. **5**(2), 139–144 (2004)
33. Kim, H.S., Pourdeyhimi, B., Abhiraman, A., Desai, P.: Characterizing structural changes in nonwoven fabrics during load-deformation experiments. J. Text. Apparel **1**(1), 1–6 (2000)
34. Kim, H.S., Pourdeyhimi, B.: Computational modeling of mechanical performance in thermally point bonded nonwovens. J. Text. Apparel, Technol. Manag. **1**(4), 1–7 (2001)
35. Kim, H.S., Pourdeyhimi, B., Desai, P., Abhiraman, A.S.: Anisotropy in the mechanical properties of thermally spot-bonded nonwovens: experimental observations. Text. Res. J. **71** (11), 965–976 (2001)
36. Kim, H.S., Deshpande, A., Pourdeyhimi, B., Abhiraman, A.S., Desai, P.: Characterizing structural changes in point-bonded nonwoven fabrics during load-deformation experiments. Text. Res. J. **71**(2), 157–164 (2001)
37. Kothari, V.K., Patel, P.C.: Theoretical model for predicting creep behaviour of nonwoven fabrics. Indian J. Fibre Text. Res. **26**, 273–279 (2001)
38. Laufer, B.: The early history of felt making. Am. Anthropol. **32**(1), 1–18 (1930)
39. Liao, T.Y., Adanur, S.: Predicting the mechanical properties of nonwoven geotextiles with the finite element method. Text. Res. J. **67**(10), 753–760 (1997)
40. Lin, J., Xu, Z., Lei, C., Lou, C.: Effect of Fiber Arrangement on the Mechanical Properties of Thermally Bonded Nonwoven Fabrics. Text. Res. J. **73**(10), 917–920 (2003)
41. Michielsen, S., Wang, X.: Rapid morphology (property) changes at the bond periphery in thermal point-bonded nonwovens. Int. Nonwovens J. **11**(2), 35–38 (2002)
42. Michielsen, S., Pourdeyhimi, B., Desai, P.: Review of thermally point-bonded nonwovens: materials, processes, and properties. J. Appl. Polym. Sci. **99**(5), 2489–2496 (2006)
43. Mishakov, V., Slutsker, G., Stalevich, A.: Modeling the viscoelasticity of nonwoven material with consideration of the irreversible strain component. Fibre Chem. **38**(1), 50–54 (2006)
44. Mueller, D.H., Kochmann, M.: Numerical modeling of thermobonded nonwovens. Int. Nonwovens J. **13**(1), 56–62 (2004)

45. Petterson, D.R.: “Mechanics of Nonwoven Fabrics”, Indutrial and Engineering Chemistry, vol. **51**(8), 902–903 (1959)
46. Pourdeyhimi, B., Ramanathan, R., Dent, R.: Measuring fiber orientation in nonwovens. Text. Res. J. **66**(11), 713–722 (1996)
47. Pourdeyhimi, B.: Mechanical performance of thermally bonded nonwovens. Notes, NC State University, NCRC, USA (2003)
48. Price, D.S., Jones, R., Harland, A.R.: Soccer ball anisotropy modelling. Mater. Sci. Eng., A **420**(1–2), 100–108 (2006)
49. Rawal, A.: A modified micromechanical model for the prediction of tensile behavior of nonwoven structures. J. Ind. Text. **36**(2), 133–149 (2006)
50. Ridruejo, A., González, C., LLorca, J.: Damage micromechanisms and notch sensitivity of glass-fiber non-woven felts: An experimental and numerical study. J. Mech. Phys. Solids. **58** (10), 1628–1645 (2010)
51. Ridruejo, A., González, C., LLorca, J.: Micromechanisms of deformation and fracture of polypropylene nonwoven fabrics. Int. J. Solids Struct. **48**(1), 153–162 (2011)
52. Ridruejo, A., González, C., LLorca, J.: A constitutive model for the in-plane mechanical behavior of nonwoven fabrics. Int. J. Solids Struct. **49**(1), 2215–2229 (2012)
53. Russell, S.J.: Handbook of Nonwovens. Woodhead, Cambridge (2007)
54. Sabuncuoglu, B., Acar, M., Silberschmidt, V.V.: A parametric finite element analysis method for low-density thermally bonded nonwovens. Comput. Mater. Sci. **52**(1), 164–170 (2012)
55. Sabuncuoglu, B.: Development of parametric finite element modelling methods for nonwoven materials including rate dependent material behaviour. Ph.D. thesis, Loughborough University (2012)
56. Shiffler, D.A.: An examination of the stress-strain curve of crimped polyethylene terephthalate staple fibers. J. Text. Inst. **86**(1), 1–9 (1995)
57. Silberstein, M.N., Lhai-Ling, P., Boyce, M.C.: Elastic-plastic behaviour of nonwoven fibrous mats. J. Mech. Phys. Solids **60**(2), 295–318 (2012)
58. Stenemur, B.: Method and device for monitoring fibre orientation distribution and web uniformity on running webs of paper and nonwoven based light diffraction phenomenon. INDA J. Nonwoven Res. **4**, 42–45 (1992)
59. Tanchis, G. (ed.): The Nonwovens, 1st edn. Fondazione Acimit, Italy (2008)
60. Wang, X.Y., Gong, R.H.: Thermally bonded nonwoven filters composed of bi-component polypropylene/polyester fiber. II. Relationships between fabric area density, air permeability, and pore size distribution. J. Appl. Polym. Sci. **102**(3), 2264–2275 (2006)
61. Wang, X., Michielsen, S.: Morphology gradients in thermally point-bonded poly(ethylene terephthalate) nonwovens. Text. Res. J. **72**(5), 394–398 (2002)
62. Wood, E.J.: Applying fourier and associated transforms to pattern characterization in textiles. Text. Res. J. **60**(4), 212–220 (1990)
63. Wust, C.J.: Private Communication (2013)
64. Xu, B., Ting, Y.: Measuring structural characteristics of fiber segments in nonwoven fabrics. Text. Res. J. **65**(1), 41–48 (1995)
65. Xu, B., Yu, L.: Determining fiber orientation distribution in nonwovens with hough transform techniques. Text. Res. J. **67**(8), 563–571 (1997)